Three dimensional representation and analysis of individual bead and packed bed scale chromatography using X-ray computed tomography and focused ion beam microscopy

A thesis submitted to University College London for the degree of Doctor of Engineering

Thomas Francis Johnson

In collaboration with Pall Biotech

Department of Biochemical Engineering

University College London

Bernard Katz building

London

WC1E 6BT

I, Thomas Francis Johnson, confirm that the work presented in this thesis is my own. Where information has been derived from other sources, I confirm that this has been indicated in the thesis.

………………………………

Date:

Acknowledgements

I would firstly like to thank Professors Dan Bracewell and Paul Shearing for all of their support, guidance and advice imparted during the four years of the project at UCL. Several other people at university have been extremely helpful during this doctorate, notably Francesco Iacoviello, Josh Bailey, Leon Brown and Bernhard Tjaden from the EIL group and Greta Jasulaityte from Biochemical Engineering. Jim Davy, Mark Turmaine, Suguo Huo and Ecaterina Ware are thanked for their assistance concerning electron microscopy and focused ion beam microscopy at UCL, LCN and Imperial College London respectively.

I would also like to acknowledge the significant contribution from Pall Biotech at Portsmouth, particularly my industrial supervisors Peter Levison and John Welsh, who have been instrumental in organising the project and enabling me to perform research in an industrial setting. Dave Hayden, Rick Morris, Richard Gutman, Nigel Jackson, Jon Brown and Majid Rezai have been tremendously helpful during my time spent and working with Pall.

Lastly, I would like to extend to my gratitude to my family; parents Peter and Julie, brothers Andrew and Robbie, grandparents Keith and Joan, uncle Glenn, Roberto and finally Catrin.

Publications relating to thesis

The following publications have been produced during this project that forms the major part of the results presented in Chapters 2, 3 and 4, with the reference number provided.

TF Johnson, PR Levison, PR Shearing and DG Bracewell, **X-ray computed tomography of packed bed chromatography columns for three dimensional imaging and analysis.** Journal of Chromatography A, 2017, 10.1016/j.chroma.2017.01.013, Reference 169.

TF Johnson, JJ Bailey, F Iacoviello, J Welsh, PR Levison, PR Shearing and DG Bracewell, **Three dimensional characterisation of chromatography bead internal structure using X-ray computed tomography and focused ion beam microscopy.** Journal of Chromatography A, 2018, 10.1016/j.chroma.2018.06.054, Reference 160.

Abstract

Understanding the detailed, internal geometry of chromatography bead and packed bed structure remains a challenge, which is addressed in this thesis by using tomographic techniques to both visualise and quantify microstructural characteristics at both scales. Two main approaches were investigated for the purposes of producing accurate representations: X-ray computed tomography and focused ion beam microscopy, both providing high-resolution capability for imaging geometric features, enabling comparison between material types and techniques when considering suitability for chromatography structural research.

At the bead scale, X-ray computed tomography and focused ion beam microscopy were used for imaging and comparison of the three bead types, with optimal cubic pixel sizes of 32nm and 15nm achieved respectively. Despite the superior resolution attainable for focused ion beam microscopy, drawbacks of intensive preparation requirements and the necessity for physical slicing and thus destruction highlighted that pixel dimensions were not the only consideration for sub-micron tomographic imaging. Tortuosity, which impacts important performance metrics such as transfer rates, was found to be below 2 in all cases due to the high porosities exhibited, with average pore size greatly influenced by the overall resolution.

At the packed bed scale, X-ray CT was the sole technique selected using two different systems, with one system only capable of sufficiently imaging the harder ceramic samples, albeit achieving an overall superior pixel size of 2.7µm. Optimisation of X-ray conditions was required for each different material and corresponding equipment in order to achieve 3D representations of sufficient quality; to both visually display the packed bed structure in addition to providing the capability of quantifying key metrics relating to chromatography geometries and thus performance. Porosity readings of approximately 35% were in agreement with values obtained using established techniques and values, with radial discrepancies identified that were expected due to wall-effects impacting packing densities.

Two industrially relevant chromatography processing considerations were examined using X-ray CT: fouling and packed bed compression. Both scales were investigated for fouling, with individual beads imaged between cycles to measure the change in simulated diffusivity due to foulant impregnation. Compression of packed beds was imaged before, during and after excessive flow through columns, where visual and quantitative changes to aspects such as simulated permeability were compared between states. The values obtained in both of these studies based upon real systems were compared to changes in porosity and tortuosity factor by applying erosion-dilation to structure in an original state.

Impact statement

Chromatography is a ubiquitous downstream operation in high-value, high-complexity bioprocesses such as antibody and therapeutic protein manufacturing. The considerable expense involved with purchasing, operating and maintaining industrial scale packed beds results in research efforts to better understand and reduce negative impacts of aspects such as compression and fouling, which both are related to changes in chromatography bead and packed bed structure due to commonplace issues at scale when using poorly clarified feeds.

The structure of chromatography beads and beds has typically been analysed by using techniques such as inverse size exclusion chromatography and mercury porosimetry. Increasingly imaging approaches such as electron microscopy and confocal have been applied successfully to identify detailed chromatographic structure, including for visualising fouling both internally and externally on cycled beads to link to performance. However, these approaches have been limited by a combination of resolution, field of view and material penetration and so have not been sufficient to image the detailed internal structure of a bead, or a packed bed beyond microfluidic approximations that may not accurately represent industrial scale columns that are influenced by wall effects etc.

The research presented here addresses the shortcomings of using established imaging methods for both successful visualisation and quantification of internal structure of 3 commonly used chromatography bead materials and corresponding commercially available packed beds. This was performed by developing and optimising methodologies for representative imaging at both scales using two different 3D imaging techniques: focused ion beam microscopy and X-ray computed tomography, which have achieved respective pixel sizes of 15nm and 32nm at a level sufficient to resolve internal bead porous geometry.

Visualisation of structure enables a greater understanding of chromatography structure at both scales, also enabling quantification of key aspects such as porosity and pore sizes that are compared to existing values in literature. In particular, tortuosity has been of interest to investigate given the difficulty in defining and quantifying this in chromatography that has presented a considerable range of values, which has been possible by using the 3D geometry based on imaging performed combined with established simulation software. Simulation has also been applied here to determine changes in diffusivity and permeability to chromatography structure as a result of fouling and compression, providing a platform for both further high quality imaging of chromatography systems that can be used as a basis for representative evaluation of both 3D characteristics and industrially relevant applications.

Structure of thesis

This thesis is comprised of six chapters: an introduction and literature review chapter, four results and discussion chapters and a final conclusions and future work chapter that are related back to the thesis impact statement aims and objectives; which is discussed here and at the start of the introduction to **Chapter 1**.

After defining the project aims, objectives and desired outcomes, **Chapter 1** reviews the project concepts that formed the basis of research performed in later chapters. An initial literature review of liquid chromatography and the industrial relevance is presented, highlighting key areas of research. Prevalent imaging techniques for chromatography structural investigations such as electron microscopy are discussed with relevant examples of imaging-based bead characterisation. Current limitations with techniques used in literature are addressed as a justification for high resolution 3D imaging at both scales, where viable candidates are evaluated with relevant examples, with two selected for use in the project.

The four results chapters are split between two methodology development and image acquisition optimisation chapters for each technique and two analysing tomographic datasets to quantify key structural characteristics at both scales, comparing between both techniques. **Chapter 2** begins with initial electron microscopy sample preparation of 3 bead materials before detailing the approach taken and considerations for using focused ion beam microscopy on beads. **Chapter 3** focuses on how high quality imaging was obtained at both scales using X-ray computed tomography including optimisation strategies for each material.

Chapter 4 uses optimised data from previous chapters and processes images into a form suitable for quantification of porosity, tortuosity and other parameters of interest, enabling comparison between materials, tomographic techniques and to established values in literature that used non-imaging approaches. **Chapter 5** examines compression and fouling, two industrially relevant chromatographic issues. Fouled bead structure are simulated for diffusivity in addition to previous parameters, whilst compressed beds are simulated for permeability, allowing for comparison between structural states.

Chapter 6 provides conclusions and outcomes of the research presented and the benefit of performing these studies to chromatography literature. A ‘Research implementation and impact’ section is included to evaluate the opportunities for using the work presented here in academic, industrial and entrepreneurial settings including future research to be considered.

Table of contents

Chapter 1

Introduction and Project concepts review – requirements for 3D representation of chromatography beads and beds

Chapter 2

Individual bead preparation and imaging using focused ion beam microscopy

Chapter 3

Individual bead and packed bed imaging using X-ray computed tomography

Chapter 4

Physical characterisation of individual bead and packed bed geometry from imaging and digital processing

Chapter 5

Tomographic representation of compression and fouling of chromatography systems

Chapter 6

Conclusions and future work

List of Tables

Chapter 1

Chapter 2

Chapter 3

Chapter 4

Chapter 5

List of Figures

Chapter 1

Chapter 2

Chapter 3

Chapter 4

Chapter 5

List of common abbreviations

FIB – Focused ion beam

X-ray CT – X-ray computed tomography

CLSM – Confocal laser scanning microscopy

CPD – Critical point dried

LFOV – Large field of view

HRES – High resolution

Chapter 1

Introduction and project concepts review – requirements for 3D representation of chromatography beads and beds

1.1. Thesis aims and objectives

The research presented in this thesis was performed with the primary aim of visualising and subsequently quantitatively evaluating chromatography individual bead and packed bed structure using tomographic approaches. Completion of this aim has been subdivided into several sequential objectives that needed to be completed in order to achieve this goal.

The first step was to assess the current state of chromatography research that has been performed with imaging being a major component of literature studies, both in terms of technical feasibility and capability of investigating industrially relevant considerations. This would enable determination of areas that could be improved upon by either adapting techniques that have already been used, or translating research in other fields that have used different imaging methods in ways that could be applied to chromatography research at either individual bead or packed bed scale for representative structural evaluation at high resolution in 3D for both visualisation and geometric quantification purposes in **Chapter 1**.

Initial experimental objectives involved achieving and subsequently optimising imaging quality for each respective technique, material and scale to produce high quality datasets that are representative of the sample in question; either individual bead internal structure or packed bed configurations within a column in **Chapters 2** and **3**. Documentation of issues encountered in each case and optimisation requirements was an important requirement in providing future studies with the methodology required to image chromatography materials using either tomographic technique investigated here. Comparison between approaches in terms of resolution, technique suitability and other factors was also of importance.

Producing representative seed data from each technique at both scales would enable both visual and quantitative evaluation of chromatographic 3D structure after digital reconstruction and processing, again requiring consideration of specific issues related to chromatography materials of interest and the scale being examined: either *intra* or *inter*-bead in **Chapter 4**.

Achieving both 2D and 3D images of individual beads would allow for discussion around the porous internal geometry of chromatography resin structure, as well as comparison to existing images, predominantly of bead surfaces captured using electron microscopy. Likewise achieving the objective of imaging a commercially available packed bed would enable visualisation of actual column structure rather than microfluidic approximations. Other tools such as distance maps applied to 3D geometries would be useful in achieving an important project aim being to have a better understanding of bead and bed structure, for instance identifying large internal voids and undesirable extensive channels between beads.

One of the major aims of the project was to quantitatively characterise chromatographic structure at both scales for aspects such as porosity and pore sizes that could be compared to existing literature values based upon established techniques, enabling comparisons to determine the accuracy of using a tomographic approach to represent bead and bed structure. Additionally the evaluation of relevant and important yet poorly defined and understood parameters such as tortuosity was of importance given the emergent capability for the use of 3D geometry to be simulated for factors including tortuosity in **Chapter 4**.

After demonstrating technique capability for visualising and quantifying chromatographic structure of various materials, the final aim of the project was to apply the high resolution imaging processes developed to industrially relevant issues in **Chapter 5**, with compression and fouling selected for study. In addition to visualising and quantifying changes to 3D structure, respective simulation of liquid phase considerations such as diffusivity and permeability in each case would be used to meet the aim of achieving a greater understanding of how structural changes to impact parameters relating to performance.

1.2. Introduction

This thesis aims to produce 3D representations of real chromatography systems at two scales: within an individual bead and an entire commercially relevant packed bed, with various commonplace materials to be investigated in each case. This would form the basis for visualisation and quantification of aspects such as porosity and tortuosity to gain a greater understanding of chromatography structure, with comparison to established methods of evaluating beads and beds used to benchmark and assess the accuracy of approaches taken to produce 3D datasets at either scale, with approaches to evaluate tortuosity considered particularly useful given the relatively poor definition and evaluation in literature.

A major requirement of the project would to be to perform imaging of chromatographic materials, contributing to knowledge beyond the increasing adoption of imaging techniques in order to gain a greater understanding of bead structure, or investigate structural changes during commonplace applications such as lifetime changes to resin. Two imaging methods in particular have been used extensively in literature: electron microscopy and confocal scanning laser microscopy, which are examined with examples in the literature review. The high resolution achievable with electron microscopy has enabled detailed surface studies of chromatography beads, whilst confocal allows for optical sectioning to probe material penetration, although each technique lacks the major advantage exhibited by the other.

Therefore this project aims to perform sectioning, either destructive or non-destructive, at a resolution sufficient to resolve detailed internal chromatography bead structure as well as entire packed beds of a scale beyond that of microfluidic chambers that may exhibit attributes such as wall effects that are of particular relevance to industrial scale chromatography. Several tomographic techniques available that have been used in other areas of research are reviewed and compared with examples in the literature review, with two selected for chromatographic research purposes at individual bead and packed bed scales in this thesis: focused ion beam microscopy and X-ray computed tomography.

Focused ion beam microscopy allows electron microscopy resolution capabilities whilst physically sectioning, whilst X-ray CT is a non-destructive method with equipment specifications suitable to both scales of interest, without the need to interfere with samples. Literature studies for both of these approaches for other applications such as battery research have used both techniques for both visualisation and quantification of detailed, porous structures where analogous parameters of interest have been evaluated, for example porosity and tortuosity based upon a representation of a sample imaged in 3D.

There are also an ever increasing number of software tools available and corresponding increasing complexities to analyse 3D structures, with some key outputs of interest to this thesis outlined at the end of the literature review. In particular, the capability to simulate fluid flow through porous structure is of interest at bead and bed scales that are driven by different characteristics, primarily being diffusion and convection respectively. Simulation of these attributes on real structures imaged in 3D could aid in understanding of the structural aspects at both scales, particularly considering aspects such as compression and fouling.

Overall the literature review resulted in focused ion beam microscopy and X-ray computed tomography being selected for 3D imaging of chromatography beads and columns in order to visualise the detailed internal structure that has been difficult to observe using conventional imaging methods, also enabling quantification and simulation of the geometry.

1.3. Literature review summary

Packed bed liquid chromatography is a subset of bioseparation technology vital to purification chains of bio-therapeutic manufacturing processes, for example antibody production. Chromatography is discussed here in the context of structural characteristics concerning process performance at bead and bed scales, including key areas of research such as bed compression and lifetime usage, referring to literature where applicable.

The use of imaging as a technique for producing three dimensional representations of chromatography materials is examined, highlighting electron microscopy and X-ray computed tomography as standout approaches available. These are suggested as the main candidates for tomographic investigations at packed bed and individual bead scales, with comparisons between key tomographic techniques available and relevant examples.

1.4. Chromatography

1.4.1. Introduction

The purpose of a bioseparation process is to extract and potentially purify a desired product from other components, utilising an array of available technologies to do so [1] - [3]. Bioseparation has been used and developed throughout history, for example from cloth filtration in the Roman era to modern day reverse osmosis in order to purify water [1], [4]. The broad spectrum of disciplines that bioseparation covers; from agriculture to bio-ethanol production [5], results in various methods that can be employed to perform Bioseparation processes [3], often used in a series of techniques in order to achieve the final product form.

Bio-pharmaceutical production is one of the most complex challenges for bioseparations engineering [2]; often requiring a chain of unit operations for product capture and purification [3] using a multitude of approaches in succession that exploit particular characteristics to isolate and purify products. Bioseparation principles are typically used in downstream processing stages, [6] with a general overview flowchart shown below in **Figure 1**.

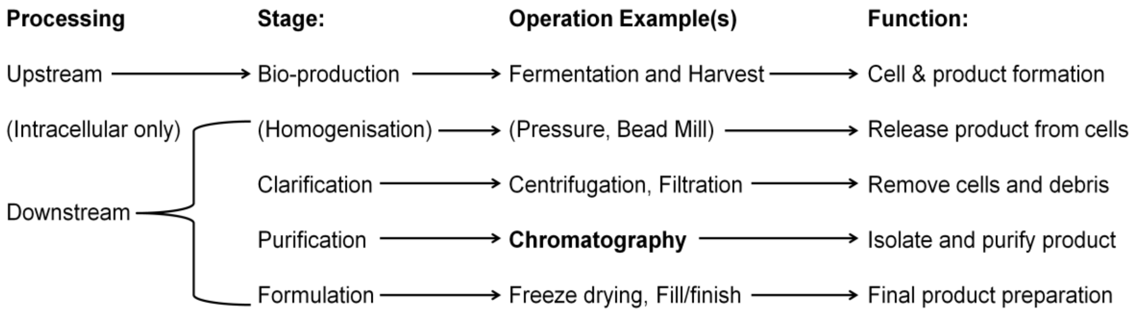

Figure 1: Stage depiction of typical bioprocessing operations. Adapted from Polykarpou [6].

This review focuses on liquid chromatography in a biomolecule purification context. Liquid chromatography is used in disciplines such as biotechnology, with the first example of chromatography demonstrated in 1906 to separate pigments and dyes [7]. This has progressed into modern protein and antibody purification which is ubiquitous in pharmaceutical production, essential in modern life for a multitude of healthcare needs.

The most commonly adopted method of liquid chromatography in bioprocessing is in packed bed form, although it is important to note that alternatives such as membranes and monoliths do exist and have been demonstrated to be effective purification unit operations, but have not been widely used by industry compared to conventional chromatography [3], [8].

The slow uptake of new high-value purification methods despite promising outlooks [8] highlights the heavy reliance on conventional packed bed chromatography for both academic and commercial research and processing. Since the bioprocessing industry is generally considered to be conservative in terms of making drastic changes and so this may also contribute to the relatively slow uptake of alternative bio-purification methods.

A column is loaded with micro-scale spherical beads, referred to as the sorbent or stationary phase of the packed bed, which performs the intended separation process [9] - [11]. The method for packing a column typically depends upon the scale and overall volume to be used, from manual packing of smaller analytical variants to bespoke equipment required for effective large scale column preparation. Pre-packed versions are becoming more popular at smaller scales due to the convenience of not requiring time and a sufficiently experienced operator to pack a column to a desired quality. Afterwards, a feed stock containing the intended product is passed through the column during processing and interacts with the stationary phase, saturating the packed bed as shown in **Figure 2**.

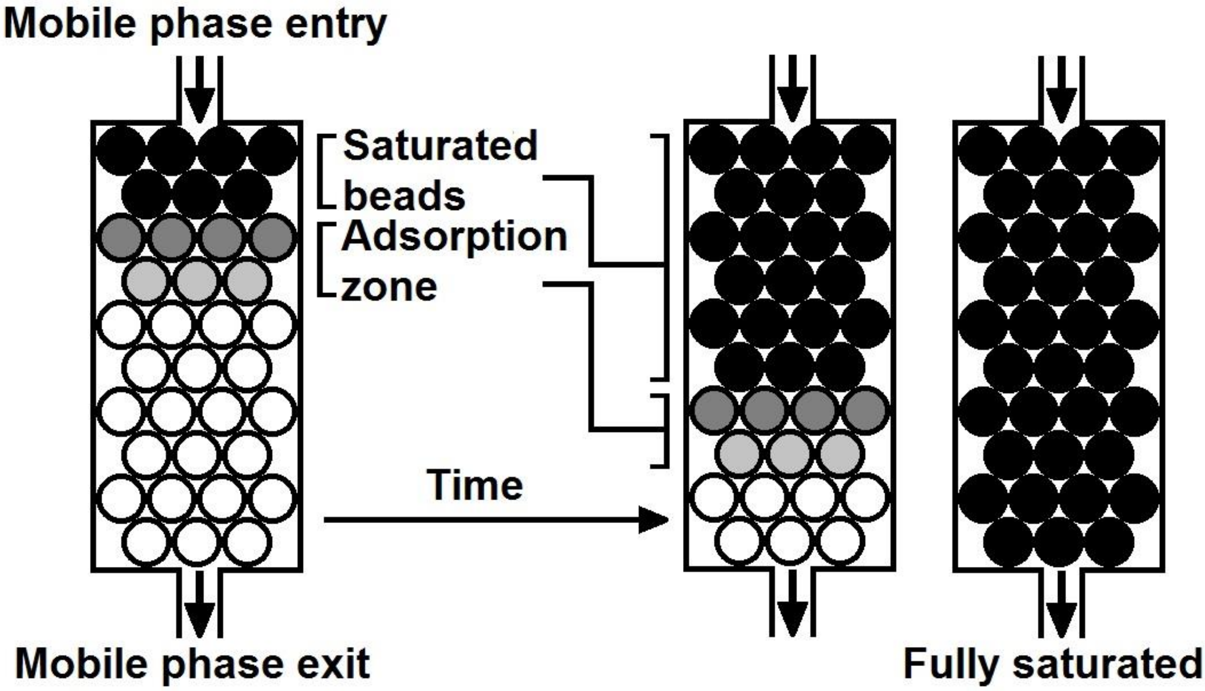

Figure 2: Visualisation of a packed bed of sorbent beads. Flow of mobile phase from the top of the column saturates the bed to capacity until no more can bind. Adapted from Doran [9].

The selection of sorbent is based upon the composition of the mobile phase so that differential migration of the mobile species can be achieved. This will result in the components of the feed materials exiting the column at different time, resulting in separation that is demonstrated in **Figure 3** that ideally occurs with no overlap of desired product and impurities that can then be isolated for further bioprocessing operations [2], [9, 10].

The ideal scenario for operation is that the different components exit from the column in distinct, concentrated pulses that may be detected and isolated with ease. However, it is possible that the peaks obtained are broad; and so may overlap with other sample constituents, resulting in poor separation [1]. This issue is more prominent when the desired product has similar characteristics to the impurities in the mobile phase [10].

Various aspects influence the spreading of the concentration peak. Axial and eddy based diffusional effects result in a distortion of ideal plug flow mechanic, due to increased solvent deviation from an ideal or average path, which can be exacerbated by poor column packing [9] by generating dead ends or channels that distort overall plug flow. Non-equilibrium effects due to mass transfer limitations such as movement across the stationary phase boundary layer, also significantly impact the process performance for chromatography [9].

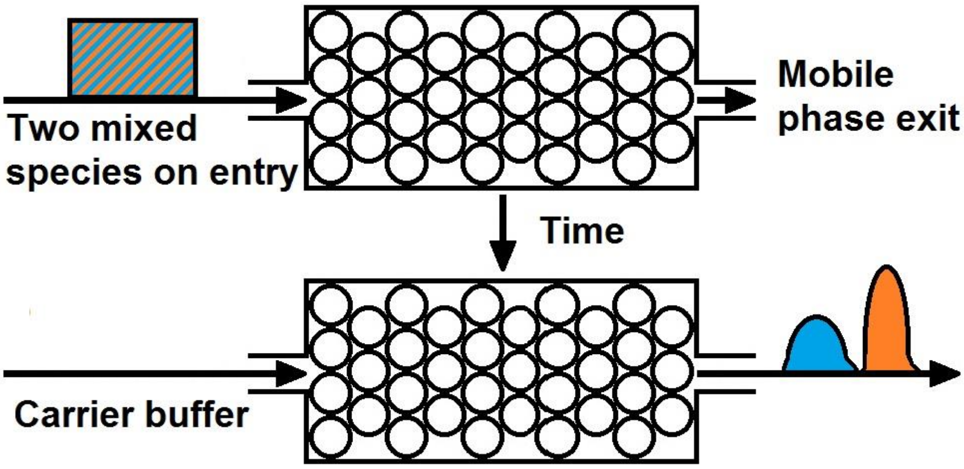

Figure 3: Representation of chromatographic protein separation. Two mobile phase species differentially migrate for different column exit times. Adapted from Bailey and Ollis [10].

The separation capacity of a chromatographic step is highly influenced by the specific adsorption isotherm of the product onto the sorbent, which is often determined empirically [12]. The conditions of the mobile phase (pH, conductivity etc.) are also important to manipulate adsorption/desorption to the column, which allows for a chromatography process to either bind and elute the product selectively, gradient select or for capture of impurities.

The effectiveness of a chromatographic step is also influenced by the available surface area for binding [9], which is dependent on the three dimensional (3D) structure and material of construction used for the beads. Commonly used materials for generation of the porous structure include agarose or cellulose, as well as harder materials including ceramics or polystyrene. Packed bed performance is commonly estimated by Height Equivalent Theoretical Plates, with a higher plate count indicating a better basis for separation [13].

Two other key aspects that impact packed bed chromatographic performance are process-fouling and bed compression. Process-fouling occurs when a significant level of impurities are present in the feed stream and remain in the column after use, particularly relevant for industrial processing where cell culture debris may not be clarified to an ideal quality which could include homogenate material from host cells [9], [14, 15]. Large foulants can result in blinding of the bead surface pores that reduces dynamic binding capacity and inhibiting mass transfer, resulting in decreased separation performance [9, 10], [12]. Cleaning of columns between batches is often used to reduce foulant levels and recover performance for subsequent use because sorbents are too expensive to discard after each run, with industrial re-cycling of sorbents over 100 times commonplace [9], [16, 17].

Packed bed compression occurs due to viscous drag imparted by the mobile phase on the stationary phase when deformable materials of construction are used for the sorbent, such as agarose [18, 19]. This results in limitations to flow rates that may be used in order to avoid bed collapse, which is of particular consideration for industrial scale processing due to the reduced friction-based wall support from larger column dimensions [20, 21].

Therefore, many aspects and issues that are presented require consideration for analytical or industrial chromatography processing, as resolving different compounds to maintain individual, concentrated pulses is a desired quality and mode of operation. Methods such as increasing available surface area for mass transfer can reduce these detrimental effects, but this may not always be possible [9]. Therefore a commonplace technique is to tailor the sorbent type used to the product that is to be isolated based upon an array of characteristics.

1.4.2. Types of Chromatography

The performance of a chromatographic step depends on various factors, with one of the most important being the selection of sorbent for the process. Due to the molecules in a feed stream having distinct characteristics, the selection of an optimum bead type will rely on several criteria [2] including the type of interaction that occur between phases [1].

There are many biological, chemical and physical phenomena that have been exploited for chromatographic purpose [11], with size, charge and shape being commonly used as a method for resolution [9]. Four commonplace types of chromatography include size exclusion, hydrophobic interaction, ion exchange and affinity; with mixed modes possible.

Size Exclusion Chromatography relies on two species of interest having molecular size and shape differences greater than 10% in order to achieve differential migration [22]. As the mobile phase enters the column, smaller molecules can penetrate the porous microstructure of the individual beads and are retained in the internal structure for a longer time than larger particles, which are rejected by smaller pores or the whole bead altogether [23] - [25].

Therefore, larger molecules take a less tortuous path through the bed compared to retained species and so exit the column earlier which enables isolated collection, as seen in **Figure 4** [10]. Size Exclusion Chromatography sorbents are relatively inexpensive, although the separation performance and aspects such as yield compared to other techniques is reduced, resulting in commonplace use for analysis rather than industrial processing [2].

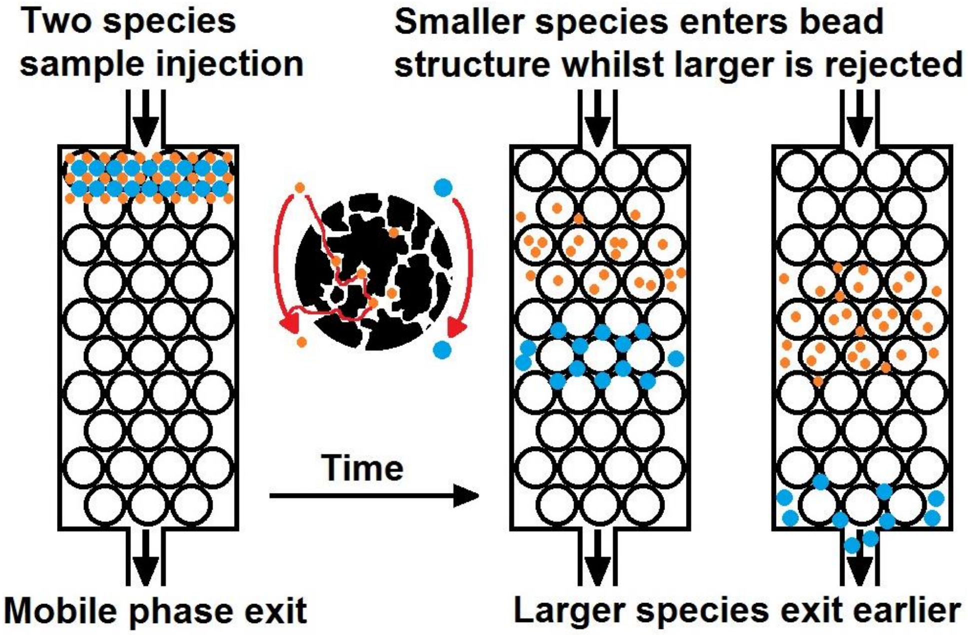

Figure 4: Size Exclusion Chromatography mechanism. Beads reject larger molecules from the internal structure, causing faster column exit. Adapted from Striegel *et al*. [26].

Hydrophobic Interaction Chromatography (HIC) relies on differentiation based upon hydrophobicity, the tendency of non-polar molecules to minimise polar interactions [3], with sorbents typically having hydrophobic groups attached such as phenyl [9]. Initial equilibration of an HIC column [27] is performed by increasing polarity of the mobile phase, resulting in binding of hydrophobic molecules to the sorbent due to loss of solvation whilst hydrophilic species will remain in the mobile phase and exit the column [10, 11]. Salt levels are then reduced gradually in order to release different molecules based upon their hydrophobicity that enables separation, isolation and selective capture of a product [9].

Ion exchange chromatography (IEX) utilises complimentary ionic charge of both the stationary and ionic phases for selected adsorption and desorption [28, 29]. Both anion and cation approaches rely on charge characteristics of the intended product to be isolated and whether bind and elute or product flow through modes are preferred in the process [9].

After initial column preparation, the mobile phase species that have complimentary charge to the stationary phase bind to the sorbent groups, whilst non-complimentary groups repel and exit the column [9, 10]. Once the product and similar species are bound, elution is performed by gradually adding salt to increase ionic strength of the buffer, resulting in desorption of the bound components [2]. This enables the desired product to be isolated from similarly charged species, with an example being cation based CM Ceramic HyperD F™ [30].

Mixed mode sorbents also exist which typically combine hydrophobic and ionic interaction strategies by having multiple ligand types, potentially enhancing purification of certain species which has resulted in Mixed Mode being commonly used for High Pressure Liquid Chromatography [31]. However, the novelty of Mixed Mode mechanisms indicates that further optimisation of the technique for large scale purification is required before industrial uptake can be achieved, with an example sorbent being cellulosic MEP HyperCel™ [31].

Affinity chromatography is ubiquitous in many purification processes, with the stages used for affinity chromatography operation follow the equilibrate, load, wash, elute and regenerate steps used for the previously discussed methods [7]. The separation strategy relies on the ligands that enable specific and reversible binding of a wide range of molecules that is ubiquitously used in antibody capture stages of the majority of patented bioprocesses [9].

The ligand bound to the stationary phase is designed so that adsorption of the product onto the ligand is highly favourable relative to other unwanted feed constituents, allowing for highly specific entrapment of the product as seen in **Figure 5** [2]. The high specificity for high value products of interest is one of the driving factors for affinity chromatography being prevalently used for bioprocess applications [10], however the resin is often very expensive.

The high cost of necessary bioprocessing stages such as affinity based chromatography capture is an area of particular interest for pharmaceutical manufacturers to improve quality in order to extract the most performance and life out of resins [32], particularly given the continual advancements of upstream production [17], [33]. Optimisation of a whole bioprocess chain is important to maximise important factors such as yield and purity in order to maximise efficiency and reduce issues encountered at final steps such as chromatography [34]. Whilst overall performance in terms of binding can be achieved relatively easily, the main impetus is generally to extend the number of column re-uses.

One of the most commonplace affinity chromatography types is Protein A [35, 36] which has been utilised for many antibody based capture and purification based chromatography stages [37]. It has been used in almost every patented bio-pharmaceutical process with Synagis® being a rare exception [38]. This widespread adoption demonstrates the current reliance on packed bed chromatography using various methods of separation is likely to continue for the foreseeable future [8].

Therefore there are several approaches to chromatographic separation that can be undertaken to differentiate species within a feed. Whilst the overall choice of sorbent and type of chromatography is based upon separation capabilities, there are often several feasible choices and so metrics such as yield and purity decide the approach taken.

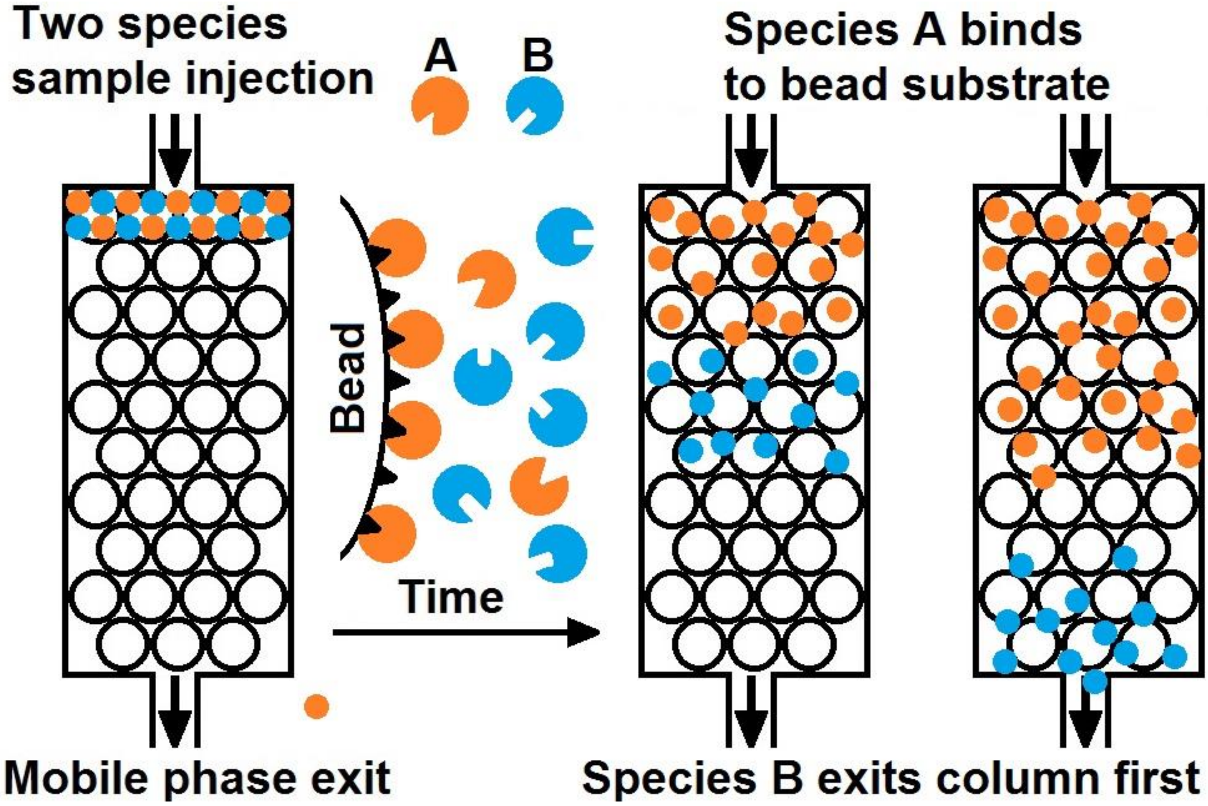

Figure 5: Demonstration of Affinity chromatography mechanism. Molecule A has a greater affinity for the stationary phase than B, indicated by the complimentary fit, causing selective binding under preferential conditions and removal of B. Adapted from Bailey and Ollis [10].

1.4.3. Industrial relevance

Bioseparation technologies have been used for centuries to produce goods for monetary gain, with a modern example being biologically derived products [10, 11], [39]. A key example in the biotechnology sector is monoclonal antibodies for therapeutic use, with total market sales exceeding $80billion in 2016 [40, 41], as shown in **Figure 6** [17], [42]. High value products are commonplace in the biotechnology sector, with the nine most expensive mAb therapies over the last decade costing over $200,000 per patient per year [43].

Packed bed chromatography is an essential and ubiquitous component of a bioprocess chain for monoclonal antibody production, displayed in **Figure 1**. A typical bioprocess is sub-divided into capture, intermediate purification and polishing before product finishing [10], [44], with **Figure 4** demonstrating that different products undergo an individual chain with often unique setups, although will likely share the overall approach taken.

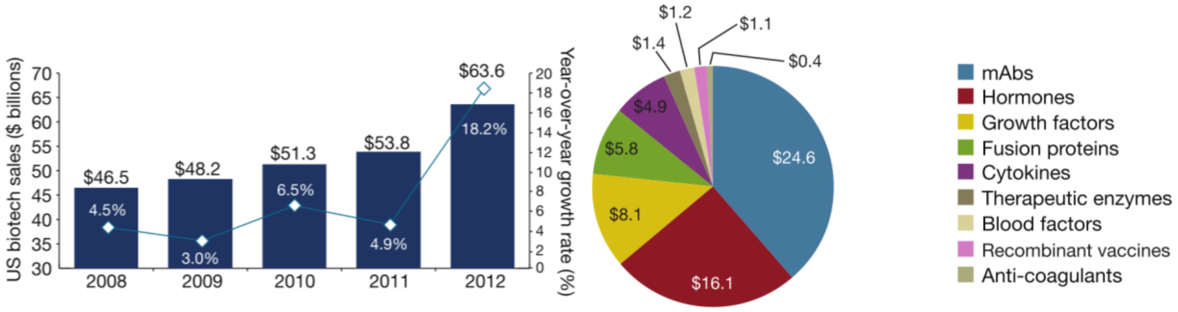

Figure 6: Economic performance of the Biotechnology sector. From Aggarwal [42].

Whilst a variety of methods are used for intermediate purification and polishing, Protein A affinity chromatography is almost exclusively used for capture, with a unique exception noted in **Figure 7B** [38], [45] - [47]. It is important to consider that industrial scale chromatography presents further challenges for processing, such as effective bed packing and compressibility due to the large volumes of sorbent used, as well as dynamic binding capacities, column life-time and re-usability based upon performance loss [48].

Whilst methods to evaluate these resin characteristics currently exist and have been useful for directing research and development of chromatography systems in different ways, the exact mechanistic behaviour of sorbents in larger columns during long term processing is not always possible to determine without extensive optimisation efforts [6], [34], [49]. Therefore improvements to this area could help control ever increasing costs for manufacture [17].

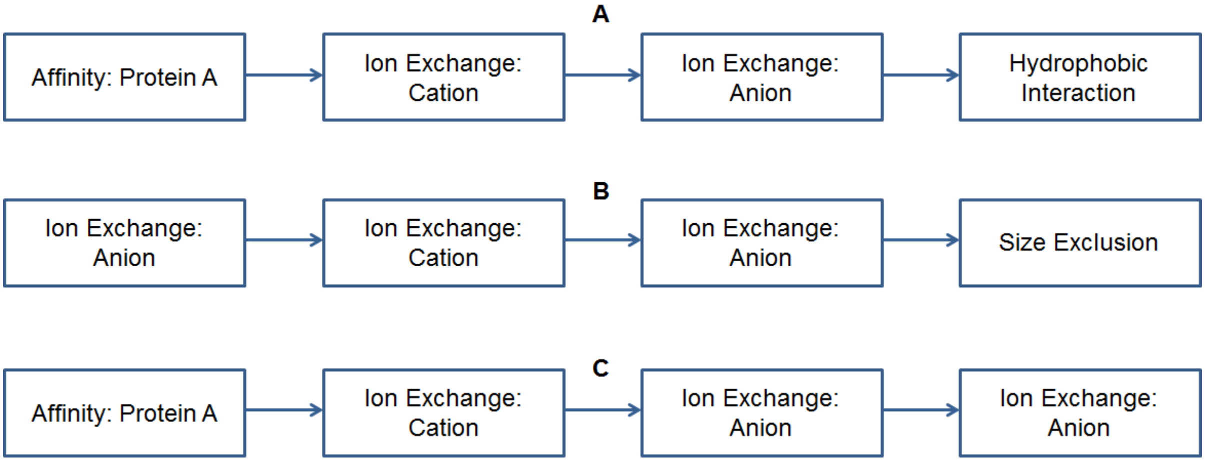

Figure 7: Examples of chromatography chain for patented products on the market.
A: Chain for Herceptin®, note that not all intermediate steps are shown in each case.
B: Chain for Synagis. C: Chain for Remicade® Adapted from Sommerfield and Strube [38].

1.5. State of chromatography research

1.5.1. Introduction

Research into chromatography and its applications is a worldwide effort with both interests from academic and industrial standpoints. These institutions often have shared goals as research and development for both parties involves improving existing systems by either incremental gains or utilising emergent advances in relevant technology in order to augment or adapt equipment for improved performance; or expansion to the relevant applications that a chromatography platform of interest could be used for. Improvements to understanding of chromatographic behaviour of products or sorbents are also of importance for academic or industrial research that would be important in furthering Bioseparation knowledge or releasing a new chromatography system to the market respectfully.

A main objective of research into chromatography is to increase the efficiency and effectiveness of a processing chain [28]. A major concern within industry is that the performance gains seen in upstream production in terms of titres and resultant impurities, are not being matched by the developments seen in downstream operations. Full scale antibody or product manufacturing often requires columns with large diameters up to 2 metres that present various performance and logistical issues, as well as considerably large volumes of expensive sorbents that need to be packed, used and maintained sufficiently.

Therefore, further scaling up of packed beds beyond two metres was considered in an industrial setting, but has since been dismissed. This indicates that either packed bed sorbents must improve [28], or a switch over to alternative technologies such as membranes or monolith systems to complement or replace current packed bed technology in order to match upstream advancements in titre [8]. Although this review focusses on packed bed chromatography, some aspects considered will be analogous to alternative techniques that may be of interest [50, 51] to industrial manufacturers for purification similar to packed beds.

Current volumes for the largest scale capture step columns are up to 5m^3 of expensive resin that has to handle feeds that are becoming much richer in products and impurities; increasing dynamic binding capacities (DBC) of sorbent would be a desirable goal [28]. Current dynamic binding capacities observed are of the order of tens of grams bound per litre [52], for example Protein A MabSelect SuRe™ obtaining capacities of 40g/L [19] although this is dependent on the degree of optimisation in terms of yield and purity etc.

Although it is anticipated that sorbent dynamic binding capacities will improve, the predicted maximum capacities are expected to improve by less than an order of magnitude, even when factors such as surface chemistries and cross linking, bead size and structure, bed packing, cleaning, re-usability of sorbents and operational conditions are optimised [28]. This indicates that enhancing capacity alone will not accommodate the increasing upstream titres.

One area of interest for chromatography is the use of pre-packed columns [53] or single use technology, which is being adopted throughout the process chain for biopharmaceutical manufacture [54]. Employment of single use systems can negate the need for ancillary, cleaning and preparative based operations, saving time that may be used for increasing other areas of process productivity. It must be noted that drawbacks do exist for single use technologies, such as increased process cost of goods and reliance on supply vendors [55].

It is unfeasible for all chromatography experiments and research to be performed at industrial scale due to time and cost restraints, particularly in cases when screening a variety of potential ligands. Therefore ultra-scale-down techniques are applied in order to perform approximations whilst minimising the amount of material required to do so [56].

Ultra-scale-down or pilot-level studies are often the basis for academic based chromatographic research, where an abundance of materials and scaled instruments may not be possible. However there are issues concerning the differences between research and industrial scales, which include: column wall support, compressibility of column, pressure tolerance, column collapse and packing attributes, amongst other considerations [56].

For industrial operation it is often the case that the chromatographic separation processing requires less time than the preparative and ancillary operations involved [28]. If a single-use disposables based method is to be avoided, then efficiency of processing should be optimised, which is a main objective of continuous based chromatography research [57]. Therefore, areas of dual feed flow-rates and Simulated Moving Bed Chromatography are important areas of research for developing technology at industrially relevant scales [3], [57].

In addition to integral aspects of chromatography that impact step performance such as binding capacities, the *inter* and *intra*-bead structure are essential to maximising available surface area for mass transfer. Flow paths at both scales are tortuous which maximises phase interactions, with visualisations displayed in **Figure 8**. Efficient packing of beads into columns [58] is also of paramount importance to performance that is often measured using height equivalent theoretical plates (HETP) [16], [59]. It is commonplace practice to ensure that an HETP reading is sufficient for efficient chromatographic operation, as values lower than expected may suggest inherent issues such as channelling within the packed bed.

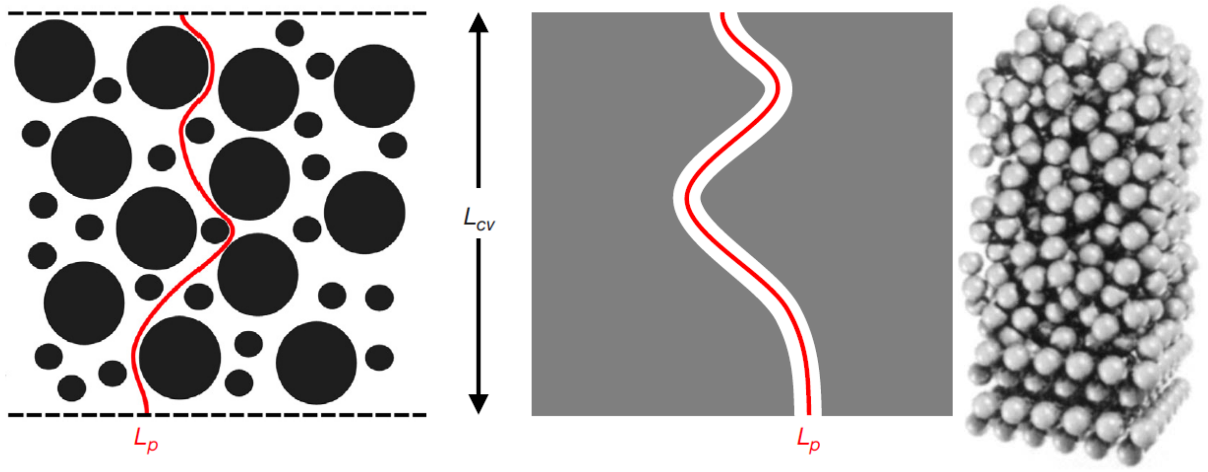

Figure 8: Physical concepts of tortuous flow through chromatography beds and beads. **Left-centre**: Two commonplace representations of tortuous paths. From Tjaden *et al*. [60]. **Right**: Simulation of an ideal (bottom) versus expected packed bed. From Vissers *et al*. [61].

The representations in **Figure 8** display how the mobile phase path has to travel through the packed bed and individual bead in a winding fashion, enabling interactions with chemical groups for chromatographic separation purposes. Whilst aforementioned height equivalent theoretical plates are used as an indicative packing quality measurement, the reality of packing is that plates do not ideally sit layered on top of each other and so heterogeneity impacts key physical characteristics such as tortuosity that can be considered as the actual path length over the minimum distance, with **Figure 8** also displaying theoretical plates as well as a realistic simulated micro-packed bed overlaid in a 3D render.

Process-fouling and the impact on chromatographic performance is one of the major areas of bioprocess research due to fouling being a commonplace issue in laboratory and industrial scale chromatography [37], [62]. In particular, the focus on improving re-use of expensive sorbents by identifying the components that cause the fouling and the most effective methods for removing foulants by cleaning for column re-use [12], [14], [62] by minimising foulant interaction as a result of robust cleaning regimes between cycles.

Due to the relatively soft materials used to produce chromatography beads, compression of packed beds is a common phenomenon that can reduce performance or render a column irreversibly unusable [21]. This is of particular issue when using excessive flow-rates and thus pressures on large packed beds that are often used for industrial applications that would be very costly to replace. Considerations such as friction due to wall support have been investigated and modelled in literature such as Keener *et al*. [20] in order to determine and predict the highest flow-rates achievable without significant mechanical deformation.

Therefore, a wide range of research subjects are based upon packed bed chromatography that have a common aim of improving process effectiveness and robustness, particularly in relation to industrial scale manufacturing requirements. Research into the structure of chromatography beads and packed beds has been performed using an array of techniques to relate physical and structural characteristics to overall sorbent and column performance.

This review will examine some key studies that relied on imaging chromatography materials or similar as the primary method for experimental research, with the aim of evaluating current approaches for their capabilities when visually investigating beads and beds that could be credible for use in producing 3D representations for quantitative analysis.

1.5.2. Bead surface structure studies

A large proportion of chromatographic structural studies focus on imaging the surface of beads due to the relative ease of imaging access compared to the internal structure, combined with the availability of established technology. Optical microscopy has been used in several cases in order to image the external surface of beads, enabling both visualisation of individual bead, in addition to the packed bed environment, as seen in **Figure 9**.

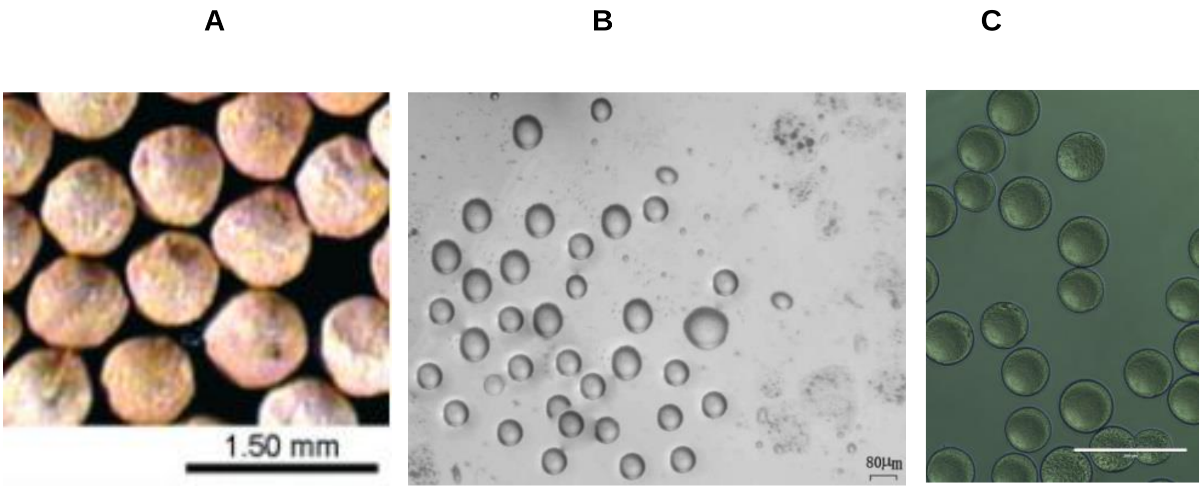

Figure 9: Comparison of example bead surfaces using optical microscopy.

A: Poly-acrylamide, oil in water formation based bead. From Zhang *et al.* (2004) [63].

B: Cellulose micro-particle, water in oil formation. From Lin *et al.* (2009) [64].

C: MEP HyperCel (cellulose) beads. From **Appendix**.

The images in **Figure 9** demonstrate that optical microscopy can be used to successfully image beads when not packed in a column. Using optical microscopy in these studies enabled observations that particles are not necessarily uniform in size or perfectly spherical; another factor in preventing ideal plate formation in a column impossible. Determination of particle size distributions based upon micrographs would also be possible that could be linked to improving manufacturing homogeneity feedback loops or changes to the sorbent.

However, these optical microscopy studies did not image beads in a column setting or any structural surface detail relating to the intricate pore network required to achieve a high internal surface area to volume ratio due to resolution limitations. Therefore in order to visualise finer features at the individual bead scale, other approaches were required where electron microscopy was the major technique employed to visualise surface details.

Examples of electron micrographs used in studies that investigate bead surface structure are displayed in **Figure 10**, where distinct differences in surface features can be observed between different bead types in terms of both the material characteristics such as roughness in addition to the general type of pores present on the surface. This initially suggested that a technique based upon electron microscopy could be a suitable candidate for imaging the internal structure of the beads due to the ability for resolving structure of various materials.

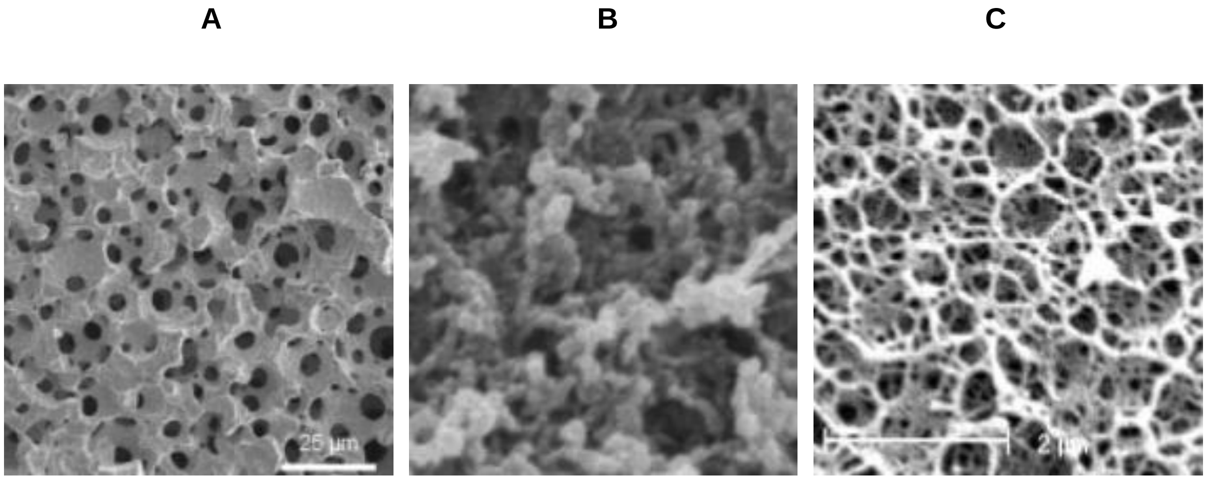

Figure 10: Comparison of example bead surfaces using Scanning Electron Microscopy.
A: Poly-acrylamide, oil in water formation based bead. From Zhang *et al.* (2004) [63].
B: Cellulose based HyperCel Q by Pall Corporation. From Angelo *et al*. (2013) [24].
C: Virgin MabSelect (agarose) bead. From Nweke (2017) [65].
Note that magnification, operating equipment and systems vary between sources

From **Figure 10A** Zhang *et al*. [63] states that the average pore size is approximately 4µm which is considerably larger than the typical sizes expected at 100nm or below which is acknowledged by the author in relation to the regularity that the overall structure exhibits. Image **10B** of a cellulosic material does not display clearly defined pores throughout as observed in **10A**, although does exhibit a porous structure. **10B** has also been chemically fixed with osmium tetroxide, although Angelo *et al.* [24] state that there is little difference in images generated between fixed and non-fixed samples and so the advantages gained in material contrast may be outweighed by the additional steps, potentially changing the sample from the true state. **10C** displays a relatively open, mesh like structure that has clear voidage, but also suggests a less regular pattern of repeating features in comparison to **10A**.

One of the overall objectives of the project considers quantitative analysis of chromatography bead structure. By being able to effectively image the chromatography bead structure in detail, rudimentary calculations of pore sizes etc. would be feasible using this approach, which is investigated in **Chapter 2**. However, 2D determination of true pore diameters could be difficult, particularly for less ordered structures such as **10B** and **C** because the pore boundaries may not be discernible without knowing the surrounding geometry, which would be available if a 3D based approach was undertaken.

Therefore electron microscopy has been demonstrated to be extremely effective for imaging the detailed surface structure of chromatography beads, and has seen increased use for relating the visual details obtained to performance based characterisation. However the main drawback for imaging the entire structure of chromatography beads using electron microscopy is the lack of material penetration that is essential for internal visualisation.

1.5.3. Bead internal structure studies

Whilst external imaging of several bead types using optical microscopy approaches have been discussed for the surface of sorbents, fewer studies have attempted to image the internal composition and structure. This is most likely due to the associated difficulty with using imaging techniques such as optical and electron microscopy. The use of slicing or boring into a chromatography bead has been explored in the literature [18], [24], [66, 67], but has produced limited success. An example of internal structure investigations is presented in **Figure 11**, where Confocal Scanning Laser Microscopy has been applied in order to visualise material transfer of Bovine Serum Albumin through a bead over time [68].

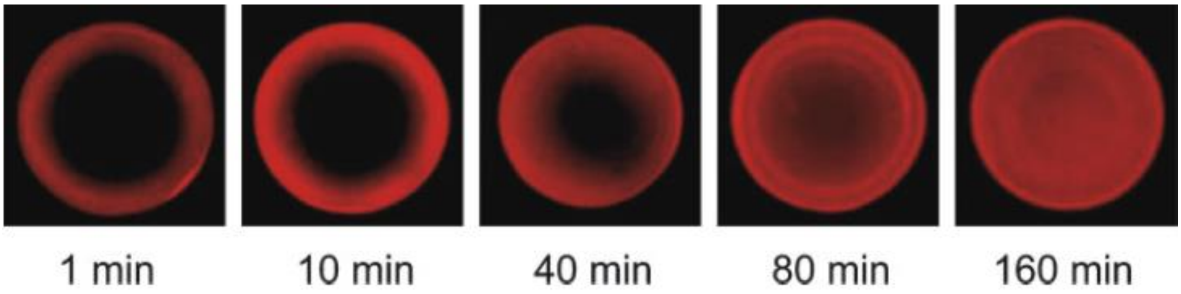

Figure 11: Adsorption of Bovine Serum Albumin through a bead observed using CLSM. Diffusion of the material through the bead occurs over time. From Siu *et al*. [68].

Figure 11 displays the diffusion of BSA representing a product of interest penetrating through a chromatography bead over time. This experiment was performed using incubated perfusion as opposed to industrial column conditions, but demonstrates how a protein is able to access the entirety of the bead, albeit at diffusion limited rates. It can be observed that after 40 minutes, the penetration of the material through the bead on the bottom right of the image appears to be less compared to the top left of the bead. Whilst this is not discussed in the article, it may indicate that there is heterogeneity within the porous bead structure that could be an attributing factor to this phenomenon although this may also be attributed to fluorescence re-adsorption which can be corrected for digitally afterwards [69].

Therefore, whilst studies such as Siu *et al*. [68] demonstrate that techniques such as Confocal Scanning Laser Microscopy are capable of visualising potential interactions that occur within an individual bead, the structural details of the internal porous network cannot be resolved using this approach and so is not suitable for the initial objectives of the project of producing accurate representations of packed beads and beds in an unused state.

Overall, the two requirements of imaging the internal structure and at a sufficient resolution to visualise the smallest porous features could be achieved using CLSM and electron microscopy approaches. However, these techniques as used in the highlighted studies did not achieve both of these simultaneously at the individual bead scale and so would not be suitable for 3D representation. Further examination of imaging capabilities with relevant literature is discussed later in this chapter in relation to the technique itself, however these surface and internal visualisation studies demonstrated the interest in using imaging techniques for characterisation of chromatography materials that has been particularly prevalent in CLSM and EM use. Another key requirement of the project for imaging was to consider changes to beads and beds due to commonplace industrial applications.

1.5.4. Column usage studies

The importance of process-fouling to chromatography performance and research has also resulted in imaging techniques being employed to examine spent sorbents on the surface and internally, with examples displayed in **Figure 12** [62]. These studies considered progressive fouling over time and the resulting impact on protein uptake rate and dynamic binding capacity due to the covering the of the porous structure by a film of impurities.

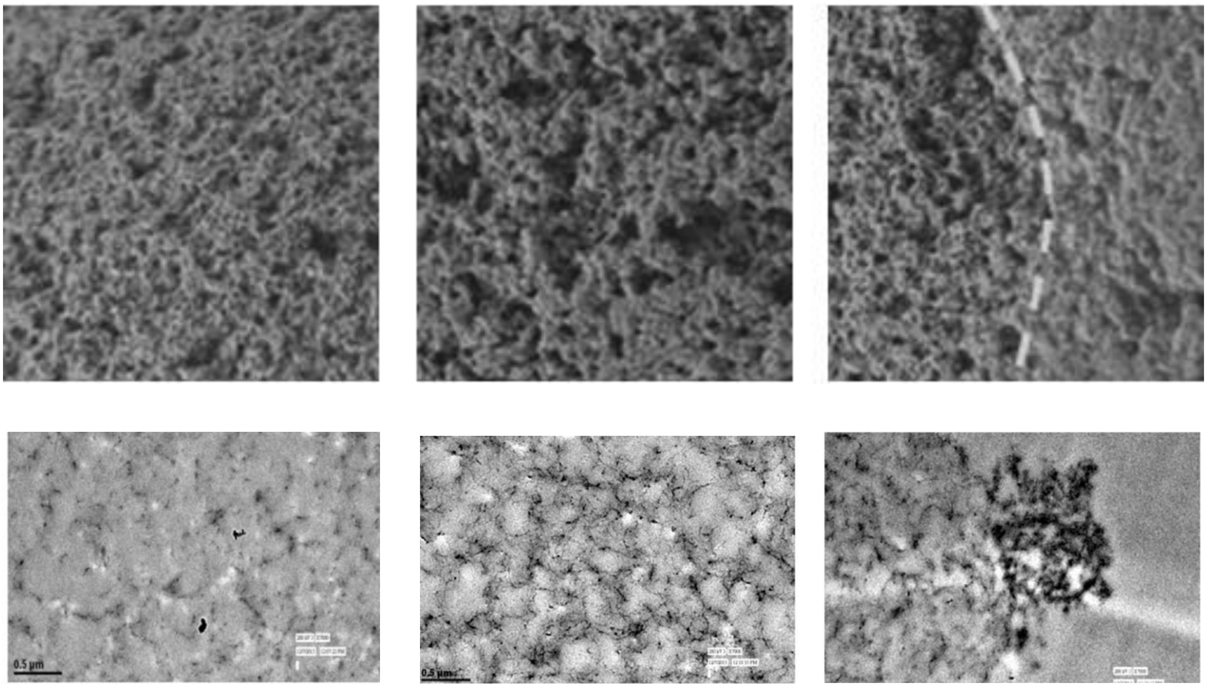

Figure 12: Scanning Electron Microscopy of a bead surface with progressive fouling. Fouling increases from a clean bead on the left to a heavily fouled bead surface on the right, where pore blockage can be observed via loss of detail that impacted protein uptake rates.
Top: Fractogel® from Close *et al*. [62]. **Bottom**: MabSelect SuRe from Pathak *et al*. [70]

In the leftmost image of **Figure 12**, the sorbents have not been used for chromatographic processing, so possesses no foulant material. It can be observed that the surface of the material is relatively homogenous in terms of appearance. The fouling of the sorbent was performed using an approach in Iskra *et al.* [71], where it was found that fouling did have an impact on sorbent performance over a lifetime which relates to the visual changes observed.

In the middle image, where the sorbent has been partially fouled, the image displays a resemblance to the unused bead, except that the surface appears more heterologous, with areas of flatter material, which was found to be lipids, DNA and other proteins which were analysed using mass spectrometry by Iskra *et al.* [71]. The rightmost image of **Figure 12** shows extensive fouling of the sorbent where part of the surface appears to be impacted sufficiently (left of the hashed line) that the pore structure is blinded, inhibiting mass transfer to the inner structure, decreasing performance [62]. This considered the surface only, with **Figure 13** demonstrating approaches to observe foulants within the bead structure.

Figure 13 visualised fouled agarose beads to examine impurities that are adhered to the bead surface after processing. Cell debris was labelled with BacLightRed and DNA was labelled with PicoGreen, which can be observed to have adhered around the surface of the bead, with an overlay of the two constituents on the right [68]. Host cell protein contaminants were explored in both papers of **Figure 12** and **13** concluding on similar contaminants observed that cause fouling, with Siu *et al*. [68] recommending that effective cleaning, storage and regeneration methods to be investigated and optimised in order to reduce the issue of impurity fouling [68] and thus extend the lifetime of a sorbent.

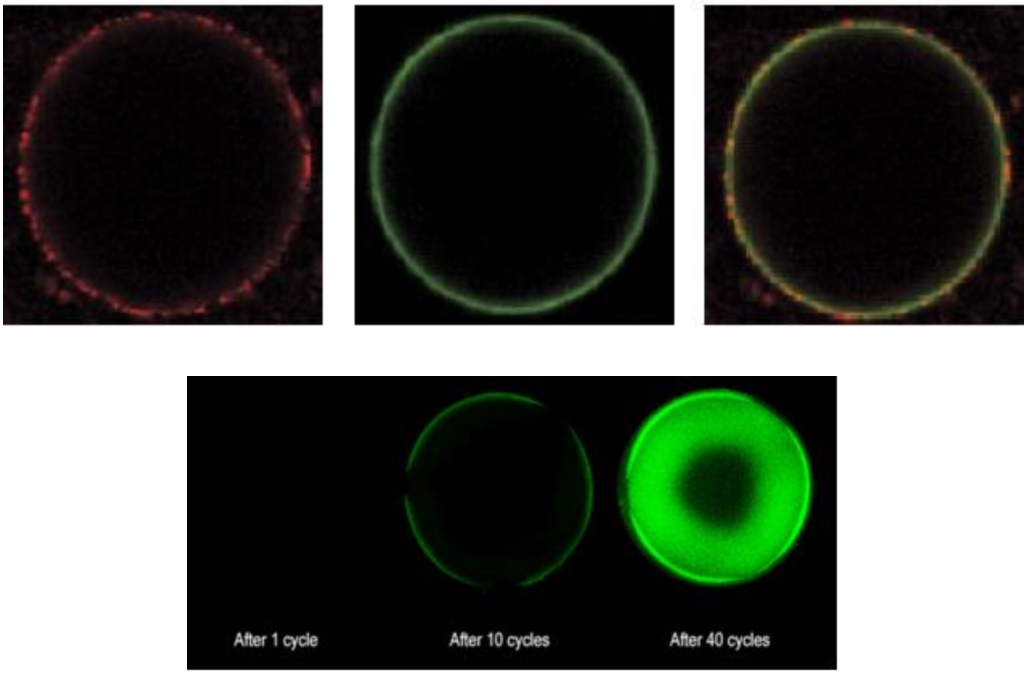

Figure 13: Confocal Scanning Laser Microscopy used to observe bead foulants. **Top**: Visualisation of cell debris, DNA and overlay on a bead surface. From Siu *et al*. [68]. **Bottom**: Lipid adsorption representing feed impurities over 40 cycles. From Jin *et al*. [12].

The images in **Figure 13** further visualise the accumulation of impurities and debris on the surface of chromatography beads when exposed to foulant rich feeds. As observed in **Figure 12** where the degree of surface coverage increased over cycles, in **Figure 13** the CLSM images suggest that not only do foulant levels on the exterior of the bead increase over a lifetime, but there was also considerable penetration within the internal structure. This would not only reduce transfer between within and between bead porous spaces, but also prevent either bind and elute or product flow through mode from effectively functioning.

This emphasised the requirement for bioprocesses to use cleaner feeds or more effective *inter*-cycle cleaning regimes in order to remove impurities in order to prevent surface saturation and internal structure penetration as discussed by Siu *et al*. [68]. This is of particular interest and difficulty for large, industrial scale columns where there is a considerable amount of sorbent within a packed bed that needs to be effectively cleaned many times for often impure and non-homogenous feed material [32], [72]–[74].

All of the studies displayed and discussed here have been at the individual bead scale, because imaging all of the beads in a representative scale chromatography packed bed did not appear to be prevalent; although microfluidic [75] approximations are evaluated later in the chapter. This was attributed to the difficulty of imaging through many beads packed into a bed whilst achieving sufficient field of view and resolution requirements simultaneously.

Not only does this limit visual representations of the 3D structure of true packed beds to modelling approximations [76], [77, 78], but also prevents true structural characterisation of beads and beds in their actual state when undergoing commonplace issues such as fouling and compression. Bed compression may be visible if a packed bed experiencing viscous drag was imaged, which could be correlated to results from key studies such as Keener *et al*. [20] to investigate the impact of dynamic fluid flow through a column before, during and after on bead position and morphology within a packed bed but still requires imaging.

1.6. Section conclusion and requirements for imaging

The research discussed in this section used an array of imaging techniques to characterise and demonstrate various aspects of chromatography, considering both surface and internal aspects of beads in relation to performance. Based upon the studies considered here, there is a need for improved imaging technique usage at both bead and bed scales to further structural understanding of chromatography materials relating to mechanistic performance.

The two main literature technique categories for imaging beads were using electron microscopy and confocal laser scanning microscopy. In the case of electron microscopy studies, resolution of the detailed porous structure of the surface could be achieved but no sub-surface studies alongside these were made, although Ioaniddis [18] has discussed a physical boring method for observing below the surface of a sample. Regardless of the approach undertaken, a physical sectioning method would be required for viewing the internal porous network whilst not causing damage and thus changes to features imaged.

For CLSM, material sectioning of individual beads has been demonstrated to be viable without physical intervention that has been useful for demonstrating internal bead diffusion as well as identifying foulant accumulation [12], [14], [68]. However, resolution limitations render CLSM unsuitable for imaging detailed bead structure, with packed bed scale investigations being the more suitable scale, which is discussed later in the chapter.

By considering the entire 3D structure of individual beads and packed beds, tomographic representations can be generated, enabling both physical and process considerations to be evaluated and compared to findings from related studies, which could include aspects discussed by Angelo *et al*. [24] for porous bead characterisation, Close *et al*. [62] for process-fouling and Keener *et al*. [20] for bed compression, as well as other aspects such as tortuosity and flow paths [79] both for the individual bead and packed bed porous structure.

The studies presented as examples for bead imaging were relying on 2D imaging, particularly in the case of electron microscopy whereas 3D visual sectioning of CLSM beads may have been undertaken. This limitation combined with either lack of resolution or capability of internal imaging suggest that EM and CLSM imaging in the manner in which they have been used for these studies are not suitable for 3D representation of individual beads or packed bed chromatography systems; requiring alternative technique evaluation.

Therefore, a review of suitable imaging techniques was performed in order to determine methods that could be used in order to produce 3D representations of individual beads and packed beds. This would rely on the imaging technique specifications in addition to examples in literature based upon direct chromatography material imaging as well as any relevant or approximate studies of interest that could aid in selecting suitable approaches.

Alternative examples were required for review as using 3D imaging approaches for observing chromatography systems at either scale was seemingly not prevalent in literature. However, many current computational studies rely on theoretical structures which could be greatly enhanced if real column or bead geometries could be used as a basis for modelling.

1.7. Imaging techniques for tomographic representation

1.7.1. Introduction

Imaging of materials across many areas of research has enabled further understanding of mechanistic behaviour, utilising a vast array of imaging techniques available [80]. Whilst some common objectives of imaging techniques are to accurately collect, store and visualise samples [81]; the specific method of how this is performed dependent upon the technique used, ideally selected for compatibility with the project aims and object being examined [82].

Early approaches to produce imaging techniques were used by the Roman Empire, where convex glass was used to magnify objects [80], which enabled users to observe smaller objects at a greater level of detail. Improvements in the quality of the glass obtainable for lenses in addition to placing multiple in series resulted in early versions of the optical microscope, enabling very small objects to be observed in greater detail and magnification.

The creation and development of more advanced techniques such as the electron microscope in the 20th century onwards [80], enabled resolutions orders of magnitude greater compared to optical microscopy, achieving imaging of nanometre scale features. Invention of many other imaging and microscope based technologies has been applied across various disciplines, such as medical imaging [83] and materials science.

Given that bead diameters are approximately 50µm to 100µm and pores can be as small as 10nm, different imaging techniques are required for individual bead and packed bed scales, which present different challenges for producing tomographic representations [18], [24], [84] such as resolution limit, field of view, sample preparation and digital reconstruction need to be addressed by each candidate technique to be discussed for chromatography imaging.

The first imaging method to be evaluated was electron microscopy. This was selected because of the already existing and prevalent use of this approach in chromatography literature for high resolution surface structural imaging. This inherent adoption of electron microscopy in chromatography imaging research provided a suitable benchmark with several examples for consideration and comparison to potential approaches that have had less exposure in the field. Overall the comparison of techniques and examples would form the basis for initial experimentation into 3D representation of chromatography systems.

1.7.2. Electron Microscopy and Tomography

1.7.2.1. Introduction

Electron microscopy (EM) is a technique that has been used across various disciplines in order to image objects at higher magnifications, superior to those used for other microscopy techniques, whilst retaining resolution and a wide depth of field [85]. The invention of the first viable electron microscope is credited to Knoll and Ruska in 1931.

Ruska received a Nobel prize in 1986 for continued developments in the field [86], which included expanding applications and commercialisation efforts in the late 1930's onwards to enhance areas of research which require imaging [87]. Developments in research by Claude and Palade into chemical fixation of specimens allowed for higher quality imaging [88], with continued advancements of EM enabling more advanced image analysis at finer resolutions.

In order to produce a two dimensional image using an Electron Microscope a dry, flat and metallically coated sample is inserted into a chamber under vacuum conditions required for imaging as seen in **Figure 10**, although 'environmental' imaging does exist for samples incompatible with preparation processes at the expense of image quality [88] - [91]. An electron beam is produced from a tungsten filament by thermionic or field emission, with lanthanum hexaboride filaments used as alternatives for thermionic systems [85], [92].

The electron beam is then manipulated by condenser lenses and interacts with the sample in the chamber by either scanning the surface or transmitting through thin specimens depending on the type of Electron Microscope used [85], [92, 93]. There are several methods of electron interaction with sample atoms as displayed in **Figure 14B**, which enable surface detail as well as elemental composition to be determined by an array of probes that are often linked to a Charged Coupled Device (CCD) for visualisation [85].

As with other imaging methods such as optical microscopy, there are technology and technique variations within Electron microscopy that have characteristic advantages and limitations, with technique compatibility relative to the sample being an important consideration. As well as the two major scanning and transmission modes, it is important to consider other types of EM that are available that may have been more appropriate, such as Cryo-Electron Microscopy which is more suited to samples which require moisture [94].

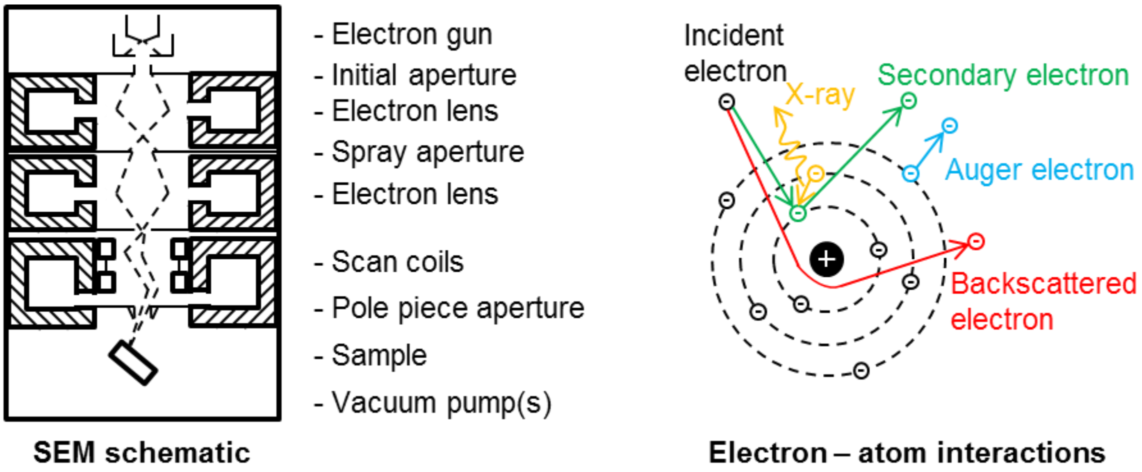

SEM schematic

Electron – atom interactions

Figure 14: Concepts of Electron Microscopy for image generation. Adapted from Goldstein *et al*. [85]. **Left**: Schematic of a conventional SEM relay, note that different types of systems may have alternative or additional equipment. **Right**: EM detection mechanisms.

Transmission electron microscopy (TEM) is configured so that the sample is placed between the condenser and objective electromagnetic lenses [92], differing from the set up seen in **Figure 14A**. TEM generates an image by forming a magnified image on a CCD based upon electrons that have transmitted through and interacted with a sample, which must be no thicker than ~200nm otherwise no electron signal can transmit through the slice [95].

This means that despite TEM being capable of achieving sub-nanometre resolutions and thus identification of even the smallest features, there are several limitations that need to be considered that may not be applicable to particular samples, for example cutting thin slices of soft bead materials to view the internal structure presents several difficulties, as discussed and attempted by Ioaniddis [18] and Angelo *et al.* [24] using different cutting approaches. Processing an entire bead with via many thin sections would also be labour intensive and also susceptible to damage of individual slices before or during imaging.

The other major method used is scanning electron microscopy (SEM), which rather than analysing electrons that have transmitted through a sample relies upon reflected electrons and X-rays from the incident sample surface, negating the need for thin sectioning [85]. However, cutting through a sample of interest would be required for imaging the internal, 3D structure of a chromatography system. Another consideration is that SEM resolution capabilities are generally inferior to TEM counterparts when requiring nanometre scale feature definition, although this is also equipment dependant. Either TEM or SEM approaches investigated would have to be able to successfully image different chromatography materials that may not be entirely suitable for conventional EM.

1.7.2.2. Chromatography bead imaging using Electron Microscopy

Despite issues with sample preparation and slicing via a microtome being documented by Angelo *et al*. [24] particularly for the relatively soft cellulosic sorbents, **Figure 15** displays efforts where EM has been used to image agarose and cellulose surfaces as well as the internal structure of chromatography beads in addition to those seen in **Figure 10**.

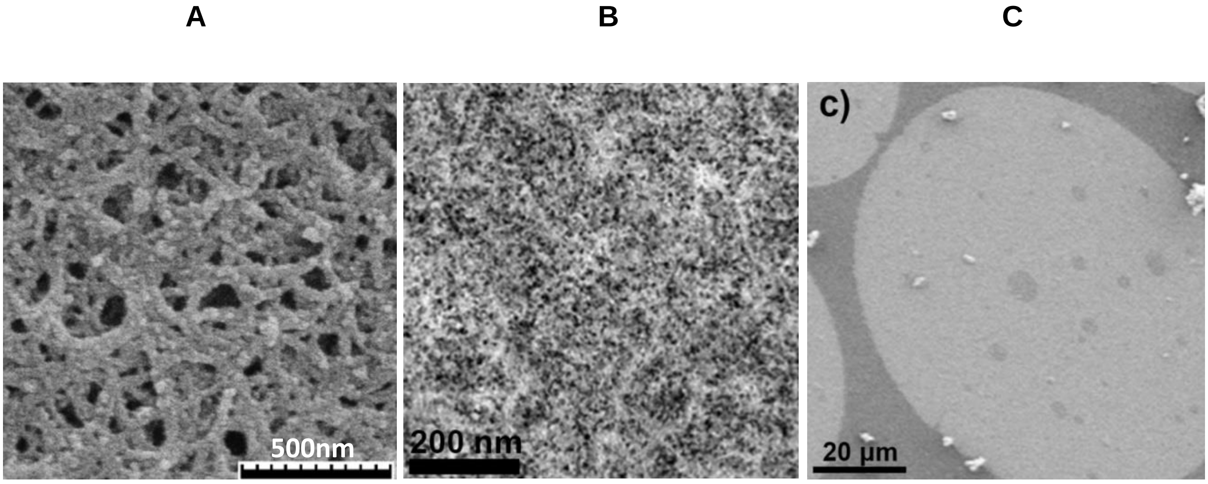

Figure 15: Examples of Electron Microscopy use for bead visualisation.
A: SEM of Q Sepharose FF, high adsorbed protein concentration. From Bowes *et al*. [96].
B: TEM of HyperCel STAR AX section using TAGO fixation. From Angelo *et al*. [24].
C: TEM of HyperCel Star AX section showing void spaces. From Angelo *et al*. [24].

Figure 15A displays an agarose bead loaded with sample protein, where the overall structure compared to **Figure 10C** has a similar topography, but the protein thickened the agarose fibres, reducing pore sizes and hence diffusional and mass transfer capabilities, discussed by Close *et al*. [62] when considering foulant impact on performance [12], [68].

Angelo *et al*. [24] investigated the structural properties of cellulose based MEP HyperCel, determining pore size profiles as well as discussing sorbent preparation techniques, highlighting that processing undertaken should minimise changes to the samples, with heavy ion fixation, critical point drying and finally gold coating used for bead samples [64], [88], [97]. Angelo *et al.* [24] discussed the need for certain preparative steps for EM imaging whilst also considering potential changes to samples that may occur due to bead processing.

1.7.2.3. Physical sectioning techniques

Whilst the pixel size and field of view achievable using EM approaches are sufficient for individual bead scale imaging as seen in several literature examples, issues of sample preparation and lack of material penetration present problems for non-ideal samples. This is particularly important when considering wet, non-conductive beads producing tomographical representations due to the lack of material penetration for imaging, which necessitates an approach incorporating physically sectioning the samples with microtomy and focused ion beam microscopy to be reviewed in terms of preparative techniques for EM imaging.

For both microtomy and focused ion beam microscopy, sample preparation requires embedding into epoxy or silica material to displace air within the internal porous structure [89], with heavy metal staining often performed to improve image contrast between the sample and embedding material. Angelo *et al*. [24] fixed chromatography beads for EM with osmium tetroxide, with example images displayed in **Figures 10B** and **12**. Epoxy embedded samples are then typically polished to a desirable flat surface that exposes the sample.

Microtomy involves using a sharp micro-knife in order to cut micrometre-scale slices of sample that are then individually processed for either optical or electron microscopy [89]. The individual images are then reconstructed using computer software into a three dimensional representation or viewed individually and analysed, with Angelo *et al*. [24] and Bowes *et al*. [96] both using microtomy and Electron Microscopy in order to observe the structure of a sorbent, with Ioaniddis [18] discussing issues with bead microtomy.

A major issue with conventional microtomy for tomographic representations is that sample preparation is labour intensive and time consuming, not guaranteeing success or changes to the sample [89]. Therefore, a more suitable variant for tomography requiring many slices to be made is serial block face electron microscopy (SBFSEM) [98], which utilises a microtome within an SEM where the blade removes a thin layer of sample from the top, with the new exposed block face imaged and subsequently cut away [89], reducing the amount of preparation required of slices using conventional microtomy slicing approaches.

An example of SBFSEM in a related field of membrane technology by Reingruber *et al*. [99] successfully produced 3D renders of porous structure at pixel sizes up to 25nm and overall dimensions up to 46μm over hundreds of slices. This enabled visualisation of the membrane structure, pore connectivity and quantification of important physical characteristics such as porosity and average pore diameters, being desirable outcomes for materials in the project.

The other major tomographic approach identified was focused ion beam microscopy that also uses an electron microscope in order to produce high quality images [100], although an additional heavy ion crossbeam is applied that enables high quality imaging and the ability to cut through a sample [101]. A source of heated gallium or helium is flowed along a tungsten gun, where an applied electric field causes emission from the tip of the source gun, causing the ion beam to be accelerated and focussed and onto the surface of the subject [101].

Whilst electron interactions as seen in **Figure 14** are used to produce an image in conventional EM, the secondary crossbeam ions are of a significantly greater mass and thus can bombard and remove material from the sample surface. This allows for cutting of material away from the surface to isolate a volume of interest that can then examined or removed for other purposes such as preparation of a thin slice for TEM imaging.

By milling the sample surface to expose a protrusion of interest, subsequent slice and view using the gallium ion and electron gun respectively enables a series of high resolution micrographs to be generated, which can then be used to generate a three dimensional reconstruction of the sample [89], with an example of examining a porous structure using FIB microscopy performed by Robinson *et al*. [102]. It is important to note that alternative focused ion beam techniques such as lift-out exist [103, 104]. Major drawbacks of focused ion beam include limited volume of interest and slow processing times [101], with faster milling of samples potentially causing heat based damage to the surface [105]. **Figure 16** displays FIB microscopy use in existing literature, with investigation available in **Chapter 2**.

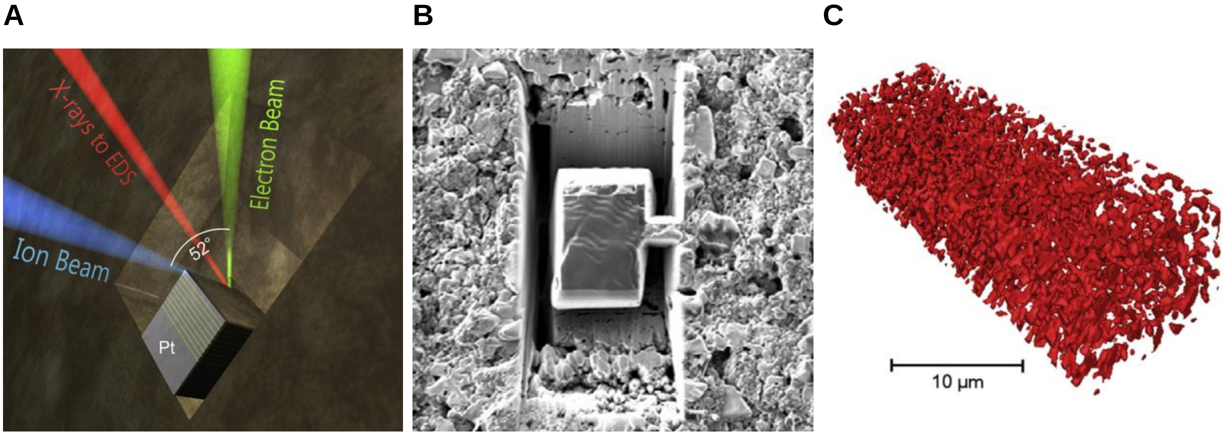

Figure 16: Focused ion beam microscopy approach to porous material tomography.
A: Schematic of the focused ion beam based slice and view. From Zankel *et al*. [89].
B: Focused ion beam trench milling around a volume of interest. From Shearing *et al*. [103].
C: Reconstruction of a pore phase from FIB lift-out for imaging. From Robinson *et al*. [102].

The schematic in **Figure 16A** demonstrates that focused ion beam microscopy relies upon alignment of the sample for milling, with tomography requiring a trench to be cut around the volume of interest, as viewed in **Figure 16B** where lift out was performed on a small protrusion. Sequential slice and view results in hundreds of images of the block face to be collected and reconstructed into a three dimensional volume, with an example in **Figure 16C** of a pore phase of a lithium anode, enabling subsequent quantitative analysis.

Therefore, Electron Microscopy has been discussed as an already popular choice for observing and analysing the structure of chromatography bead surfaces particularly due to benefits such as sub-nanometre resolution and elemental analysis capability, however issues of sample preparation are discussed by Angelo *et al*. [24] as well as the requirement for physical sectioning. Microtomy in the form of serial block face and focused ion beam microscopy appear to be suitable techniques for producing tomographic representations, particularly in consideration of the specific chromatography materials in this project.

1.7.3. X-ray computed tomography

1.7.3.1. Introduction

X-ray computed tomography (CT) is the other major technique to be discussed, with the overall principle being reconstruction of many images to produce two dimensional slices that can be stacked into a three dimensional construct [106]. The first machine was produced in 1967, earning Hounsfield and Cormack a Nobel Prize in 1979 for the invention and development of the technology, which is now the cornerstone of modern radiology in medicine for non-invasive imaging of the body [107]. Whilst clinical use and research is the best known utilisation of the technique, materials science and other disciplines use X-ray computed tomography as an investigative tool, for example Oldendorf [108] demonstrated that tomography using X-rays could identify objects obscured in two dimensions.

The main method of action is that a source produces X-rays which penetrate and interact with a sample before being detected on after transmitting through to produce a signal. By capturing a lot of information over many rotational angles of the sample [106], back-projection mathematics can be applied to reconstruct the individual projections into a 3D volume [109] - [111], with a schematic of an X-ray CT system available in **Figure 17**.

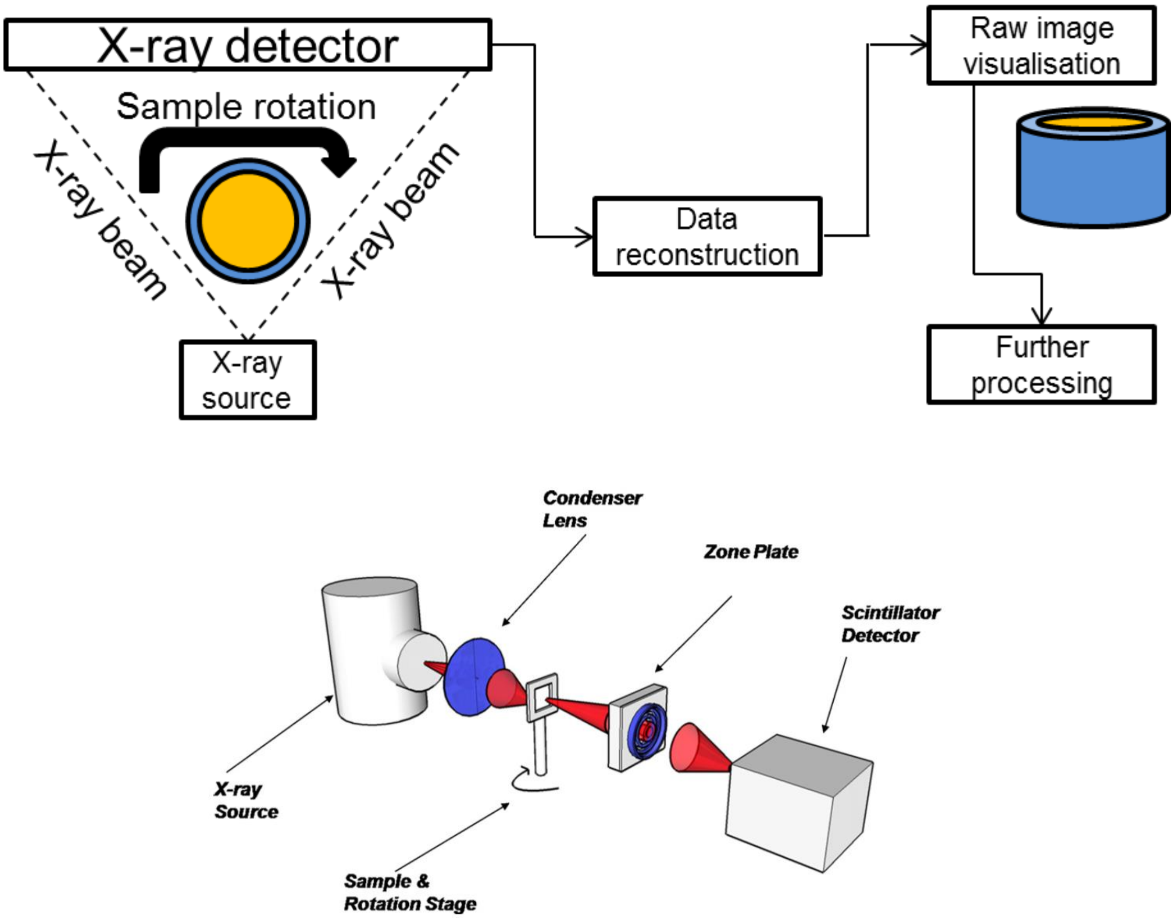

Figure 17: Concepts of X-ray computed tomography.

A: Overall process for X-ray CT acquisition. Adapted from Peyrin and Douek [106].

B: Schematic for lens based X-ray 'Nano' CT imaging. From Shearing *et al*. [112].

The X-ray source configuration historically was a rod shaped beam, although modern equipment uses fan or cone beams, with further parameters such as X-ray elemental source and primary accelerating voltages which enable manipulation of X-ray energies emitted, enabling optimisation for specific samples [109]. X-ray interaction with a specimen including scattering, hardening and adsorption that results in attenuation of signal is detected after sample interaction, which is then translated into digitally readable information [106], [109].

The X-ray profile generated is dependent on several factors such as the energy input and the type of metal used to produce the X-rays, requiring tailoring to the sample or system being considered [106]. Tungsten is a commonplace choice for metal targets due to the wide range of X-ray emission spectra achievable, although alternatives such as Molybdenum are suitable for imaging less dense materials; with filters also available in order to manipulate and optimise image generation beyond that achieved using a source alone [106].

Whilst X-ray scanners for clinical purposes do not require sub-micron resolutions, there is an increasing interest and application of systems that can achieve this at sufficient quality; with several studies discussing the current and future directions of X-ray computed tomography to improve spatial resolutions below 10nm, with the Zeiss XRadia U810 Ultra being an example which uses Fresnel plates for high resolution phase imaging [113] - [115].

Withers [113] discusses three major issues that need to be overcome in order to improve resolution limits for X-ray computed tomography: beam stability, instrument manufacturing quality and sample sizes. The issues with stability can result from using relatively low beam fluxes, which result in poor signal to noise ratios and greater risk of image blurring and artefact generation that is not desirable for producing high quality 3D representations.

Improving and refining instruments such as Fresnel lenses would enable greater manipulation and resolution due to the improved overall quality, accuracy and robustness of machinery. Small sample sizes are required due to the general rule of resolution being limited to approximately a thousandth of sample size, leading to high error sensitivity and therefore imaging of relatively larger objects such as chromatography columns would not achieve a high resolution, requiring smaller objects to be imaged in detail separately [113].

1.7.3.2. Examples and project use

The lack of direct investigations into chromatographic sorbents using X-ray computed tomography for highly detailed visualisation results in difficulties when determining whether the technology is suitable for imaging the detailed structure of chromatography beads due to resolution required being at the limit of what an X-ray computed tomography machine can perform. Therefore, existing analogous studies are examined that use X-ray computed tomography using sub-micron voxel sizes to investigate [116] porous materials.

The two main studies to be examined were performed by Izzo *et al*. [117] and Shearing *et al*. [118], with Izzo *et al*. highlighting the advantage of non-destructive methods of X-ray computed tomography compared to required material sectioning for Electron Microscopy purposes. Izzo *et al*. [117] reported a spatial resolution of 42.7nm, whilst Shearing *et al*. [118] used a Gatan X-ray Ultra-microscope, which has a resolution greater than 60nm as reported by Mayo *et al*. [119], with reconstructed data displayed in **Figure 18** of both 2D and 3D images based upon X-ray CT scans of porous materials.

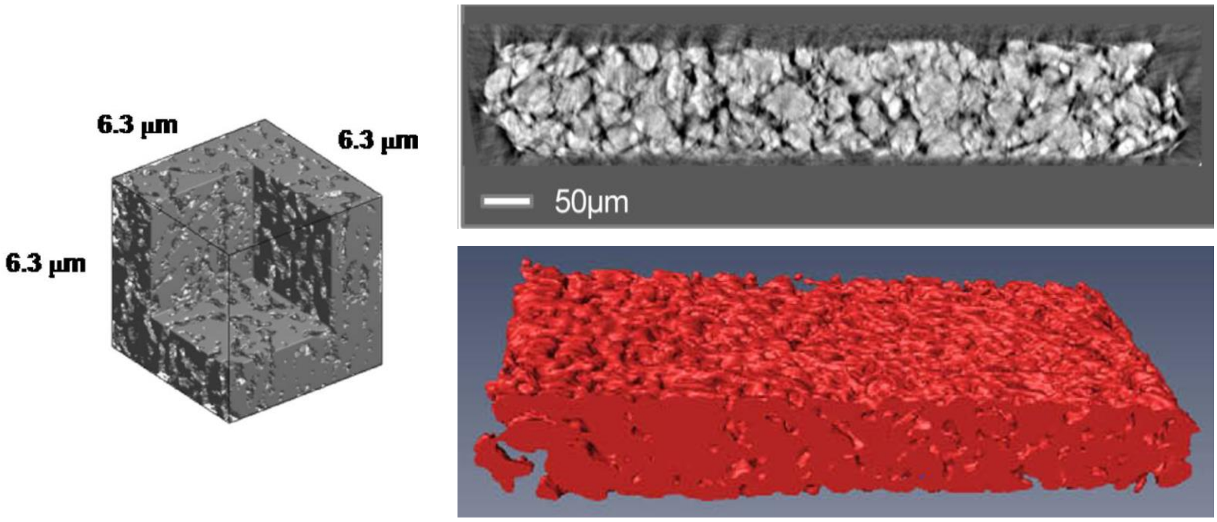

Figure 18: X-ray computed tomography for application on porous materials.
Left: 3D reconstruction of a fuel cell, spatial resolution of 42.7nm. From Izzo *et al*. [117].
Top: Individual 2D reconstructed slice of a Lithium-ion battery. From Shearing *et al*. [118].
Bottom: Rendering of 300 tomographic slices of a Li-ion battery. From Shearing *et al*. [118].

Quantitative data was presented including: porosity, pore size distribution and tortuosity for each case, with Shearing *et al*. [118] concluding that highly detailed tomographic imaging enable examination of existing theories, which may be better understood from geometric data. A Subsequent study by Chung *et al*. [120] provided further analysis of Li-ion batteries when using a 3D model in order to investigate tortuosity [121, 122] in relation to performance. Analysis of porous structures was performed by Tariq *et al*. [123] in **Figure 19**.

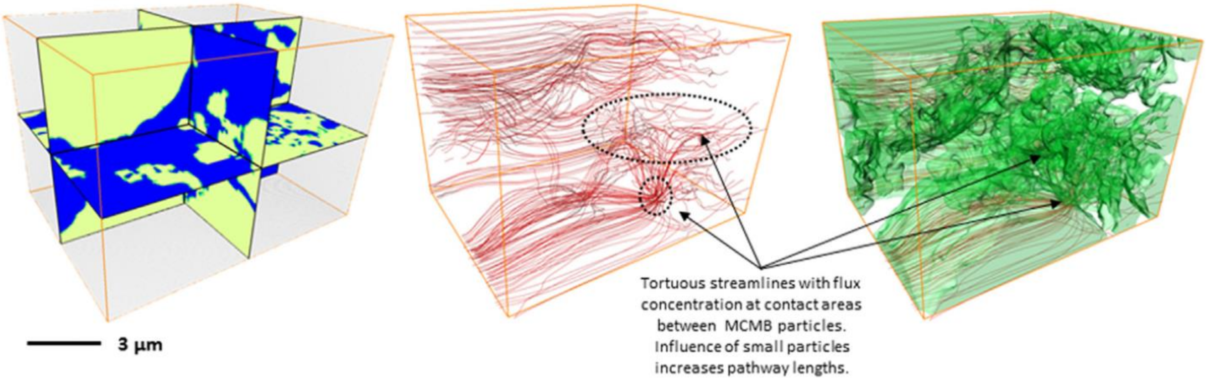

Tortuous streamlines with flux concentration at contact areas between MCMB particles. Influence of small particles increases pathway lengths.

Figure 19: Analysis of lithium-ion battery geometry from X-ray computed tomography. Tortuosity and flow paths through a micro-structure were of interest. From Tariq *et al*. [123].

Aspects considered by Tariq *et al*. [123] of tortuosity and flow paths through a porous microstructure are analogous to both individual bead and packed bed scales of chromatography systems. Therefore, X-ray computed tomography is a major candidate for producing three dimensional representations of individual beads as well as packed beds [124], assuming that pixel size limitations can be overcome on equipment at the bead scale to observe the detailed, internal porous micro-scale structure of an individual bead, with potential to produce tomographic representations using X-ray CT. This technique is to be used for both individual bead and packed bed scale investigations separately using different equipment in each case, with X-ray CT investigated at both scales in **Chapter 3**.

1.7.4. Supporting technique: Optical Microscopy

Optical microscopy is one of the most widespread and commonly used forms of imaging, due to the relative simplicity and early applications compared to more modern techniques, with the 2014 Nobel prize in chemistry awarded to Betzig, Hell and Moerner for improving the resolution limit of fluorescence based optical microscopy [125] - [127]. A longer existence has enabled many developments and variants of optical Microscopy to be produced that useful for different applications; for example dark-field and phase-contrast light microscopy are techniques that do not solely rely on the attenuation of light as with common bright-field, presenting differing advantages and thus useful applications [125].

Electromagnetic waves such as visible light interact with matter through diffraction, refraction, reflection and adsorption, with diffraction and refraction being the main mechanisms for conventional optical microscopy and light diffraction systems displayed in **Figure 18** [125], [128] - [130]. Optical microscopy will be used as a supporting characterisation technique for the project to initially observe and measure bead diameters and size distributions in **Chapter 2** by processing and analysing.

Conventional optical microscopes use a series of convex glass lenses to magnify an object to a desired scale at an eyepiece where either a human or capture device can observe and record the image [125], [128]. For light diffraction systems, Mie scattering principles are applied when laser deviation via particles causes a diffraction to be produced, enabling analysis of the particle sizes [131]. In general, smaller particles cause a greater degree of beam diffraction compared to larger ones, with the diffraction coefficient specific to the material being observed required in order to relate results with scatter patterns generated.

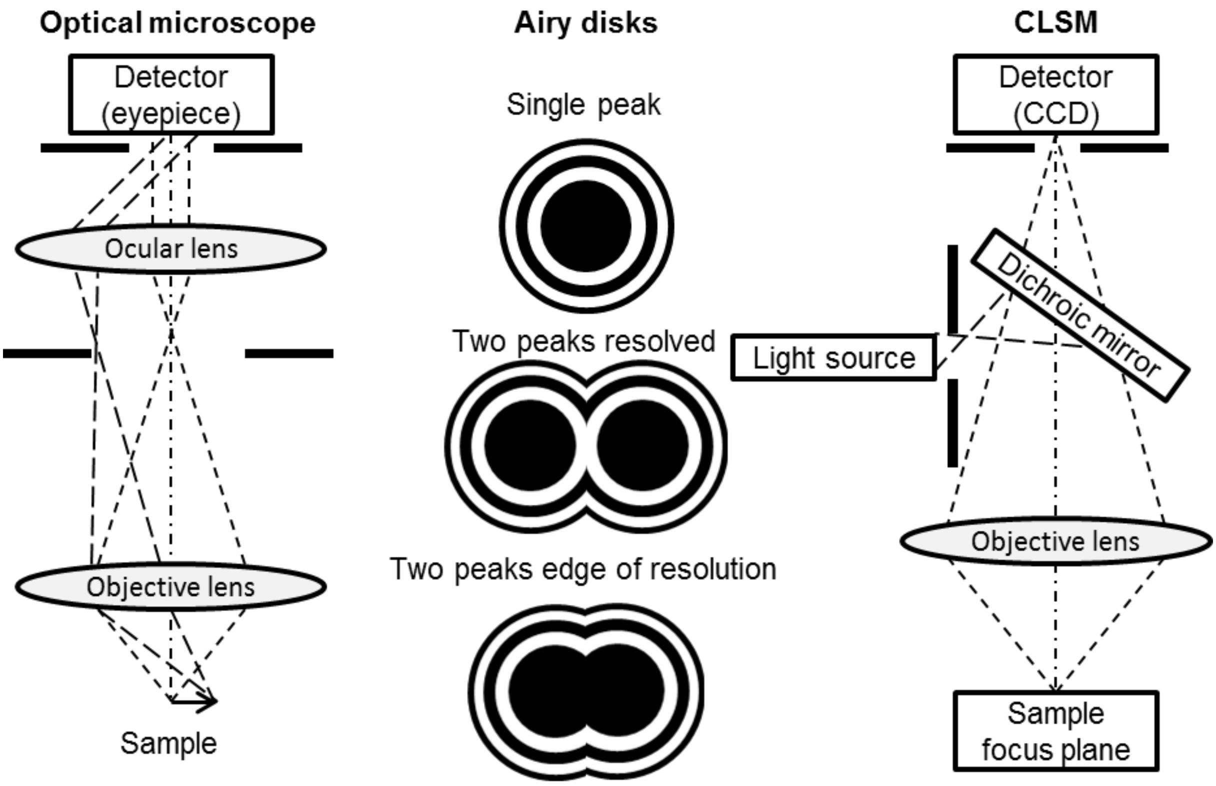

Figure 20: Concepts of Optical Microscopy. Adapted from Bordo and Rubahn [132].
Left: Optical microscope schematic in simplest form, equipment is often more complicated.
Centre: Concept of resolution via Airy disks, where separation of peaks is required.
Right: Schematic for confocal laser scanning microscope used in current studies.

Optical microscopy has a resolution limit of approximately 200nm which is insufficient for pore imaging, but can be used for overall bead imaging but not the intricate porous detail, as shown in **Figure 9**. This has limited the use of optical microscopy to particle sizing, although conventional methods have little material penetration and so would require sample preparation and sectioning to observe the inside of a bead [89], [133]. This is analogous to one of the major electron microscopy limitations encountered; with microtomy of embedded samples the most feasible approach in this case. However, the perceived inability of conventional microscopy to resolve detailed structure suggested it not to be suitable.

An optical method that has the advantages over conventional microscopy is Confocal Laser Scanning Microscopy, which has a superior resolution limit and the capability to optically section samples due to the use of fluorescent tags, negating physical cutting [69], [134] - [137]. Literature examples are displayed in **Figures 11** and **13** that use CLSM to image various different types of chromatography bead to observe internal phenomena such as product diffusion and foulant impregnation over bead usage respectively.

Shapiro *et al*. [138] and Gerontas *et al*. [77] used Confocal Laser Scanning Microscopy to image a 1.5µL micro-column for analysis in order to characterise flow and mass transfer phenomena. **Figure 21** displays key examples from using confocal laser scanning microscopy for chromatography bead imaging in a microfluidic packed bed setting and subsequent modelling of transfer phenomena based upon the 3D structure represented.

The resolution and field of view limits achieved in relevant studies suggests that Confocal Scanning Laser Microscopy may not be effective for commercial scale columns that would exhibit industrially relevant characteristics such as wall effects [77], [138]. Gerontas *et al*. [77] concludes that effective tomographic approaches would be required in order to image packed bed systems that go above the scale achievable using the CLSM approach [139], although microfluidic channels have been visualised at 75µm diameters [140].

Therefore whilst optical imaging has not been deemed suitable for tomographic imaging for detailed internal porous networks or commercial size columns, existing studies have successfully used optical imaging for characterisation of particle size in literature, which is investigated in **Chapter 2** with optical microscopy being a supporting technique to electron microscopy and FIB microscopy. Using quantitative evaluation and computational modelling approaches to simulate chromatography performance and other aspects as in **Figure 21** is also of interest and so is investigated and discussed in **Chapters 4** and **6**.

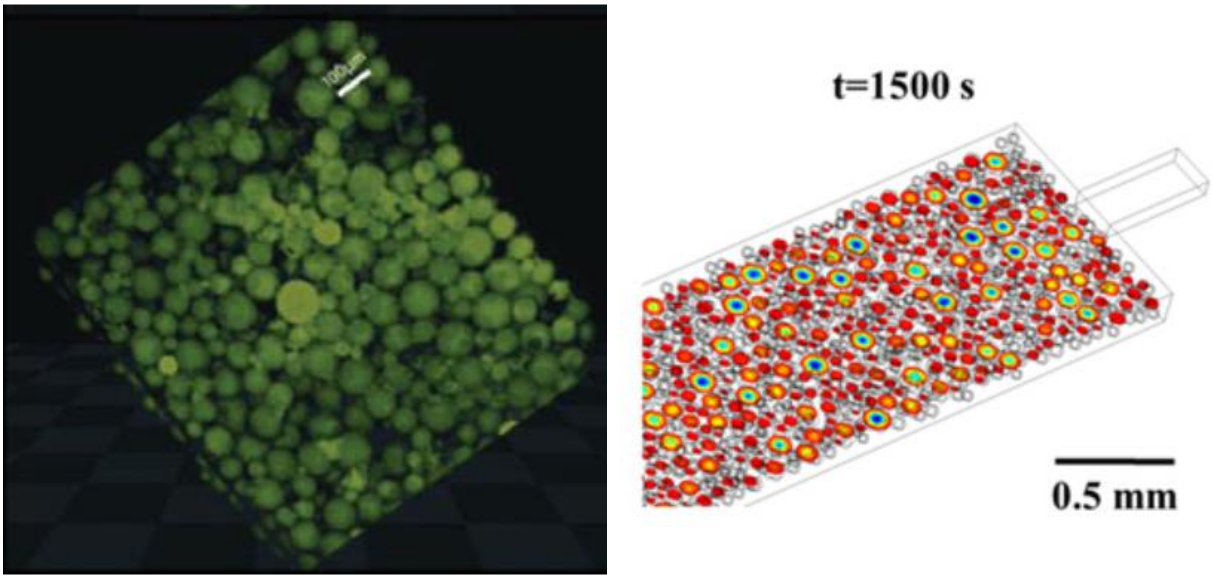

Figure 21: Use of confocal optical imaging to model mass transfer.
Left: Confocal images of the microfluidic packed bed. From Shapiro *et al*. [138].
Right: Adsorbed lysozyme concentration of simulated beads. From Gerontas *et al*. [77].

1.7.5. Alternative technique to note: Nuclear Magnetic Resonance Imaging

Whilst not used in the project, the following imaging technique will be briefly discussed in terms of image generation, exemplar studies relating to the field and potential applications to chromatography representations, as well as why it was not selected for project use. Atomic force microscopy and scanning tunnelling microscopy were also considered but dismissed.

Nuclear Magnetic Resonance Imaging is another technique that can produce three dimensional representations without the need for physical sectioning, with a widespread use in the medical industry, with the importance of the technique highlighted by 3 Nobel prizes in 1952, 1991 and 2003 for Magnetic Resonance Imaging based research and development [141] - [143]. The positive proton in the nucleus of a hydrogen atom is the target, where under a magnetic field the nucleus will precess about a magnetic axis at a frequency related to the gyromagnetic ratio of the particle and the magnetic field applied [144].

The application of a magnetic field polarises the sample, with most protons aligning with the field but some against; by inserting energy in the form a specific radiofrequency, a proportion of protons will enter the higher energy state against the magnetic field [145, 146]. Returning the original low energy state via spin-lattice and spin-spin relaxation releases energy of the system that can be detected; by doing this in three magnetic directions then tomographic data can be generated as in **Figure 22** [146].

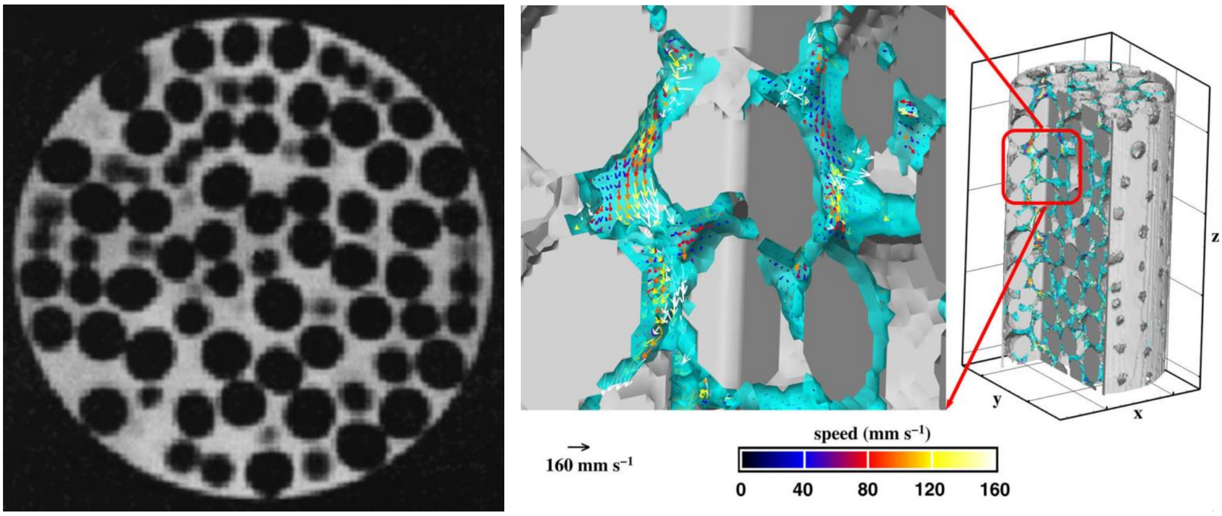

Figure 22: Magnetic Resonance Imaging of packed bed catalytic systems.
Left: Raw visual data of a place slice through a column. From Sederman *et al*. [147].
Right: Visual representation of modelled fluid velocity in a column. From Sankey *et al*. [148].

The images in **Figure 22** demonstrate that Magnetic Resonance Imaging is capable of producing three dimensional reconstructions of packed beds and perform quantitative analysis, fluid velocity profiles being the area of interest investigated by Sankey *et al*. [148]. However, Gladden and Alexander [146] state that the resolution limit of Magnetic Resonance Imaging is 10µm at best, with the studies presented in **Figure 22** using bead sizes above 1cm which is not applicable to chromatography beads, so NMRI was not investigated [149].

1.7.6. Technique comparison for chromatography imaging suitability

Of the four imaging techniques discussed, only X-ray computed tomography has the potential to produce tomographic representations at both individual bead and packed bed scales, with Optical Microscopy and Magnetic Resonance Imaging infeasible for this study due to resolution limitations, whilst Electron microscopy was not suitable for column scale studies due to the large field of view limitations and lack of scalable material penetration.

Based upon this, Magnetic Resonance Imaging and Confocal Laser Scanning Microscopy were excluded for experimental studies, whilst conventional Optical Microscopy was selected as a supporting characterisation tool rather than a technique to achieve the project aims and objectives, with initial bead particle size characterisation available in **Chapter 2**.

Therefore, Electron Microscopy and X-ray computed tomography were the major techniques that need to be compared in terms of the ability to produce tomographic representations of chromatographic systems. X-ray CT will be used at both scales and so can be compared between bead and bed imaging, however no other 3D imaging method was deemed suitable for column representation and so no *inter*-technique comparisons could be performed. At the bead scale X-ray CT and electron microscopy in the form of microtomy and FIB microscopy were selected [89], enabling potential comparison between these methods for beads.

The major advantage of using an electron microscopy based approach compared to X-ray CT is the superior resolution achievable relevant to the bead scale. This will enable clear definition of internal bead microstructure, with exemplar studies displayed in **Figures 10**, **12** and **15**. Given that DePhillips *et al*. [25] suggests that typical pore diameters are of the order of tens of nanometres, the maximum resolution achievable using X-ray computed tomography is of comparable magnitude and thus a feasible approach. However, when approaching the limits of machinery specifications then further issues may be encountered.

A relative drawback of Electron Microscopy is the required preparation of material before imaging, including physical sectioning. Angelo *et al*. [24] commented on the issue of altering the sample when performing preparation stages, where the least destructive approach should be taken. Whilst physical sectioning techniques are appropriate for some samples, the further preparation in terms of embedding as well as mechanical and thermal damage caused by sequential cutting and imaging are considerations to make when producing tomographic representations that may have additional imaging artefacts present.

1.7.7. Image processing and analysis

Once imaging has been optimised to achieve desired results, the next stage is to process data in order to produce a representative tomographic geometry of the packed bed or individual bead structure. This includes removing artefacts introduced by either sample preparation or the imaging process that unwantedly implemented imaging defects. This process can be performed by programs such as ImageJ®, MATLAB® and Avizo® amongst others [150, 151], with comparisons between ImageJ and MATLAB investigated in **Chapter 2** for characterising chromatography bead size distributions.

An important consideration to make for image processing of tomographic volumes is to ensure that bead material phases can be clearly segmented from the buffer or void volume both within and between chromatography beads depending upon the scale investigated. Other issues such as excessive imaging noise or poorly defined edges between phases could lead to misrepresentation, with material specific imaging optimisation explored in **Chapters 2** and **3** in order to minimise artefacts and thus the burden on image processing in order to produce accurate digital representations.

The digitally reconstructed and processed volumes are then to be quantitatively analysed using software to determine key parameter values in relation to existing literature as well as between the three materials to be investigated: agarose, cellulose and ceramic.

Porosity, tortuosity, surface area to volume ratio and pore sizes in the three dimensional spaces are the main characteristics for investigation as these structural aspects impact chromatography performance and can be compared between and within packed beds. For example the positional based porosity differences between a columns edge and the centre, with image processing and quantitative analysis investigated in **Chapter 4**.

As well as examining physical characteristics using a 3D approach, consideration of chromatography system use in terms of process phenomenon that result in changes to the packed bed or bead structure are also of interest for tomographic image processing and analysis. Packed bed compression is investigated in **Chapter 5** where main analysis goals involve investigating the degree of movement before, during and after fluid flow through the column at different rates where comparison of flow paths could be compared. **Figure 23** displays an example process from image acquisition through image processing of digital reconstructions that would enable quantitative characterisation of the sample.

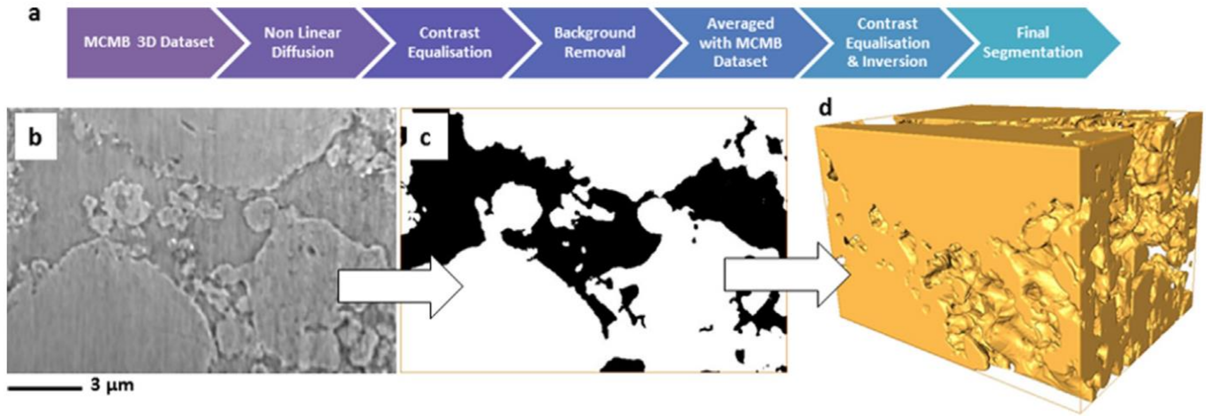

Figure 23: From raw image to volume to be analysed. Raw images are segmented into phases and then reconstructed into a 3D volume for analysis. From Tariq *et al*. [123].

In order to perform correct segmentation using the watershed method such as those seen in **Figure 23** from raw 2D slices, often preparative correction to the original volume is required. The degree to which image processing is required before segmentation depends on several factors: the type of imaging performed, the sample material, feature size requirements for resolution and degree of optimisation performed; where maximising image quality from good sample and imaging preparation often reduces the amount of image processing required.

The raw 2D slice in **Figure 23** does not display two binary phases, although boundaries are clearly defined. Removal of noise within phases is required in order to prevent false porous structure where there is none and likewise in the void sections. Boundary definition can also be harder to accurately define with poor signal to noise ratios that could detrimentally impact segmentation efforts, with image processing ideally minimised by good quality acquisition.

A key advantage of obtaining tomographic data is the capability for dynamic modelling of processes, which in the case of chromatography could be adsorption rates as investigated by Gerontas *et al*. [77] in **Figure 21**, with **Figures 22** and **24** displaying other examples of modelling transfer though porous structure from tomographic modelling. Different values are typically visualized using colour heat maps, which can highlight high areas of flux or diffusion pathways which relate tomography to structural performance. Modelling and the potential for tomographic imaging of chromatography materials are discussed further in **Chapter 6**, with **Figure 24** displaying visual outputs from virtual computation on porous structures. These representations further understanding of how the porous structure is traversed by a mobile phase, with the 3D modelling able to highlight the degree of connectivity and flux.

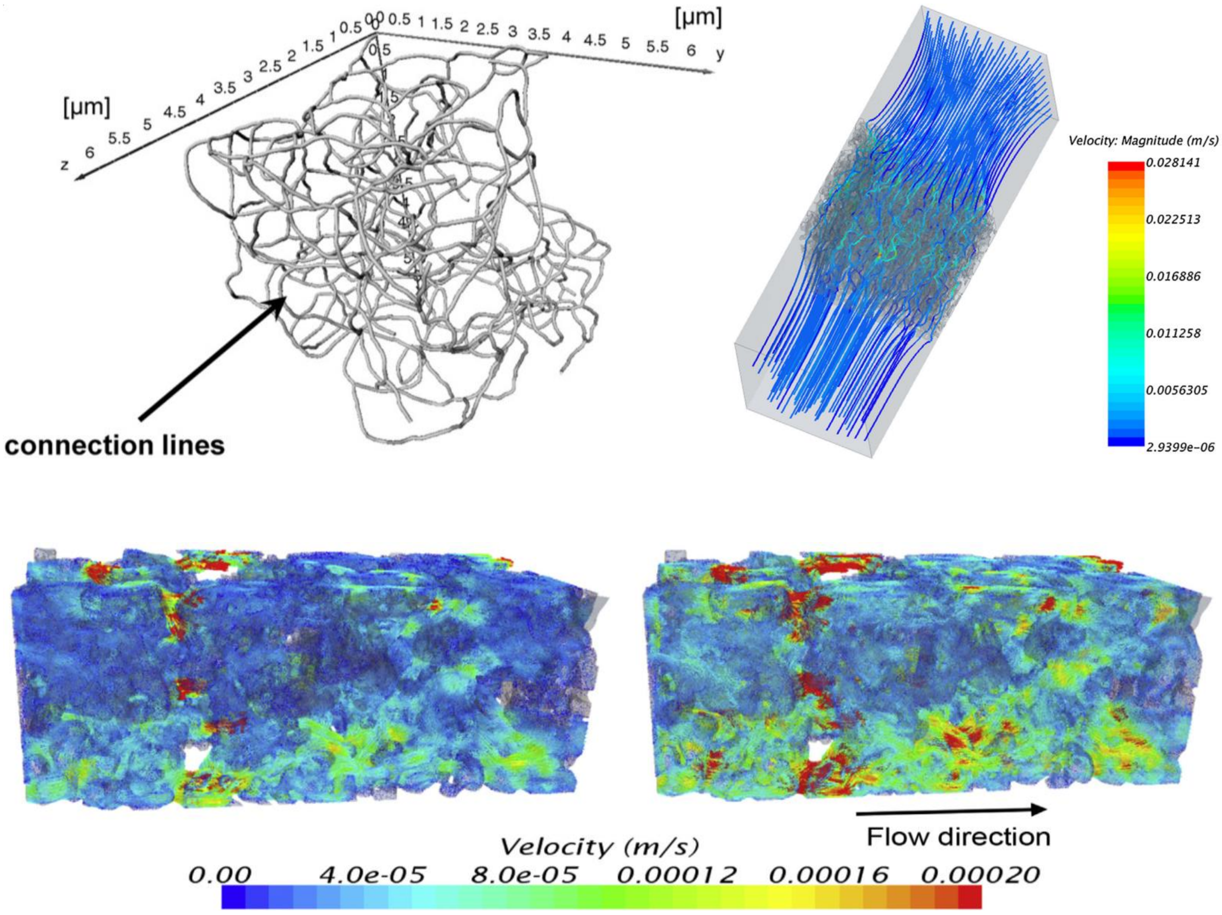

Figure 24: Modelling of porous networks for flow based visual evaluation.

Left: Pore connectivity map of a membrane filter sub-volume. From Reingruber *et al.* [99].

Right: Velocity profiles within a monolithic structure. From Jungreuthmayer *et al*. [152].

Bottom: Flow through an anode at different porosities (higher on right). From Lu *et al*. [153].

Current commercially available software such as Avizo [123] is often sample agnostic and is not specifically tailored for chromatography materials, with **Figure 24** displaying an overall process. Whilst this does enable similar approaches to be taken to existing studies of other generic materials, it also means that software specific to chromatography sorbents were not readily available and so either required generation of bespoke code to perform an action or a different approach altogether for example examining surface ligand structures.

1.8. Chapter Summary table

Section	**Technique**	**Explanation**	**Key Literature**
Chromatography	Liquid packed bed	Micro-beads packed into a column to purify products	[3], [9], [10], [38], [42]
	Types of chromatography	Size, Hydrophobicity, Ion exchange, Mixed mode, Affinity	[10], [19], [52], [57]
	Key studies	Structural characteristics, fouling, compression, scale-up	[13], [20], [21], [24], [62]
Imaging and Tomography	Electron microscopy	Electron interaction with sample enabling sub-nm resolution	[24], [62], [85], [89], [102]
	X-ray computed tomography	Non-destructive reconstruction into 3D volumes via radiographs	[106], [113], [118], [123]
	Optical Microscopy	Visible light imaging, CLSM enables sample penetration	[77], [125], [135], [138]
	NMRI	Magnetic field manipulation to produce 3D representations	[144], [146], [147], [148], [149]
	Tomographic imaging analysis	Processing raw data for quantification and modelling	[88], [99], [116]

Table 1: Summary of Project concepts review of **Chapter 1**.

1.9. Chapter Conclusion

Liquid chromatography in the form of packed beds has been an ubiquitous part of industrial bio-therapeutic downstream processing for decades, and will continue to be essential in the future of biochemical engineering, even with the advancement of alternative separation technologies such as membrane chromatography and monoliths. This relevance is underlined by the extensive and broad areas of related research that continue to provide further insight and improvements to commercially applicable products and processes.

Various imaging techniques have been employed in order to investigate, visualise and quantify key characteristics of chromatography beads and packed bed systems. For bead scale studies, electron microscopy has been used in a multitude of studies to observe the porous surface structure due to the sub-nanometre resolution achievable and relate images to performance and processing aspects, for example Angelo *et al.* [24], [154] using both SEM and TEM to produce micrographs of cellulose based HyperCel materials whilst also discussing important considerations such as the impact of sample preparation. However one of the main drawbacks of conventional EM is the lack of material penetration.

Whilst both electron microscopy and CLSM have been effective at imaging chromatography materials for various applications, they are not solely capable of imaging the sub-micron, internal porous structure of chromatography beads and commercially available chromatography packed beds in 3D. By achieving this at both scales, various geometric characteristics of beads and beds could be better understood and provide information that relates the overall, detailed structures to function, performance and industrial applications.

Tomographic imaging has been applied in other disciplines such as battery and fuel cell investigations to determine the 3D structure of materials [155] - [157], enabling quantification of various parameters such as porosity and tortuosity and modelling of random walks and flux through the geometry that would be of analogous interest to chromatography systems, particularly the internal structure of beads due to diffusion limitations of structure.

Therefore based upon the review, electron microscopy using microtomy and focused ion beam, as well as X-ray computed tomography have been selected to image chromatography structures in 3D and compare between the techniques. Sample preparation, EM and FIB were selected for investigation in **Chapter 2**, with X-ray CT at both bed and bead scales optimised in **Chapter 3**. Processing and quantification based upon imaging was discussed in **Chapter 4** before applying tomographic knowledge to compression and fouling in **Chapter 5**.

Chapter 2

Individual bead preparation and imaging using focused ion beam microscopy

2.1. Summary

This chapter investigates the initial characterisation and electron microscopy based sample preparation requirements for chromatography beads followed by tomographic imaging using focused ion beam. Three commonplace chromatography bead materials were investigated: agarose, cellulose and ceramic, with critical point drying followed by gold coating found to be the most effective preparative approach for electron microscopy imaging, with particle size distributions used to determine any noticeable impact on beads due to the drying processes. Further quantification of cellulose samples was also performed by measuring 2D surface pore diameters based upon electron micrographs that are commonly used in literature.

Focused ion beam and microtomy were investigated for tomographic imaging suitability for the individual beads once the preparation stages had been optimised, although microtomy was not successful and so focused ion beam was the sole technique employed for this study. Ceramic samples achieved a cubic pixel size of 15nm, however difficulties with processing the softer agarose and cellulose resulted in compromised pixel sizes up to 40nm.

2.2. Introduction

As discussed in **Chapter 1**, electron microscopy via microtomy and focused ion beam were selected as suitable imaging candidates for generating tomographic representations of chromatographic sorbents at the individual bead scale. These approaches should be capable of imaging at a resolution deemed sufficient to identify the smallest features of bead internal structure that has been used in several studies to image the surface of resins [62], [70], allowing for further understanding in various studies that are discussed in **Chapter 1**.

Agarose, cellulose and ceramic chromatography beads were selected for initial characterisation due to their commonplace use in academic and industrial chromatography applications, as well as differing physical characteristics that enable *inter*-material observations. The cellulose beads have previously been investigated by Angelo *et al.* [24] for structural characteristics, with electron microscopy data presented in the study [24] to be used as a basis for comparison for achieving high resolution imaging via serial sectioning.

In addition to electron microscopy based approaches being the main tomographic imaging technique in this chapter, optical microscopy was utilised for initial characterisation of beads in relation to sample preparation. This aspect is investigated as it is the first stage in the overall process, with any issues arising here detrimentally impacting subsequent steps.

2.3. Electron Microscopy

The concepts of electron microscopy examined in **Chapter 1** indicated that whilst resolution limits would not be an issue when considering individual bead scale imaging, a major hurdle to investigate would be sample preparation requirements, particularly when considering moisture containing, non-metallic materials such as chromatography beads that are made of relatively soft materials which could potentially compromise overall EM imaging standards.

Despite the importance of sample preparation for eventual image quality and the impact on the rest of the process up to final quantification, the subject is not well documented in studies when considering preparation impact [65] on bead image generation when using electron microscopy, although Angelo *et al.* [24] does discuss the potential of structural changes from the true form due to preparation techniques which is expanded upon by Nweke *et al.* [65]; with critical point drying selected by both studies to prepare for electron microscopy imaging.

Therefore, the first investigation for using electron microscopy to image individual beads will be the optimisation of the preparation technique used to produce representative samples for each material, with direct comparisons to Angelo *et al*. [24] possible due to investigation into the same cellulosic MEP HyperCel beads, albeit only in a 2D context in that study.

The three aspects to be considered for sample preparation are: ethanol content in buffer, drying method and gold coating of sample after drying. Angelo *et al.* [24] also included aldehyde and osmium fixation steps which improve image contrast [85], which will be included during critical point drying based preparation as a standard procedure.

The inability of electron microscopy techniques to penetrate sample surfaces necessitates physical sectioning of beads that have been prepared to a sufficient quality in order to produce tomographic data. In **Chapter 1**, two main techniques were suggested for investigation in the forms of microtomy and focused ion beam approaches.

Microtomy involves thinly slicing samples using a sharp knife to produce thin sheets of material that can then be imaged via SEM or TEM; using the series of micrographs to reconstruct a 3D volume for tomographic analysis, with Serial Block Face Sectioning Scanning Electron Microscopy [89] using Gatan 3View® technology [98] a viable candidate for final imaging. However, initial experimental investigations were unsuccessful for slicing chromatography beads and so were not extensively explored, as discussed in this chapter.

Therefore focused ion beam was selected as the sole electron microscopy based method for producing tomographic representations of agarose, cellulose and ceramic chromatography beads. A FIB microscopy approach does not require mechanical slicing of an embedded sample as milling is performed using a gallium ion beam and so negates the main issue found when attempting microtome slicing, although does still present challenges that have been discussed in **Chapter 1** which need to be considered whilst using FIB microscopy.

The main topics to be discussed in relation to FIB of chromatography beads include sample preparation requirements and impact on original sample condition, overall image quality and contrast achievable in relation to spatial resolution and definition between bead and epoxy phases. X-ray CT is explored in **Chapter 3** as an alternative tomographic imaging technique that is used for examining the same bead types, with comparison between the two made.

2.4. Materials and methods

2.4.1. Bead preparation

Capto™ Adhere (GE, Sweden), MEP HyperCel and CM Ceramic HyperD F (Pall Biotech, USA) respectively made of agarose, cellulose and ceramic material were investigated in parallel for all experiments, and so will be referred to as the sample or sorbent. 1mL of sorbent was inserted into a 1.5mL Eppendorf Tube® for storage at room temperature, unchanged samples are to be referred to in this way to distinguish from others.

2mL of sorbent from the same source was then inserted and packed into a 1cm diameter column, with plastic inlet and outlet tubes connected to using ultrapure water from a Millipore Advantage A10 and absolute ethanol as feed sources, with the system controlled by a GE ÄKTA™ Explorer. Inlet flux of 0.8mL per minute was used throughout the process, with two column volumes applied at each stage. The percentage of ethanol to water at each stage was as follows: 0%, 20%, 40%, 60%, 80% and finally 100%. The column was then opened, removing half of the packed bed and placed into a 1.5mL Eppendorf tube, noted as 100% ethanol preparation for further experimental processing.

The column in 100% ethanol was then re-packed, with a flux of 0.8mL per minute again used for the inlet, with one column volume applied at each stage. The percentage of ethanol to water for sequential runs was as follows: 80%, 60%, 40% and finally 20%. The column was then opened, with the remainder of the sorbent placed into a 1.5mL Eppendorf tube at room temperature, noted as down to 20% ethanol column preparation in experiments. Samples were then dried, although some did not undergo a drying process, referred to as 'undried' or 'environmental'. Samples were either dried using air drying or critical point drying. For air drying, 0.2mL of sorbent was placed onto a petri dish under a fume hood at atmospheric conditions for 16 hours before insertion in dry form into an Eppendorf tube for storage.

For critical point drying [158], glutaraldehyde fixation was performed on a polycarbonate filter containing sample for 30 minutes, with subsequent wash stages and fixation in osmium tetroxide for one hour. Dehydration of the sample was performed by ethanol gradients of 25%, 50%, 75% and 100%, with stages lasting 5 minutes. Sample coated with ethanol was then inserted into a Gatan Critical Point Dryer and sealed inside, where carbon dioxide gas was inserted and vented over a period of two hours. Once 8.3bar and 37^{o}C had been reached, gas is vented and temperature reduced to STP for specimen removal and storage.

For conventional optical imaging of beads for particle size characterisation, an AMG EVOS® X1, was used at a magnification of 10X to view samples, which were re-suspended in 0.5mL of the corresponding ethanol concentration (20% or 100%, unchanged buffer ethanol concentration was 20%) and placed in transparent culture flask wells onto the optical microscope platform. Ten images per sample were captured via CCD and subsequently entered into ImageJ® v1.48 and a MATLAB® v2014a system for diameter analysis, as seen in **Figure 25**. Determination of diameters and area was based and upon and adapted from established programs commonly used for these purposes, such as the 'Find Circles GUI' plugin. For laser diffraction experiments, a Malvern Mastersizer 2000 was used with sample sizes of 0.4mL dispersed in MilliQ purified water to obtain laser obscuration between 15-20%. Three repeats of each sample were measured, with the average recording presented.

2.4.2. Electron microscopy and focused ion beam

The coated or uncoated samples were placed onto Scanning Electron Microscope aluminium platforms applying less than 0.1mL of sample via spatula; carbon tape was required for non-environmental samples. Beads to be coated were then inserted into a Bio-Rad E4500 and exposed to gold sputtering for two minutes under an argon atmosphere, before being inserted into high vacuum conditions or variable pressure in a JEOL (Japan) JSM 6480LV in **Figure 28** to **30** for imaging, where Energy Dispersive Spectroscopy (EDS) with INCA software was used on the SEM for elemental analysis. Accelerating voltages were varied between 2keV and 15keV at various magnifications, which were both noted on each image. Note that a JEOL JSM 7401FE was used in place of the other SEM for **Figure 31**.

For preparation of CPD beads for microtomy and FIB, 250µL of sample in 100% ethanol was inserted into a 1.5mL Eppendorf tube. A solution of Embed 812 sorbent, Dodecenylsuccinic annhydride, nadic methyl annhydride and benzyl dimethyl amine was mixed, with 100, 80, 50 and 7 parts of each material respectively whilst avoiding bubble formation [159]. The mixture was inserted into a 10cc syringe and stored at -20^{O}C when not in use.

For epoxy embedding, the epoxy mixture was mixed with a hardener (Struers, USA) in a 15:4 ratio, again avoiding bubble formation. Small quantities of samples were separated via brass coils in a 250mm diameter Struers mould. The epoxy-hardener mixture was then poured in slowly and incubated in a vacuum chamber for 24 hours. Surface polishing was performed using silicon carbide of increasing grit ratings: 600, 1,200, 2,400 and 4,000 before final diamond polishing. Hardened pucks were adhered to aluminium stubs using Struers Leit C conductive cement before gold coating (Agar Scientific, USA) and bridged with silver to ensure conductivity between all components to minimise electrostatic charging.

For unsuccessful microtomy attempts, a Thermo Scientific™ (USA) HM325 microtome was used. FIB experiments were performed using a Zeiss (Germany) XB1540 ‘crossbeam’ system under vacuum conditions. Samples were moved into position by observing an internal CCD monitor and rotated to 54º followed by alignment of the scanning electron and gallium ion beam paths onto the sample, as observed in **Figure 25**. Primary accelerating voltages between 1KeV and 10KeV in secondary electron detection mode were used throughout imaging using the focused ion beam system, where individual bead outlines could be identified in the embedded epoxy. An FEI (USA) Helios NanoLab™ 600 crossbeam system was used for final cellulose processing and imaging due to equipment issues with the equipment, however overall stages performed were in-line with the intended approach.

Once a bead of interest had been identified, platinum deposition on the relevant area was performed to achieve a 1µm layer thickness with dimensions of 20µm to protect the sample and reduce milling streaks. Gallium ion milling was used to cut a ‘U’ shaped trench to surround the sample using an initial milling current at 1na, cutting a trench with dimensions of 30µm by 20µm at a depth of 30µm to expose the coated protrusion of 15µm by 10µm.

Further polishing of the protrusion edges was performed at a milling current of 200pa followed by 100pa to achieve smother surfaces. Slice and view tomography was also performed by milling at 100pa, with a spatial voxel size of 15nm selected in order to be able to view the entire block face during sequential milling of the protrusion and scanning electron microscopy imaging at an accelerating voltage of 1KeV. 2D JPEG images from slice and view imaging were saved in each case for subsequent processing in **Chapter 4**.

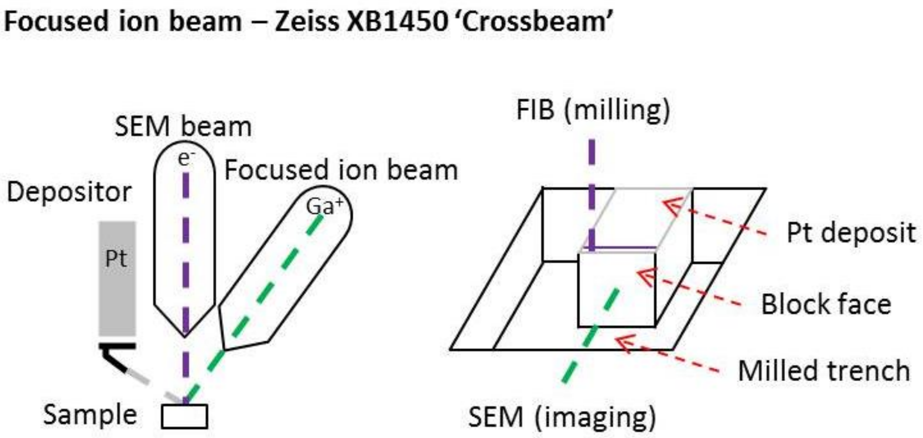

Figure 25: Focused ion beam schematic for tomographic slice and view.
Left: Key sections of the crossbeam system, displaying the depositor, milling and imaging apparatus above the sample with relevant beam lines depicting location of action.
Right: Cut trench before sluice and view, demonstrating the location of platinum deposition above the protrusion and sequential milling and imaging. From Johnson *et al*. [160].

Ceramic samples maintained the 15nm voxel size during final slice and view, however alterations to agarose and cellulose settings were required. A revised 20nm pixel size for width and height was used alongside a 40nm depth for each slice was selected for both materials, as this was found to be the closest to the desired cubic 15nm pixel size which also considerably reduced the artefacts and imaging issues. The averaged dimension size was 25nm which was still superior to 32nm achieved using high resolution X-ray CT.

2.5. Results and discussion

2.5.1. Bead preparation

The three variables of column preparation, drying technique and gold coating produced 18 permutations for investigating preparation at the individual bead level. Optical microscopy was used to investigate particle size distributions and any changes due to preparation approach, with examples of cellulose increasing in size due to ethanol in literature [161] and hence distorting the true physical appearance of the chromatography beads. Mastersizer laser diffraction as well as conventional optical microscopy was used for comparison, with ImageJ and MATLAB image processing used to identify whether using different software programs and analysis strategies resulted in the same quantitative results.

Figure 26 displays the image processing applied to the resin and the results obtained for using fresh, unaltered sorbent. Gold coating wasn't included in the preparation study for particle size distribution as the coating thickness was not expected to significantly impact bead diameter. The results in **Figure 26** display that the two systems produce distributions that have similar averages and variance for each sample, verified by using a statistical analysis of variance test; demonstrating that the average and variance in each case between MATLAB and ImageJ approaches can be attributed to natural variation of measurements.

However, the use of the same images on different systems did result in not entirely identical particle size distributions, highlighting that image processing requires optimisation in order to produce representative data without inducing artificial error [162], particularly considering that tomographic data-sets are 3D. Optical microscopy in conventional and laser diffraction forms was performed for the 9 permutations, with results shown in **Table 2** and **Figure 27**.

Results from **Table 2** indicated that there was no significant change at a 5% confidence level to cellulose bead size due to the preparation approaches measured using a Mastersizer (P=0.39 between 9 sample datasets for each permutation taken in triplicates) but was found to be different to optical microscopy counterparts (P=0.03 between Mastersizer and optical microscopy dataset values). Optical microscopy results may have improved in reliability and accuracy if the sample size was increased, however this was deemed unnecessary for the purposes of this study. The results displayed in **Figure 27** for all 3 materials further demonstrate that any alterations that occur are not macroscopic and so may only impact the detailed structure, that required imaging using a more suitable technique in **Figure 28**.

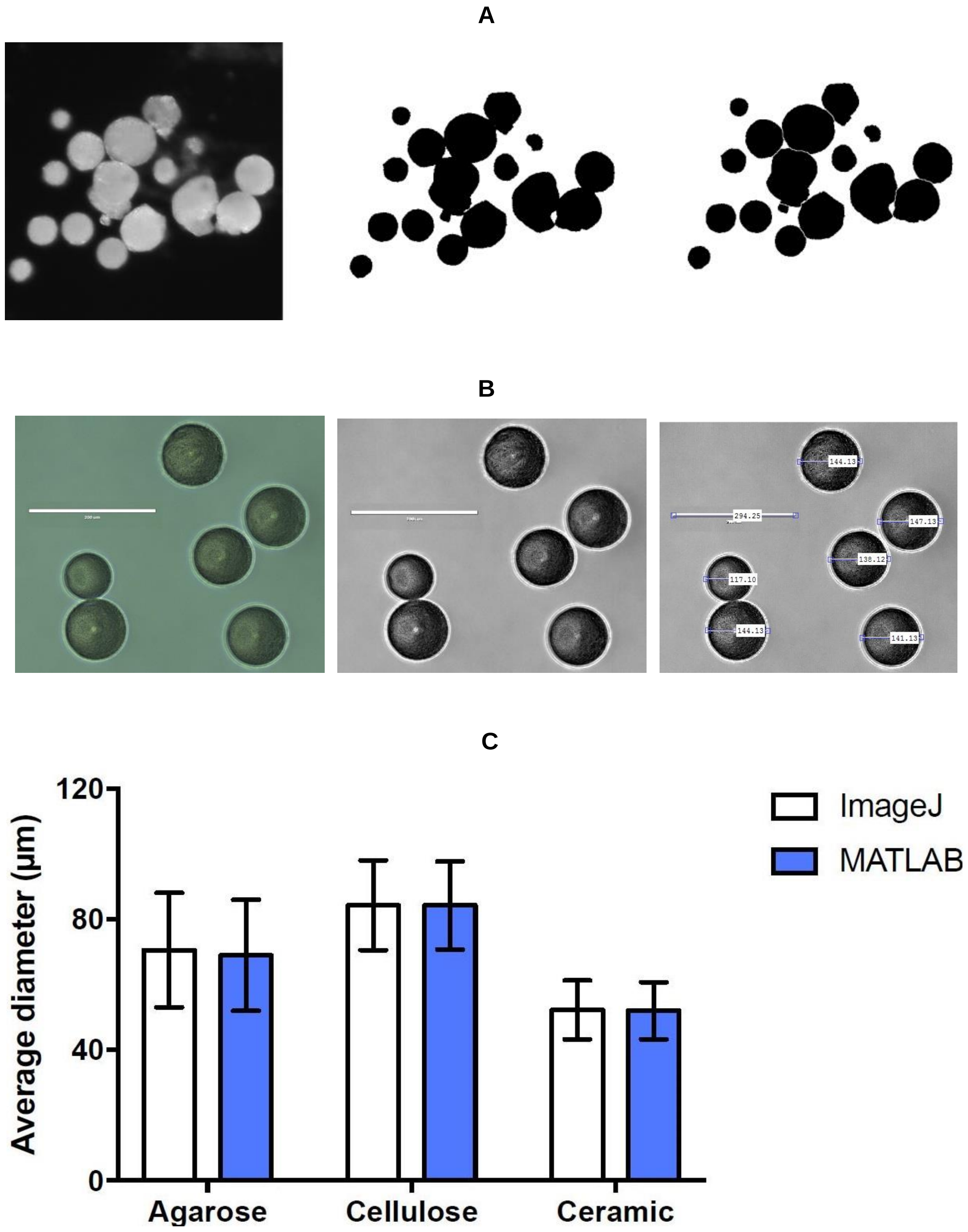

Figure 26: ImageJ and MATLAB image processing and fresh sorbent profiling results

A: ImageJ processing of images based using material segmentation and area calculations.

B: MATLAB processing of images based upon direct diameter determination.

C: Average bead diameter of bead materials when 10 optical images of over 1,000 beads processed via ImageJ and MATLAB systems using the approaches displayed in **A** and **B** respectively. Approach based upon individualising beads and measuring the bead diameter.

Method	Preparation technique	Bead preparation approach (µm)		
		Unchanged	100% ethanol	20% ethanol
Mastersizer	Environmental	89 ± 15	89 ± 14	90 ± 14
	Air dried	88 ± 14	88 ± 15	89 ± 15
	Critical point dried	88 ± 15	86 ± 16	88 ± 14
Optical microscopy	Environmental	85 ± 20	83 ± 12	79 ± 17
	Air dried	86 ± 9	84 ± 11	85 ± 12
	Critical point dried	83 ± 12	87 ± 7	80 ± 14

Table 2: Bead size distributions using optical microscopy and Mastersizer measurements of cellulose samples. Three runs per permutation were performed for Mastersizer measurements, with a total of 1,403 beads over 10 images per material for optical results. P=0.39 for *inter*-sample Mastersizer results but P=0.03 when compared to microscopy.

Electrostatic accumulation and discharge detrimentally impacting image quality at higher magnifications [85], with environmental and air dried samples displaying sodium chloride layer formation on the surface that obscured the chromatography bead structure, as can be seen in **Figures 28 A-D** and **29 A-D**. Critical point dried samples in **Figure 28 E** and **F** enabled successful imaging of cellulosic chromatography bead surface with no salt layer either visualised or detected in **Figure 29 E** and **F**. These findings were also found for agarose and ceramic samples, with examples displayed in **Figure 30** and the **Appendix**.

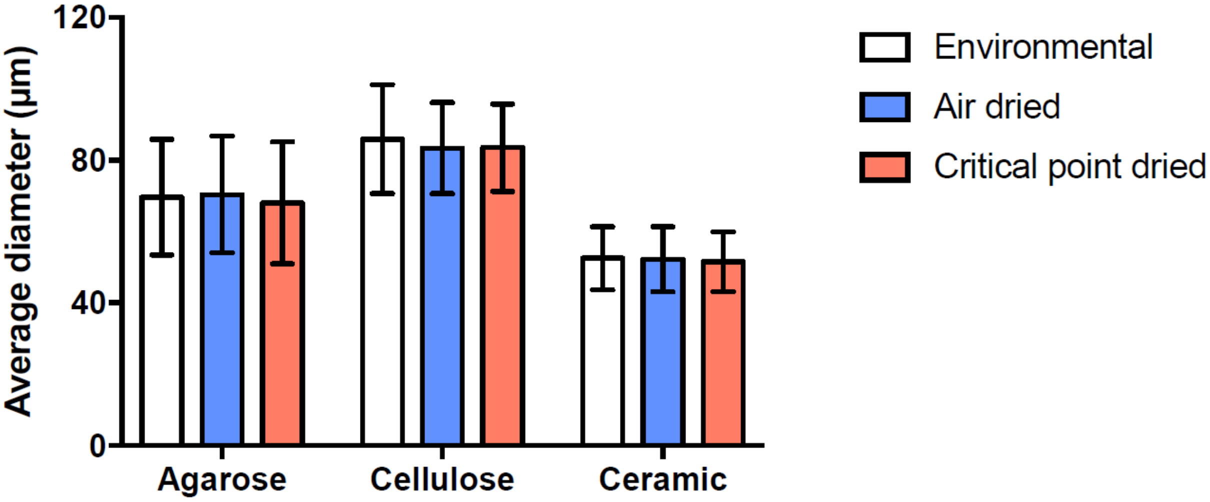

Figure 27: Average bead diameters for each material based on environmental, air dried and critical point dried techniques. Ethanol preparation (unchanged, 100% and 20%) were found to have no impact on diameter and so were collated, with 10 images per method analysed.

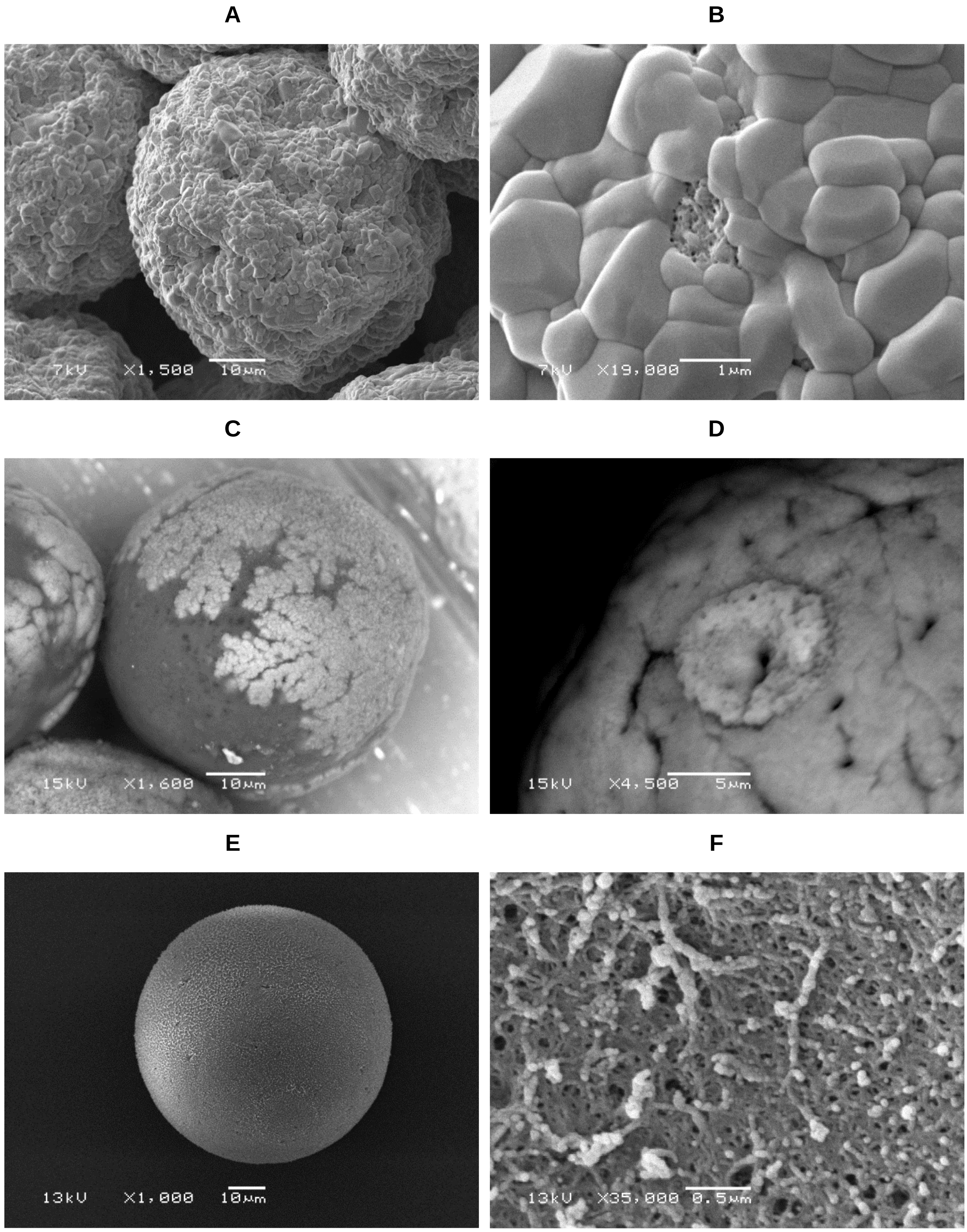

Figure 28: SEM visual data of cellulose bead surface structure based upon preparation.

*Please refer to the **Appendix** for further electron micrographs and expanded versions.*

A and **B**: No column preparation, air dried, uncoated cellulosic bead.

C and **D**: No column preparation, environmental, uncoated cellulosic bead.

E and **F**: 100% ethanol preparation, critical point dried, gold coated cellulosic bead.

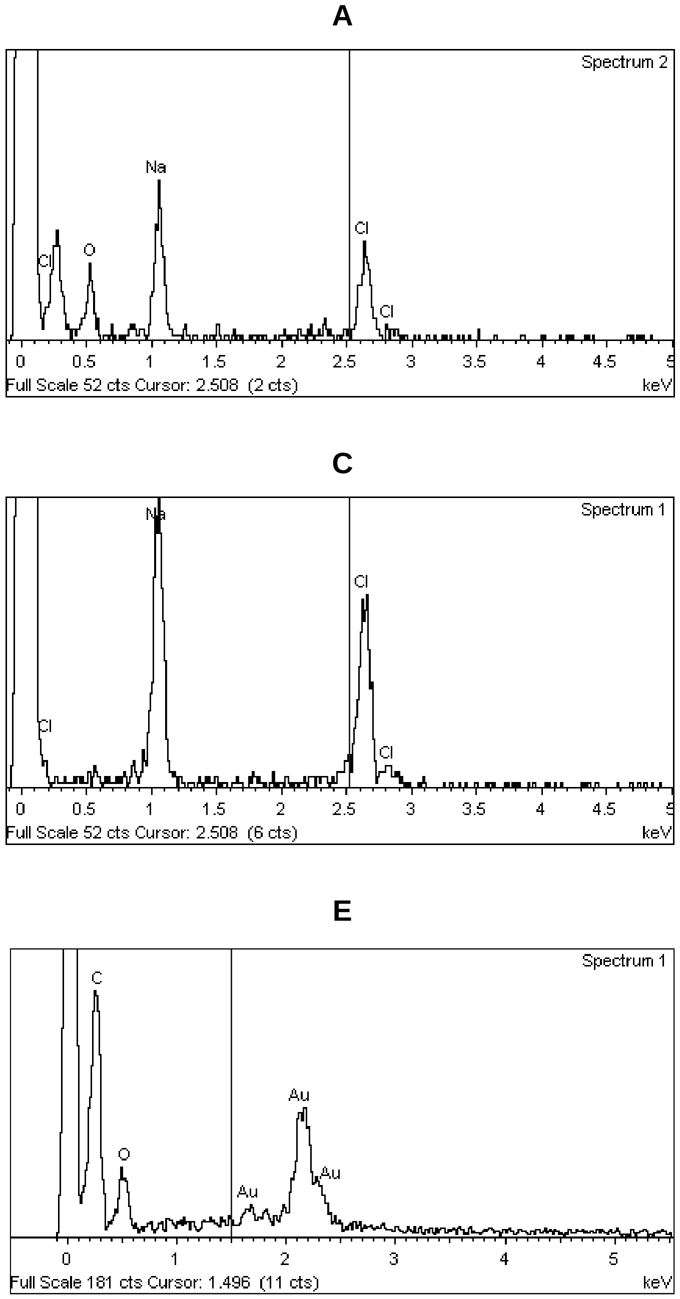

B

Element	**Weight (%)**	**Atomic (%)**
Oxygen	36	41
Sodium	52	39
Chlorine	12	20
Total	100	100

D

Element	**Weight (%)**	**Atomic (%)**
Sodium	35	41
Chlorine	53	39
Oxygen	12	20
Total	100	100

F

Element	**Weight (%)**	**Atomic (%)**
Carbon	65	71
Oxygen	35	29
Total	100	100

Figure 29: Energy dispersive X-ray spectroscopy results for cellulose bead analysis. Rows presented correspond to those presented in **Figure 28** via SEM images.
A and **B**: No column preparation, air dried, uncoated cellulose bead.
C and **D**: No column preparation, environmental, uncoated cellulose bead.
E and **F**: 100% ethanol preparation, critical point dried, gold coated cellulose bead.

The images and corresponding EDS data displayed in **Figures 28** and **29** respectively demonstrate that using an appropriate drying technique and gold coating are important requirements for producing representative quality images for an EM approach.

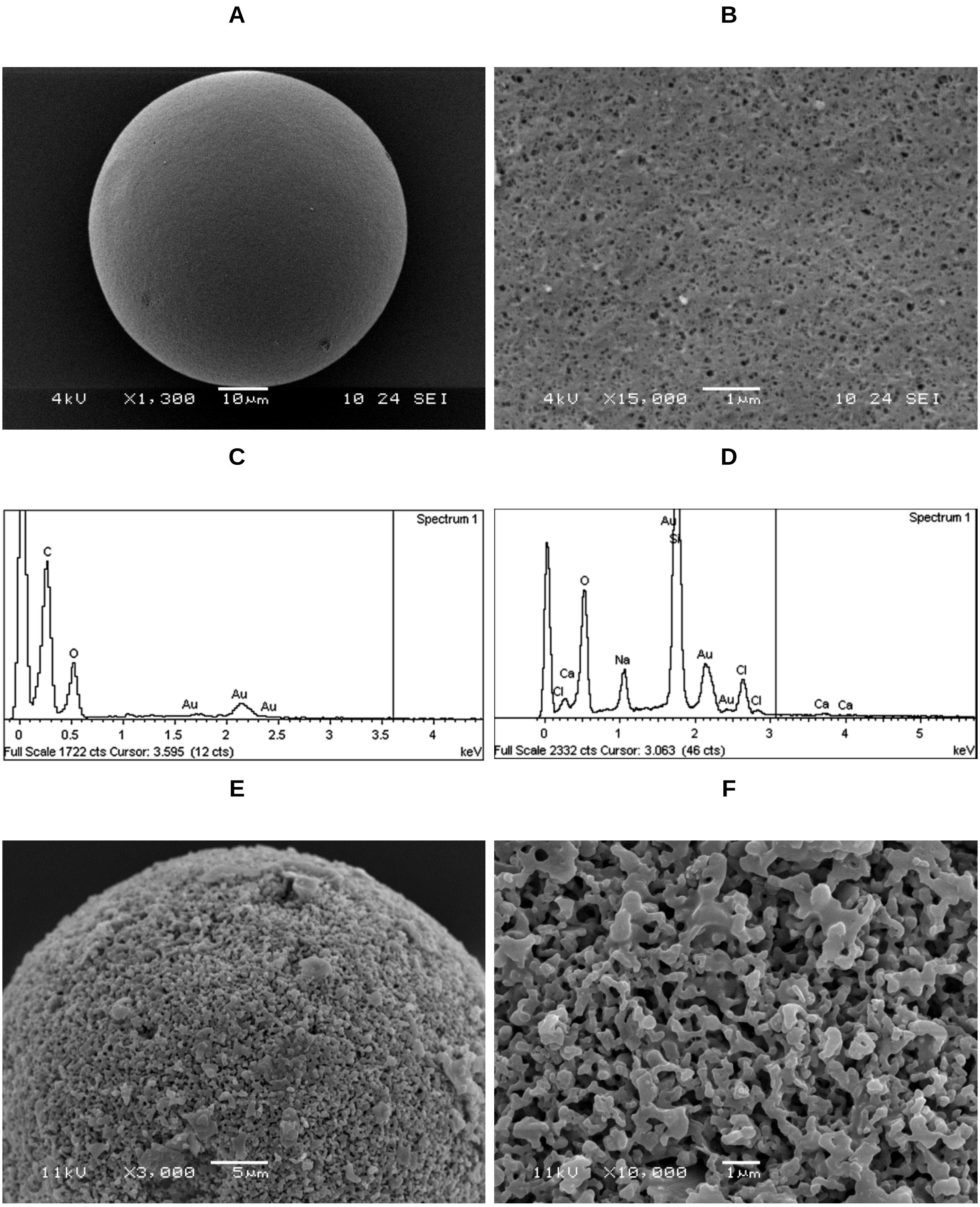

Figure 30: Examples of agarose and ceramic bead preparation method investigations.

A and **B**: Electron microscopy images of Critical point dried agarose beads.

C: Energy dispersive X-ray spectroscopy results for agarose bead analysis.

D: Energy dispersive X-ray spectroscopy results for ceramic bead analysis.

E and **F**: Electron microscopy images of unaltered, air dried, gold coated ceramic beads.

Further electron micrographs of agarose and ceramic beads are available in the **Appendix**.

In addition to different particle size distributions of the three materials as shown in **Figure 27**, it can be observed from **Figure 30** that the surface structure between the agarose, cellulose and ceramic beads is drastically different, which would impact geometric aspects to be investigated such as tortuosity. Therefore, critical point drying in addition to gold coating was deemed to be the most suitable method for preparing all chromatography bead types investigated. Although there are alternative preparation approaches available such as freeze drying [163], they were not deemed suitable due to damage caused to softer samples [65].

As discussed by Angelo *et al*. [24], preparation of chromatography bead samples may cause changes to the material that result in images obtained not being an exact representation of the spheres in their native state. Therefore as no discernible benefits could be observed from ethanol preparation, this was not carried forward for further sample preparation, with the overall results from the chromatography bead preparation investigation and the resulting recommendations for individual bead preparation for subsequent electron microscopy, focused ion beam and X-ray computed tomography studies displayed in **Table 3**.

In addition to ensuring that chromatography bead preparation was performed so that samples were representative of the true structure, the quality of the imaging apparatus was of importance for capturing the finer features of chromatography structure. Whilst focused ion beam is compared to X-ray computed tomography throughout **Chapters 3** and **4**, different machinery using the same technique also provides differences in imaging quality.

Consideration	Conditions	Results	Recommended
Bead drying	Environmental	Poor quality imaging	No
	Air	Salt layers	No
	Critical point	*Clean and dry material*	*Yes*
Ethanol preparation	*None*	*No change*	*Yes*
	100%	Surface changes to polymers	No
	20%	No changes	No
Gold coating	*Yes*	*Stable imaging and EDS*	*Yes*
	No	Electrostatic build up	No

Table 3: Investigated and selected conditions for chromatography bead preparation. Recommended conditions to be used for the remainder of the project for bead preparation are indicated in *italics*, applicable to all materials investigated. Suggestions here are subjectively based on micrograph and EDS results and are not quantitatively evaluable.

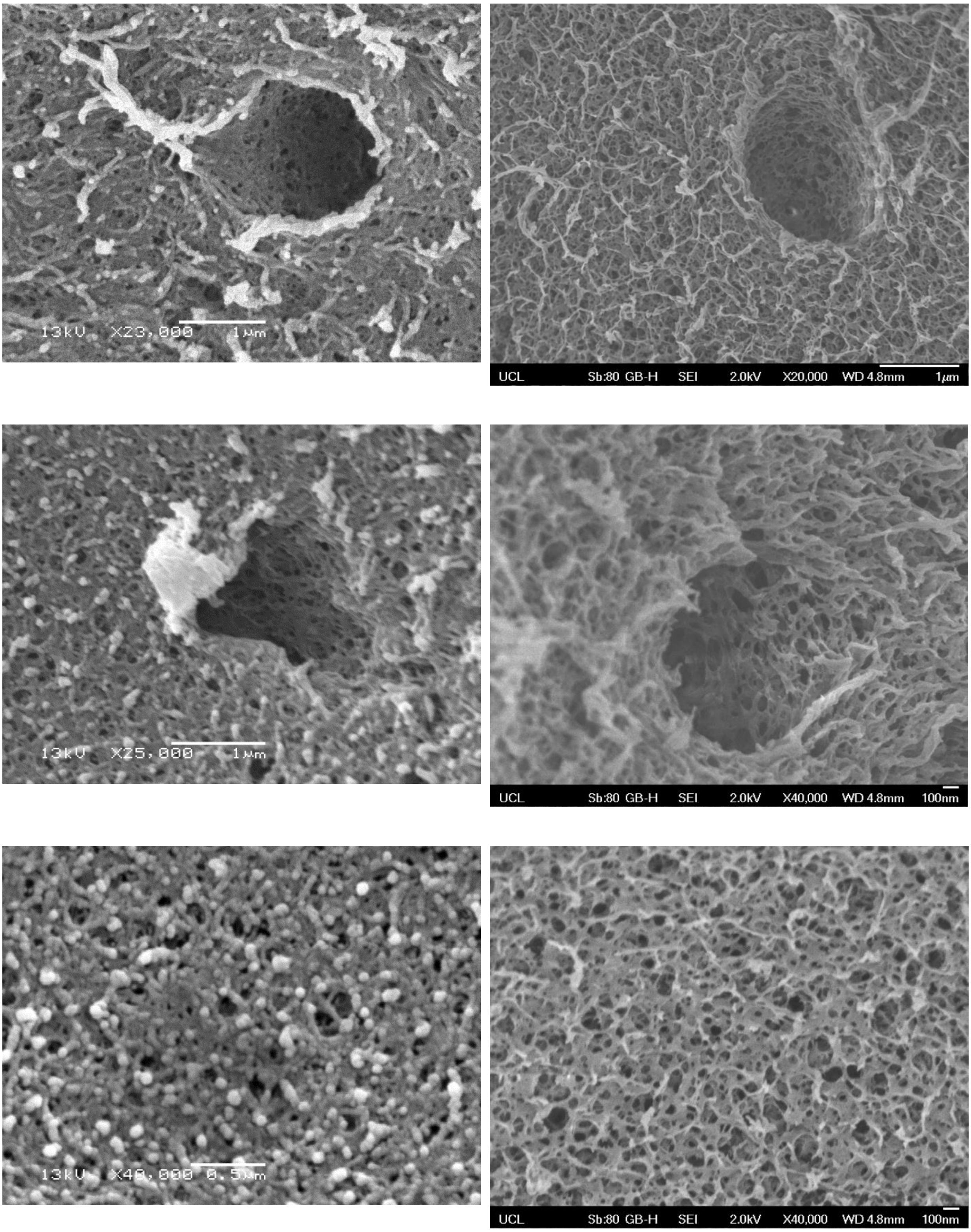

Figure 31: Comparison of thermal SEM to field emission SEM using cellulose beads.

Left: Unaltered, critical point dried, gold coated beads imaged using *thermal* SEM.

Right: Unaltered, critical point dried, gold coated beads imaged using *field emission* SEM.

Note that the same bead was not imaged in each case but similar structures were found.

Further SEM images have been made available in the **Appendix**.

For **Figures 28** to **30** a tungsten thermionic emission SEM system was used, which is considered to be inferior in terms of image quality to lanthanum hexaboride or field emission systems [85]; although the JEOL JSM 6480LV used for the bead preparations study did have energy dispersive X-ray spectroscopy analysis capability. Therefore, a field emission scanning electron microscope was used to examine the critical point dried and gold coated samples in order to compare the image quality compared to the thermionic system. **Figure 31** displays side-by-side comparisons of similar structures found on chromatography beads between thermionic and field emission SEM systems, with other examples in the **Appendix**.

It can be observed from **Figure 31** that the field emission images are of higher quality compared to thermionic counterparts. The detailed structure is clearer with improved definition between the cellulose and pore phases, with electrostatic discharge also being less of a notable issue at higher magnifications for field emission imaging. Therefore in order to produce accurate measurements of bead surface pore sizes, high quality imaging using a field emission SEM is required, with the focused ion beam system having a field emission SEM. Based upon the images gathered, pore size measurements were made using MATLAB for cellulosic images as the more ‘open‘ porous structures of agarose and ceramic beads were not deemed representative to quantify from 2D images alone, with **Figure 32** displaying the pore diameter distributions obtained.

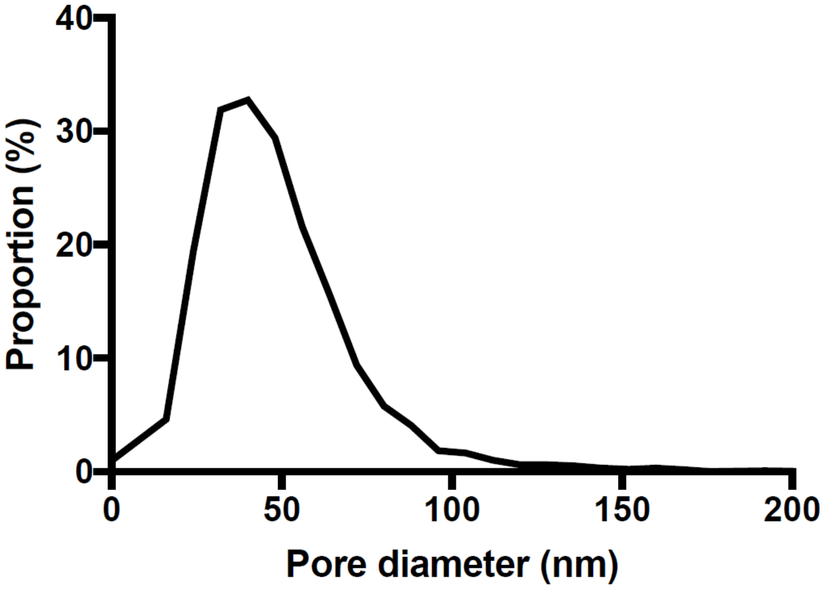

Figure 32: Pore size distribution profile of beads from SEM images and MATLAB processing. 5,297 pores were identified and measured based on MATLAB analysis of 18 scanning electron micrographs. Average pore size and *standard deviation*: 36nm, *19nm.*

The results from **Figure 32** display pore sizes ranging from sub-10nm to over 100nm, demonstrating the vast range and heterogeneity of the detailed porous surface structure. Angelo *et al*. [24] and Tatárová *et al.* [23] state the mean pore radius for cellulose beads to be 8.8nm and 23.7nm respectively using ISEC measurements, with DePhillips *et al*. [25] suggesting mean diameters between 10-100nm for typical chromatography beads.

Angelo *et al*. [24] does state that pore size estimations for electron microscopy measurements were between 10nm – 50nm, and all of the average pore sizes for the MEP HyperCel that Angelo was investigating were found to be within this range. However relying on 2D images of the surface for quantification of structural aspects such as pore diameters does have several limitations to consider before relying on results as an accurate representation of overall bead geometry that can be overcome by using a 3D approach.

One of the main issues is that by using a non-penetrating EM approach constrains the area of interest to only surface pores as opposed to the entire, internal structure which limits the relative amount of structure that can be imaged per bead considerably. The 2D surface may not fully represent the overall porous geometry due to the limited visual data obtainable over a single plane, although this may not be as much of an issue for qualitative observations.

This section investigated preparation of agarose, cellulose and ceramic chromatography beads for SEM imaging, with critical point drying and gold coating found to be the most effective techniques for obtaining high quality samples, in agreement with discussion by Angelo *et al*. [24] and Nweke *et al.* [65] on sample preparation. Bead and surface pore size distributions were also produced based upon optical and electron microscopy images. The optimised bead preparation was carried forward into subsequent tomography based investigations including focused ion beam microscopy and X-ray computed tomography.

2.5.2. Focused ion beam microscopy

The inability of conventional electron microscopy techniques to penetrate samples thicker than 200nm indicates that bead cutting is required to produce 3D representations. As discussed in **Chapter 1**, the two most suitable techniques are microtomy or focused ion beam. Both methods have relative advantages and disadvantages to consider, with each approach having examples of imaging and analysis of porous materials [89, 99], with discussion concerning the technique elaborated upon by Zankel *et al*. [89] in **Chapter 1**.

However, initial microtomy investigations yielded various problems with little experimental success even before attempting high quality imaging of chromatography beads. The slice production process could only achieve thicknesses of 10µm, as anything thinner would disintegrate. Ideal slices would be of the order of tens of nanometres, so several orders of magnitude improvement would be required for sufficient tomographic imaging. The softer bead materials were attributed to the lack of useful results in this case, also highlighting the requirement to perform optimal sample preparation throughout the entire procedure.

Whilst microtomy was not pursued for further investigations and improvements, two major advanced techniques that would be of interest for future investigations include cryostat-microtomy and [94] and Serial Block Face Scanning Electron Microscopy (SBFSEM) [98]. Using a cryo-microtome or EM system provides stability benefits when imaging soft materials such as agarose and cellulose, but may compromise on overall resolution. Major advantages of SBFSEM include imaging of the block face so thin, disintegrated slices would not be as problematic resulting in smaller increments being cut that increase the amount of depth information. However, overall microtomy was not investigated further due to the lack of chromatography bead success and the availability of an alternative EM based technique.

Therefore, focused ion beam was used as the primary tomographic imaging method using electron microscopy, where heavy-metal gallium ions are used to bombard a sample surface in order to remove material, as discussed in **Chapter 1**. As with microtomy, chromatography beads were required to be embedded in epoxy under vacuum in order to provide a continuous, solid phase. The chemical fixation steps performed enabled differentiation between chromatography bead and epoxy material by enhancing relative phase contrast, which was also used by Angelo *et al*. [24] and is commonly used for EM sample preparation.

Hundreds of chromatography beads were embedded in each sample in order to maximise the chance of finding a bead suitable for focused ion beam after polishing, where an ideal chromatography bead would have been polished so that some of the upper material has been removed. Selection of viable candidate beads relied upon diameter and EDS verification, with a sufficient cross sectional area required for further preparative stages.

Figure 33 displays a typical sample for focused ion beam, with two different materials produced on one stub as the same processing stages were used for all materials, in addition to an SEM image within the focused ion beam system where the insides of the clip can be seen that separated the cellulose from ceramic beads. Searching the contained regions for the most suitable samples for tomographic imaging also required the smoothest regions of the epoxy puck, where some undesirable scarring can be observed on the EM surface.

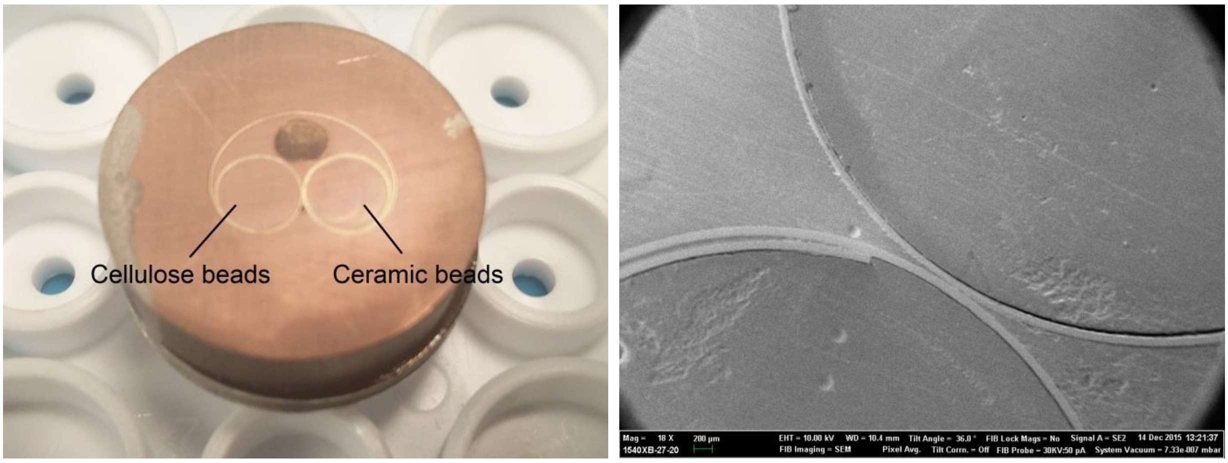

Figure 33: Preparation of samples for focused ion beam tomographic imaging of beads.
Left: Epoxy embedded, polished sample containing beads. From Johnson *et al*. [160].
Right: Scanning electron micrograph of the sample within the focused ion beam system.

The epoxy puck in **Figure 33** had been finely polished with silicon carbide and diamond paste, with a flat surface ideal for EM imaging in order to dissipate electrostatic charging effects, where gold sputtering was also applied and a conductive silver bridge observable on the very left between the puck and stub in order to further reduce charging artefacts during imaging. Air pockets or bubbles outside of the sample clips, for example seen above both clips are not detrimental to imaging; however epoxy impregnation would have to be repeated on a new sample if significant air bubbles were found to interact with the beads.

After FIB and EM beam alignment, bead identification was required on the polished surface, with excessive amounts of beads used in preparation to increase the likelihood of finding suitable samples for investigation. After identifying suitable bead candidates and focused ion beam system alignment, a preparatory trench was milled on each sample. This was performed in order to produce a protrusion encompassing the bead volume, where the block face could be accessed on one end for subsequent slice and view image acquisition.

Therefore material surrounding the central bead volume was removed by gallium ion milling, with **Figure 34** displaying both the overhead 'U' shape trench milled using the focused ion beam as well as the view from the imaging angle on the right captured using SEM of a cellulose block face before platinum deposition. This is typically performed before trench formation so that preparative cutting is accurate and block face preparatory polishing before imaging does not cause any damage. Deposition after isolating the protrusion of interest could also cover the block face with material, thus requiring milling to expose a clean face.

The trenches displayed in **Figure 34** did not have platinum deposition performed in order to demonstrate the difference in surface smoothness to the final images during slice and view in **Figure 35**. Platinum deposition was a long process to perform and so was only used in final optimisation and imaging, where initial investigations were instead used to refine the approach used and determine the sample preparation quality. This was particularly useful for examining the degree of epoxy impregnation into the structure and determining the viability of imaging the detailed structure of surrounding beads for each prepared sample.

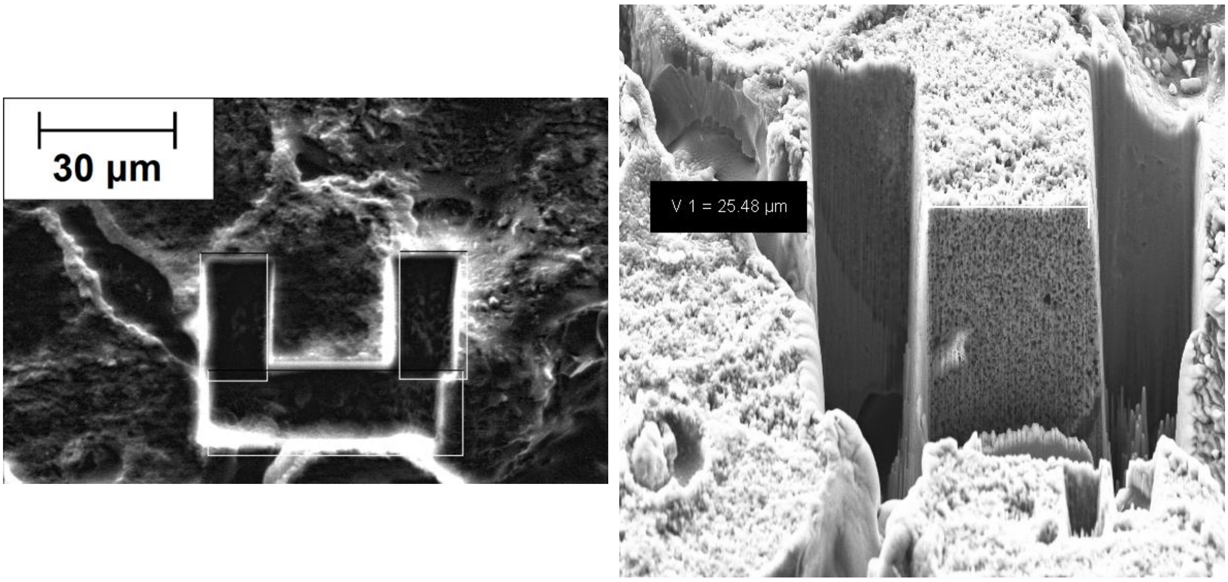

Figure 34: Trench formation around a chromatography bead structure.
Left: Focused ion beam overhead image of the preparatory 'U' shaped trench.
Right: SEM image of a prepared trench for slice and view. From Johnson *et al*. [160].
Note that the examples shown here are not of the dimensions used for final slice and view of chromatography bead materials, and are missing platinum deposition in each case.

When milling using the focused ion beam, there are several considerations to make in order to subsequently produce high quality images. The first is that the sample must be formed under vacuum in order to minimise the amount of trapped air within the chromatography structure, which provided two challenges to resolve. The first issue is that air pockets disrupt the continuous solid phase that detrimentally impacts the ion beam that may result in streaking or other artefacts due to the change from material to void. Secondly, having air reveals material behind the desired area, requiring image processing to correct the changes in distance due to air pockets and the movement of the sample, discussed in **Chapter 4**.

Whilst air bubble entrapment was not entirely avoided, formation under vacuum did minimise this issue. Smaller air pockets were not identifiable from the initial surface views discussed in **Figure 33** and so were only revealed after milling. This highlighted the importance of having many beads available for milling, as only being able to identify poor samples after considerable time using a destructive technique such as FIB microscopy necessitated alternative beads to be viable for investigation and final imaging procedures.

Whilst sample preparation improvements resulted in air pocket reduction, small bubbles were always found between bead structures in the epoxy phase. This informed the selection criteria for slice and view imaging, as samples with poor impregnation would be disregarded and would require searches in other areas, or remaking of the epoxy puck altogether if continued instances and issues were identified throughout a particular sample.

For final slice and view FIB microscopy of the three chromatography bead materials, platinum deposition was required in order to form a smooth surface covering the volume of interest before trench milling was performed. This enabled higher quality slices to be produced at the desired nanometre scale depths, as non-deposited samples would be at an increased risk of milling damage due to relatively rough, uneven surfaces for slice and view that would negatively impact subsequent processing and quantification stages. A non-deposited sample is displayed in **Figure 34** as opposed to in **Figure 35** where all beads have a covered top. This improves conductivity of the sample and so reduces electrostatic charging that would present issues with signal to noise as well as artefacts such as bright streaks across the area of interest that would distort phase boundaries.

Another key consideration to make is that the milling current used impacts the quality of the samples, both from trench preparation to slice and view, with the trade-off between sample damage caused and time required to mill. For initial trench milling, a higher milling current was used as a relatively large amount of material was required to be displaced and the quality of edge cuts was not a priority, as at a lower current it would have taken a long period of time to complete. Alternative equipment such as the Zeiss NanoLab specialise in even finer slicing to produce higher quality imaging, however this was deemed unnecessary for this study as the intended pixel size of 15nm was within the capabilities of the systems used.

After the initial trench was formed, a lower milling current was used to polish the edges of the trench to removed damaged material, with slice and view imaging where sequential removal of material and SEM imaging was performed at a lower current. Agarose, cellulose and ceramic block faces during slice and view are available in **Figure 35**, where again differences in structure can be observed between the materials.

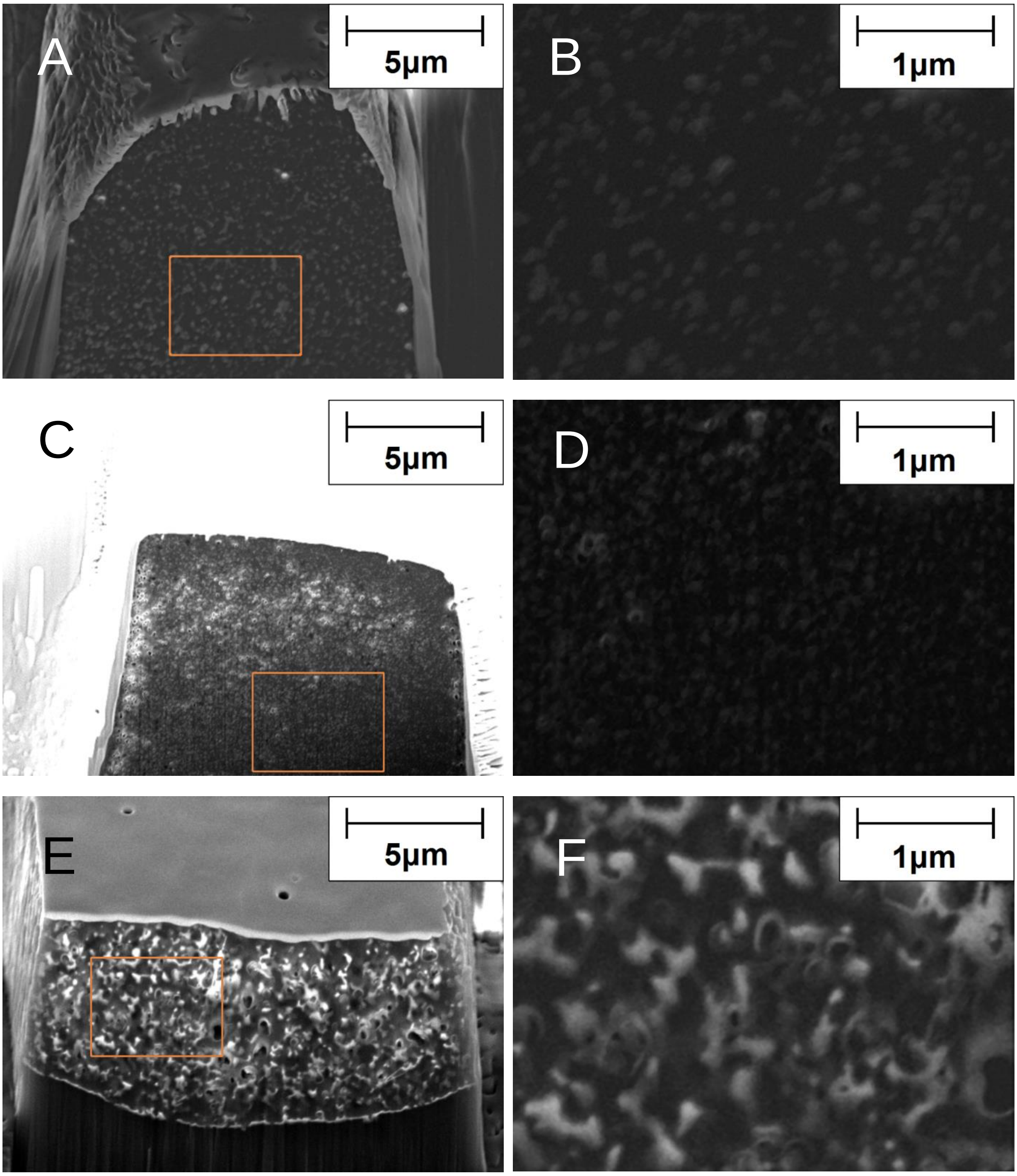

Figure 35: Block face images of beads during FIB. Adapted from Johnson *et al*. [160].

A: Agarose slice and view image 37 of a total 73 of slices acquired for this dataset.

B: Agarose image 37 magnified from **A** and indicated by an orange box.

C: Cellulose slice and view image 60 of a total of 117 slices acquired for this dataset.

D: Cellulose image 60 magnified from **C** and indicated by an orange box.

E: Ceramic slice and view image 167 of a total of 419 slices acquired for this dataset.

F: Cellulose image 167 magnified from **E** and indicated by an orange box.

This demonstrated that the materials have different structural features and characteristics internally as well as on the surface that has been examined in other studies and **Figures 28** to **31**. The high resolution capability of FIB was able to identify these structural differences visually, whether this is indicative of any quantitative differences in terms of key aspects such as tortuosity or 3D pore sizes is investigated in **Chapter 4** between FIB and X-ray CT.

For the ceramic sample, the characteristic shell around the material can be observed; both from **Figure 35E** near the start of slice and view processing as well as **Figure 35F** which was captured near the end of slice and view processing, where the block face had moved further back as the prior material had been removed, requiring adjustment in order to frame slices in the correct manner as discussed in **Chapter 4** and seen in **Figure 51**.

The intended voxel size was 15nm for direct comparison, which was achieved for the ceramic sample, however agarose and cellulose beads required a compromise of 20nm width and height, with a 40nm slice depth. This was due to the softer materials being less stable under slice and view imaging, with the sample itself degrading and the image being greatly distorted at the original resolution until the closest settings could be found. This was undesirable but required for imaging agarose and cellulose for quantification in **Chapter 4**.

2.6. Chapter conclusion

This chapter investigated the preparation required for chromatography bead imaging using EM as the main requirement for successful, high resolution FIB microscopy of three materials. As discussed in the chapter, both the sample and the imaging apparatus used are vital for producing high quality representations of bead structure. This was the main driver behind investigating and optimising both aspects within this chapter as focus on early stage processing would reduce issues encountered downstream, with critical point drying found to be the most suited and in agreement with literature that allows for imaging using FIB microscopy and also for individual bead X-ray computed tomography in **Chapter 3**.

Whilst a small pixel size relatable to the pore sizes determined using conventional SEM, considerations such as the extensive preparation requirements must be taken into account. Another factor was the destructive manner of tomographic imaging using focused ion beam, the sample is not recoverable as the material is displaced, with the beads already embedded in the epoxy; many of these factors will be compared to X-ray CT in **Chapter 3**.

Chapter 3

Individual bead and packed bed imaging using X-ray computed tomography

3.1. Summary

X-ray computed tomography was selected for three dimensional representations of both individual bead and packed bed systems, considering the same agarose, cellulose and ceramic materials as in **Chapter 2**. The ability to image at both scales enabled comparison between approaches taken for individual bead and packed bed tomography, as well as to using focused ion beam based tomography. Optimisation of X-ray conditions was found to be crucial for high quality imaging at both scales, with the non-destructive technique being beneficial for comparing different settings for each sample being advantageous.

At the individual bead scale, samples prepared from the previous chapter were used for imaging optimisation to achieve different goals: pixel size comparable to focused ion beam and sufficient field of view to image a whole bead. At the packed bed scale, imaging was performed on two different X-ray CT systems was undertaken in order to produce accurate representations for all three materials in 1mL commercially available pre-packed columns.

3.2. Introduction

As with the focused ion beam investigations in **Chapter 2**, agarose, cellulose and ceramic beads and packed beds were the materials of interest for this study with 1mL pre-packed columns chosen for packed bed scale imaging and 1mL QFF HiTrap™ for agarose packed beds. These columns are commercially available as opposed to other studies which use microfluidic representations for imaging and subsequent modelling [77], [138] that may not be entirely representative of industrial scale column issues such as wall effects [20], with Gerontas *et al*. [77] suggesting tomography as a credible approach for real column imaging.

Whilst larger size columns were considered for investigation, a key trade-off between field of view and pixel size meant that imaging larger packed beds was expected to detrimentally impact the quality of imaging, which needs to be decided between pixel size achievable and smallest feature size of the sample. This was because, as discussed in **Chapter 1**, the inverse relationship between resolution obtainable relative to the size of the sample.

Therefore a 1mL pre-packed bed size was selected for experiments as this was determined to be sufficiently large enough in to exhibit aspects similar to industrial scale columns unlike microfluidic counterparts, whilst not being bigger than necessary that would compromise overall image quality. Individual bead size selection was not customisable, however the range of bead diameters identified could mean that selection of smaller beads may be necessary for the field of view when using nano scale X-ray CT equipment.

For single bead imaging, the pixel size would ideally be nanometre scale or as close as possible because of the pore sizes suggested in existing literature [24]; however any issues that compromise quality had to be taken into account at the limits of a systems capability as seen with the softer agarose and cellulose when performing FIB slice and view in **Chapter 2**. For 1mL pre-packed beds, other techniques were deemed to be either entirely unfeasible or lacking sufficient resolution capabilities such as NMRI in relation to 50-100µm bead sizes, where X-ray CT was deemed as a suitable imaging candidate, as discussed in **Chapter 1**.

3.3. X-ray computed tomography

As discussed in **Chapter 1**, X-ray computed tomography was selected for investigating chromatography systems in part due to the potential for imaging at both individual bead and packed bed scales. Other important characteristics for X-ray computed tomography included non-destructive and non-invasive imaging, reduced preparation requirements, field of view and pixel size adaptability to required scales as well as existing studies that image and evaluate porous microstructures that are analogous to chromatography bead structure.

One major consideration for using X-ray computed tomography at both scales is that the most suitable conditions are selected in order to produce accurate representations of the three different materials. This is particularly important when considering that subsequent image processing and quantitative analysis relies on producing accurate portrayals of individual beads and packed beds. Therefore optimisation takes great emphasis in this chapter and the approach taken to achieve high quality tomographic imaging.

3.4. Materials and methods

3.4.1. Individual bead scale X-ray computed tomography

Critical point dried beads from **Chapter 2** of agarose, cellulose or ceramic construction were placed onto the top of a sharp, Struers epoxy coated dresser pin under an optical microscope, before storage of samples for at least 24 hours before use, as seen in **Figure 38**. The prepared pin was concentrically held in place before X-ray CT using a Zeiss Xradia 810 Ultra (Pleasanton, USA) [164] - [168], with a schematic displayed in **Figure 36**.

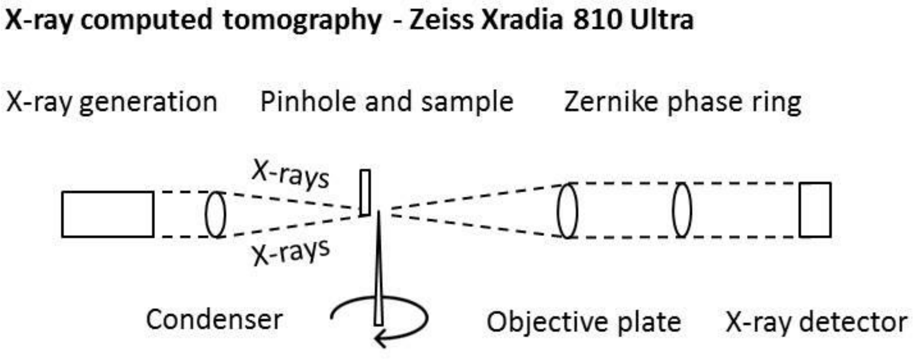

Figure 36: Individual bead scale imaging schematic using X-ray computed tomography. Emitted X-rays from a chromium target are focused onto the individual bead sample on top of a pinhead using lenses and a pinhole. An objective plate is used to direct the X-rays towards the detector, with a Zernike phase ring also available. From Johnson *et al*. [160].

For X-ray generation across all samples, some conditions used were identical in all cases. A primary accelerating voltage of 35KeV was applied using a non-interchangeable chromium target. 40 frames for each of the 1,601 projections over 180º of rotation were collected for each sample regardless of exposure time applied. Standard adsorption, regular phase and advanced Zernike phase contrast modes were selected for separate image acquisitions of each sample. Regular phase contrast data-sets were chosen for final optimised acquisition of all chromatography beads, with advanced Zernike found to be unsuitable for all materials. Standard adsorption mode was produced acceptable results for ceramic bead imaging, however was insufficient for the softer agarose and cellulose beads due to shrinking.

Two different scales were also used: Large field of view (LFOV) and High resolution (HRES) that have respective voxel sizes of 63nm and 16nm and field of view up to 63µm and 16µm at binning 1. It was noted that approximately 10% of the outside frame of view produced poor quality projections, so beads of 50µm diameter or less were selected for final imaging, with the top of each bead used for imaging when using HRES, as can be clearly seen in **Figure 40C**. Due to poor signal to noise ratio in all cases when applying binning 1 on HRES imaging, binning 2 was required to resulted in a final HRES pixel size of 32nm.

For reconstruction of samples after X-ray computed tomography, Zeiss XM Reconstructor software was used to correct for centre of rotation and beam hardening artefacts. TXM files were produced of approximate sizes between 5 and 15GB containing three dimensional representations for both large field of view and high resolution samples of each material.

3.4.2. Packed bed scale X-ray computed tomography

1mL pre-packed chromatography columns in the form of MEP HyperCel and CM Ceramic HyperD F variants were supplied by Pall Biotech, with an example PRC column displayed in **Figure 41A**. Agarose based QFF HiTrap™ 1mL columns were acquired from GE Healthcare, Sweden. Individual columns were mounted in a concentric RS 20.3mm Danaher drill chuck (London, United Kingdom), where the chuck teeth held the lower plastic attachments outside the intended field of view for each column in place during scanning.

Samples were inserted into an X-ray computed tomography system and positioned so that the whole column was concentrically in view, with the axial position set to 5mm from the start or exit from the column as well as the middle to scan 3 different volumes. The position and rotational correctness were confirmed before X-ray computed tomography at each location, with **Figure 37** displaying the overall schematic for the two systems used: a Nikon XT H 225 ST (Tring, United Kingdom) and a Zeiss Xradia Versa 520. The imaging field of view was filled in each case by the internal packed bed chamber for each system to maximise voxel quality, achieving 65x magnification using a Nikon XT H 225 ST system at 3,142 projections.

For optimisation of Nikon XT H 225 ST sample imaging, various parameters were investigated as displayed in **Table 4** in relation to the primary accelerating voltage applied. For each case, the current used was accordingly set to achieve an overall power output of 20W or achieve a maximum grayscale rating of 60,000 without the sample obscuring the field of view, depending upon which was encountered first during scan set-up.

Before use, calibration of the stage and auto-conditioning of the tungsten filament were performed in addition to stigmation correction and alignment using a patterned material to ensure that the system was focused correctly before use. For Zeiss Xradia 520 use, a tungsten metallic source was used in each case with accelerating voltages investigated between 50Kev-150KeV at an exposure of 30s using either a 4X or 0.4X objective lens. Zeiss XM Reconstructor software was used as before to produce 30GB TXM files.

Selection of pixel size for Versa 520 use was based upon producing a representative comparison to Nikon settings whilst meeting operation recommendations set by the manufacturer in terms of image quality, with 1,601 projections captured at 25 frames each.

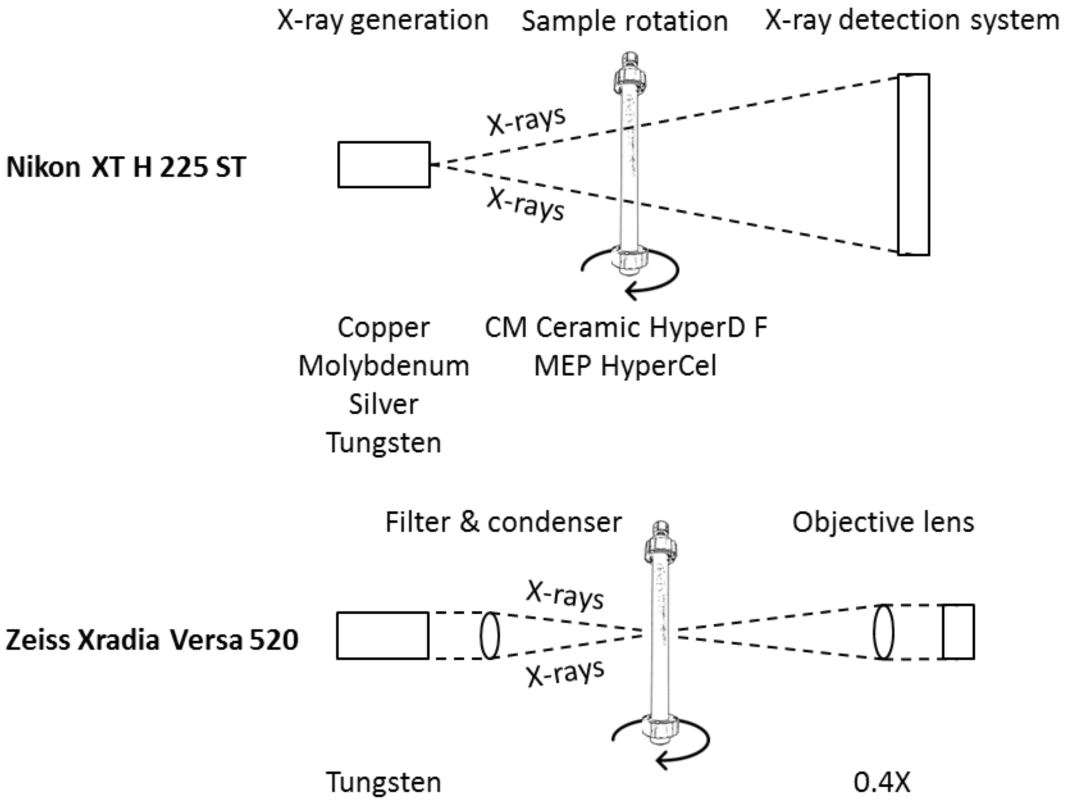

Figure 37: Packed bed scale imaging schematics using X-ray computed tomography. For Nikon XT H 225 ST use, X-rays were generated via electron bombardment onto one of four metallic targets, with an X-ray detection system receiving signal based upon the changes to the X-rays depending upon interactions with the sample. For Zeiss Xradia Versa 520 imaging, the generated X-rays were filtered and then condensed onto the sample using an X-ray lens. An objective lens was then used to focus the X-rays after sample interaction onto an X-ray detector of various selectable magnifications. From Johnson *et al*. [169].

Optimisation and successive selection of credible imaging condition candidates was performed using the overall iterative procedure in **Figure 42**, with Nikon X-Tek software used for correcting the centre of rotation, beam hardening and noise reduction of samples in order to produce packed bed reconstructions at 1mm height by 5mm diameter of the packed bed chamber in the form of VGI and VGL volume files being approximately 30GB in size.

Optimisation aspect	Parameter range
Metallic target	Copper, molybdenum, silver or tungsten
Primary accelerating voltage	80KeV – 225KeV
Digital gain	1X or 2X
Number of frames	1, 2, 4 or 8
Ring artefact removal	Fast acquisition with ring artefacts, or slow without
Number of projections	180 – 4,000

Table 4: Parameters and ranges investigated for Nikon XT H 225 ST imaging.

3.5. Results and discussion

3.5.1. Individual bead scale X-ray computed tomography

In order to perform individual bead scale X-ray computed tomography, suitable preparation was required in order to be able to rotate the bead without any obscuration during imaging, that negatively impact the volume of interest. Critical dried beads of agarose, cellulose and ceramic construction from **Chapter 2** were used for this comparative investigation, although gold coating and ethanol preparation were not performed because those additional steps would add further changes from the native state, as discussed by Angelo *et al*. [24].

Using beads in the unaltered state was also investigated; however the buffer within the bead added another phase to the scanning, detrimentally impacting image quality. In order to have the sample rotating without obscuration, a single bead was placed in the top of a pinhead, as shown in **Figure 38**. One major consideration to make was that the bead had to be positioned perfectly atop the pinhead, as if a bead was slightly displaced to one side, then obscuration of the bead by the metal pin would occur during some frames of rotation.

Ensuring that the bead also stayed in place on top of the pinhead was also crucial, particularly when considering that scan times were up to 24 hours each, requiring the bead to stay in the same position without being obscured by the pinhead for any rotation-projections received. Therefore, different adhesives were investigated: generic superglue, contact adhesive and epoxy. The pinhead was inserted into the adhesive and wiped to minimise the amount of residue on the pinhead so that the bead would adhere but not be embedded by the material, where adhesive can be seen at the base of **Figure 39B**. Epoxy was found to be the most effective and durable in all cases when only using a small amount of residue on the pinhead, although all were credible options for bead adherence to the tip.

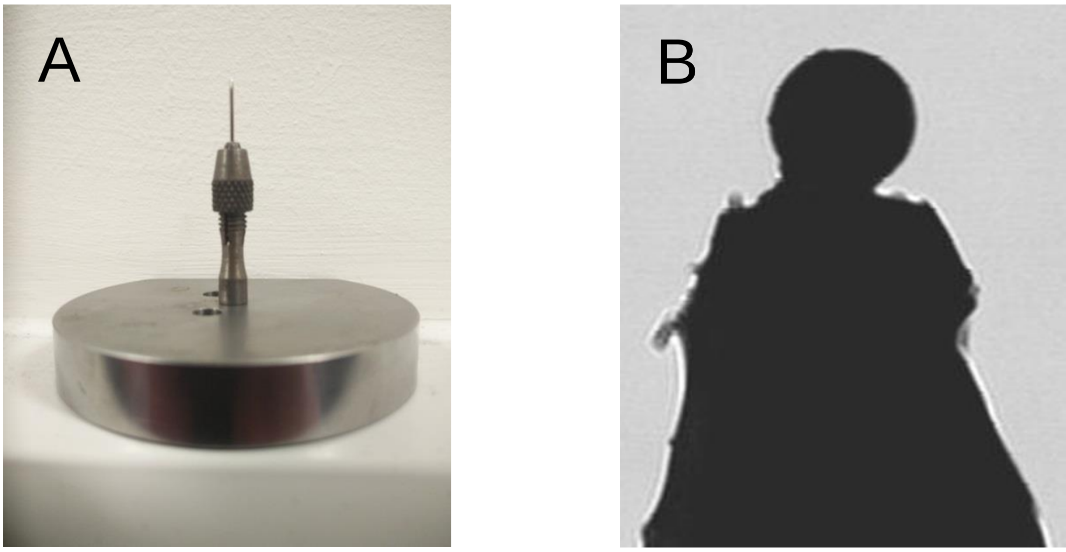

Figure 38: Individual bead scale bead mounted pinhead setup. **A**: Pin clamped to the holding chuck for insertion into the X-ray CT system. **B**: Adhered bead atop the pinhead.

After adhering the beads into place on top of a pinhead, the samples were left for at least 24 hours before scanning, both to enable the epoxy adhesive composite to harden and to ensure that the bead would remain in place over time. The pinhead for scanning was held in place by a rotationally concentric chuck as can be seen in **Figure 38** for insertion into the Zeiss Xradia Ultra 810, with magnets at the bottom of the chuck holding the construct in place on a corresponding rotating stage. For X-ray computed tomography imaging at the bead scale, selection of the optimal imaging parameters was investigated in terms of whether to use absorption or phase imaging based upon the final quality of bead reconstructions for each of the approaches used [170]. **Figure 39** displays X-ray CT slices obtained during imaging using different settings during optimisation processes.

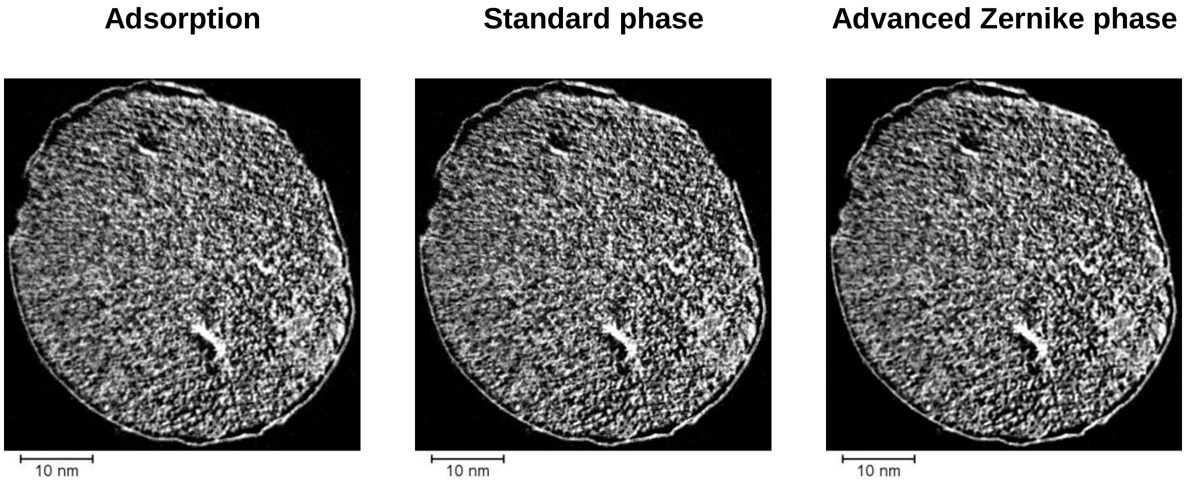

HRES Binning 2 – 32nm voxels **HRES Binning 4 – 64nm voxels**

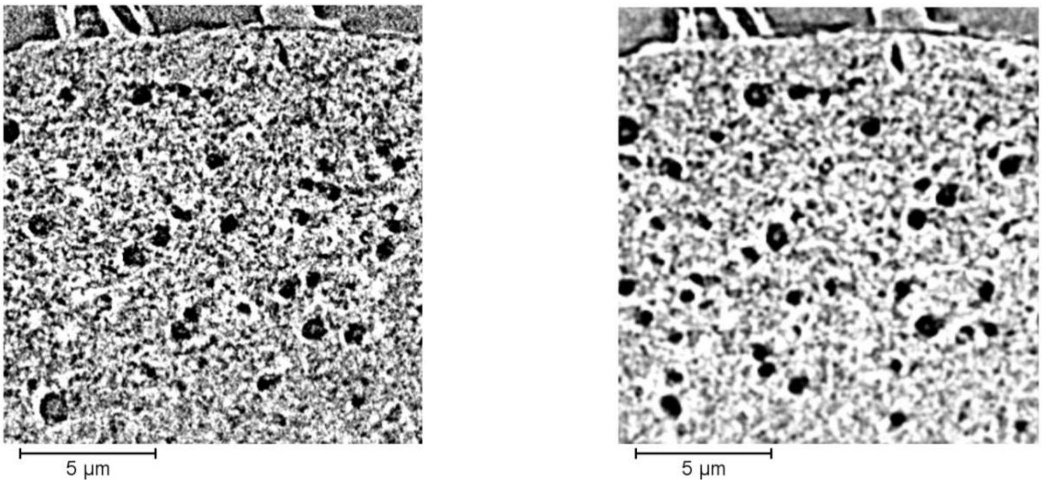

Figure 39: Imaging optimisation of chromatography beads. **Top**: 3 Imaging modes used on ceramic beads, all successful. **Bottom**: Cellulose bead imaging at different binning settings.

The images in **Figure 39** in LFOV mode were taken horizontally sliced through the material and all HRES counterparts were at the top of the bead, away from the impregnated epoxy. For phase imaging a Zernike plate is added in order to measure the changes in phase of the X-rays as they pass through the sample [113], as discussed in **Chapter 1**. It can be observed that at the top of **Figure 39** the ceramic slices look very similar visually as imaging was found to be effective in all modes used, although some distortion effects were noticeable for phase imaging, particularly for Advanced Zernike data-sets where the edge enhancement between material and void phase were excessively pronounced. This was found to be advantageous for regular phase samples, as better defined boundaries where noise was less of an issue aided in accurate reconstruction. For advanced Zernike, further enhancements were found to be detrimental to defining detailed porous features.

However, for agarose and cellulose samples adsorption was not found to be viable for imaging and no successful reconstruction could be performed. This was attributed to poor signal to noise ratios and the reduced density differences to X-rays between the softer materials to the void, preventing boundaries being successfully distinguished. Advanced Zernike was more successful but was found to produce artefacts throughout reconstructed volumes, whilst standard phase contrast produced the most representative results.

Therefore standard phase contrast was applied for all materials for parity purposes, even though adsorption was acceptable when imaging ceramic beads. This decision was also informed by the pixel size achievable in each mode, where lower X-ray counts for adsorption would require a greater degree of pixel mergence, referred to as binning, that would increase pixel size by factors of 2 from the original 16nm relative to the phase modes.

Examples of X-ray CT binning of the same image acquisition are displayed in **Figure 39**, although the overall images similarities there are clear differences regarding the detail displayed. This was typified by the smoother appearance of the binning 4 example at the expense of detail, where the decision for correct binning required acquiring an optimised pixel size without suffering from artefacts and noise so that the finest features could be resolved. The other major issues encountered with agarose and cellulose beads was shrinkage during X-ray exposure, displayed in **Figure 40**.

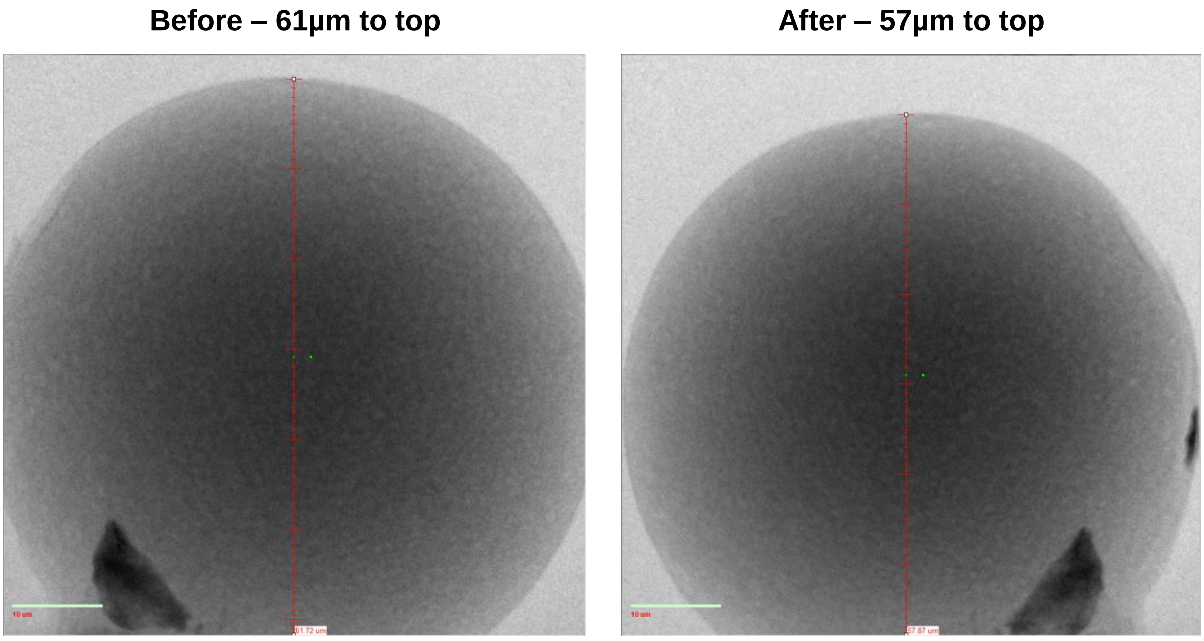
Before – 61µm to top

After – 57µm to top

Figure 40: Cellulose bead shrinkage due to X-ray beam exposure. Measurable levels of agarose and cellulose bead shrinkage for several samples was detected after ~12 hours.

It can be observed in **Figure 40** that after 12 hours of X-ray beam exposure, the sample has shrunk considerably, distorting the softer agarose and cellulose structure throughout a scan and thus was unusable. Control experiments were performed to determine whether other factors were causing shrinkage such as exposing the bead to the air or leaving the sample in the system away from the beam suggesting X-ray beam based degradation.

Samples shrinking are a major issue and detrimentally impact final representations from difficult to remove streaking artefacts to rendering reconstruction of the digital volume impossible. This is because as the sample shrinks, the structure being imaged changes and moves, resulting in rotationally projections being misaligned or having imaged entirely altered features in the wrong field of view, which results in overall poor image quality.

Whilst shrinkage relationships to set-up parameters and time were not thoroughly investigated as beam time was used instead for imaging optimisation, it was found that shrinkage occurred throughout beam exposure and so minimising overall scan time for agarose and cellulose samples was required, mediating the issue from unrepresentative volumes to imaging artefacts requiring removal to produce more representative data-sets.

This limitation required minimisation of exposure time for agarose and cellulose samples to negate degradation effects, which could be achieved at the expense of reduced signal to noise ratio in each case. The three approaches to improve this were to either use a different phase mode that reduced this effect for example Advanced Zernike, increase binning to reduce noise at the expense of pixel size and finally accept greater signal to noise issues that would then be amended during image processing, discussed further in **Chapter 4**.

The trade-off found to be most effective for both samples was to use Standard Zernike at binning 2 with manageable artefacts that were primarily found to occur outside of the internal volume of interest. These issues highlighted that whilst X-ray CT did not require as extensive preparation in relation to FIB microscopy, several considerations were still required in order to produce representative digital volumes of chromatography beads.

After selection of mode, binning and other optimisation factors had been addressed, then final imaging of the three materials was performed. Two different scales were investigated in each case, denoted as large field of view (LFOV) and high resolution (HRES), with respective voxel sizes of 63nm and 32nm. 2D slices of each bead type are displayed for both modes in **Figures 41** and **42** from standard phase imaging, where LFOV was capable of imaging entire beads whilst the HRES counterparts required a field of view compromise for the improved pixel size and so the top of each bead was imaged. Being a non-destructive technique, the same bead could be imaged and compared for both LFOV and HRES.

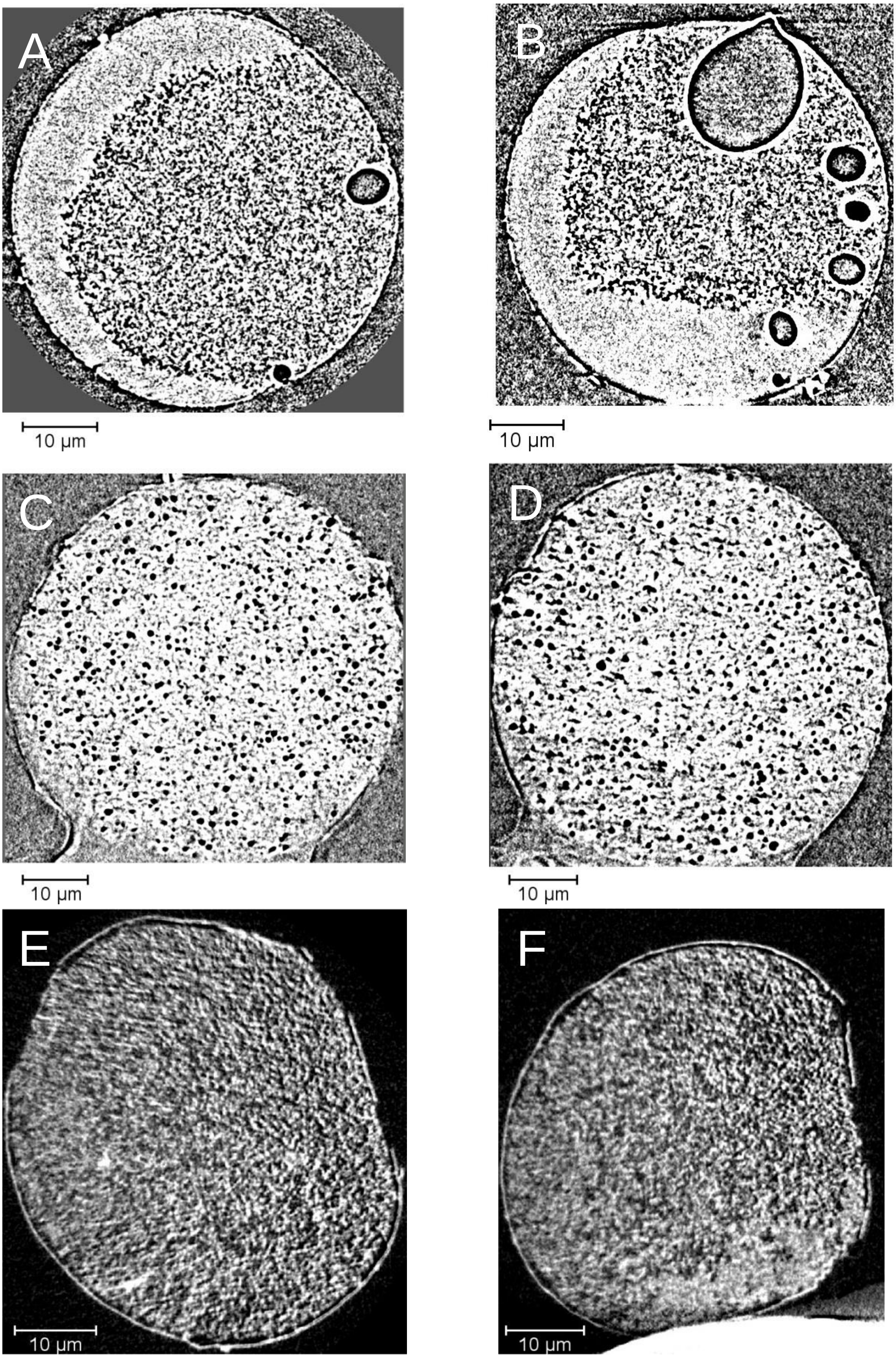

Figure 41: Individual bead imaging using large field of view mode with a 63nm voxel size. **A** and **B**: Agarose. **C** and **D**: Cellulose. **E** and **F**: Ceramic. From Johnson *et al*. [160].

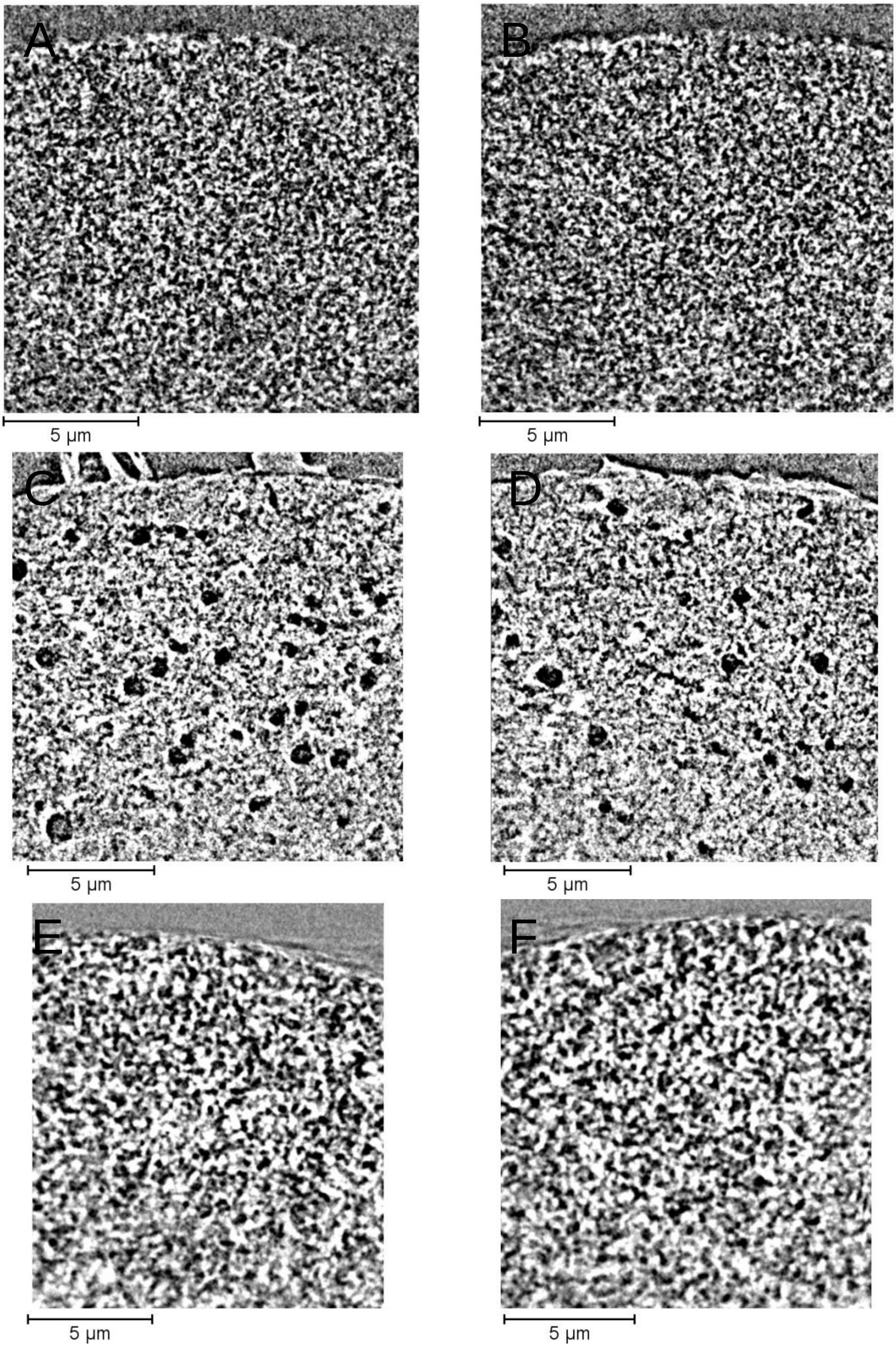

Figure 42: Individual bead imaging using high resolution mode with a 32nm voxel size. **A** and **B**: Agarose. **C** and **D**: Cellulose. **E** and **F**: Ceramic. From Johnson *et al*. [160].

In the large field of view images displayed in **Figure 41**, detailed internal structure can be seen throughout all slices displayed, demonstrating that X-ray CT was capable of imaging the internal bead geometry after optimisation efforts. Approximately 1,000 axial slices for each bead were produced, with the selected images displayed in **Figure 41** being through the centre of each sample to maximise visual data provided.

For the agarose beads in **Figure 41A**, the detailed porous structure can be observed to have very small features that appear to have a high degree of interconnectivity. Considerably large voids were observed throughout the structure up to 10µm in diameter, similar to those seen in Angelo *et al.* [24] who used a microtome. At the bottom of each sample in **Figure 41A**, a loss in contrast was attributed to impregnation of the adhesive into the internal structure. There was still enough unaltered internal volume for extraction to process and analyse the reconstructions in **Chapter 4**, although did highlight the potential for X-ray CT to investigate other materials such as foulants inside of beads, as discussed in **Chapter 5**.

In the case of the cellulose bead, the overall spherical structure can be observed on the right, as well as the attachment to the pinhead at the bottom of the image. Many large, circular pores can be observed in both images throughout the cellulose structure that seem to have a limited degree of interconnectivity to the surrounding smaller features, with dual-peak pore sizes reported using mercury porosimetry [171]. The achieved voxel size of 63nm may not have been capable of resolving the finest features, with Angelo *et al*. [24] suggesting pore diameters smaller than this could be observed with improved pixel sizes.

The ceramic bead displayed the characteristic outer shell surrounding the remainder of the bead, as seen in **Figure 35** of **Chapter 2**. The structure displays a greater degree of porous interconnectivity compared to the cellulose sample, however 2D slices were deemed to not be sufficient to claim this, with further quantitative analysis performed in **Chapter 4** to determine whether visual indications are justified relative to quantification.

HRES counterparts for each bead are displayed in **Figure 42**, where the improved pixel size of 32nm was applied at the expense of overall field of view. The top of each bead from LFOV mode was imaged in order to allow for direct quantitative comparison of geometry to the 63nm counterparts, investigated in **Chapter 4**. The top of each bead rather than the centre was selected in order to minimise the amount of surrounding material that X-rays would need to transmit through to reach the volume of interest, having approximately 16µm dimensions. Whilst there would still be some bead obscuration of the HRES scans, being close to the surface was the least compromised position without physical intervention of samples which was not desirable, considering the advantageous non-destructive approach.

If any surrounding material had been of issue to scan quality, then lift-out preparation [103] using focused ion beam on an epoxy embedded sample, where the pucks produced in **Chapter 2** would be suitable. A 15µm cube would have been cut for each bead type that would not have any surrounding material, however considerations such as excessive processing requirements and epoxy-bead resolution prevented this from being explored.

By achieving an improved voxel size of 32nm in HRES mode compared to the LFOV counterpart, more intricate features and detailed structure can be observed by obtaining eight times as many pixels in the same volume. If no extra binning had been required then this would have improved the pixel size to 16nm, comparable to the FIB results for ceramic beads. However the poor signal to noise ratio and other imaging issues resulted in binning 2 being required, placing HRES between FIB and LFOV in terms of pixel size achieved. The reduced field of view when imaging at an improved pixel size was not ideal but necessary.

For all samples, a further degree of detail can be observed in the internal bead structure, in particular where finer features can be discerned. This was particularly applicable to the cellulose sample, where using LFOV mode the bead exhibited large, circular pores but very few features smaller than that, whereas by improving the pixel size in **Figure 42B** a more intricate structure alongside the main channels could be observed in all slices. Overall, this section investigated the use of X-ray computed tomography at the current cutting edge of technology in order to image chromatography bead internal structure, combining high resolution with a non-destructive approach required in **Chapter 2** for FIB microscopy.

3.5.2. Packed bed scale X-ray computed tomography

X-ray computed tomography was also selected for imaging of packed bed systems, where no other imaging candidates were deemed feasible due to issues including Nuclear Magnetic Resonance Imaging not having the resolution capabilities in order to image particles in the 50 to 100µm range that was quantified during characterisation in **Chapter 2**.

As well as being able to achieve a sufficient pixel size, the main benefit for using X-ray CT for this study was the non-destructive approach meaning that new columns would not have to be altered in order to image the 1mL pre-packed beds. Alterations to a column before scanning could have detrimentally impacted the *inter*-bead geometry which would have resulted in potential misrepresentation. **Figure 43** displays the a PRC column used to house cellulose or ceramic beads in addition to a radiograph taken during X-ray CT acquisition.

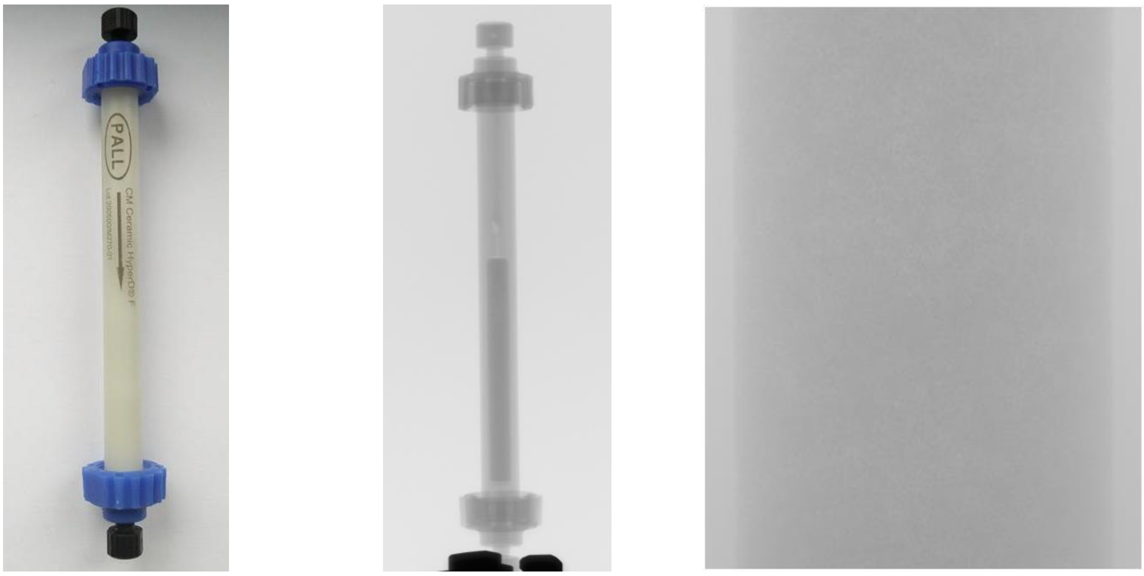

Figure 43: 1mL pre-packed columns used for X-ray computed tomography imaging.
Left: Image of a whole PRC 1mL ceramic column, with an outer column dimension of 8mm.
Centre: Radiograph of a whole PRC 1mL column during X-ray CT imaging.
Right: Radiograph of column chamber 5mm from chamber top, maximising field of view.

The packed bed of interest within the PRC column displayed in **Figure 43** was situated in the lower half of the white polypropylene section below the arrow, as can be seen from the central radiograph by the darker portion. The metallic chuck can be seen at the bottom of the image, where it was important to not obscure the volume of interest.

During imaging of chromatography columns, in order to maximise the detail obtained the column had to be placed as close as possible to the X-ray source so that the packed bed chamber occupies the entire field of view whilst rotating, as can be observed on the right of **Figure 43** where the outline of the chamber can be seen close to the edges of detection. Whilst this provides greater detail through horizontal slices, the axial field of view is reduced to the extent that the column had to be imaged in segments in order to observe the top, middle and bottom of each packed bed for all 3 materials.

In order to produce accurate representations of the packed bed structure for each material, individual imaging optimisation was required that investigated various parameters available in **Table 4**. Selecting the optimal primary accelerating voltage was one of the major requirements for each material, as the X-ray profile emitted is important for producing X-ray contrast between plastic, bead and void phases within the column. The overall optimisation approach used for improving image quality of all three materials is displayed in **Figure 44**.

Stage 1: Imaging of ceramic and cellulose pre-packed columns in 10kV increments from 80kV to 225kV for each relevant target available (copper, molybdenum, silver and tungsten for the Nikon XT H 225 ST). Other settings were adjusted appropriately for each individual acquisition run based upon user manual recommendations.

↓

Stage 2: Selection of best image sets from stage 1 for each target, with 5kV increments either side of each selected data set performed and compared. For example, an image set chosen at 140kV would be imaged at 135kV and 145kV for improved quality settings.

↓

Stage 3: The best data set for each target was selected and compared to other target winners for each packed bed type after re-imaging at higher quality settings. The overall winner for each column on each machine was then selected for subsequent analysis.

Stage 1: Imaging a ceramic column at 100kV using a tungsten target on a Nikon system. → *Stage 3*: Imaging a ceramic column at 140kV using a tungsten target on a Nikon XT H 225 ST system.

Minimised frames and projections, low exposure time, multiple ring artefacts and non-optimised conditions. → Increased frames and projections, greater exposure time, ring artefacts reduced and optimised conditions.

Figure 44: Optimisation process undertaken for packed bed imaging using a Nikon CT. Key parameters investigated are displayed in **Table 4**. From Johnson *et al*. [169].

The optimisation process in **Figure 44** enabled optimum definition for each parameter investigated when considering the three different materials. High primary accelerating voltages of 200KeV and above required a copper filter, but in all cases this was found to produce poor quality data. The primary accelerating voltage was deemed to be important to optimise parameter alongside the metal target used, which impacts the profile and peak emission X-rays produced, with the right combination required to representatively image.

Whilst several setup parameters investigated were found to be a trade-off, increasing the number of frames, projections and reducing ring artefacts by stopping the stage between projections were found to improve imaging, however by doing this each scan was lengthened, so settings where a diminishing return of image quality were to be determined.

This improvement can be observed for a cellulose slice in **Figure 45**, with the lower frame captures having poor signal to noise ratio, making the beads difficult to define. Therefore, whilst final imaging should use a high frame count in order to maximise quality, extending scan times with no real gain was avoided. For optimisation studies, lower frames per projection were used in order to be able to perform many scans using different set-up permutations. For example, **Figure 45B** was imaged 3 times as fast as **45D** but could be used for set-up comparison using the same number of projections.

Once images of sufficient quality had been produced after optimisation of all 3 materials, scan time minimisation efforts were performed in order to determine whether shorter runs could achieve the same results based upon already optimised X-ray conditions. In particular, the relationship between number of frames and projections was investigated as to whether having a greater number of projections with lower frame counts was better than more frames at a reduced number of projections. Whilst reconstructions were found to be of sufficient visual quality at reduced projections under optimised conditions, several issues such as artefacts and relatively poor signal to noise ratio were identified using software. This resulted in standardisation in terms of the number of frames and projections for this study, whereby 4 frames for each 3,142 projections were used regardless of other settings, although further reduction in scan time would be desirable and was a key consideration for further research.

Table 5 displays the metal target used for each system as well as the primary accelerating voltage selected based upon the optimisation approach displayed in **Figure 44**. The current in each case was set in order to maximise the greyscale available from the detector, which was also dependent upon the digital gain and exposure time settings. The current required would slightly change if a part replacement such as a filament was changed due to expiry, however the same approach of maximising greyscale whilst remaining below 20W was used.

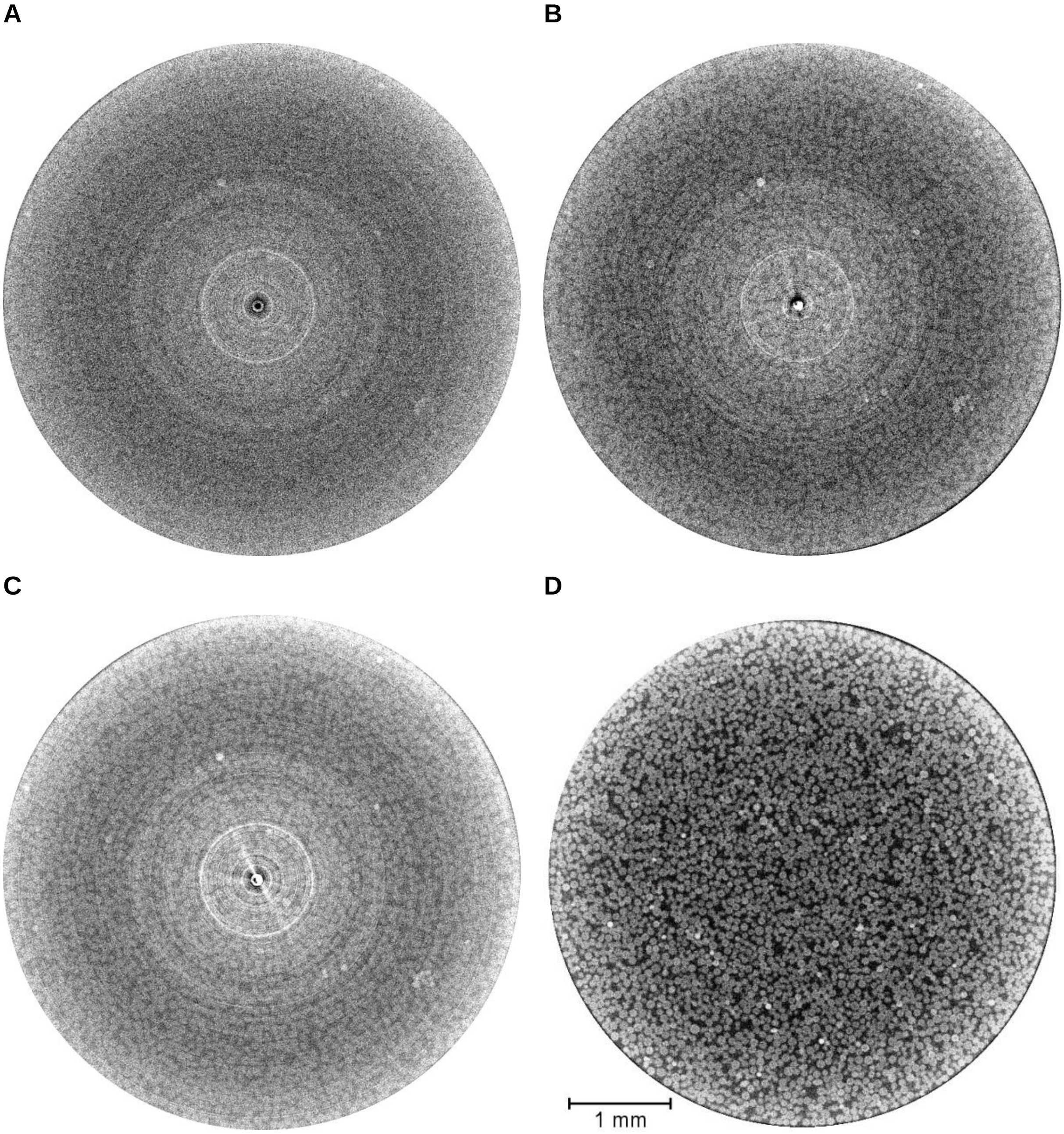

Figure 45: Comparison of frames (F) and Reduced Ring Artefacts (RRA) for cellulose optimisation. Optimised conditions available in **Table 5**. **A**: 1F, **B**: 2F, **C**: 4F, **D**: 4F RRA.

Whilst some considerations during optimisation were a trade-off, other aspects of set-up had more obvious parameters for the highest quality imaging. For example, digital gain was always set to 1X as whilst higher values were beneficial for filament lifetimes, artificial brightening resulted in detrimental contrast loss. Having too many conditions without an obvious optimal setting necessitated an iterative process, as using a design of experiments approach was not feasible for non-quantitative, subjective image quality determination.

Table 5 displays the key optimised characteristics for each material and X-ray CT system used. 3,142 projections at 4 frames each with an exposure time of 1s was used in each case for the Nikon final image acquisition, where increasing the number of projections, frames and exposure time further just produced diminishing returns in terms of overall image quality.

For Zeiss optimisation only one target type was available, with other set-up considerations based upon the primary accelerating voltage and current applied where the count number and transmission are set to recommended levels by adjusting exposure times accordingly.

Equipment	**Sample**	**Target**	**Voltage (KeV)**	**Pixel size (μm)**
Zeiss Xradia Versa 520	Agarose	*Did not image to satisfactory standards*		
	Cellulose	*Did not image to satisfactory standards*		
	Ceramic	Tungsten	60	2.7
Nikon XT H 225 ST	Agarose	Silver	100	4.4
	Cellulose	Silver	100	3.1
	Ceramic	Tungsten	140	3.1

Table 5: Optimised conditions for final packed bed scale imaging using X-ray CT. Optimal imaging conditions were selected based on optimisation. Adapted from Johnson *et al*. [169].

It was found that whilst optimisation was performed individually for each material, the same set-up for the polymer based agarose and cellulose packed beds was found for Nikon XT H 225 ST imaging and a different target and primary accelerating voltage found to be optimum for ceramic column representations, achieving a voxel size of 3.1μm in each case. Given that the spot size for Nikon reflection imaging was 3μm, no further improvement could be obtained without switching to a transmission target with the only target metal available being tungsten. For all agarose and cellulose columns on both systems, no image settings were found that could successfully image the packed beds when using a tungsten target despite further optimisation efforts, preventing Versa 520 from being used in subsequent stages.

Tungsten has a different X-ray profile and a higher energy emission peak compared to the other metals investigated [172]. The relatively lower density of the polymers resulted in poor differentiation between bead and buffer phases so poor definition was achieved when relying on a non-interchangeable tungsten target, however the higher energy resulted in high quality images for the denser ceramic beads, with **Figures 46** displaying 2D Nikon bed slices.

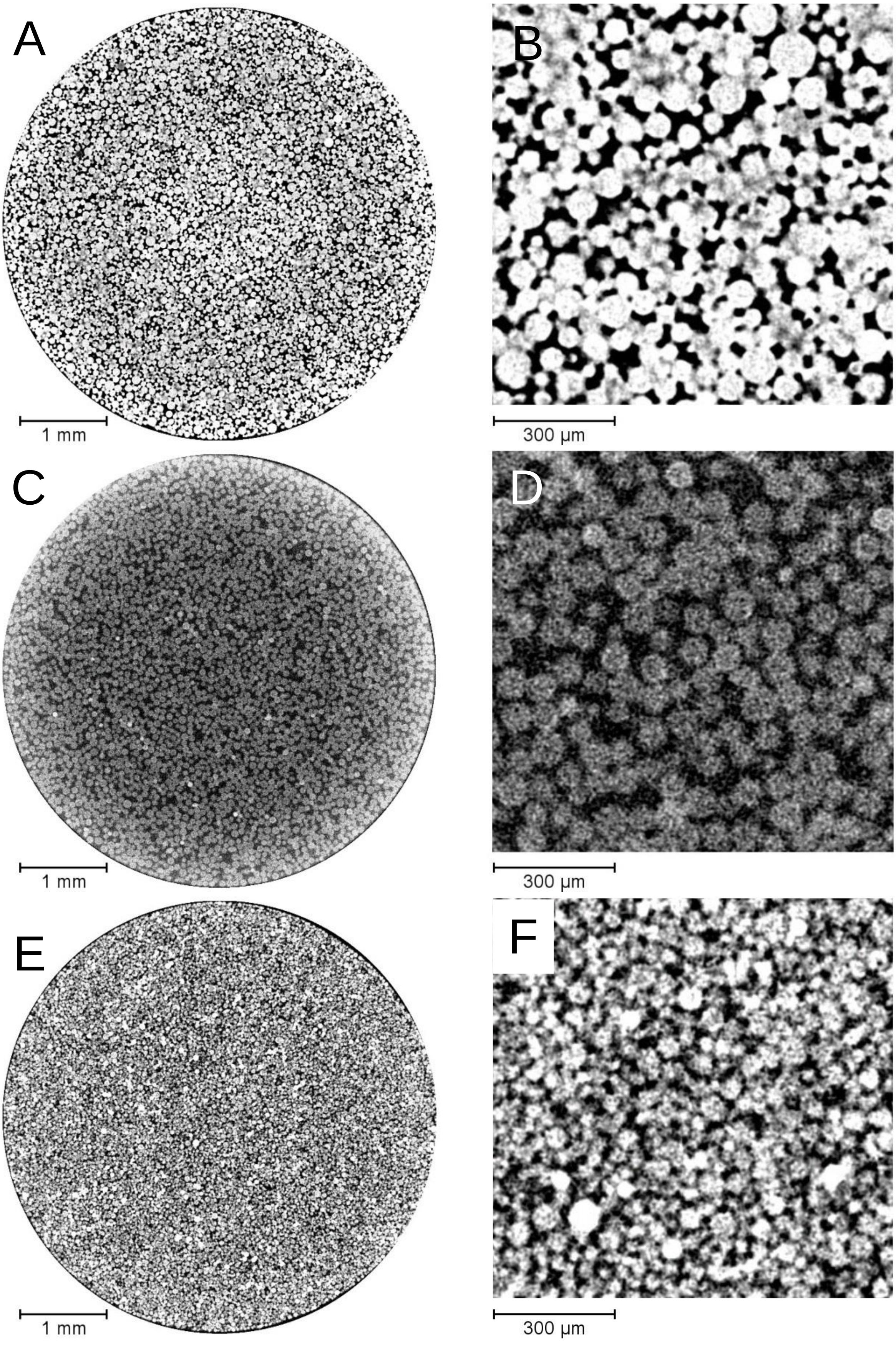

Figure 46: Packed bed imaging using a Nikon XT H 225 ST.
A and **B**: Agarose. **C** and **D**: Cellulose. **E** and **F**: Ceramic. Adapted from Johnson *et al*. [169].

The slices displayed in **Figure 46** demonstrate that X-ray computed tomography is capable of imaging individual beads across the entire packed bed system. The three materials can be observed to be different from each-other, where in particular the reduced sphericity and smaller average diameter for ceramic beads can be seen compared to the agarose and cellulose packed beds, with similar findings also discussed in **Chapter 2**.

The ceramic packed bed as seen in the close up in **Figure 46F** appears to have a closer packing configuration compared to the polymer counterparts, although quantitative analysis concerning packing attributes and relating structure to performance is explored in **Chapter 4**. Agarose imaging required a larger field of view by 2mm and so compromised pixel size.

These two dimensional slices presented in **Figure 46** required reconstruction before they could be obtained, with noise reduction and beam hardening reduction required. An example of beam hardening can be observed in **Figure 46C**, where for the cellulosic packed bed, the outer section is considerably brighter than the centre. This was due to relative attenuation of X-rays as they pass further through a thick sample that result in a lower grayscale value.

Whilst this has been corrected, a bright halo is still visible but is only required to the extent that the bead edges can be clearly defined that would detrimentally impact quantification without processing. One of the main problems encountered even with optimised imaging was that the bead-to-bead boundaries were not always well defined; particularly for agarose and cellulose samples despite being more spherical than the ceramic counterparts, and so clusters appeared conjoined rather than individual entities. This issue is further discussed in **Chapter 4** along with other image processing requirements based upon imaging performed here and in **Chapter 2** that could be resolved using either universal or individual treatment.

Whilst all three materials could be successfully imaged using the Nikon system, the limitation of only having a tungsten target available prevented reconstructions of suitable quality for the softer materials and thus direct comparisons between equipment, with tungsten based efforts on the Nikon also not being successful for agarose and cellulose packed beds.

However, for Zeiss imaging of ceramic samples an improved pixel size of 2.7µm could be achieved whilst imaging the same field of view as the Nikon equivalent. This could have been further optimised to below 1µm if desired by using a higher magnification lens, however was deemed to be unnecessary given that a field of view sacrifice would have been required. Investigating key aspects of bed structure such as packing density differences due to wall effect etc. was one of the main justifications for imaging columns in 3D and so the field of view was favoured over raw pixel size obtained, with slices displayed in **Figure 47**.

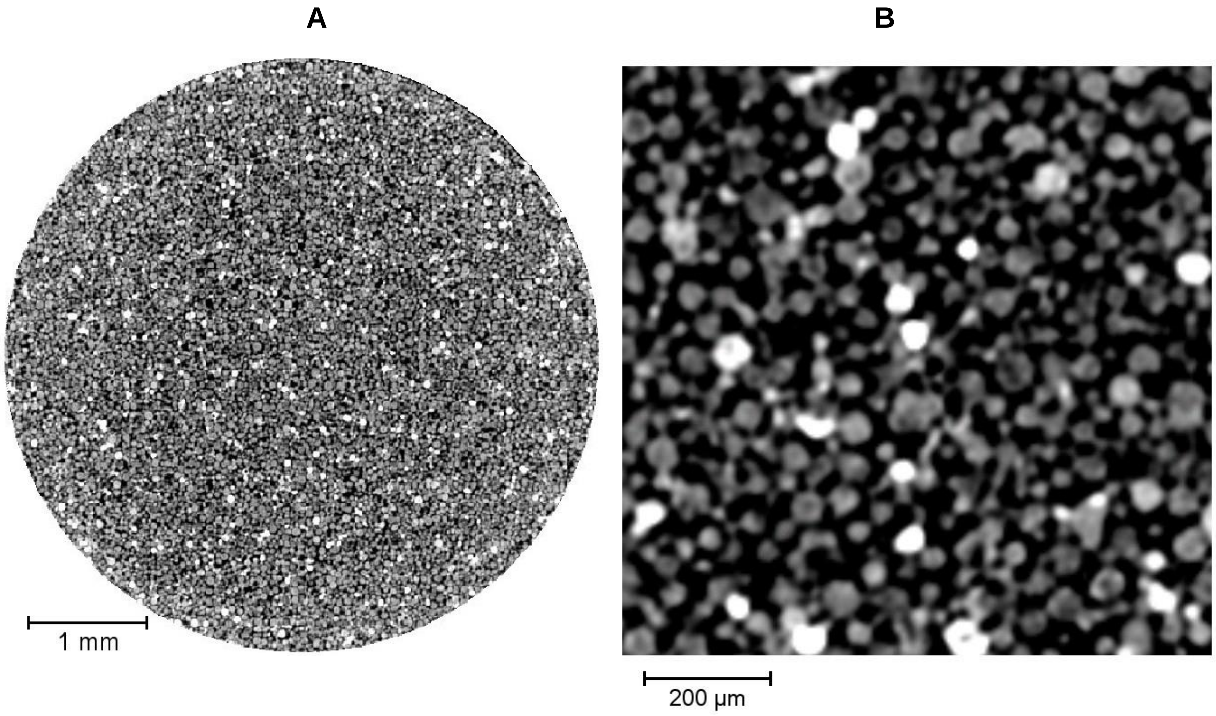

Figure 47: Packed bed imaging of a ceramic packed bed using a Zeiss system.
A: Packed bed slice. **B**: Zoom of a central section of a 2D slice. From Johnson *et al*. [169].

Compared to the Nikon imaging of the same ceramic packed bed, having an improved pixel size was particularly important when considering that ceramic beads were the smallest of the 3 materials used in the study and so would be capable of better defining the finest details and void-bead boundaries. The most drastic advantage observable for the close-up Zeiss compared to the Nikon counterpart was the improved quality within each phase, indicative of a high signal to noise ratio from each reconstructed projection.

This was desirable as having a reduced degree of imaging issues and artefacts would reduce the amount of image processing required in **Chapter 4**, thus presenting a more representative and less altered digital version of the true packed bed structure for quantitative evaluation of aspects such as *inter*-bead porosity and tortuosity.

For each packed bed, the top, middle and bottom were separately imaged; this was due to the aforementioned loss in field of view in order to improve image quality. A 1mm height was achieved with the 5mm diameter to produce a 10GB TXM file of the column volume as axial data near the edges of the field of view was found to be blurred after reconstruction even after optimisation for Nikon scans, attributed to the use of a cone beam scanning method.

For a ceramic column, the entire packed bed was sequentially imaged by moving the sample by 1mm axially after every scan, although this was deemed unfeasible for quantitative analysis both due to the considerably large data-set generated as well as the large quantity of lengthy scans required to complete the imaging process. A spiral scan approach that is becoming commercially available for various X-ray CT systems would be the most suitable method for future research in order to image an entire column axially at high quality. Smaller segments from the top, middle and bottom were selected as the volumes were deemed to be representative of the overall column state and configuration from their position.

This section investigated and discussed the use of X-ray computed tomography for producing tomographic optimisation and representation of chromatography beads as well as packed beds. Comparisons were drawn between X-ray CT and focused ion beam at the bead scale, as well as the trade-off concerning voxel size and field of view achievable. Overall this study investigated the optimisation of X-ray CT high resolution systems for imaging both individual beads and packed beds without the need for physical sectioning.

3.6. Chapter conclusion

X-ray computed tomography has been demonstrated to be an effective technique for imaging chromatographic structures at both the individual bead and packed bed scales for all three materials examined used in academic and industrial bioprocessing. The non-destructive and non-invasive three dimensional imaging enabled structural representations of the samples without the requirements of extensive preparation or interference, required for focused ion beam being the other individual bead tomographic approach in **Chapter 2**.

Successful imaging at two different scales and resolution magnitudes demonstrated the versatility of X-ray CT, albeit with optimisation efforts still requiring final trade-offs. This prevented imaging of the detailed internal structure of chromatography beads at the packed bed scale due to a restricted voxel size being too large to resolve any pore geometries, although this was achieved using the Zeiss Ultra system when imaging a single sphere.

Optimisation of imaging was a particularly important aspect across all tomographic data-sets because the image processes required to produce accurate representations greatly impacts the image processing required as it is desirable to have as little alterations as possible to the original image files. These X-ray CT images therefore comprise the information that eventually is used for characterisation of key structural aspects investigated in **Chapter 4**.

Chapter 4

Physical characterisation of individual bead and packed bed geometry from imaging and digital processing

4.1. Summary

After imaging individual beads and packed beds using focused ion beam and X-ray computed tomography, raw image files were processed using ImageJ and Avizo software to generate representative 3D volumes. Major steps of removing noise, segmenting material from void phase, as well as segmenting conjoined beads at the packed bed scale are discussed and compared between both imaging techniques used as well as the three materials imaged in the previous chapters: agarose, cellulose and ceramic. **Figure 48** displays the overall concept from raw image acquisition to evaluation of structural aspects.

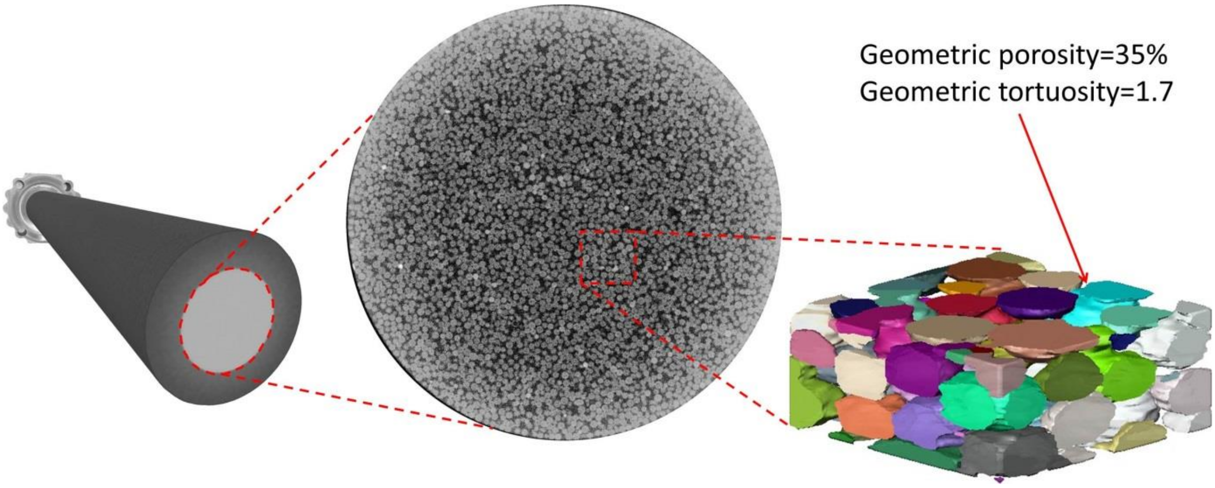

Figure 48: Overall concept for the tomographic image process and analysis.
Scanned chromatography sample (left) was reconstructed into raw image data (centre), where image processing removed artefacts (for example the bright encapsulating halo visible) and segmented material from void phase to produce a representative volume. Sub-volumes from finalised datasets (right) were then evaluated for values such as porosity.

After processing was complete for each volume, analysis was performed in parallel for all samples at both scales, with Avizo and MATLAB used to determine sample porosity, tortuosity, surface area to volume ratio and average pore sizes. This was evaluated in sub-volumes, enabling positional based analysis and comparison of the tomographic structures, with image processing and analysis reviewed near the end of **Chapter 1** for reference.

4.2. Introduction

Based upon the optimised imaging conditions for individual beads and 1mL packed beds as identified in **Chapters 2** and **3**, raw data-sets required image processing in order to perform representative, quantitative analysis of the tomographic structure across scales and between materials. From each imaging technique, there were differences in the file format, the total volume imaged and the cubic voxel size in each case, with **Table 6** displaying the values obtained at each scale. Whilst in most cases the total raw volume was slightly larger whilst imaging, any poor quality or superfluous volume was cropped to reduce the files sizes being processed and remove extraneous, lower quality data which improved processing times.

Technique	**Scale**	**Dimensions**	
		Total volume	*Optimal cubic voxel*
Focused ion beam	Bead	15µm, cubic	15nm (up to 40nm)
X-ray computed tomography	Bead LFOV	40µm, cubic	63nm
	Bead HRES	10µm, cubic	32nm
	Bead Adjusted	10µm, cubic	63nm
	Nikon packed bed	5mm diameter, 1mm height	3.1µm
	Zeiss packed bed		2.7µm

Table 6: Dimensions from tomographic imaging performed in previous chapters.

Whilst each sample had different characteristics as well as issues such as imaging artefacts, an overall process was developed in order to minimise the amount of deviation required when processing all samples, available in **Figure 50**. However, in some cases such as bead mergence, some additional and non-parallel steps were required before analysis.

4.2.1 Image processing

As reviewed in **Chapter 1**, the purpose of image processing in this context was to produce representative tomographic volumes based upon FIB and X-ray CT approaches in **Chapters 2** and **3** respectively. Whilst imaging optimisation was performed in order to produce tomographic volume files that were as accurate as possible, they were all required to be converted into a format that enabled quantitative analysis of key physical characteristics.

Raw 2D or 3D volumes were to be loaded into tomographic software in order to perform image processing stages to clean and identify phases: void to material for individual beads and buffer to bead phases for packed beds. Accurate reconstruction of the material would then enable visualisation of the 2D and 3D chromatographic structure in addition to production of tomographic analytical representations of aspects such as distance maps.

In addition to this, removal and correction of artefacts that were present in the data such as noise was possible by using image processing, where issues caused by any prior steps such as sample preparation or imaging itself could be rectified. However as previously discussed, excessive image processing can also result in changes to the representative structure of the beads and beds and may produce artefacts rather than removing them.

4.2.2 Physical characterisation

After image processing, physical characterisation of the samples via quantitative analysis was required in order to determine the values obtained via tomography for important chromatographic characteristics related to overall performance. Aspects such as porosity and tortuosity compared in **Figure 57** and **59**, surface to volume ratio and average pore sizes were the main attributes for evaluation of the three dimensional structure, with a review of the importance and impact these factors available in **Chapter 1** and visual demonstrations of tortuosity calculations displayed in **Figure 49** between geometric and transfer versions.

Producing sub-volumes within the main sample enables positional based analysis and evaluation; for example the column edge and centre, can be made quantitatively and will be used as a basis of comparison to existing literature values and theories, as well as between the three material types and the impact of imaging technique voxel size on results.

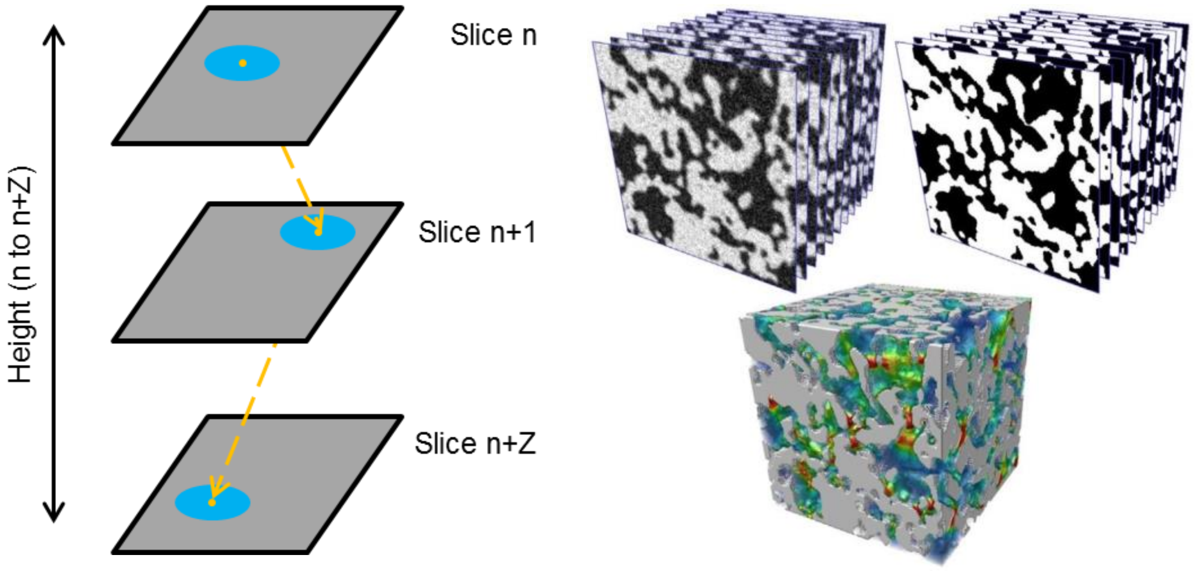

Figure 49: Calculating geometric versus tortuosity factor. **Left**: geometric porosity via centroid path calculations, adapted from Avizo manual [173], **Right**: tortuosity factor using TauFactor from 3D simulation in order to evaluate flux density From Cooper *et al*. [174].

4.3. Materials and methods

Output files from tomographic imaging in **Chapters 2** and **3** were used as the inputs for software based image processing, although the files produced were different in some cases. For all X-ray CT samples, three dimensional volume files were generated in the form of TXM for all bead scale data-sets as well as for the ceramic packed bed samples imaged using a Zeiss Xradia Versa 520; whilst for other packed bed scale data-sets imaged using a Nikon XT H 225 ST VGL, VGI and VOL files were produced. These volume based data-sets were directly loaded into Avizo Fire 9.0 for image processing and subsequent analysis, with steps were performed in parallel for all X-ray computed tomography samples at both scales.

For focused ion beam samples, the data-sets were comprised of a series of two dimensional electron micrograph JPEG slices, with hundreds of images per sample available. Before insertion into Avizo Fire 9.0, processing of slices was required for alignment of each block face before samples could be loaded onto Avizo Fire 9.0. **Figure 49** displays the overall process flow sheet used for producing digital representations and performing subsequent quantitative analysis of tomographic samples. Fully binarised and processed volumes were also added into MATLAB plugin TauFactor [174] for tortuosity factor calculation.

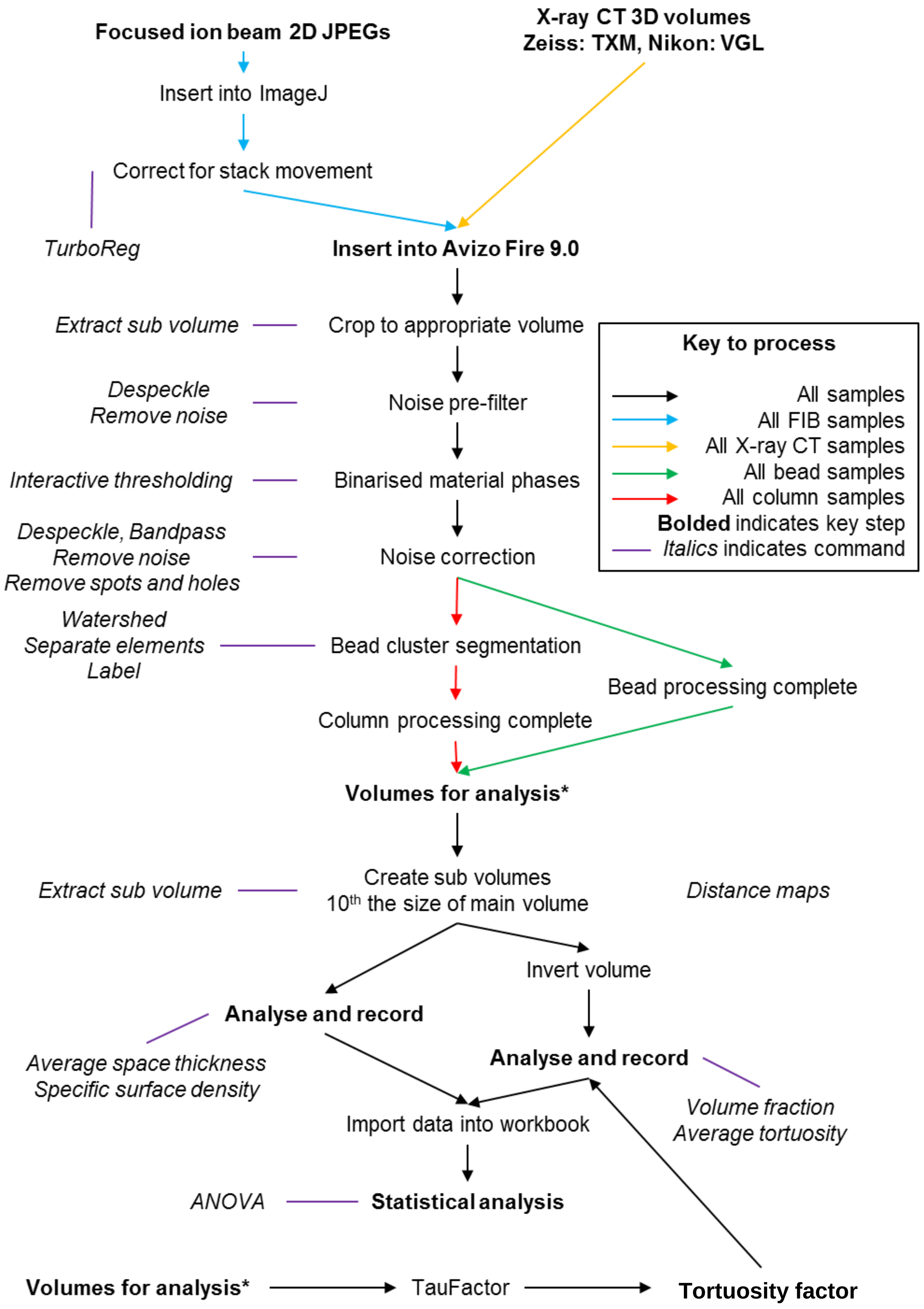

Figure 50: Overall schematic for digital image processing and analysis. *Appears twice. Processing or measurement functions (purple line) can be accessed using ImageJ or Avizo.

4.3.1 Image processing

In order to produce 3D volume files from raw X-ray CT datasets; TXM from TXRM for Zeiss scans and VGI/VGL from XTEK for Nikon equivalents, dedicated reconstruction software was required in each case, being XM Reconstructor and XTEK Reconstructor respectively. Major considerations in all cases was identifying the centre of rotation, the degree of beam hardening and noise levels requiring correcting using manual and automatic approaches.

X-ray CT files could be loaded directly onto Avizo Fire 9.0 in the form of TXM or VGI/VGL 3D datasets, but focused ion beam slices required alignment of the block face due to the removal of material resulting in the block face being successively further away after each slice. The TurboReg plugin for ImageJ was used to align the slices so that the block face appeared in the same position throughout the slice deck rather than shifting throughout.

Figure 51 displays the before and after effect on the same ceramic slices, where an orange box is used as a reference point for where the block face is positioned in the first slice shown in **Figure 51A** and **C**. Before alignment, the block face migrates away in **Figure 51B** from the orange block and so is no longer imaging a cubic volume, however remains in place after TurboReg use in **51D**, although other factors such as block movement from the sensor were accounted for in 3D representations used for visualisation and quantification.

After appropriate alignment and subsequent fine-tuning of the slice positions, the slices from focused ion beam imaging were also loaded into Avizo Fire 9.0. As can be observed in **Figure 51**, all samples were cropped to the appropriate volume as described in **Table 6** before digital processing was commenced using the Avizo graphical user interface, where commands could be selected and placed into a chain, similar to that seen in **Figure 50**. After appropriate volume cropping via the extract sub volume command, noise levels were reduced in the raw samples using despeckle and remove noise commands in order to reduce the variation of pixel intensity within both phases so true boundaries were clearer.

The interactive thresholding command was used to segment the material and void or buffer phases in each case, with the automatic determination used as a guide point and to minimise human bias, but manual adjustments using a slider were performed where deemed necessary when the segmentation was not considered accurate. Subsequent and further noise reduction via despeckle, bandpass, remove noise, spots and holes and filter commands was performed to remove any unrepresentative voxels in either phase that had not been previously identified before binary forms had been obtained to define boundaries.

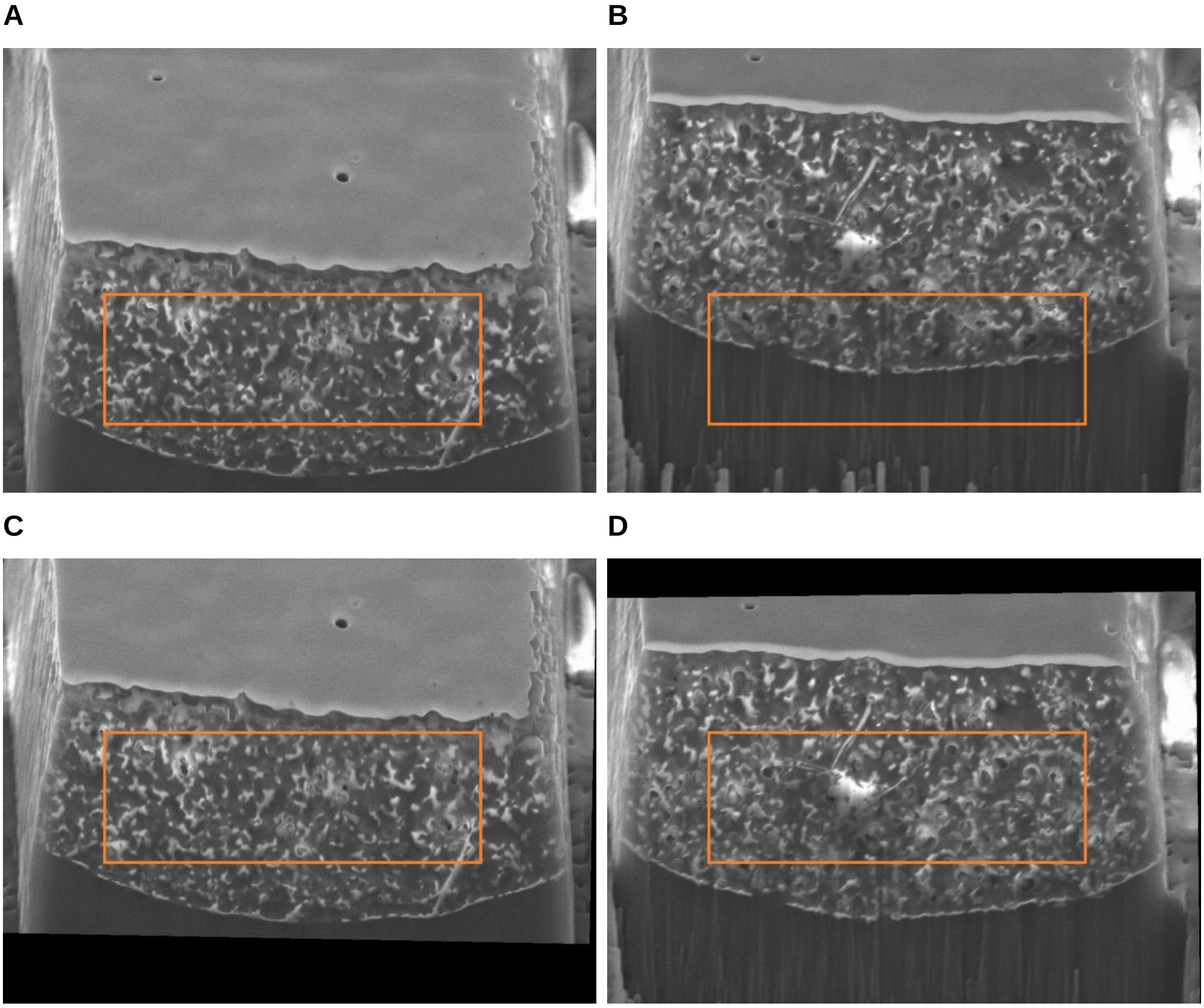

Figure 51: Alignment of the block face from focused ion beam imaging. An orange box has been drawn over the slice to highlight the position of the block face in the ceramic material.
A: Early block face slice with the area of interest near the bottom.
B: Late block face slice with the area of interest near the top of the image.
C: Early block face slice after alignment with the area of interest in the centre.
D: Late block face slice after alignment with the area of interest in the centre.

For individual bead scale samples, the image processing was complete; however in cases within the packed bed samples cases of bead mergence were observed. Therefore bead cluster segmentation via the watershed algorithm, separate commands and final labelling of individual beads within the bed was performed; with the right of **Figure 55** displaying individually labelled beads that are assigned an individual colour for identification. Final inspection and checks for each sample were performed in each case before approval. In some cases, sub-volumes were identified to be of particular poor image quality and so required considerably more image processing, with examples displayed in **Figure 54**.

4.3.2 Physical characterisation and comparison assays

Processed sub-volumes were analysed for porosity, tortuosity, surface area to volume ratio and average pore diameter by using the respective Avizo commands volume fraction, centroid path tortuosity, specific surface density and average space thickness, with results recorded and analysed for statistical significance using an analysis of variance approach (ANOVA, **Appendix**). Samples were extracted as 3D TIFFs and imported in the MATLAB plugin Taufactor, where tortuosity factor values were obtained as well as density flux maps.

At both scales literature based values were extracted based upon relevance in terms of technique used, characteristic being evaluated and material being examined. For packed bed scale studies, a comparative dextran blue assay was performed to determine the *inter*-bead porosity in each case via injection of molecules too large to penetrate the beads.

This was only applicable for ceramic beads because the softer agarose and cellulose samples were found to sustain damage during investigations and so could not be evaluated using this approach. At the packed bed scale, Three 30µL pulses of 3g/L blue dextran (Sigma Aldrich, USA) with a molecular weight of 2,000kDa was inserted into cellulose and ceramic columns using PBS buffer (Sigma Aldrich, USA) at pH 7.4, with binding issues preventing reliable agarose measurements and requiring replacement of MEP HyperCel for S HyperCel, with the difference between the two being chemical rather than structural.

4.4. Results and discussion

4.4.1 Image processing

As previously discussed, the purpose of image processing of the tomographic volumes was to produce accurate digital representations of the chromatography individual beads and packed beds for subsequent quantitative analysis. Once all volumes were loaded into Avizo® for image processing; including ImageJ® JPEG stacks of aligned focused ion beam block faces, cropping was used to remove any excess volume at the edges that often displayed poor quality, defocusing or a high degree of artefacts, see **Figure 54** examples.

However, whilst cropping was desirable before processing, Avizo only considers cubic shaped volumes which means that as well as removing unwanted data, some useful structural volume was also lost, which could have been mitigated if spherical or cylindrical cropping of volumes could be performed to be more relevant to the volume of interest for internal bead, however a sufficient volume for each sample was still extractable.

The use of noise reduction before separation and labelling of the material and void was performed in order to reduce the amount of pixel intensity variation within phases rather than to directly clarify between material and void space. However, this greatly assisted in the software determining an accurate thresholding point; where the intensity cut-off is decided between phases, because there is less local variation and so phase barriers can be identified easier by the program. Whilst minimising human interference and thus potential bias was minimised, in some cases intervention was required in cases of clear errors.

Figure 52 displays a two dimensional slice of each of the three materials at both individual bead and packed bed scales after the phases had been labelled. Overall, the three materials do have individual structural characteristics compared to each other at both scales, with the recognisable shell visible around the ceramic bead for example. Relating the visual characteristics to any differences in quantitative values was a key consideration that is discussed later in the chapter, for example when considering the lesser degree of sphericity of the ceramic beads compared to the agarose and cellulose samples as a whole.

The images in **Figure 52** have also undergone post thresholding noise reduction to remove any individual voxels that have been erroneously categorised in the wrong phase. This stage had to be undertaken carefully and appropriately in order to ensure that errors are corrected without creating new issues within the datasets as a result of overaggressive image processing. These steps were therefore treated with diligence and inspected before and after each stages to ensure that incorrect processing was avoided that would result in unrepresentative visualisation or physical characterisation of samples.

For the individual beads imaged using X-ray computed tomography, both large of field view and high resolution modes were used, with the total volume and voxel dimension available in **Table 6**. Given that the same bead was imaged in both modes but the voxel size is different, a specific large field of view sub volume was extracted in the same position as the high resolution version was imaged, allowing direct comparison between the two differing voxel sizes both in terms of visual appearance as well as quantitative analysis. **Figure 53** displays two dimensional slices at the same position for each material from both high resolution imaging and the specific large field of view volume, referred to onwards as ‘Adjusted’ or ADJ.

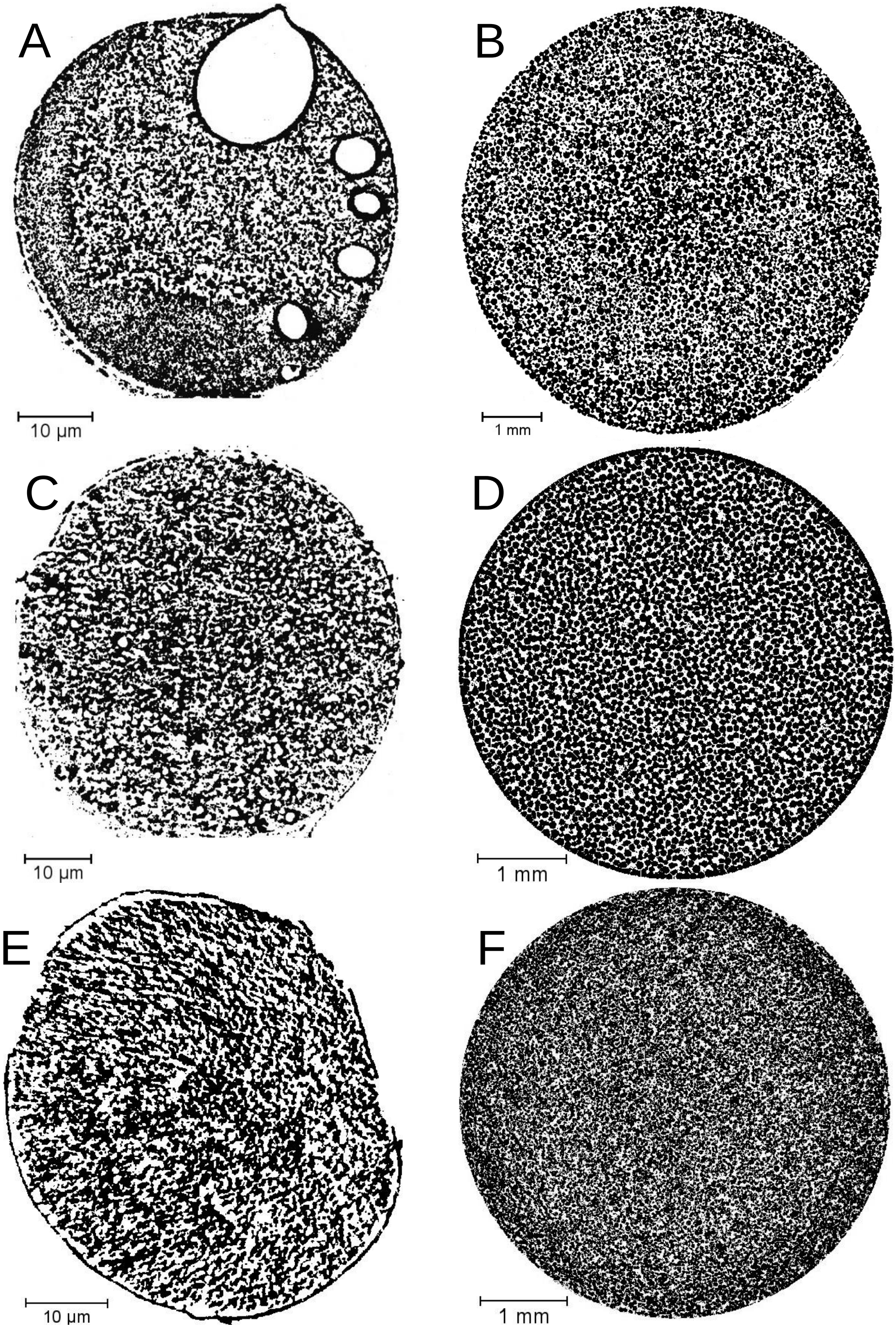

Figure 52: Processed individual bead and packed bed slices. From Johnson *et al*. [169]. **A** and **B**: Agarose. **C** and **D**: Cellulose. **E** and **F**: Ceramic. **Left**: Bead. **Right**: Packed bed.

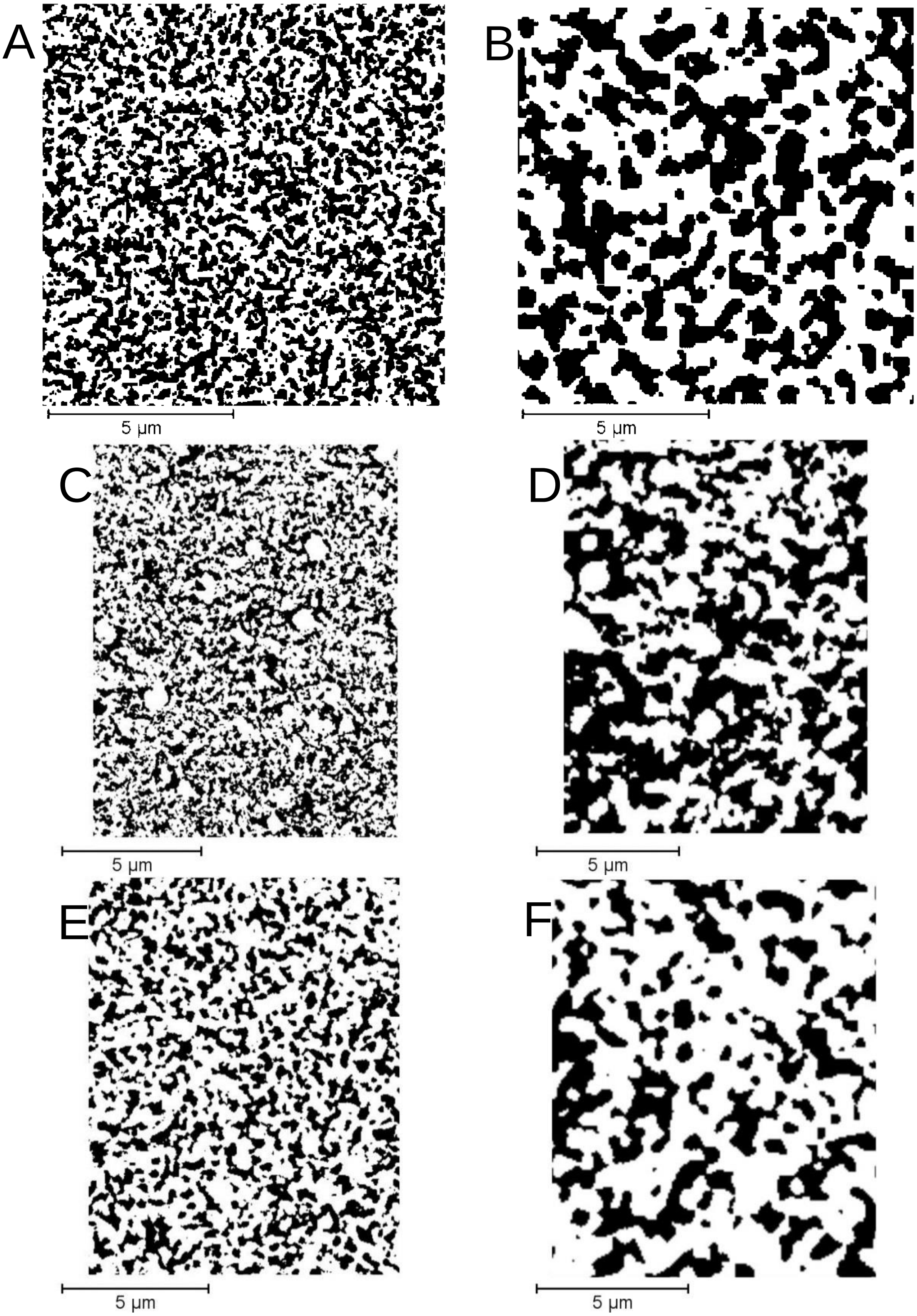

Figure 53: Individual bead high resolution versus adjusted volumes – black material.

A and **B**: Agarose. **C** and **D**: Cellulose. **E** and **F**: Ceramic. **Left**: HRES. **Right**: LFOV/ADJ.

In **Figure 52** it can be observed that the 2D slices for beads and beds corresponding to the agarose, cellulose and ceramic samples were successfully segmented from the void space and background noise. Detailed structural features can be seen in each case throughout the slices, for example the characteristic shell surrounding the ceramic individual bead. The slices also demonstrate that the different materials used for bead construction have distinct geometries, with differences between material properties evaluated later in the chapter. Artefacts were typically observed outside of the volume of interest, often being in place due to shrinkage effects that were mitigated but not eliminated for agarose and cellulose samples, with volumes that had questionable quality omitted from further investigation.

As observed in **Figure 53** where HRES and adjusted slices are compared in a similar position, it is clear in each case that the HRES versions contain far more detailed and smaller features compared to the LFOV/ADJ counterparts when observing a 2D plane slice and thus suggest a considerable difference in the overall material geometry being identified. However, conserved features between LFOV and HRES counterparts were observed, for example the large, circular pores present for cellulose materials in both images presented in **Figure 53**. The cellulosic large pores were also noticed and discussed for **Figures 52** and the raw pre-processing counterparts in **Figure 41** of **Chapter 3**.

Therefore, each material displayed a porous structure throughout the entirety of the internal volume of each individual bead using both X-ray CT LFOV and HRES approaches that visualised clear differences between agarose, cellulose and ceramic samples in terms of geometry. Disparities were also observed between the two voxel sizes used, indicating that resolution limitations could be preventing the smaller features from being discerned despite exhibiting a similar overall structure. Quantification and comparison of these differences between modes as well as to FIB samples is investigated later in the chapter.

For the packed bed slices in **Figure 52**, beads have been identified and segmented for all samples from both Nikon and Zeiss systems from the raw images displayed in **Chapter 3**, with both ceramic data-sets from respective systems appearing very similar in visual appearance due to the same column having been imaged in identical positions. The processing steps used for packed bed volumes were the same at the individual bead scale, albeit using different parameters more suited to the scale differences being processed.

However, whilst individual bead samples could be cropped to remove any artefacts or issues, this was less feasible across a whole packed bed and so further image processing to rectify issues in adversely impacted areas in the volume, which were in the minority. Optimisation efforts displayed in **Chapters 2** and **3** greatly reduced issues encountered.

Figure 54 displays comparisons between 2D slices that were based upon optimised imaging used for subsequent quantitative analysis to volumes reconstructed from compromised and poor quality X-ray CT acquisition for each of the 1mL pre-packed bed materials. For optimised imaging, each sample displays clear definition of bead to material boundaries as indicated by the high degree of sphericity observed for agarose and cellulose samples

For non-optimised equivalent packed bed slices, commonplace issues of poor boundary definition resulted in a reduction of spherical morphology for the beads in close proximity. This was a result of poor signal-to-noise ratios in both the material and void phases and the presence of imaging artefacts that contributed to compromised image processing and segmentation, often requiring excessive stages compared to optimised counterparts. The other major issue discernible between relatively good and poor slices was the degree of separation between clustered beads, where again considerable noise levels resulted in bead mergence leading to *inter*-bead boundary definition and further morphology distortion.

This combination of issues demonstrated that only high-quality, optimised samples at both scales should be used for digital visualisation and quantification of structure because poor morphology definition and artefact presence would result in unrepresentative measurement of key geometrical characteristics. This was found to be of particular importance for the relatively softer agarose and cellulose samples at both scales given the relative difficulties in imaging these materials compared to ceramic counterparts, as detailed in **Chapters 2** and **3**.

When analysing structural aspects of interest including porosity, tortuosity and pore sizes, geometrical distortions would detrimentally impact the reliability of results. In the case of porosity, incorrectly attributed material and voids immediately render results inaccurate, with aforementioned poor boundary definition of compromised samples also contributing to difficulties in representative measurement. For tortuosity and pore size evaluation, the location and size of the pores would not be representative for compromised samples, particularly at the packed bed scale where sphere separation visualised unrealistic gaps between beads, whilst this was more accurately performed for optimised sample counterparts displayed in **Figure 54** that were used for subsequent quantitative analysis.

Figure 55 shows 3D renderings of individual bead and packed bed sub-volumes for each material from HRES X-ray CT and Nikon based X-ray-CT respectively. For individual bead data-sets, tomographic visualisation of structure for all samples displayed continuous porous structure of the internal volume. At the packed bed scale, beads can be observed to have been segmented and colour-labelled so that individual beads can be distinguished from each-other and identified with unique labels that enabled rapid identification of anomalies.

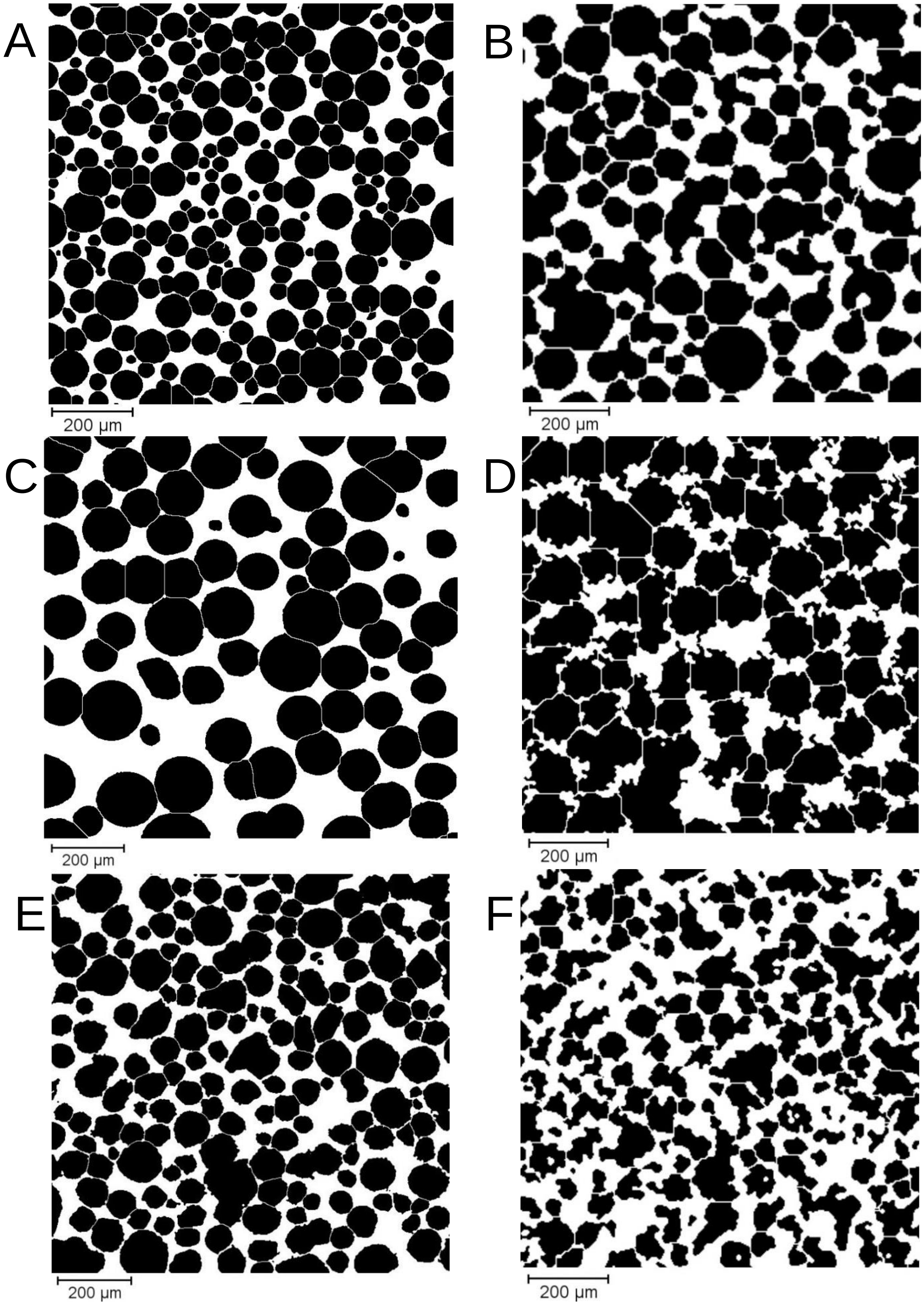

Figure 54: Impact of optimised and compromised image quality after digital processing. **A** and **B**: Agarose. **C** and **D**: Cellulose. **E** and **F**: Ceramic. **Left**: Optimised imaging and diligent processing. **Right**: Compromised imaging and difficulties processing as a result.

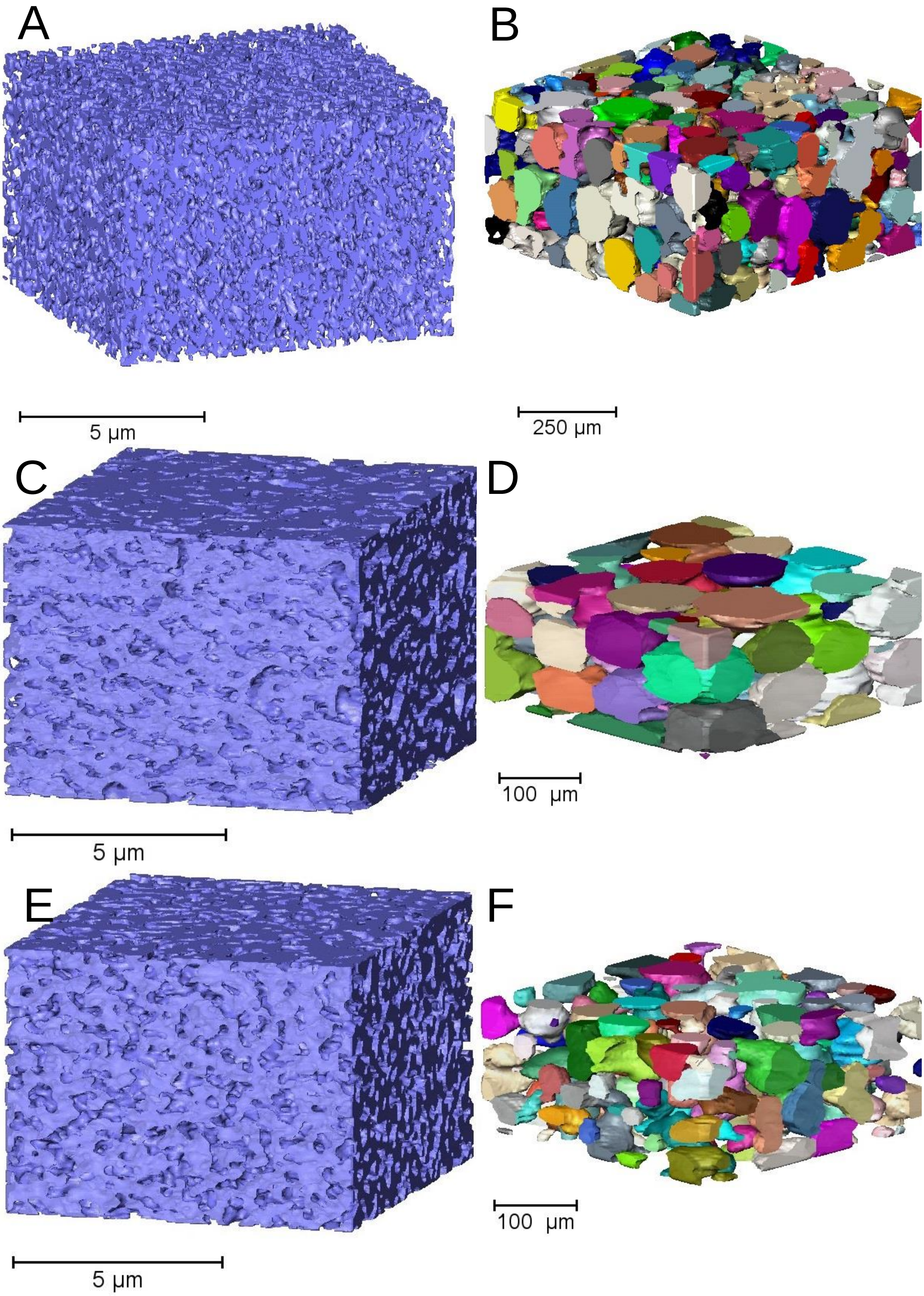

Figure 55: 3D representations of beads and packed beds. From Johnson *et al*. [160], [169]. **A** and **B**: Agarose. **C** and **D**: Cellulose. **E** and **F**: Ceramic. **Left**: HRES Beads. **Right**: Beds.

It was observed that agarose and cellulose samples appeared more spherical than the ceramic counterpart, which was also noted in previous steps at both scales. Issues including non-complete bead separation from clusters was also visible from 3D renders as the same colour would be present for beads in close proximity. However this issue was not further reduced if deemed non-detrimental to subsequent analysis, however was not a common issue that required further consideration beyond the measures already implemented here.

After final processing and visual inspections, volumes were investigated in terms of structural geometry at both scales to identify the presence of large pores or channels that would drastically reduce phase interaction and impact important factors such as tortuosity by providing 3D structures that enable undesirable axial dispersion rather than radial. This was represented by overlaying distance maps onto the volumes, with colour-coding again used to quantify and visualise the distance of a voxel in the void phase from the nearest material.

This enabled comparison between material types as well as location within a volume, for example between the edge and centre of a packed bed. **Figure 56** displays distance maps produced at the packed bed scale with 2D and 3D representations for comparison. In addition to geometry-based distance maps, the TauFactor plugin for MATLAB was used to produce flux maps for each material, with examples at both bead and packed bed scales.

These flux-density maps were generated during tortuosity factor calculations of the respective geometries, and whilst were originally intended for bottleneck identification of diffusion through batteries and fuel cells [174], this approach was analogous for the diffusion driven internal porous structure of the bead and for channel identification in packed beds.

It can be observed from the distance maps in **Figure 56A** of a ceramic packed bed 2D slice that there are no common instances of large pores or channels that would be indicated in yellow. In **Figure 56B** a cellulose bed 3D render is displayed which highlights voids of a greater size than any observed in ceramic volumes, indicated in red throughout the mesh. This was found to be more common closer to the centre of the packed beds compared to the edge which was expected due to packing density differences discussed in **Chapter 1**; however no overall trend could be detected axially beyond natural variation.

By producing accurate representations of chromatography bead and bed structure, the volumes of interest can be used for evaluative purposes beyond those displayed in this chapter; primarily being distance and flux maps with physical characterisation of aspects such as porosity and tortuosity. They provide a platform for computational and modelling efforts to examine real bead and bed geometries rather than those procedurally generated.

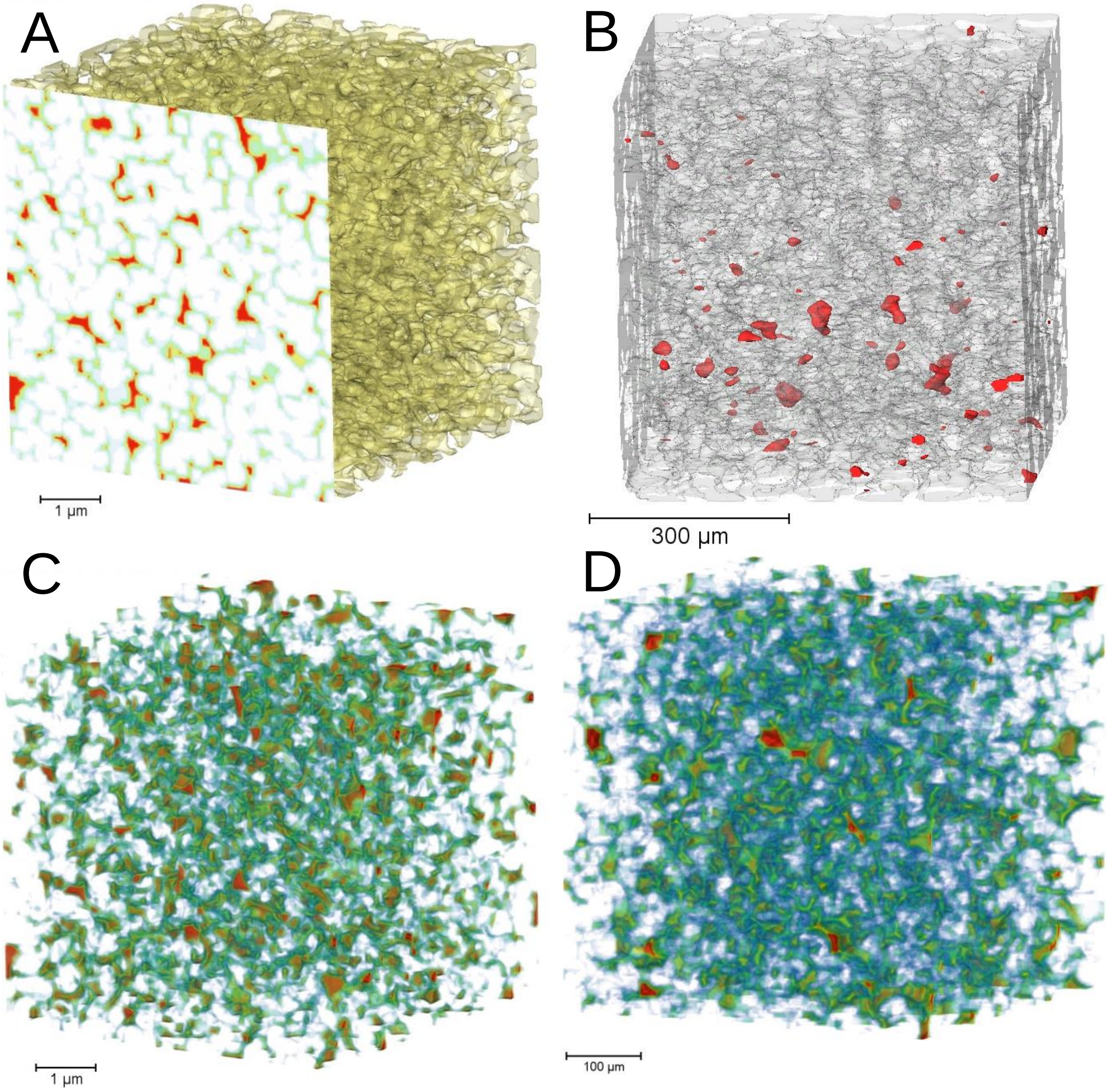

Figure 56: Distance measurement maps at the individual bead and packed bed scales.

A: Distance map of a cellulose individual bead from HRES X-ray CT. White is material, green < 100nm from material, yellow < 200nm, and red > 200nm. Overlaid on a 3D render in yellow of the remainder of the HRES volume. From Johnson *et al*. [160].

B: Three dimensional render of a cellulosic packed bed, with red inserts where voids of at least 9µm radial distance from bead material shown. From Johnson *et al*. [169].

C: Distance map of a cellulose individual bead from HRES X-ray CT. White is material, green < 100nm from material, yellow < 200nm, and red > 200nm. Volume is from the same location as the 2D overlay displayed in the top-left. From Johnson *et al*. [160].

D: Distance map of a ceramic packed bed sub-volume. White (transparent) is material, green < 10µm from material, yellow < 20µm, and red > 20µm.

The distance map visualisation in **Figure 56D** displays the heterogeneity within packed bed systems that do not ideally sit in theoretical plates. However, whilst the geometry is not perfectly ordered, this does not necessarily suggest that the packing within the pre-packed columns is poor, as this lack of homogeneity was expected and realistic packing structures have been quantified for packing quality, typically using surface area to volume ratio which is investigated later in the chapter.

This section considered the image processing requirements for producing accurate digital representations of individual bead and packed bed volumes from FIB microscopy and X-ray computed tomography based imaging, explored in **Chapter 2** and **3**. Raw volumes were imported into Avizo for noise reduction, thresholding of phases and segmentation of bead clusters in order for subsequent quantitative analysis to be performed. Two and three dimensional images were presented throughout in order to illustrate the condition of data at each key process stage, with visual distance maps also displayed in order to demonstrate that the differences in bed and bead structure could be discerned and used as a basis for direct comparison using 3D renders as well as distance and flux-map visualisations.

4.4.2 Physical characterisation

Once digitally processed, three dimensional representations had been produced for all tomographic data-sets, quantitative analysis of key structural and physical parameters of the chromatography systems could be analysed, which was performed in Avizo and MATLAB. Porosity, tortuosity, surface area to volume ratio and average pore sizes were investigated, with tortuosity calculated using two methods: geometrically based and transfer using the approach described by Cooper *et al.* [174] as discussed in **Chapter 1**. This was performed in parallel for all samples and materials based upon the 3D geometry in each case, with the software being material agnostic and not specifically for chromatography structural analysis.

At the individual bead scale, comparisons of values gathered between the LFOV, HRES, Adjusted and focused ion beam samples and to determine whether the difference in total volume and voxel size impacted the overall results obtained. For example, it was expected that the improved voxel size of HRES and focused ion beam volumes could identify smaller pore channels compared to the LFOV counterparts, although the overall impact of the smaller channels of average pore sizes may be negligible due to the calculations being made for the overall volume, with **Figure 57** displaying the average porosity and tortuosity.

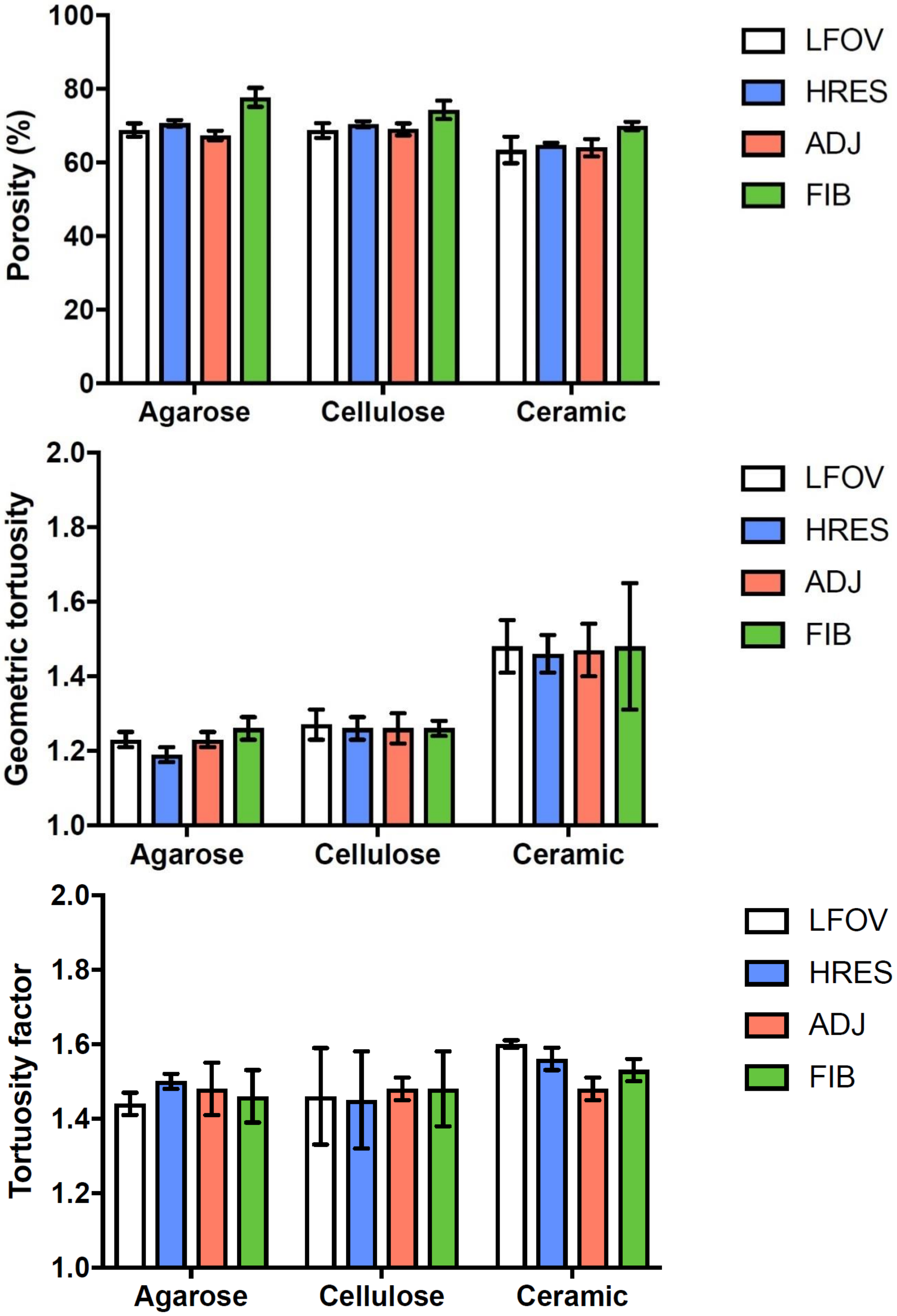

Figure 57: Porosity and tortuosity measurements at the bead scale. See **Table 7** for values.

From Johnson *et al*. [160]. **Top**: Geometric porosity from Avizo measurements. **Middle**: Geometric tortuosity from Avizo. **Bottom**: Tortuosity factor from TauFactor. Evaluation based upon a single bead sample divided into sub-volumes for analysis.

It can be observed that porosity results are similar between X-ray CT readings, verified by ANOVA analysis (**Appendix**). However, FIB values were found to be 10-20% higher in each case; closer to commonplace porosities stated using other evaluation techniques such as ISEC [24] for the agarose and cellulose samples with ceramic being in agreement [175]. This indicated that the better resolution obtained using FIB enabled smaller porous features to be better defined into the correct phase, where misplacing may occur at larger pixel sizes.

However, this was not found between ADJ and HRES X-ray CT counterparts at respective pixel sizes of 63nm and 32nm, suggesting that raw resolution may not be the best indicative measure for the porosity discrepancy and may also be dependent on other factors including the imaging technique used. Another consideration was that X-ray CT imaged the same bead in each case whilst a separate one was used for FIB tomography that also underwent relatively extensive preparation stages, albeit FIB attaining porosities in literature ranges that have been measured using other approaches such as ISEC [23-25] and porosimetry [175].

Geometric tortuosity values were also found to be considerably lower for agarose and cellulose volumes, attributed to the high porosity enabling relatively non-tortuous flow paths through the structure. However for the more advanced tortuosity factor the consideration or overall pore network complexity [174] suggested an average increase of approximately 0.2, where lower porosity ceramic values were found to be similar between tortuosity values. Inconsistencies between Avizo® and TauFactor have been previously documented by Cooper *et al*. [174] when analysing identical volumes. Existing literature values suggest a wide range from near-1 up to 6 depending upon approach taken, examples being gas adsorption and Bruggeman equation derivation [60], [175]. These tomographic readings suggest that the tortuosity values for beads are on the lower end of other literature results.

Overall, **Figure 57** demonstrated that tomographic approaches can be used to evaluate characteristics such as porosity and tortuosity using a methodology not used before. Quantification of tortuosity readings in existing literature has been loosely defined and so by implementing a 3D approach that is becoming more widespread in adoption [121] then a more representative estimation can be presented. However, caution would still be advised for taking results as direct truth both due to variation within readings and inaccuracy when quantifying porosity which has been more reliably characterised using other approaches.

Results for surface area to volume ratio and pore diameter are displayed in **Figure 58**, where unlike porosity and tortuosity, pixel size had a profound influence on values obtained where superior pixel sizes obtained using HRES X-ray CT and FIB displayed higher surface area to volume ratios and smaller pixel sizes relative to the LFOV and ADJ counterparts.

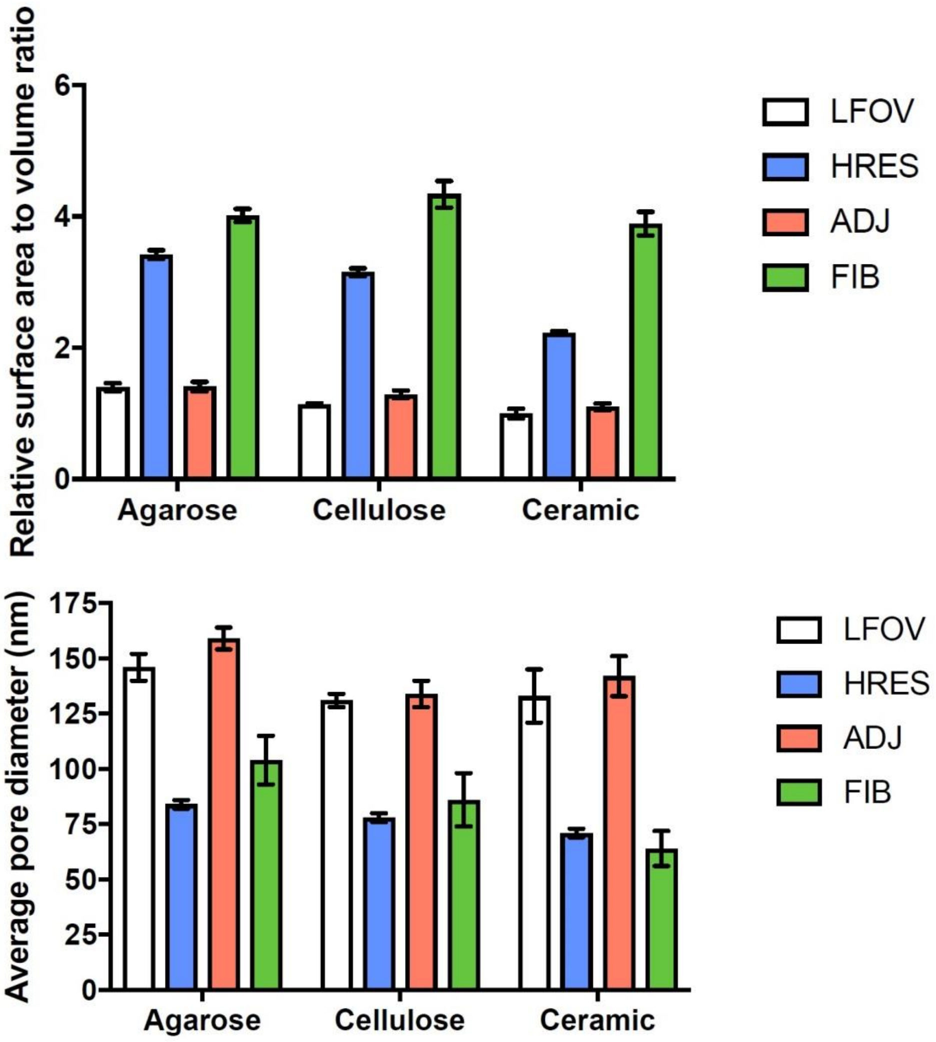

Figure 58: Bead surface area to volume and void space measurements. See **Table 7**. From Johnson *et al.* [160]. **Top**: Average pore diameter. **Bottom**: Surface area to volume ratio.

Greater surface area to volume ratios for all materials resulted when using higher resolution approaches demonstrated the capability for defining small structural features compared to LFOV X-ray CT; indicating that these may be required for true geometry identification. These values were therefore normalised and used as relative comparisons between techniques and materials rather than a definitive value in each case, see **Table 7**.

This was in contrast to porosity and tortuosity where identifying the general structure using LFOV X-ray CT was sufficient to evaluate tortuosity. Average pore sizes also were closer to the expected 50nm and below by Angelo *et al*. and others [24] when using HRES X-ray CT and FIB. Further resolution improvements would be desirable to find the optimal voxel size before pixel size did not change, but limits for both systems were already being reached.

Agarose	**X-ray computed tomography**			**Focused ion beam microscopy**
	LFOV	High Res.	Adjusted	
Geometric porosity (%)	**68.8** *± 1.8*	**70.6** *± 0.9*	**67.3** *± 1.3*	**77.7** *± 2.6*
Geometric tortuosity	**1.23** *± 0.02*	**1.19** *± 0.02*	**1.23** *± 0.02*	**1.26** *± 0.03*
Tortuosity factor	**1.44** *± 0.03*	**1.50** *± 0.02*	**1.48** *± 0.07*	**1.46** *± 0.07*
Surface area to volume ratio	**1.40** *± 0.06*	**3.42** *± 0.07*	**1.41** *± 0.07*	**4.02** *± 0.10*
Average pore diameter (nm)	**146** *± 6*	**84** *± 2*	**159** *± 5*	**104** *± 11*

Cellulose	**X-ray computed tomography**			**Focused ion beam microscopy**
	LFOV	High Res.	Adjusted	
Geometric porosity (%)	**68.7** *± 2.0*	**70.4** *± 0.8*	**69.0** *± 1.6*	**74.3** *± 2.51*
Geometric tortuosity	**1.27** *± 0.04*	**1.26** *± 0.03*	**1.26** *± 0.04*	**1.26** *± 0.02*
Tortuosity factor	**1.46** *± 0.13*	**1.45** *± 0.13*	**1.48** *± 0.03*	**1.48** *± 0.10*
Surface area to volume ratio	**1.14** *± 0.02*	**3.15** *± 0.06*	**1.29** *± 0.06*	**4.34** *± 0.20*
Average pore diameter (nm)	**131** *± 3*	**78** *± 2*	**134** *± 6*	**86** *± 12*

Ceramic	**X-ray computed tomography**			**Focused ion beam microscopy**
	LFOV	High Res.	Adjusted	
Geometric porosity (%)	**63.4** *± 3.6*	**64.8** *± 0.6*	**64.0** *± 2.4*	**69.9** *± 1.1*
Geometric tortuosity	**1.48** *± 0.07*	**1.46** *± 0.05*	**1.47** *± 0.07*	**1.48** *± 0.17*
Tortuosity factor	**1.60** *± 0.01*	**1.56** *± 0.03*	**1.48** *± 0.03*	**1.53** *± 0.03*
Surface area to volume ratio	**1.00** *± 0.07*	**2.23** *± 0.03*	**1.10** *± 0.05*	**3.89** *± 0.18*
Average pore diameter (nm)	**133** *± 12*	**71** *± 2*	**142** *± 9*	**64** *± 8*

Table 7: Physical analysis of individual bead geometry. Results from Johnson *et al*. [160]. Average values are presented in each case to three significant figures and one standard deviation in *italics*. Surface area to volume ratio was normalised against the lowest average. See the **Appendix** for examples of individual bead and packed bed statistical analysis.

For the pore sizes obtained, the minimum possible value for each imaging technique would have been the voxel size achieved for each imaging technique, which was approximately equivalent or even larger than the average pore sizes identified using alternative approaches such as ISEC for an array of sorbents and materials [23] - [25]. This suggested an average pore size of 7nm and 27nm in respective studies by Angelo *et al.* [24] and Tatárová *et al*. [23] for cellulosic MEP HyperCel beads. In addition to Angelo *et al*. [24] stating that average pore sizes using EM of cellulose resins was 50nm, it is also discussed that EM approaches may not be able to identify pores smaller than 5nm due to resolution constraints. Whilst this was true for the tomographic imaging in this case, when using sub-nanometre imaging another issue would be distinguishing between small features relative to noise.

Therefore whilst FIB could feasibly perform sub-nanometre pixel sizes, particularly if a more accurate machine or cutting source was used, X-ray CT cannot currently achieve this and the equipment and modes used were close to the current limits. Whilst there are literature examples achieving a superior resolution discussed in **Chapter 1**, these are often using machines or samples that are not compatible with the chromatography samples required.

These findings highlighted that improvement to current equipment for enhanced pixel size and stability using future technologies would be required as discussed by Withers *et al.* [113]. Novel approaches and technologies such as advanced Zernike mode investigated in **Chapter 3** did not work successfully in this study, however have clear aforementioned benefits when the technology has been further developed for softer bead materials.

Therefore, the results for both geometric and tortuosity factor at the individual bead scale were found to be within the expected 1.4 to 2 range, demonstrating that a tomographic approach can be used to quantitatively analyse the three dimensional tortuous paths through the internal structure of a chromatography bead of various materials of construction in agreement with existing literature values. However, issues arising from quantitative analysis of the processed volumes were that the porosity readings were lower than conventional measurement suggestions, albeit consistent across the imaging techniques; with average pore diameters also being larger compared to conventional ISEC measurements.

Overall the results suggested that tomographic imaging was a suitable technique to evaluate geometric characteristics of a chromatography bead, although comparisons to established methods were also useful in order to understand benefits and shortcomings. This was particularly important when using comparative techniques such as X-ray CT and FIB which displayed similarities and differences in results, attributed to pixel size achieved as well as other factors such as the degree of sample preparation required etc.

At the packed bed scale, the three materials were analysed for the same characteristics from Nikon XT H 225 ST imaging at the top, middle and bottom of the column; with Zeiss Xradia Versa volumes also available for ceramic data-sets as a comparison. Sub-volume generation was performed in order to determine the potential impact of axial position on geometry, although Schmidt *et al*. [176] have previously suggested this is not a major factor.

Sub-volumes were also compared radially across the column to investigate the degree of wall effects and relative packing density, as discussed in **Chapter 1** [61], [177]. 1mm in height was analysed at the top, middle and bottom of each column in order to provide a sufficient volume for analysis whilst keeping imaging and processing times reasonable. **Figure 59** displays the results for porosity and tortuosity between the edge and centre.

It was observed that for every sample the geometric porosity in **Figure 59A** was lower at the edge of the packed bed compared to the rest of the central portion of the column, which was also found to occur in each axial position, indicating that there was a greater packing density and thus relatively reduced porosity at the edge, with ANOVA (**Appendix**) used to confirm that column and edge results were different and not due to natural variation. It was found in **59C** where the central section of cellulose and ceramic packed beds were considered that all sub-volumes at the walls had a lower porosity compared to the centre of the overall volume.

To compare the porosity results obtained using tomography to an established technique; a pulse assay was used where blue dextran is inserted into the packed bed but is too large to enter the internal porous structure and so fills the *inter*-bead space. This enables determination of packed bed porosity. Directly relating to the tomographic readings performed at this scale that does not have resolution capabilities for imaging both scales.

Whilst binding issues were encountered with agarose based packed beds that prevented accurate porosity calculations, cellulose and ceramic evaluations were possible despite having to pulse a separate cellulose column to the one imaged. Respective cellulose and ceramic packed bed porosities determined using the pulse test were 38.3% and 34.7% which was within the ranges found using tomographic analysis and agreeing with Angelo *et al.* [24], suggesting the packed bed geometry was representative of the *inter*-porous volume.

The highest overall porosity determined was for cellulose volumes followed by agarose and then ceramic. This was expected as in **Chapter 2** the same order was found in terms of beads being the largest on average, which results in a reduction in overall packing density when considering larger spheres, resulting in an increased porosity. Overall geometric porosity values were found to be in expected ranges that agree with orthogonal evaluation.

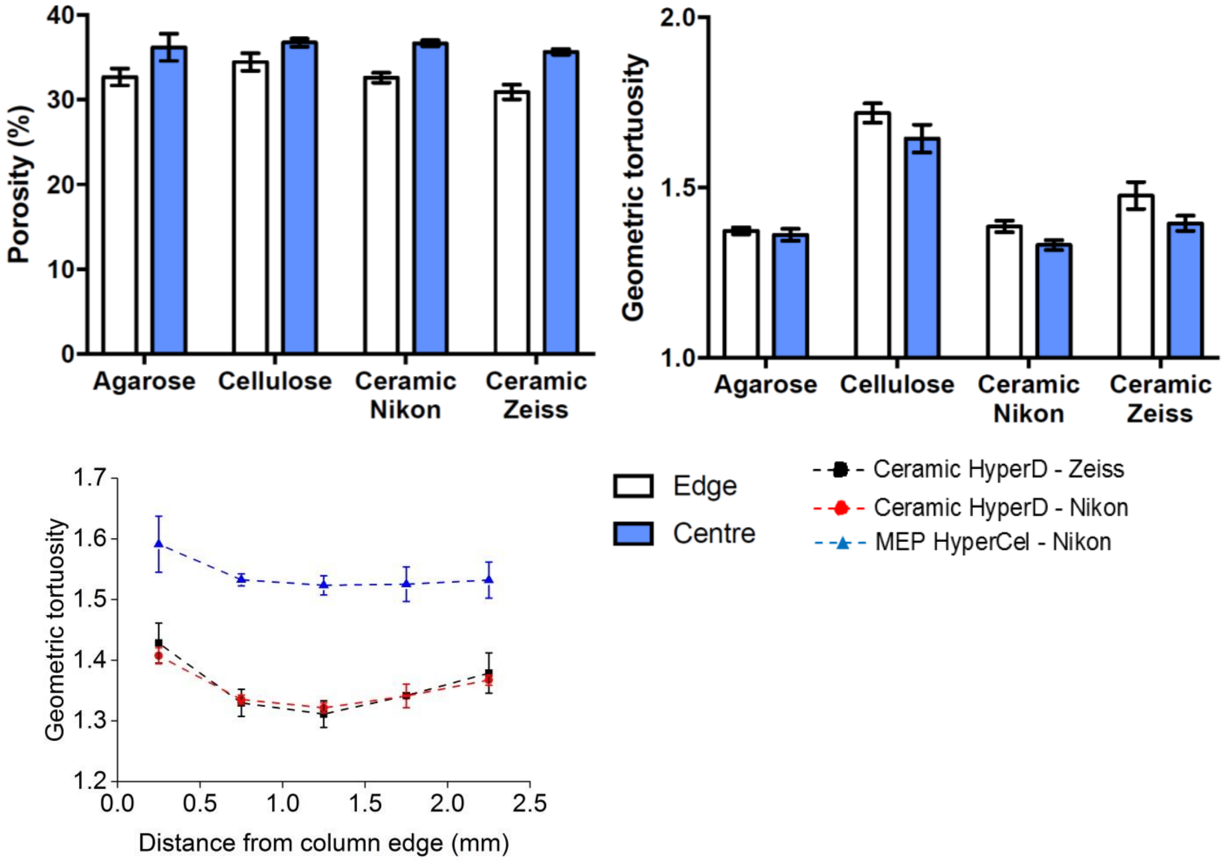

Figure 59: Porosity and tortuosity measurements at the packed bed scale. Adapted from Johnson *et al*. [169] with agarose based data added to published graphs. **Left**: Geometric porosity of 1mL packed beds from each X-ray CT system. **Right**: Geometric tortuosity of 1mL packed beds from each X-ray CT system. **Bottom**: Geometric tortuosity to distance from bed wall (chamber diameter of 5mm).

For tortuosity, geometric was the sole approach quantified because tortuosity factor relied on diffusion based calculations that were not relevant for the convection and pressure driven domain experienced between beads within a packed bed. As with previously discussed porosity measurements, a clear axial trend between column position and geometric tortuosity could not be identified, however the overall average geometric tortuosity was found to be different at the 500µm section closest to the wall versus the remainder of the centre that would indicate distortion of ideal axial plug flow due to radial flow path disparities.

In relation to the lower porosities observed at the column edge, experiencing a relatively increased tortuosity in this section was expected due to less void space for mobile phase movement relative to the more open central section in each case. Higher cellulose tortuosity was attributed to longer path navigation around larger beads despite greater porosities.

Tortuosity determinations for packed beds was not deemed to be as relatable to other studies or performance evaluation due to the pressure driven domain as opposed to the diffusion driven state within a bead, however may be useful for SEC evaluation of performance when relating both scales. **Figure 60** displays the non-standardised surface area to volume ratios and average pore sizes obtained for all materials and equipment.

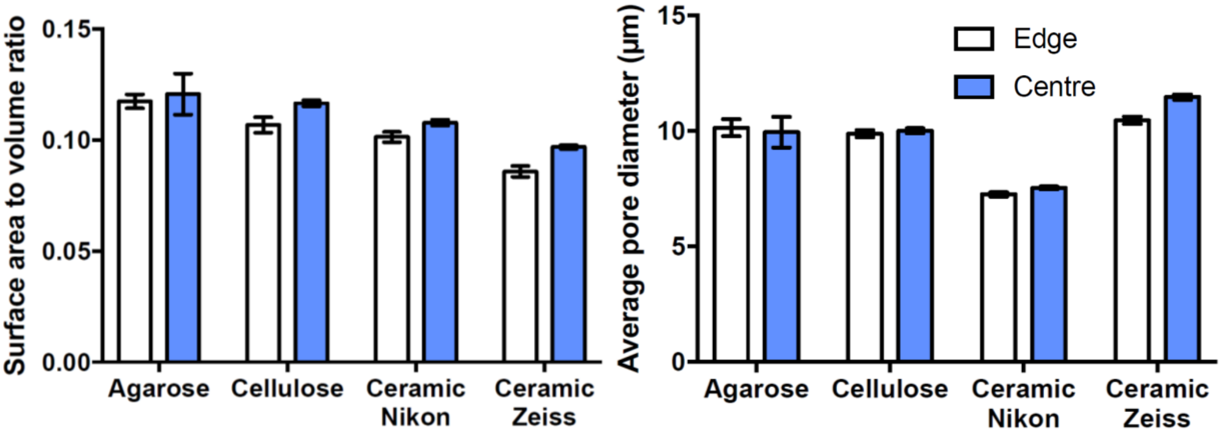

Figure 60: Column surface area to volume and void space measurements.
Adapted from Johnson *et al*. [169] with agarose data added. White – Edge, Blue – Centre.
Left: Surface area to volume ratio of packed beds from each imaging source.
Right: Average pore diameter of packed beds from each imaging source.

For the surface area to volume ratio in **Figure 60**, overall values obtained suggested a greater ratio at the centre of the column compared to the edges despite the lower proportion of beads. This was attributed to poorer definition of bead boundaries with the higher packing densities, requiring an improved voxel size to enable effective bead cluster segmentation, as it was expected that the surface area to volume ratio would be greater with a lower porosity. The surface area to volume obtained overall suggests a tight packing conformation [178].

For the average pore dimensions, there was no significant differences between the wall and centre for each material, suggesting that the packing density at the edge of the column results in fewer pores rather than reducing the pore sizes themselves, highlighting that the geometry of the beads results in a certain average pore size being common; although it is important to note that the largest pores were found closer to the centre albeit a small number that did not severely impact final calculations, with distance maps displayed in **Figure 56** and overall results for the three 1mL pre-packed beds available in **Table 8**.

Agarose	**Edge**			**Centre**		
	Top	Middle	Bottom	Top	Middle	Bottom
Geometric porosity (%)	**34.5** ± 0.3	**32.0** ± 1.5	**31.5** ± 0.6	**39.3** ± 2.7	**36.2** ± 2.5	**33.0** ± 0.9
Geometric tortuosity	**1.33** ± 0.02	**1.35** ± 0.02	**1.45** ± 0.02	**1.32** ± 0.02	**1.38** ± 0.04	**1.39** ± 0.02
Surface area to volume ratio	**0.103** ± 0.009	**0.099** ± 0.005	**0.150** ± 0.001	**0.105** ± 0.011	**0.104** ± 0.005	**0.152** ± 0.005
Average pore diameter (µm)	**20.6** ± 1.8	**21.1** ± 1.6	**19.2** ± 0.5	**18.7** ± 1.2	**21.1** ± 0.9	**19.9** ± 0.4

Cellulose	**Edge**			**Centre**		
	Top	Middle	Bottom	Top	Middle	Bottom
Geometric porosity (%)	**34.2** ±0.4	**32.3** ±2.0	**36.9** ±0.7	**37.0** **±3.3**	**38.6** ±0.4	**37.6** ±0.7
Geometric tortuosity	**1.81** ±0.04	**1.77** ±0.05	**1.59** ±0.02	**1.79** ±0.06	**1.79** ±0.02	**1.62** ±0.08
Surface area to volume ratio	**0.126** ±0.003	**0.094** ±0.007	**0.110** ±0.001	**0.121** ±0.002	**0.113** ±0.001	**0.115** ±0.008
Average pore diameter (µm)	**10.0** ±0.1	**10.2** ±0.2	**9.4** ±0.2	**10.0** ±0.2	**11.1** ±0.1	**9.0** ±0.7

Ceramic	**Edge**			**Centre**		
	Top	Middle	Bottom	Top	Middle	Bottom
Geometric porosity (%)	**32.6** ±0.8	**32.7** ±0.8	**30.0** ±0.6	**36.9** ±1.5	**36.1** ±0.9	**35.4** ±1.0
Geometric tortuosity	**1.47** ±0.03	**1.40** ±0.02	**1.42** ±0.03	**1.39** ±0.02	**1.34** ±0.02	**1.36** ±0.03
Surface area to volume ratio	**0.091** ±0.002	**0.100** ±0.003	**0.083** ±0.002	**0.100** ±0.004	**0.106** ±0.001	**0.094** ±0.003
Average pore diameter (µm)	**10.7** ±0.2	**10.6** ±0.1	**11.0** ±0.2	**11.7** ±0.4	**10.9** ±0.1	**12.1** ±0.4

Table 8: Physical analysis of packed bed geometry. Calculations for edges are based upon measurements made up to 500µm from the column walls with the centre being the remaining internal volume, with a 1mm depth used in each case. Ceramic values are averaged between Zeiss and Nikon data-sets. The mean obtained is presented in each case to three significant figures. Variance is reported to one raw standard deviation See **Appendix** for examples statistical analysis. Adapted from Johnson *et al*. [169].

It can be observed in **Table 8** that as well as having different appearances as discussed in **Chapter 3**, the three materials have different values of porosity and tortuosity etc. that would relate their distinct structure to phase transfer. Whilst there were different values obtained between column material types, each packed bed displayed changes in porosity and other parameters between the column edge and centre. Tortuosity factor was not included at the packed be scale because the simulations rely on diffusivity based relationships, as discussed in **Chapter 1**. *Inter*-bead tortuosity is likely to be governed by non-diffusional i.e. pressure driven relationships and thus TauFactor was excluded in this case.

This not only impacted the tortuous paths available to the mobile phase, but also the surface area available for mass transfer not considering detailed surface topography. Differences between central and edge results were also found to be more pronounced in the top of column samples and lowest at the bottom of the column, suggesting a more uniform packing structure had been achieved near the exit although no distinct axial differences were found.

4.5. Chapter conclusion

This chapter considered both the image processing requirements for the individual bead and packed bed scale volumes produced using X-ray computed tomography and focused ion beam, as well as characterising the chromatography systems via quantitative analysis of key geometric parameters. For image processing, ensuring parity between all samples was an important focus, as divergent processing methods would impact the final volumes for processing. Attaining the correct balance between software processing and minimal human intervention was also important to the process to ensure that any human bias was eliminated whilst also confirming that the software did not perform erroneous steps.

Physical characterisation demonstrated that a tomographic approach enabled analysis of chromatography structures that aligned with existing theories and values obtained using established, orthogonal methods. This indicated that as well as tomographic approaches to chromatography system imaging being capable of producing images and structures based upon individual bead and packed bed samples, the volumes reconstructed are accurate representations of the actual structures imaged, albeit with discussed reservations about focused ion beam results versus X-ray CT. This enabled process based aspects such as compression and fouling to be investigated in **Chapter 5** based upon imaging optimisation in previous chapters, including simulation of flow through the void phases at both scales.

Chapter 5

Tomographic representation of compression and fouling of chromatography systems

5.1. Summary

After demonstrating the capability of X-ray CT for both visualising and quantifying 3D chromatographic structure at bead and bed scales, the final major aim of the project was to apply the approaches developed in previous chapters to commonplace industrial issues. Compression and fouling were selected for tomographic investigation in this chapter on the 3 chromatography materials, where changes at either bead or bed scale could be measured.

For compression, flowrates between 1 and 32 times the recommended limit were applied to 1mL pre-packed columns, with the top of the bed imaged before, during and after flow where previously explored attributes such as porosity could be compared. Whilst ceramic samples did not exhibit any structural changes, cellulose beds did compress under flow.

For the fouling study, X-ray CT was found to lose all contrast and image quality in the presence of protein rich feeds *intra*-cycle at the packed bed scale. Image quality loss was also found to occur for fouled beads, so an erosion-dilation approach was used to mimic material penetration of beads for diffusivity simulation, found to be in line with literature.

5.2. Introduction

The two industrial issues to be investigated here: compression and fouling were identified in **Chapter 1** as particular potential areas of interest that could be both visualised and quantified using a tomographic approach. X-ray CT was selected as the sole technique to be used as FIB was only applicable at bead scale where embedding was considered an issue.

Compression of packed bed can occur that negatively impacts processing performance due to several factors that can include excessive flowrate, pressure increases due to large particulate blockages and large column diameters resulting in a lack of frictional support, often being a combination of these factors [62], [68]. This was of particular relevance to the relatively soft materials of construction used for chromatography beads, where in extreme cases of compression, the bed does not revert to the original height and is compromised.

In this study the intention was to determine whether X-ray CT was capable of detecting changes to bed scale under flow, with the same 1mL pre-packed columns used as imaged in **Chapter 3**. Analysis of key characteristics such as porosity and tortuosity could then be compared between compressed and new samples, with permeability also simulated when considering flow through the *inter*-bead space of a cellulose HRES volume.

Fouling of chromatography systems is a prevalent issue that arises due to issues such as poor *inter*-cycle cleaning [72], albeit this is caused by poorly clarified feeds entering columns that deposit foulants. As discussed in **Chapter 1**, two main imaging techniques have been used to evaluate the fouled state of beads: electron microscopy and CLSM [12], [62], [68], [70], [96]. Using a tomographic approach would enable both high resolution and internal views of fouled beads after a set number of cycles to determine the impact of foulants on structure and relate to process performance over column lifetime.

The proof-of-concept study for determining the capability of X-ray CT was to image columns at each key *intra*-cycle stage for visual comparison, as displayed in **Figure 61**. This would then form the basis of *inter*-cycle investigations, where the impact of fouling over the lifetime of a sorbent [68] could be structurally investigated when using a high resolution 3D approach to determine the structural impact of foulants on both *inter* and *intra*-bead structure

5.3. Materials and methods

5.3.1. Compression

1mL pre-packed beds in the form of Q FF HiTraps, MEP HyperCel and CM Ceramic HyperD F columns were used as in **Chapter 3**, with the beads made of agarose, cellulose and ceramic respectively. Imaging conditions were based upon previous optimisation studies in **Chapter 3**, with **Table 5** displaying final parameter selection required for each material.

However, frames were reduced from 4 to 2 and mechanical ring artefact reduction was disabled in order to reduce each scan time from 310 to 110 minutes which was required to logistically perform the before, during and after scans in one session in order to ensure parity between acquisitions. During final imaging, a 30 minute gap between scans was inserted to allow for bed stabilisation, with a 250μs time per frame required for bed height changes.

As in **Chapter 3**, a 20.3mm RS drill chuck was used to hold the columns in place, with a 20% ethanol feed closed loop attached for continuous recirculation via a peristaltic pump. Flowrates were applied between 1 and 32 column volumes per minute for each investigation. Processing and analysis was performed as in **Chapter 4**, with an XLab extension in Avizo used to simulate flow through a bed sub-volume based upon pressure drop values obtained experimentally; being 0.13bar and 1.2bar for 1 and 10 column volumes per minute through a cellulose column respectively. Ceramic pressure drops for 1 and 10 column volumes per minute were recorded as 1.3bar and 5.3bar respectively.

A cellulose central packed bed sub volume was selected for digital erosion-dilation [153] which either removed or added 6μm of diameter to each bead respectively, artificially altering the porosity and *inter*-void gaps that could either close or open flow paths different to those in the original volume. As performed at the individual bead scale in **Chapter 4**, the MATLAB plugin TauFactor was used to determine tortuosity factor for each digital volume.

5.3.2. Fouling

1mL pre-packed columns in the form of Q FF HiTraps, MEP HyperCel and CM Ceramic HyperD F columns were used as in **Chapter 3**, with the beads made of agarose, cellulose and ceramic respectively. Imaging conditions were based upon previous optimisation studies in **Chapter 3**, with **Table 5** displaying final parameters chosen, required to image the top and bottom each session before further processing steps were performed on the same sample.

When imaging processed columns, an abridged optimisation process of **Figure 44** was performed to determine whether parameters needed adjustment for buffer changes in the packed bed, however this was found to be ineffective or unnecessary in all cases as either no improvement of image quality could be found or was not required. Individual beads also used identical conditions to those established using phase contrast in **Chapter 3**, with quantification metrics outlined in **Chapter 4** for analysis of porosity and average pore size evaluated in Avizo and tortuosity factor using the MATLAB extension TauFactor [174].

For packed bed investigations an ÄKTA Explorer was used to perform typical equilibration, load wash elute and cleaning steps, with X-ray CT scanning points defined in **Figure 61**. Buffers used for MEP HyperCel cellulose columns were: 1M phosphate buffered saline (Sigma, USA) at pH 7.4 for equilibration and wash, 100mM sodium acetate at pH 5.5 with 0.5M sodium chloride for initial elution, with subsequent elution using 50mM sodium acetate with decreasing pH from 5 to 3 at a residence time of 7.5 minutes. Buffers used for CM Ceramic HyperD F ceramic columns were: 50mM sodium acetate at pH 4.5 for equilibration and washing, with elution buffers also containing 50mM sodium acetate but also including sodium chloride from 0.05M sodium chloride increasing up to 0.3M and pH from 5.5 to 8. 1M sodium hydroxide and 20% ethanol were also used for CIP and storage respectively.

For *inter*-cycle fouling investigations, these steps were repeated over a set number of cycles but were not successful as discussed in the results section. Individual agarose beads in new and fouled forms were imaged from Purolite Praestro® in jetted form having a typical bead diameter of approximately 40µm, where fouled beads were removed from the top of a packed column and confirmed to be impregnated by foulants using CLSM after 10 IgG cycles, in a similar manner to those presented by Jin *et al*. [12] before air drying and pinhead fixation before scanning using conditions optimised in **Chapter 3**. HRES volumes from previous chapters of 6.5µm dimensions including dilated versions for fouling approximation were simulated for diffusivity, with input values for input concentration, output concentration and bulk diffusivity being 1g/L, 0 and 6×10^{-11} m^2/s respectively to mimic BSA within the bead.

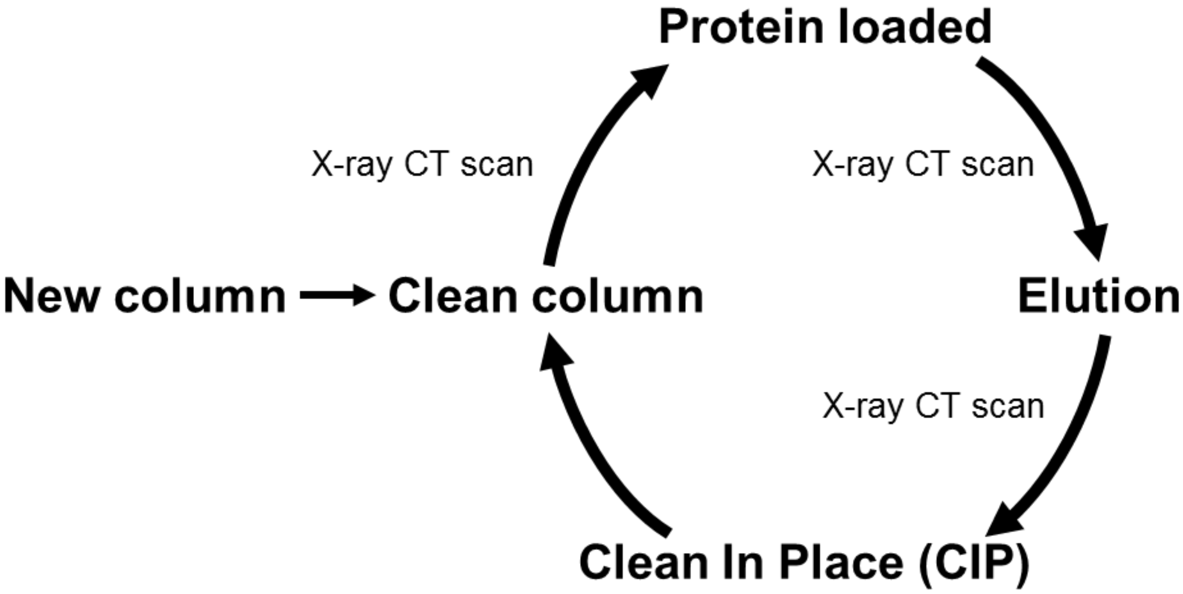

Figure 61: Overall bed scale schematic for *intra*-cycle study using X-ray CT for all materials.

5.4. Results and discussion

5.4.2. Compression

Initial investigations were performed by imaging the top of the packed bed as soon as flow commenced and whilst detailed structure could not be seen at the low exposures required, the overall bed height could be monitored, enabling overall determination as to the degree of bed height reduction occurring due to the various flow rates through the column.

Figure 62 displays the top half of each packed bed, with the cellulose and ceramic dimensions being identical, however the agarose had a 2mm greater internal diameter and thus a reduced height given that all pre-packed beds have a total volume of 1mL. It was found that at all flow rates investigated, no detectable movement occurred after 1 hour of flow for agarose and ceramic packed beds. This was expected because the agarose sorbent selected was specifically designed to encounter fast flow, although softer agarose beds may have been expected to compress due to larger diameters providing less wall support.

However, whilst the cellulose packed bed did not move within the flow rates recommended by the vendor, the bed height did reduce when flow rates double and exceeding that were applied for 30 minutes. It can be seen that at the bottom of **Figure 62** that as the applied flow rate was increased between runs, the bed height reduced further over a 30 minute period, beyond which no further compression could be observed up to 6mm of compression. It was found that after leaving the packed bed for a further 30 minutes after flow, the original bed height was restored and often within one minute. However, at 32 column volumes per minute there was still a gap between the top of the packed bed and the chamber entrance, indicating the compression had not fully reversed in that time and so would have either required more time or been irreversibly compressed which is undesirable in real scenarios.

Overall, it was demonstrated that X-ray CT was capable of imaging the dynamic change in bed height of compressing cellulose columns as well as reversion to the original state within the flow rates investigated beyond the suggested operating parameters. At the resolution and 4 frames per second used to capture the bed height movement, effectively real-time imaging was achieved. Upon success of the macroscopic X-ray CT investigation, improved pixel sizes of 3 µm achieved in **Chapter 3** were applied to determine the extent of bead movement before, during and after compression for all 1mL pre-packed column types.

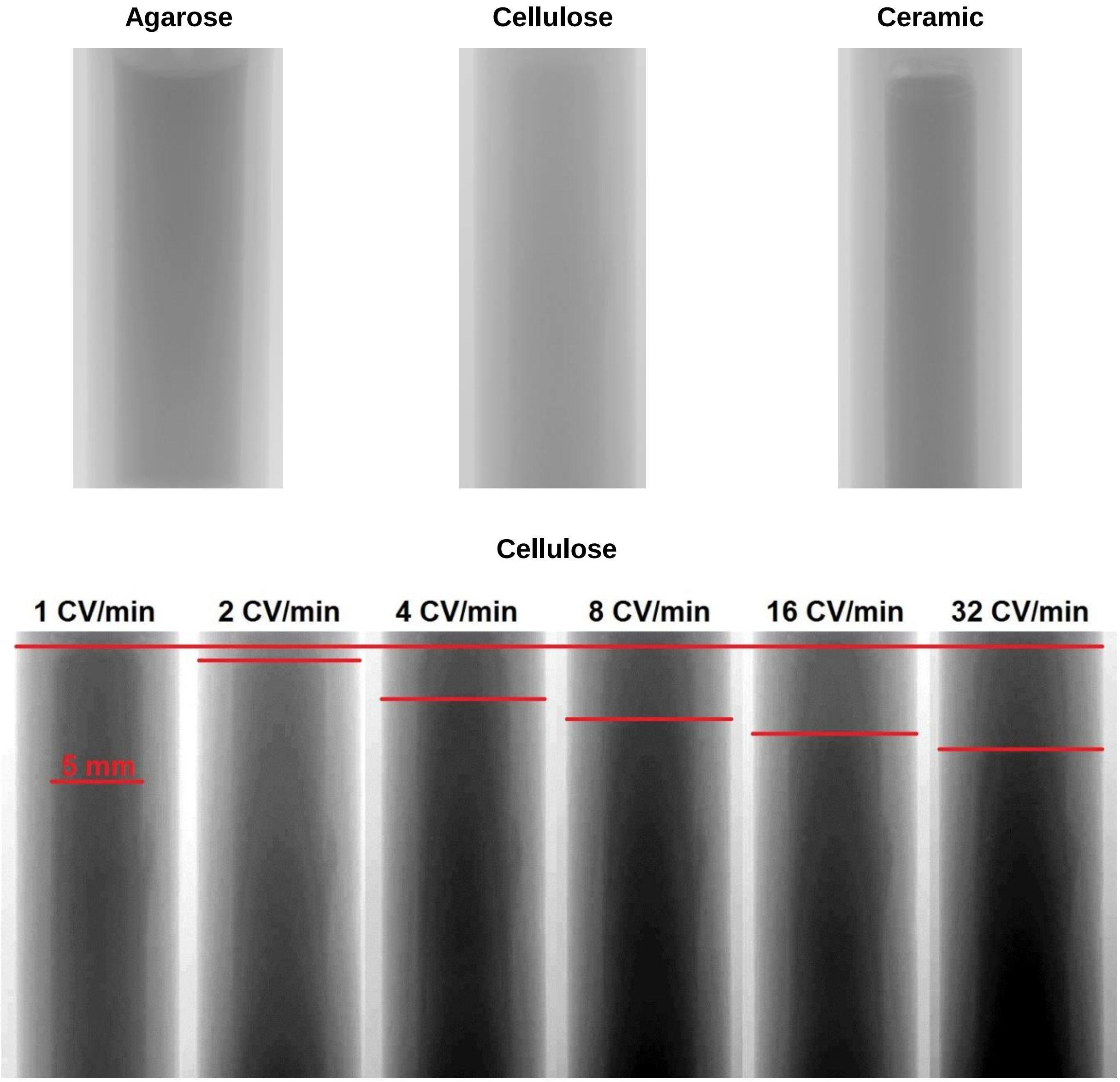

Figure 62: Macro-scale compression of cellulose packed beds. No movement was detected at the top of agarose and ceramic packed beds, with the top of the compressed cellulose beads indicated by surrounding red markers in comparison to the original top red line.

It can be seen in **Figure 63** that for both agarose and ceramic packed beds, there is no discernible sign of bead movement or compression even at the most extreme flowrate investigated. This was supported by performing geometry overlays in each case, where in particular the bright spots in the ceramic slices gave a clear indication that the beads were not moving even during 32CV/min ethanol flow, further demonstrating the rigidity of the ceramic pre-packed beds that would be highly suitable for column conditions that would exert considerable pressure on the beads if required in an industrial setting.

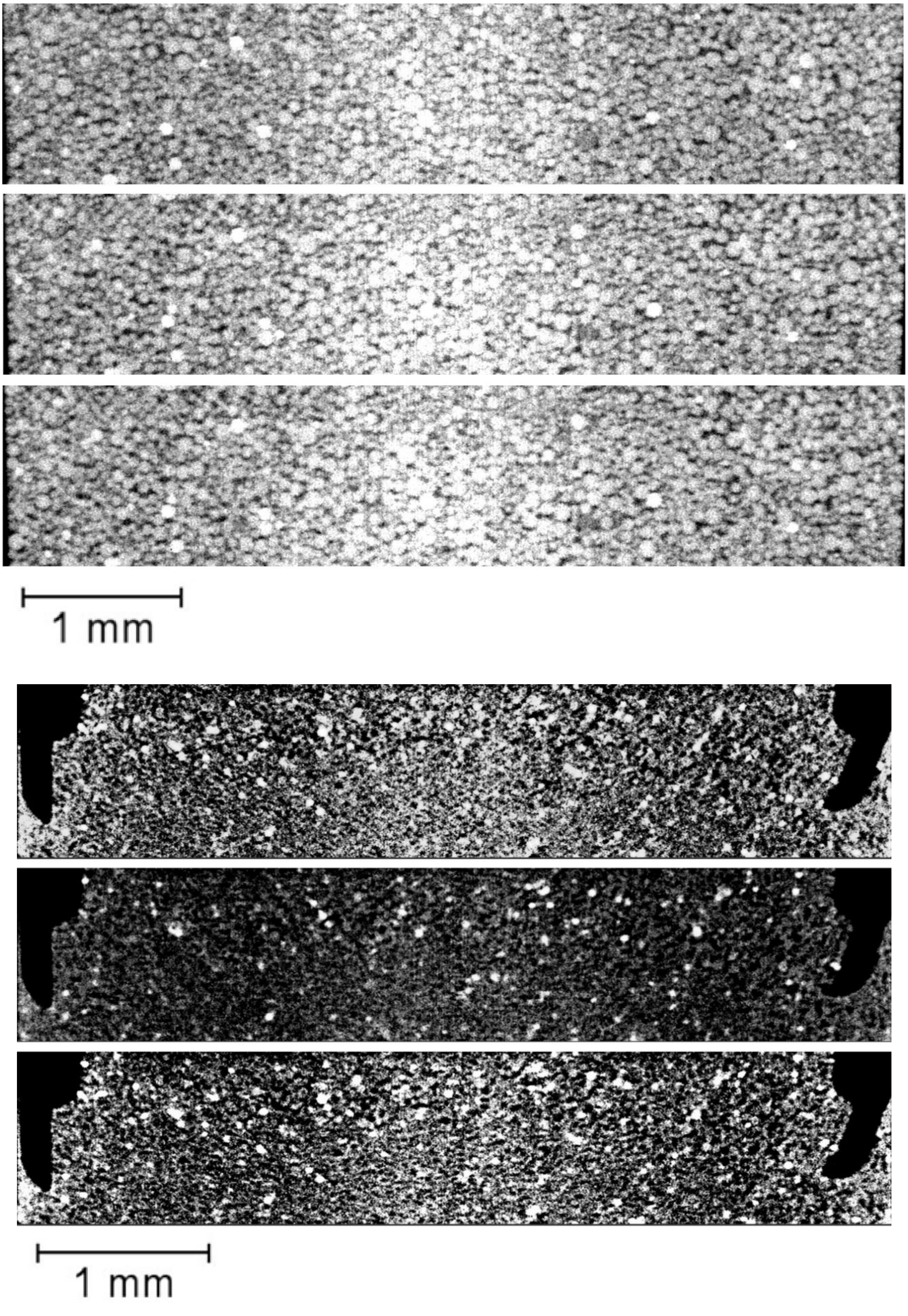

Figure 63: Agarose and ceramic packed beds before, during and after compression. **Top**: Agarose packed bed entry at 1CV/min. **Bottom**: Ceramic packed bed entry at 32CV/min.

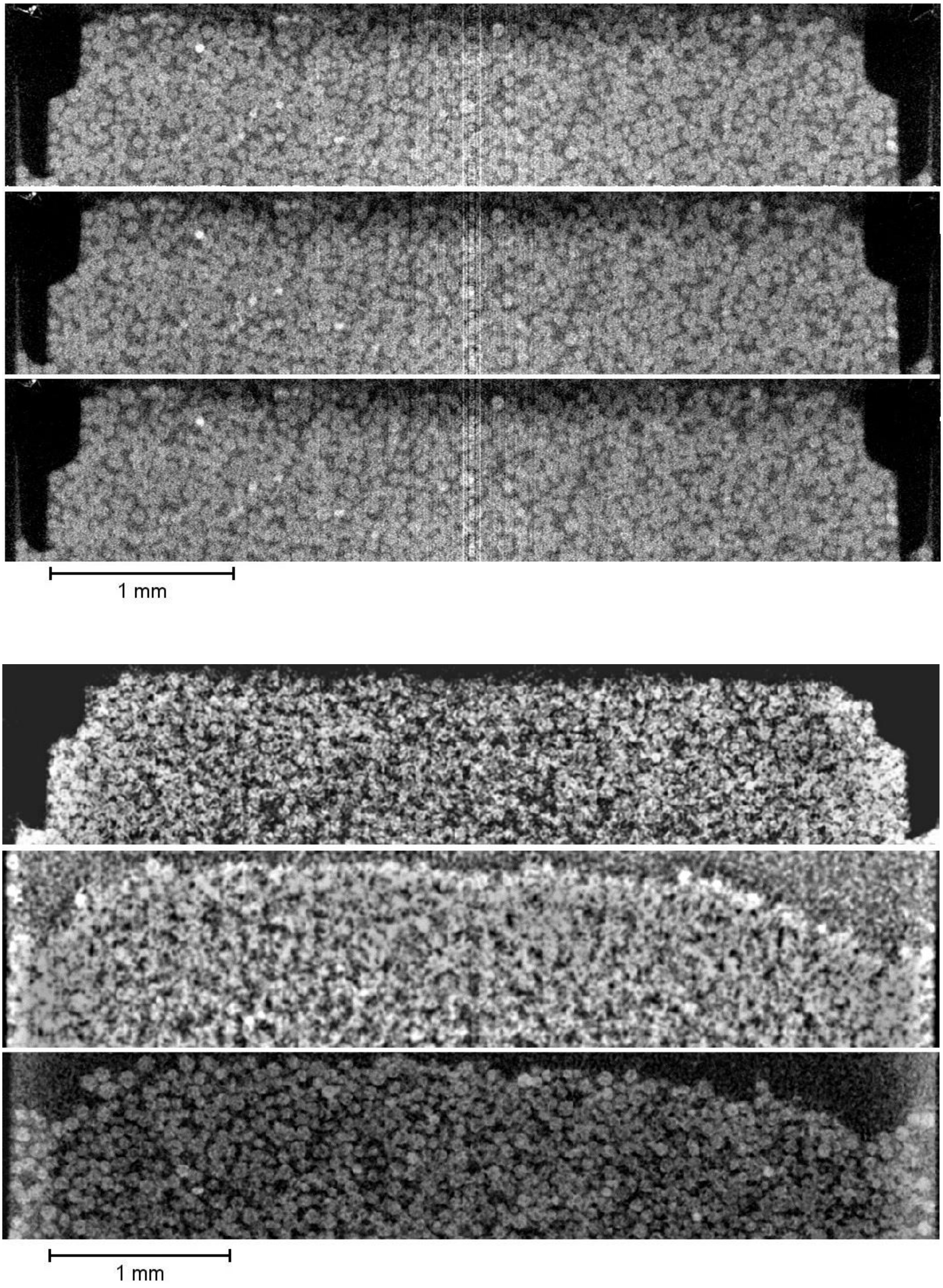

Figure 64: Cellulose packed beds before, during and after compression. **Top**: Cellulose packed bed entry at 1CV/min. **Bottom**: Cellulose packed bed entry at 10CV/min.

For the cellulose packed bed displayed in **Figure 64**, no bead movement and thus compression was detected at the recommended limit of 1 column volume, however clear disparities are observed using when applying a 10CV/min flow rate. This demonstrated that X-ray CT was capable of imaging changes in the packed bed structure before, during and after flow-based compression albeit at conditions unrepresentative of actual conditions that would be applied for analytical or processing chromatography applications.

It was also noted that the irreversible compression occurred to a cellulose packed bed after applying 32 column volumes per minute for 150 minutes, although scan quality was compromised during flow and so could not be analysed. Whilst all other flowrates had demonstrated reversible compression in the 30 minute timescale before final imaging, the final column at the most extreme condition was left for a week after compression before being re-imaged, with a visual 2D sub-volume from a 3D render displayed in **Figure 65**.

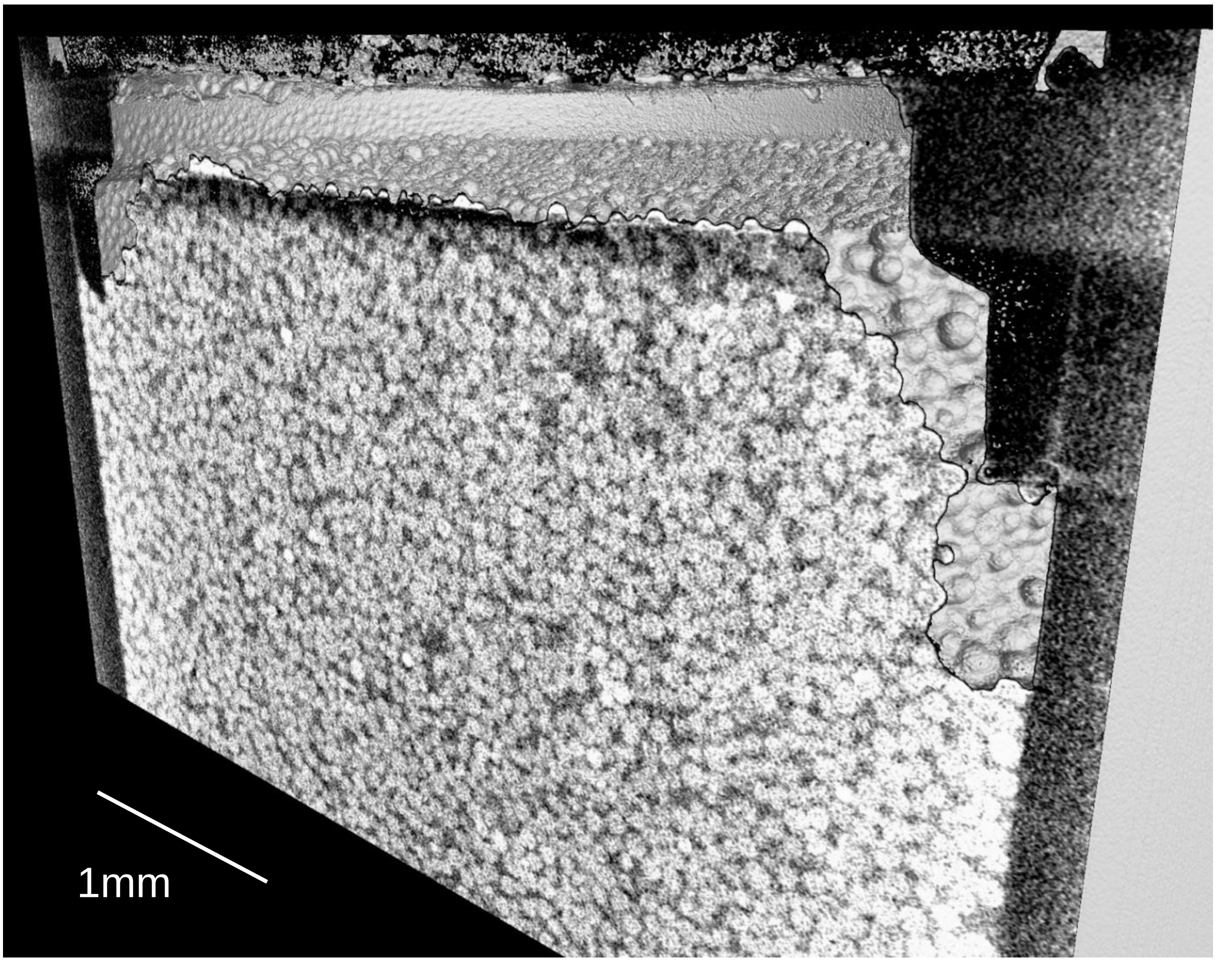

Figure 65: Irreversibly compressed cellulose packed bed after excessive flow. Column was left for 1 week after 150 minutes of flow at 32CV/min before X-ray CT imaging.

It was observed from **Figure 65** that even after a week following compression at 32 column volumes per minute flow, the cellulose packed bed had not returned to the top of the chamber and there was a clear gap to the original position that had not been filled by the packed bed structure. This verified that under extreme flow regimes that even densely packed columns can compress and undergo permanent changes and that X-ray CT was capable of confirming this, enabling visual comparison between packed bed materials. As previously discussed in **Chapter 1**, irreversible compression for industrial scale columns can result in entire bed failure via collapse that would require replacement of the sorbent.

After demonstrating that X-ray CT is capable of imaging changes to *inter*-bead structure within the packed bed due to compression in addition to macro-scale movements, image processing and quantification as demonstrated in **Chapter 4** was performed to each packed bed volume before, during and after compressive flow. **Figure 66** displays distance and flux maps for a central sub-volume at the top of the three materials before compression, whilst **Figure 67** displays the cellulose cut-out before, during and after compression at 10CV/min flow based on X-ray CT scans at reduced frames and projections. Artefact presence was an issue due to compromised imaging in order to logistically complete all scans in one session.

As previously discussed in **Figure 56** of **Chapter 4**, distance maps were useful for displaying the extent of *inter*-bead pore space morphology and heterogeneity for each sample despite a high packing density which was demonstrated in **Table 8** of **Chapter 4**. By visualising a 2D slice on a 3D overlay in each case, the entire sub-volume can be assessed; however the smaller gaps and velocities were made transparent for visualisation in order to enable clearer identification of relatively large voids in the pre-packed bed structure although this was deemed unnecessary for the 2D slice. A similar approach was applied when visualising the flux maps, with a pressure drop applied across all samples to represent 1CV/min flux where no compression occurred for materials in **Figures 66** and **67**.

The distance maps in **Figure 66** and the top images of **Figure 67** further displayed differences in regards to *inter*-bead structure as previously discussed in **Chapters 3** and **4**. As expected, the larger voids enabled a higher velocity to be obtained by the mobile phase through the packed bed structure for all three materials using identical simulation inputs. Whilst these effects were observed to be relatively minor for these sub-volumes, across the whole column this could lead to detrimental effects such as band broadening as discussed in **Chapter 1** which could be exacerbated by poorly packed columns. Further improvements to these simulations would include consideration of interactions between mobile phase and beads in addition to examining the whole column which was unfeasible in this case in terms of both the amount of X-ray CT scans required at a high resolution and computing power.

Figure 67 displays a cellulosic sub-volume before, during and after flow-based compression at a 10CV/min flux, with the convection simulation based upon values obtained when running the column during X-ray CT imaging. As observed in **Figure 67**, the bead geometry at the column entrance was changed as a result of compression and did not fully revert in **Figure 68** which suggested three different tomographic structures. The change in bead conformation resulted in different distance and flux maps being generated in **Figure 67**.

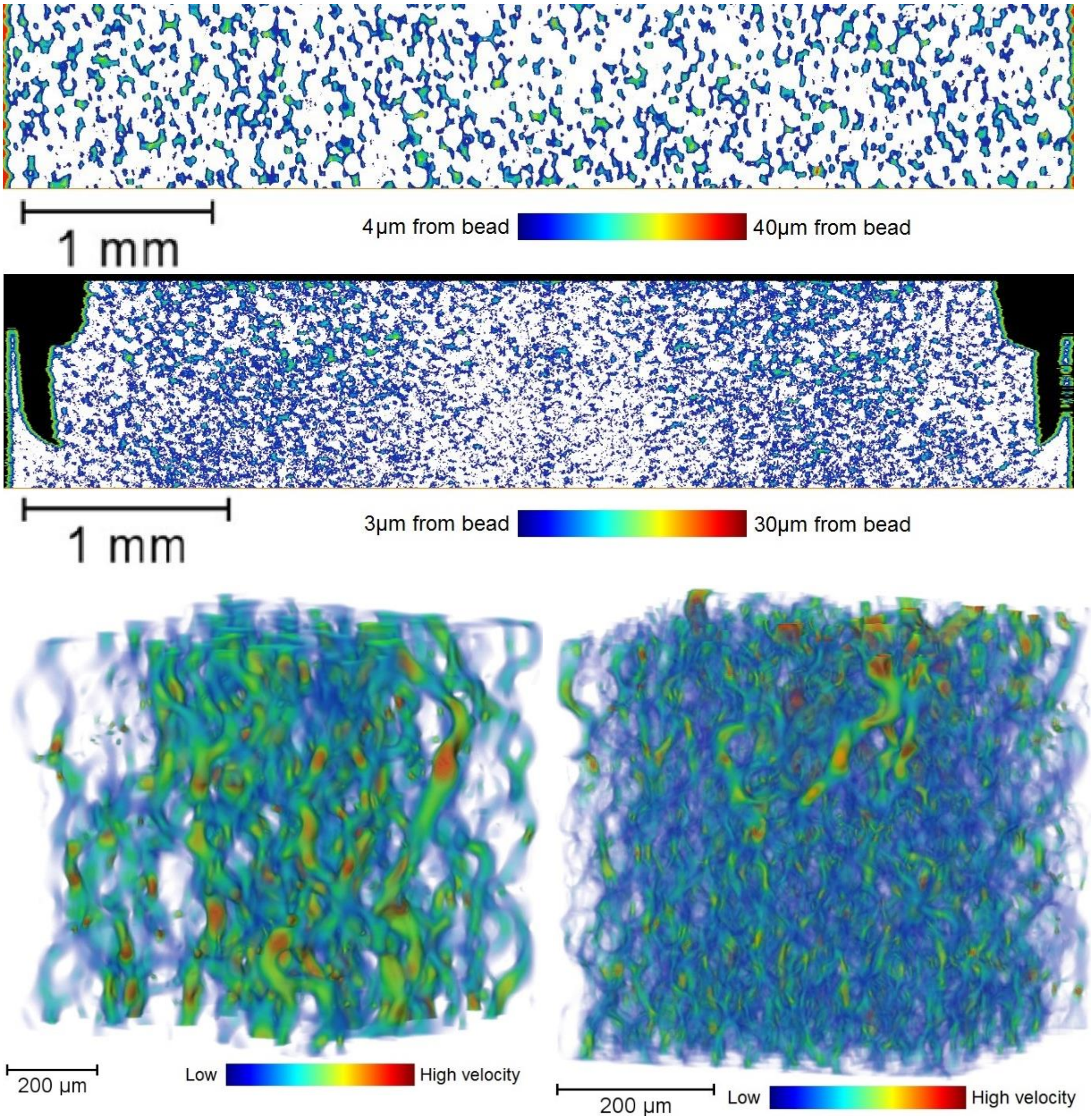

Figure 66: Packed bed flux maps and flow path visualisation. Images were taken from the entrance of the column. **Top**: Agarose distance map. **Middle**: Ceramic distance map. **Bottom-left**: Agarose centre relative velocity. **Bot-right**: Ceramic centre relative velocity.

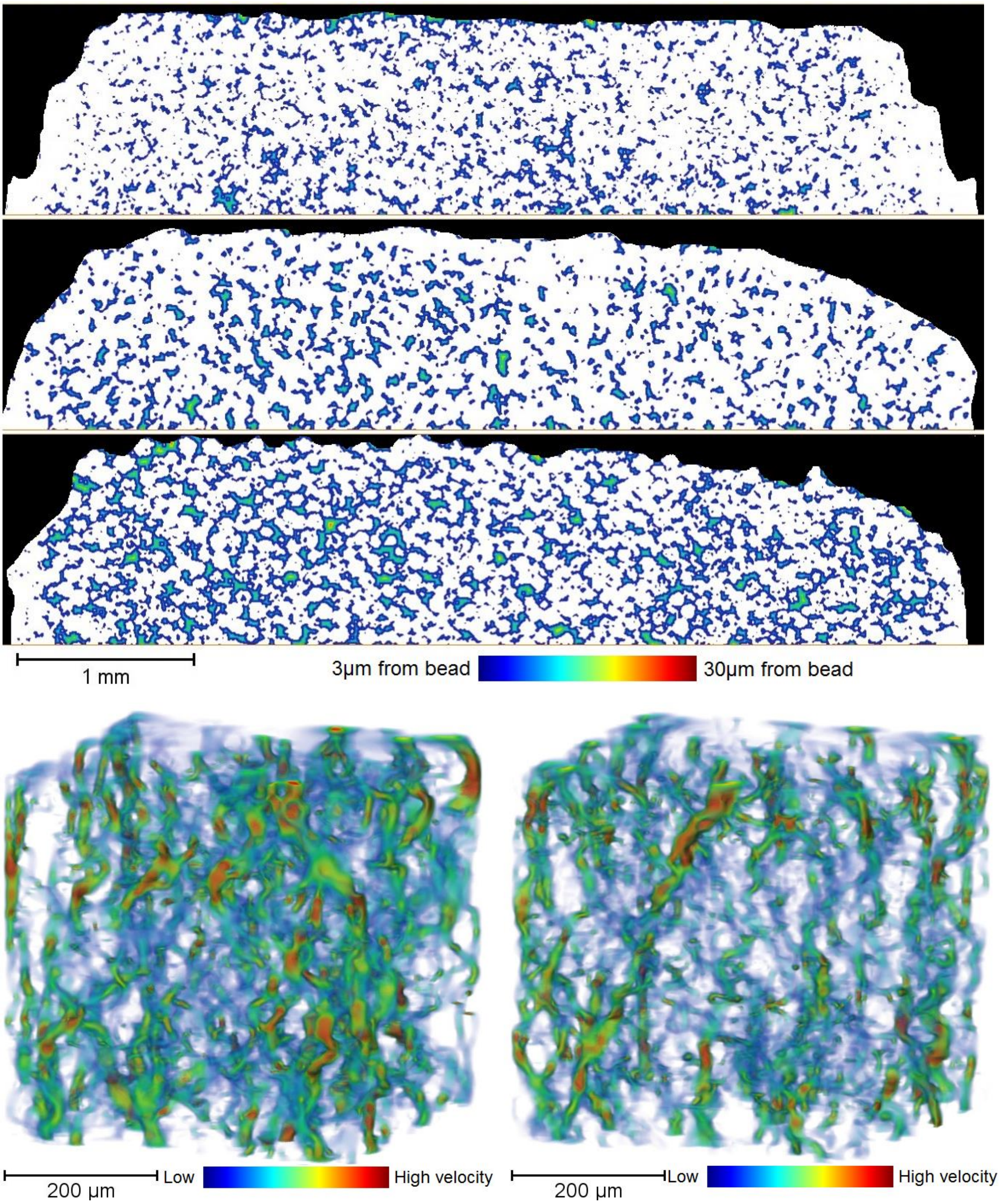

Figure 67: Cellulose distance and flux maps during 10CV/min compression. **Top**: Cellulose before, during and after distance maps corresponding to compressed states as presented in **Figure 64**. **Bottom**: Velocity profiles at the same co-ordinates based upon Avizo XLab permeability simulations. Results are reported in relative rather than absolute values. **Bottom-Left**: Top-edge sub-volume before compression. **Bottom-Right**: Top-edge sub-volume during 10CV/min flow. These two sub-volumes were also used in later analysis.

Once under compression, the sub-volume displayed a reduction in the larger *inter*-bead voids, however the already tightly packed structure had very few cases where compacting could occur due to less than 10% of overall volume height reduction; although larger voids were observed after flow and the same overall morphology was different to the scan before compression, the required compromises to imaging quality should be accounted for.

Changes in cellulosic bed morphology due to excessive compression could be visualised in distance and flux maps; therefore quantification of porosity, pore size, tortuosity and permeability were measured for each sub-volume in order to quantitatively identify the impact that extreme flow-based compression had on cellulosic packed bed structure. **Figure 68** and **69** display results of porosity, pore size, tortuosity and permeability of cellulose beds.

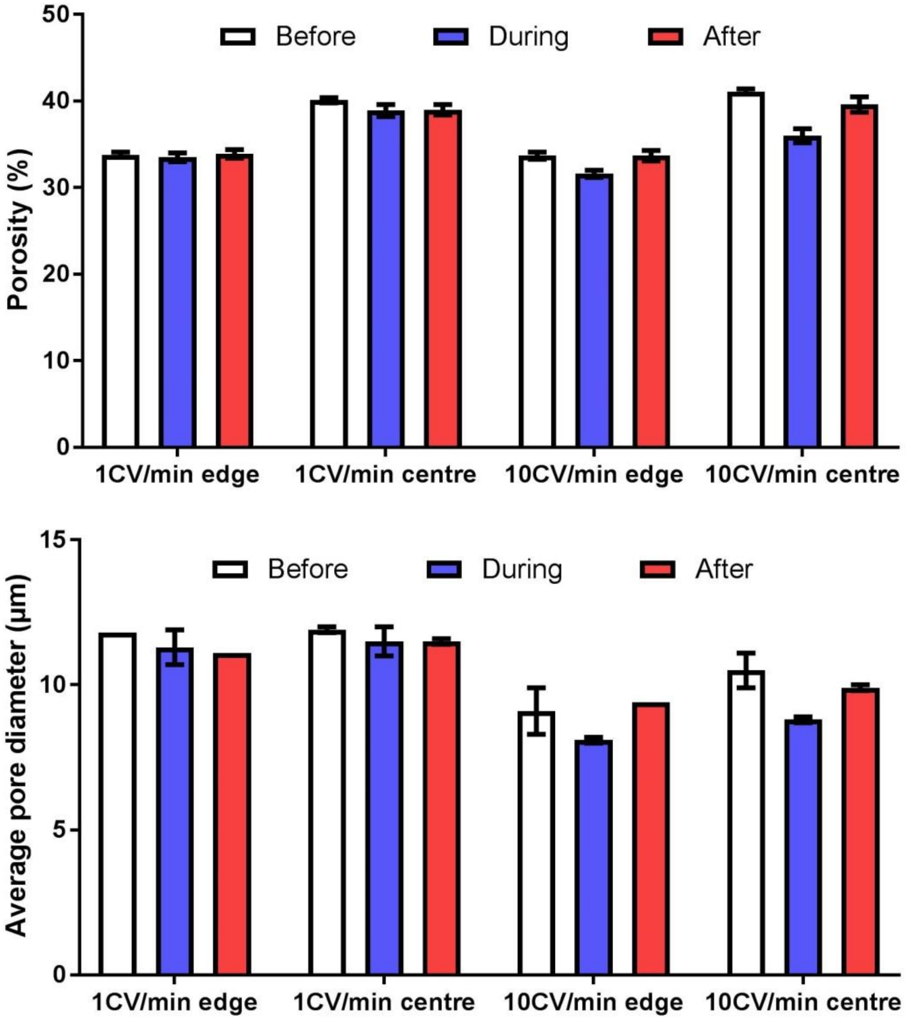

Figure 68: Porosity and average pore size measurements for cellulose columns. See **Table 9** for numerical values. Results are from packed bed scale X-ray CT and Avizo analysis. **Top**: Geometric porosity of packed bed volumes. **Bottom**: Pore sizes of packed beds.

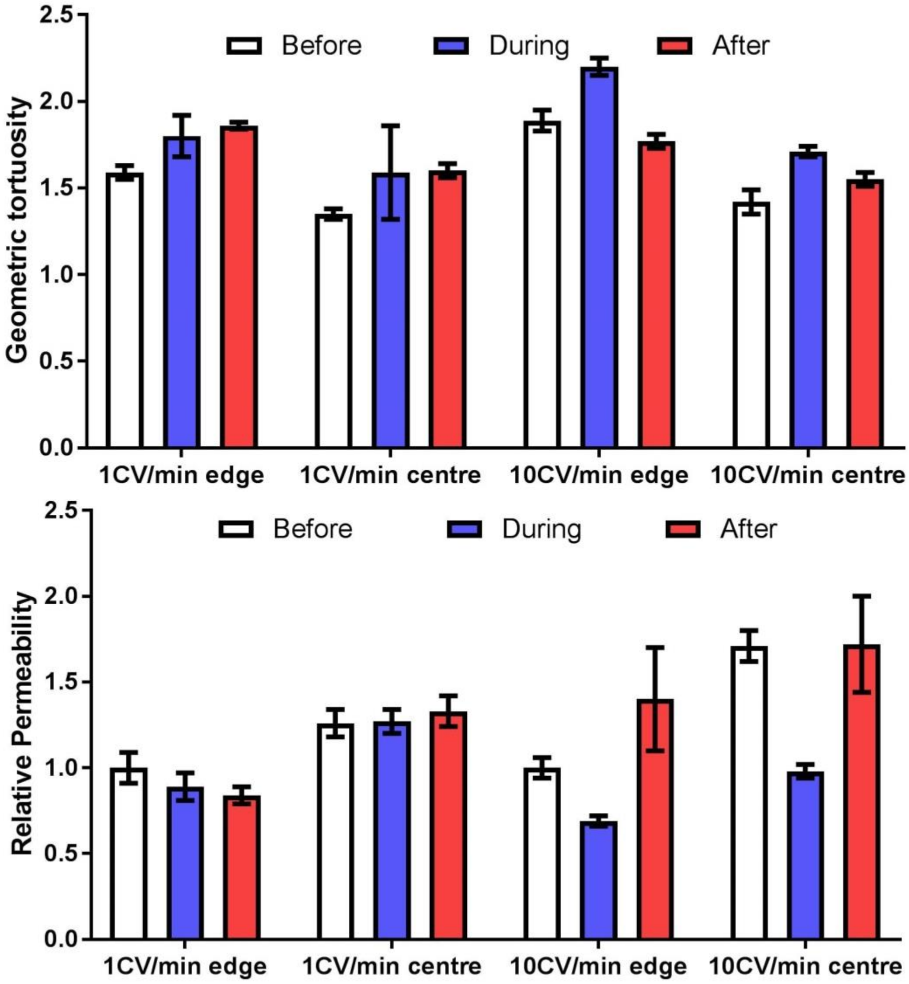

Figure 69: Tortuosity and permeability measurements for compressed cellulose columns. See **Table 9** for values. Results are from packed bed scale X-ray CT and Avizo analysis. **Top**: Geometric tortuosity of packed bed volumes. **Bottom**: Permeability of packed beds.

The decrease in porosity resulted in an increase in geometric tortuosity to the *inter*-bead network as expected, although the method of geometric tortuosity evaluation used as in **Chapter 4** does not consider the constrictiveness of the porous space beyond the slice-to-slice movement. However the change to tortuosity is not considerably large, similar to porosity and pore size alterations due to the already tightly organised column configurations available when using pre-packed beds, therefore these factors may be more changeable for poorly packed beds or scaled up variants which are more difficult to pack. Permeability also decreased under compression by 43% on average across central and edge volume at a flux of 10CV/min as visualised in the distance and flux maps in **Figure 67** before reverting to near-original levels despite irreversible compression occurring in **Figure 65**, albeit with overall bed compression permanently staying between 1% and 2%.

These results quantitatively confirmed expectations in terms of porosity, pore size, tortuosity and permeability when under extreme compression, with **Table 9** displaying the values presented in **Figures 66** and **67**. This also demonstrated that X-ray CT was capable of evaluating the impact of compression on packed bed structure under extreme conditions. Whilst other fluxes were investigated between 1CV/min and 32CV/min, they were not characterised here as the main focus of the study was to provide a comparison of extremes.

1mL/minute	**Edge**			**Centre**		
	Before	During	After	Before	During	After
Geometric porosity (%)	**33.8**	**33.5**	**33.9**	**40.1**	**38.9**	**39.0**
	± 0.3	± 0.5	± 0.5	± 0.3	± 0.7	± 0.6
Geometric tortuosity	**1.59**	**1.80**	**1.86**	**1.35**	**1.59**	**1.60**
	± 0.04	± 0.12	± 0.02	± 0.03	± 0.27	± 0.04
Relative permeability	**1.00**	**0.89**	**0.84**	**1.26**	**1.27**	**1.33**
	± 0.09	± 0.08	± 0.05	± 0.08	± 0.07	± 0.09
Average pore diameter (µm)	**11.8**	**11.3**	**11.1**	**11.9**	**11.5**	**11.5**
	± 0.0	± 0.6	± 0.0	± 0.1	± 0.5	± 0.1

10mL/minute	**Edge**			**Centre**		
	Before	During	After	Before	During	After
Geometric porosity (%)	**33.7**	**31.6**	**33.7**	**41.1**	**36.0**	**39.6**
	± 0.4	± 0.4	±0.6	± 0.3	± 0.8	± 0.9
Geometric tortuosity	**1.89**	**2.20**	**1.77**	**1.42**	**1.71**	**1.55**
	± 0.06	± 0.05	± 0.04	± 0.07	± 0.03	± 0.04
Relative permeability	**1.00**	**0.69**	**1.40**	**1.71**	**0.98**	**1.72**
	± 0.06	± 0.03	± 0.30	± 0.09	± 0.04	± 0.28
Average pore diameter (µm)	**9.1**	**8.1**	**9.4**	**10.5**	**8.8**	**9.9**
	± 0.8	± 0.1	± 0.0	± 0.6	± 0.1	± 0.1

Table 9: Physical analysis of cellulose bed geometry from compressed samples. Calculations were based upon Avizo and XLab evaluation at the centre and edges of each column using scans before, during and after compressive flow at either 1CV/min or 32CV/min. For 10CV/min flow permeability studies were conducted using the same input conditions as measured during flow. Permeability values were normalised to the 'Before edge' for each flowrate. Cellulose 1CV/min edge before: 3.52D ± 0.31D. Cellulose 10CV/min edge during: 1.14D ± 0.04D. 1CV/min Ceramic edge and centre: 1.29D ± 0.06D and 1.29D ± 0.00D. 1CV/min Agarose edge and centre: 4.49D ± 1.18D and 6.58D ± 1.60D.

This study focused upon the use of X-ray CT for visually and quantitatively evaluating compression on packed bed structure at the top of 1mL pre-packed columns. The capability for imaging at the macro-scale in real time as well as beads within the chamber before, during and after compression demonstrated the capability for X-ray CT to characterise changes to packed bed structure at the micron scale once columns had stabilised.

Both visual and quantitative analysis and demonstration of compression enabled further insight into the impact to the *inter*-bead space in terms of the pore size, tortuosity and permeability both during compression and afterwards once potential reversion to the original state occurred. However, loss in overall image quality was a perceived issue that needed to be considered when presenting visual and quantitative results, where any future studies would require further improvements to image quality and stability. Although this investigation did demonstrate the potential for tomographic approaches to evaluate changes in chromatography packed structure as a result of actual column use and applications.

The impact of reduction of porosity due to compression on tortuosity and permeability demonstrated the importance of available flow paths on mobile phase transfer through packed bed structure. Obtaining seed data of real column geometries enabled changes in porosity to be related to corresponding alterations in other characteristics; however another approach was to digitally alter the original structure to artificially alter the 3D structure in order to determine the impact on parameters of interest based upon defined changes.

In this case, a 3D central cellulose packed bed sub volume was digitally altered using erosion or dilation commands, where either 1 pixel is added or removed from the material phase respectively, resulting in a 6µm change to bead diameters in each case. This would result in *inter*-bead gaps either expanding or constricting, where sufficient dilation would close voids between beads that would reduce the number of available flow paths, with **Figure 70** displaying eroded and dilated volumes in addition to tortuosity factor results.

The 3D renders displayed the same packed bed coordinates after erosion or dilation; approximately exhibiting a 30% change in porosity from the original, highlight the considerable differences in geometry that were produced, in particular where eroded beads begin to lose spherical morphology and the dilated counterpart does display closed gaps that were previously present. As expected, a reducing porosity resulted in ever increasing tortuosity factor readings due to both the number of available flow paths and pore diameters using this predictive approach. This demonstrated that evaluation of changes to chromatography structure could be performed by either capturing real changes to bed structure or by digitally altering seed data to evaluate the impact these changes have.

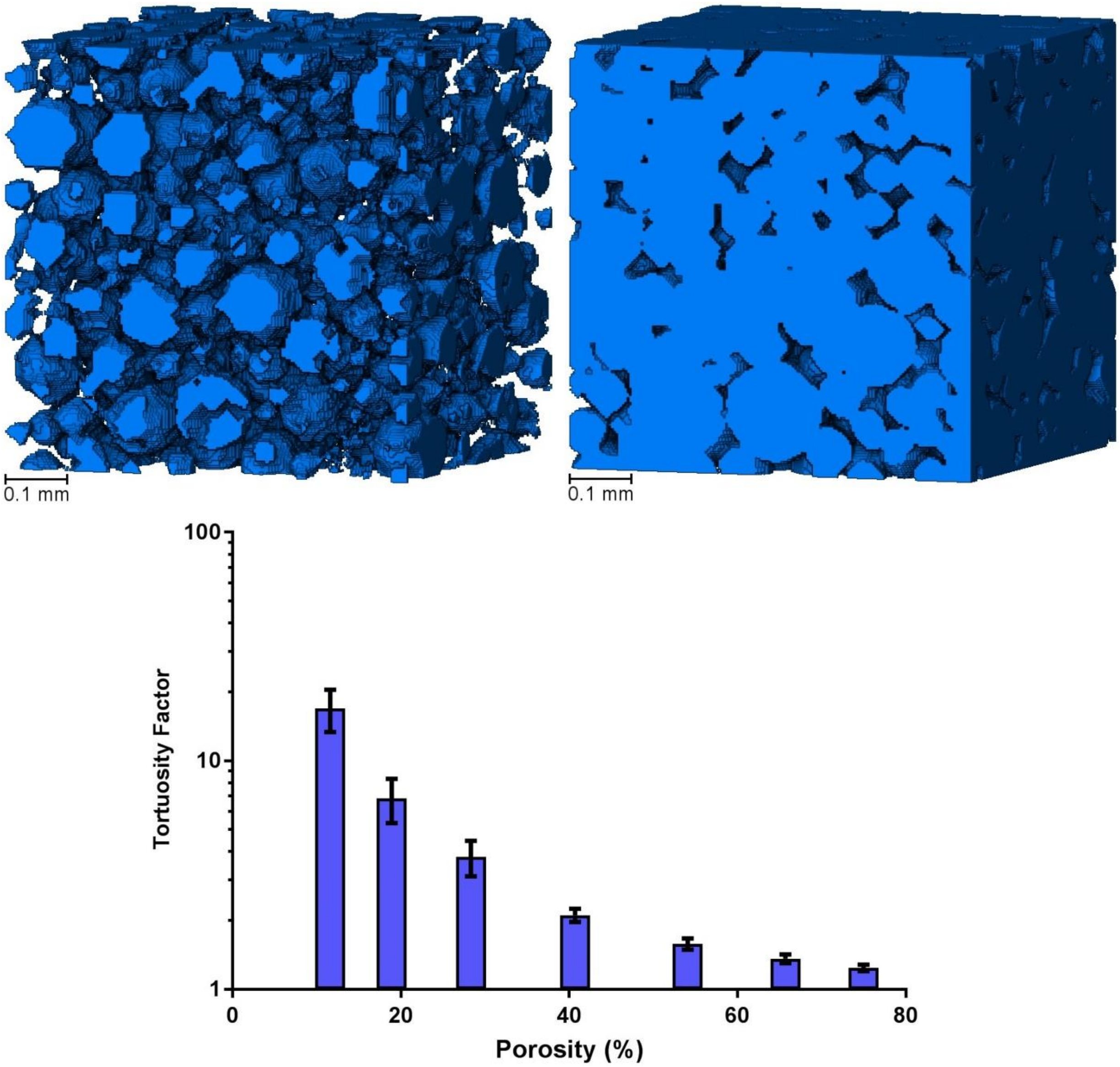

Figure 70: Erosion-dilation of cellulose packed bed structure. **Top-left**: Final eroded packed bed sub volume with a porosity of 75%. **Top-right**: Final dilated packed bed sub volume with a porosity of 12%. **Bottom**: Tortuosity factor in relation to different measured porosities for eroded and dilated sub volumes. See **Figure 55** for an unchanged packed bed 3D render.

This section investigated the impact of compressive flow through packed bed structure, where geometric changes to *inter*-bead space were both visualised in terms of distance maps and characterised aspects such as changes to porosity before, during and after compression with erosion-dilation also used to demonstrate changes in tortuosity factor resulting from porosity alteration. Simulation of flow based on real pressure drops to produce velocity maps and evaluate relative permeability, although the specific pressure drop in the region sampled would have been more accurate than estimations from the whole column.

5.4.2. Fouling

The purpose of this study was to determine whether loading, eluting and cleaning a 1mL pre-packed bed had an impact on structure and whether this could be detected within a typical cycle using X-ray CT at the column scale for agarose, cellulose and ceramic samples. Standard conditions were used for this investigation with unclarified IgG used as a feed stock as it would both allow for binding as well as typical foulant entities such as aggregates that may be sufficiently large to be imaged, with a new agarose column 2D slice displayed at the same position as loaded, eluted and cleaned stages in **Figure 71**.

From **Figure 71** it was observed that once loaded with rich feed, the image quality suffered whilst saturated with 1g/L IgG before being restored via elution and cleaning, which was also found to similarly occur for cellulose and ceramic samples albeit with differing severities, for example cellulose slices were found to be entirely clouded in the loaded and eluted stages. At 100g/L of IgG feed it was found that all agarose, cellulose and ceramic packed beds were entirely clouded until cleaned, with no other X-ray conditions found to improve image quality.

Based upon these proof of concept results indicating that foulants impacted the quality of the X-ray CT scans and thus could be an indicative measure of column status when using an exaggerated feed, then a more representative *inter*-cycle study could have been undertaken in order to relate the degree of fouling visualised to cycle behaviour. This would have enabled quantitative comparison between changes to structural values considered in **Chapter 4** such as porosity and tortuosity to common cycle performance metrics that would build upon other studies that have used EM and CLSM to image foulants [62], [68].

However, it was found that the inherent loss in quality when performing X-ray CT imaging of chromatography columns was indicative of the challenges required to accurately visualise and represent packed bed structure in the presence of protein; applying to both feed stream introduction and sorbents that used affinity and protein based functional groups such as MAbSelect SuRe and Kaneka KanCapA™ which are also used commonly in industry.

Overall, this prevented further investigation at the packed bed scale for using X-ray CT in order to relate geometric data to fouling over the life cycle of a sorbent. If achievable, this would have enabled consideration of the impact concerning feedstocks, cleaning regime and cycle number to the quantifiable changes in structure compared to typical performance measures such as yield and purity changes over the lifetime of a column that would allow for analogous comparison to approaches taken using CLSM by Jin *et al.* [12] and others.

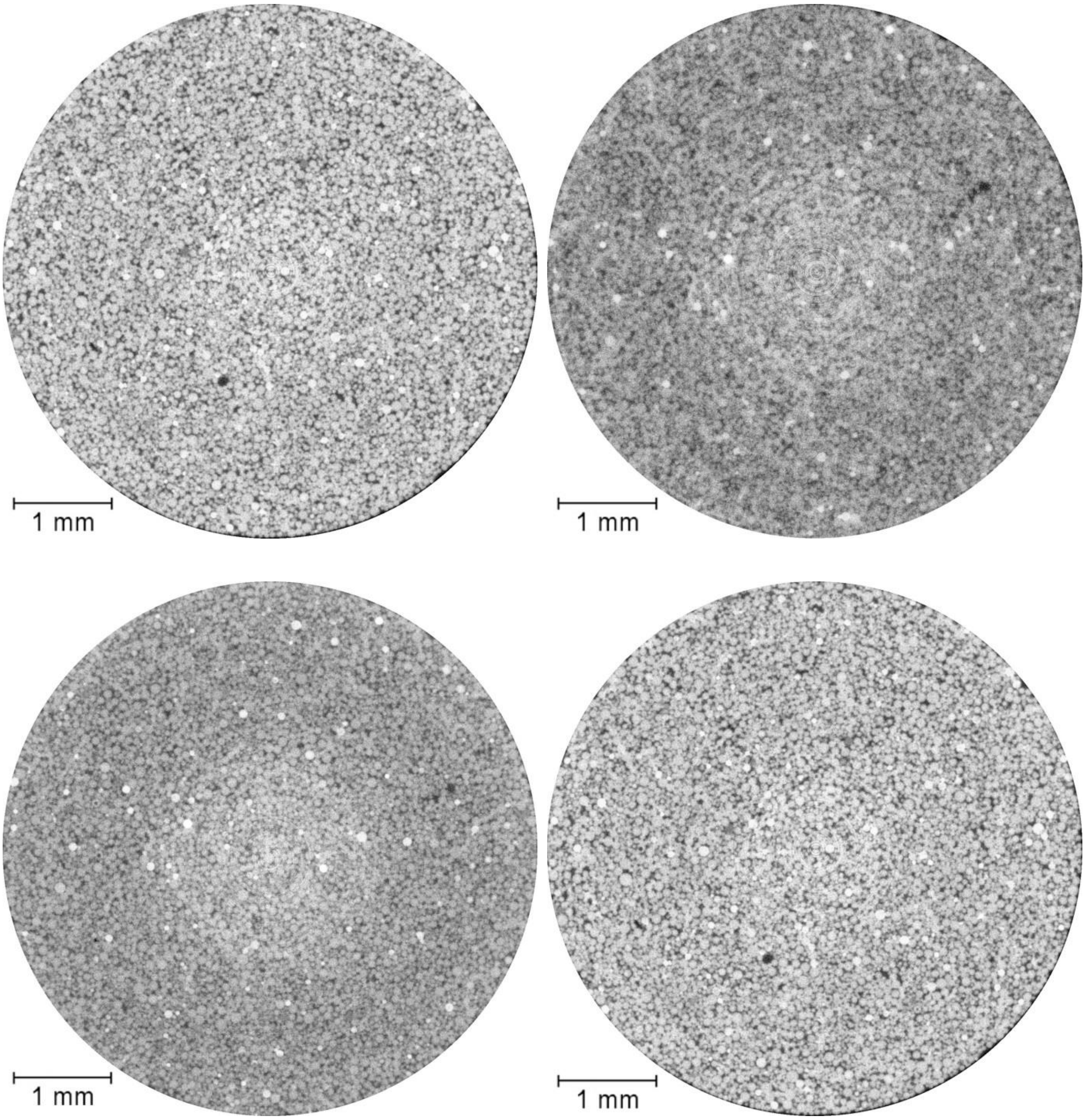

Figure 71: Agarose *intra*-cycle 2D slices at each selected processing stage. **Top-left**: New column. **Top-right**: 1g/L IgG feed exposure. **Bottom-left**: Elution. **Bottom-right**: CIP.

Contrast issues were not overcome despite extensive optimisation efforts to achieve any image quality, with X-ray setup and optimisation tested across all available equipment, target type and primary accelerating voltages available in both reflection and transmission modes for all three materials. Changes to the liquid within the column were also investigated, with typical radiocontrast agents such as barium sulphate and potassium iodide also used without success including attempts to isolate radiocontrast agents inside or outside of the beads to further increase contrast between phases, although this was also found to be ineffective.

Removal of liquid from the column by filling the chamber with air was found to restore visual quality, however was lost again once addition of any liquid phase was performed. This indicated that the combination of liquid and protein within the packed bed was resulting in the loss of contrast, as samples could be imaged with one of these aspects but not both. Further analysis suggested a loss in X-ray peak contrast from 2D radiographs was occurring even when attempting a combination of approaches already discussed, whilst drying columns for imaging was deemed unrepresentative; as the actual structure of the fouled bed would likely be altered from the true state and thus would not be beneficial to do so because measurements made may not accurately depict the true state of each column.

Therefore whilst packed bed investigations for fouling were deemed to be unsuitable for this study due to these issues, alternative approaches were required in order to determine the impact on protein rich feedstocks on chromatography structure in relation to performance. The first approach taken was to perform a digital erosion-dilation of existing, high resolution internal structure of an agarose bead, with **Figure 72** displaying the results [153]. As with the packed bed erosion-dilation test, a higher porosity resulted in a decreased tortuosity factor.

One of the main differences between packed bed and individual bead scale was that an erosion or dilation of internal bead structure had a greater impact on porosity changes compared to the packed bed scale, resulting in fewer steps away from the original geometry. This was due to the spheres undergoing a relatively smaller change compared to thin strands and fibres that comprise the internal bead structure that present a relatively higher surface area for erosion or dilation that resulted in a greater impact. Whilst the exact changes between the most eroded and dilated samples are more difficult to determine compared to shrunk or enlarged spheres, it is clear that there is a considerable disparity in terms of the amount of material present and thus the available pore space and flow paths.

The next step was to determine whether foulant material could be detected on the surface or within individual beads, a topic discussed in **Chapter 1** primarily using electron microscopy and CLSM [12], [24], [62]. Jetted agarose beads in new and fouled forms were selected for individual bead imaging based on foulant impregnation confirmation using CLSM, with jetted samples found to be desirable for imaging due to the more uniform diameters exhibited, with smaller diameters here also useful for achieving the capability for HRES X-ray CT scans to image from the top of the bead to the centre which was of benefit to diffusivity studies, as discussed later. Air drying was selected despite findings in **Chapter 2** to be used alongside counterparts undergoing critical point drying on potential removal of foulant displacement during processing, disrupting the true state of the beads, with the main issue previously encountered of salt layer formation considered unlikely and less of an issue here.

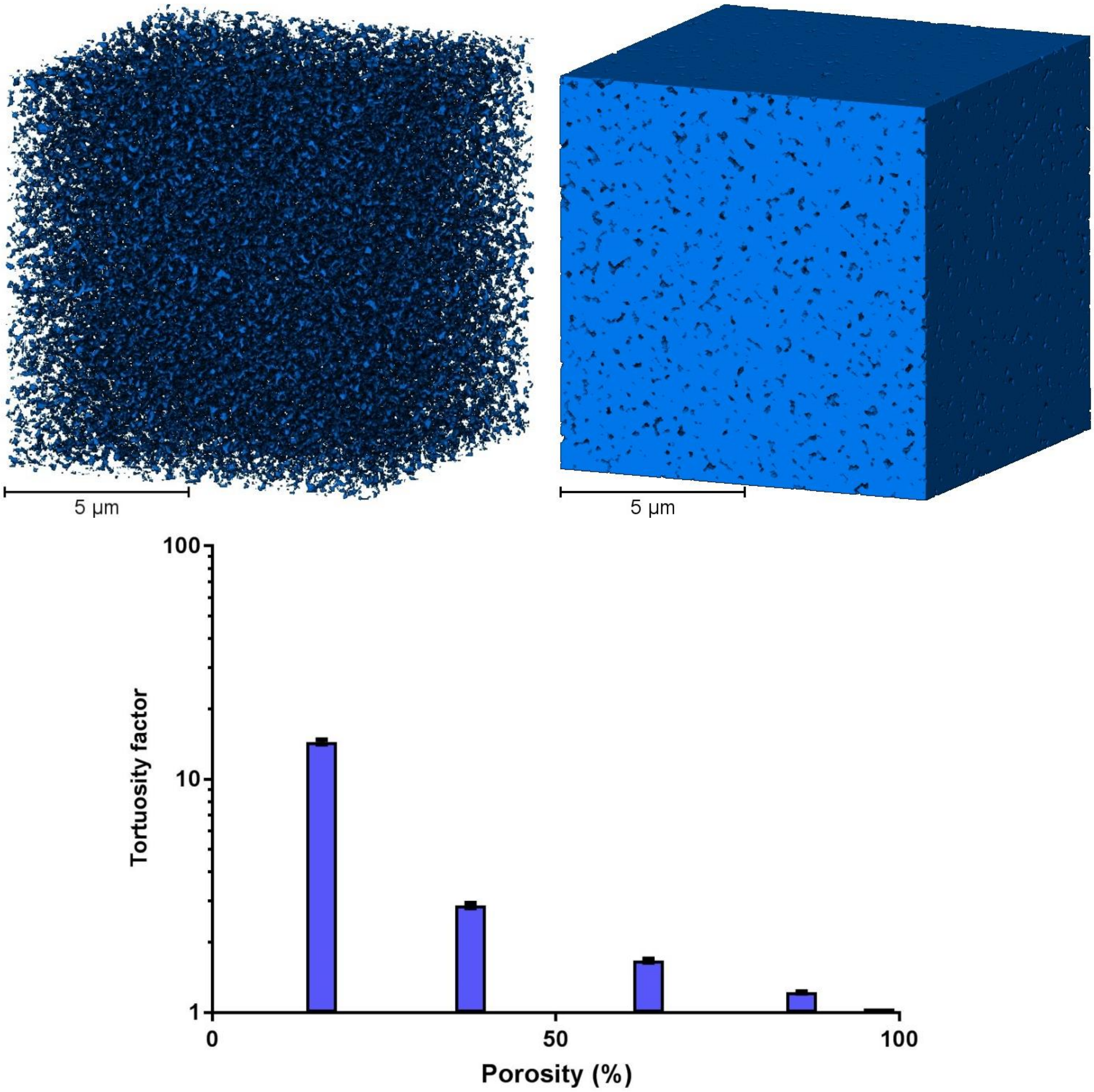

Figure 72: Erosion-dilation of agarose bead structure. **Top-left**: Final eroded bead sub volume with a porosity of 97%. **Top-right**: Final dilated bead sub volume with a porosity of 16%. **Bottom**: Tortuosity factor in relation to different measured porosities for eroded and dilated sub volumes. See **Figure 55** for an unchanged agarose bead 3D render.

Figure 73 displays the results obtained from imaging individual fouled agarose beads using LFOV and HRES approaches that were developed and optimised in **Chapter 3**. The cycled samples were confirmed to be impregnated with material by using CLSM in a manner similar to Jin *et al.* [12]. Despite not being selected for clean beads in **Chapter 2**, air drying was considered the most suitable approach as it was thought that critical point drying could disturb and displace foulants within a bead, although it has been used for an SEM study [65].

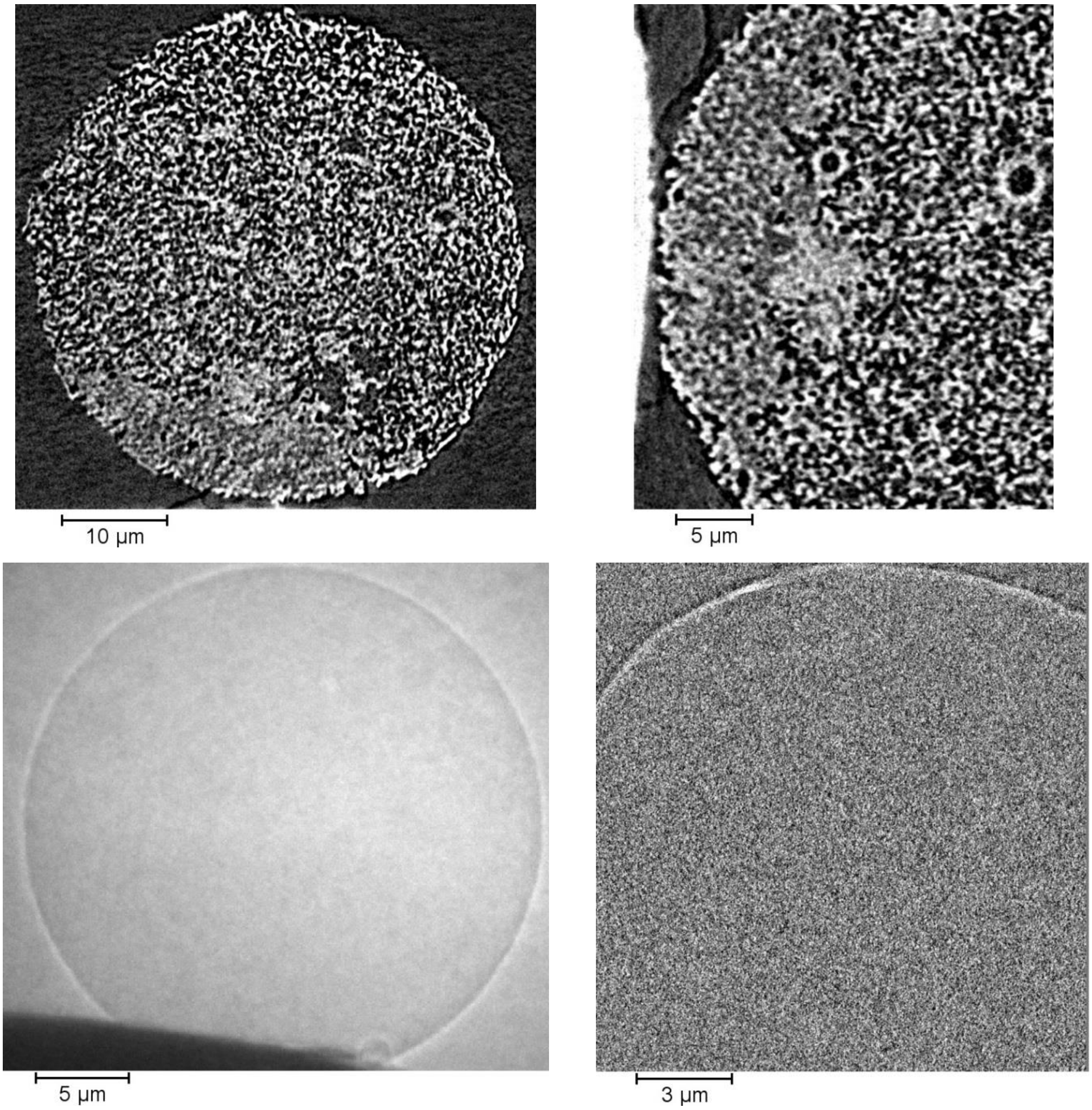

Figure 73: Visualisation of fouled agarose beads from X-ray CT scans. **Top-left**: 2D LFOV slice of a clean Purolite bead. **Top-right**: Boundary between epoxy (left side) and unpenetrated structure of a clean sample. **Bottom-left**: LFOV radiograph of a Purolite bead at 10 IgG cycles. **Bottom-right**: HRES slice of a 10 cycle Purolite bead at 32nm pixel size.

From **Figure 73** the clean Purolite bead could be visualised whilst the cycled sample could not, as was found at the packed bed scale for all materials. However, the epoxy impregnated volume was distinguishable between phases indicating that properties of the foulant materials were resulting in the contrast loss between phases for both LFOV and HRES approaches. If X-ray CT here could have identified phases as with the embedded adhesive, then further investigation would involve imaging and comparing more cycles and states.

As with column scale imaging, X-ray CT was found to be ineffective at visualising the internal structure of chromatography beads that had been cycled using both LFOV and HRES modes, even with further optimisation efforts and reinvestigation of alternative adsorption and Advanced Zernike mode. This was further confirmed when considering other agarose and cellulose beads that had been cycled between 37 and 402 times for mAb processing purposes, where a clean Purolite bead could be successfully imaged in **Figure 73** in the absence of foulants, indicating that loss of contrast would also be of issue at both scales.

This highlighted that despite the potential benefits for using a tomographic approach to compare structure between different states of usage of chromatography packed beds and individual beads due to usage, limitations prevented this from being achieved despite the methodology developed in **Chapters 2** and **3** at both scales. The presence of foulant materials was indicated by the loss in contrast of material to void or buffer phases, however the inherent lack of image quality as a result of foulant presence limited structural investigation at both packed bed and individual bead scales; with a critical point drying approach found to yield the same results for agarose and cellulose samples.

In addition to issues encountered here resulting in visualisation and hence quantification failure, this also prevented the understanding of to what degree the internal bead structure was impregnated to relate to comparative CLSM images and also whether the fibres were coated or entirely plugged. This topic has been investigated at the surface of fouled beads using SEM in various studies [62], [65], [96] for this purpose, but not for the internal 3D structure of chromatography materials that X-ray CT has been capable of for clean beads.

Therefore the results in **Figure 73** highlighted that whilst X-ray CT has been demonstrated to be capable of imaging various chromatography materials at both scales in previous chapters, limitations have prevented investigation of the impact of foulants on the structure of packed beds and individual beads. This highlighted that even if a technique could provide advantages or new approaches compared to previous investigations; such as those using CLSM and electron microscopy in this instance, experimental incompatibility to the study such as the loss in X-ray contrast due to protein presence here can prevent progress.

Whilst the actual structure of fouled beads could not be imaged, using a digital dilation approach to assess the impact of the hypothesised mechanisms of foulant impregnation: thin fibre coating or pore blocking with the number of single pixel dilations being 1 and 3 respectively on HRES volumes. Diffusivity was simulated using the Avizo XLab extension in order to mimic transfer of a 1g/L BSA product through the internal structure of an agarose, cellulose and ceramic beads to compare diffusivity coefficients to literature.

As expected, as further dilations were performed to the structure to represent either coating or pore plugging, the diffusivity coefficient decreased considerably for all materials in **Table 10**, indicating that intended products would have increased difficulty in moving through and saturating the internal bead structure during bind and elute stages. This is independent of other important factors which would further inhibit cycled bead performance which include different material characteristics between bead-fibres and foulant layers which were not accounted for here and transfer limitations to and from ligands such as protein A or which was investigated by Close *et al*. [62] when considering foulants reducing mass transfer.

Compared to the existing literature values presented for chromatography bead diffusivity coefficients, the original HRES volumes analysed were of the same order of magnitude, suggesting that simulation through the 3D internal structure of imaged chromatography beads was accurate in representing diffusion of an intended protein product, also indicating that the 32nm pixel size sufficiently imaged the overall bead structure.

	Diffusivity coefficient (m^2/s), {Geometric porosity (%)}		
	Agarose	Cellulose	Ceramic
Original	(2.3 ± 0.0) x10^{-11}, {63}	(2.4 ± 0.0) x10^{-11}, {66}	(2.4 ± 0.1) x10^{-11}, {63}
Fibre coating	(7.8 ± 0.2) x10^{-12}, {38}	(9.5 ± 0.5) x10^{-12}, {42}	(1.4 ± 0.0) x10^{-11}, {47}
Pore blocking	(9.7 ± 1.0) x10^{-16}, {4}	(4.7 ± 1.6) x10^{-14}, {8}	(1.6 ± 0.1) x10^{-12}, {17}
Literature	(7.8 to 8.0) x10^{-12} [179]	(1.9 to 12) x10^{-12} [171]	(3.6 to 4.7) x10^{-11}* [180]

Table 10: Diffusivity coefficients of agarose, cellulose and ceramic HRES beads. 1g/L of starting BSA concentration was simulated with a bulk diffusivity of 6x10^{-11} m^2/s at 23ºC and pH 7 [181] using a dynamic light scattering method. *Results reported for mAb and not BSA.

This section investigated the use of X-ray CT to visualise and quantify a second commonplace chromatography issue of fouling and lifetime usage. However experimental issues arose at both packed bed and individual bead scales where X-ray contrast was lost in the presence of foulant materials, preventing used samples from being imaged successfully. These issues highlighted that limitations may result in initial objectives to be reconsidered and adapted, where in this case digital alterations via erosion-dilation were used both to hypothetically determine changes to tortuosity factor as well as emulate two potential fouling mechanisms and the impact on simulated diffusivity of a protein product, demonstrating that determined changes to original seed data are viable when actual acquisition is unfeasible.

5.5. Chapter and experimental conclusions

The final aims and objectives of the project were concerned with investigating the impact of commonplace chromatography applications that impact the 3D structure of both scales, requiring the methodology and approaches developed in previous chapters in order to appraise the impact of compression and fouling. In particular, the optimised settings for X-ray CT scanning of various chromatography materials at bead and bed scales, as discussed in **Chapter 3**, where starting studies into compression and fouling without a previously refined imaging strategy and platform would have made imaging attempts more problematic.

In addition to building on the optimisation work from the methodology development chapters for the fouling and compression studies, the structural characteristics quantified based upon tomographic volumes in **Chapter 4** such as porosity were relevant here for measuring changes to bead and bed structure, with both geometric and simulated tortuosity being applied here to determine the change in flow path length due to either real changes to the chromatography system or by enforced digital changes via erosion-dilation of 3D structure.

The results discussed in this chapter for the two studies displayed varying degrees of success, although compromises were required in both cases. Changes to packed bed structure could be visualised and quantified due to flow based compression, however the lack of imaging success when considering fouled and cycled chromatography materials at both scales due to the inherent loss of X-ray contrast in the presence of foulants highlighted that experimental limitations could result in studies requiring changes to aims and objectives, where erosion-dilation was used here as an alternative to viably obtaining real seed data.

This suggested that for future studies, an intertwined approach of utilising digital changes to imaged structures to mimic theoretical alterations to structure may be a suitable approach to quantifying chromatography structural changes based on knowledge of mechanistic actions; whereas the focus of this project has been primarily on directly capturing the real state of beds and beads, with areas of further interest discussed in **Chapter 6**. By using theoretical changes to 3D structure for characterisation experimental limitations can be overcome if the changes to systems are known. Using digital alterations to simulate real changes to bead or bed structure would require considerable mechanistic knowledge to be valid, which may not be fully understood that would suggest directly imaging structural changes would be more suitable. The work presented in the results chapters demonstrate that 3D seed data can be generated based on real beads and beds, providing various avenues for future research.

Chapter 6

Conclusions and future work

6.1. Conclusion

This thesis demonstrated the capabilities of tomographic imaging in the form of X-ray CT and focused ion beam for visualising the detailed 3D structure of chromatography individual beads and packed beds as a basis for quantification of characteristics such as tortuosity, as well as providing insight into industrially relevant processing considerations including packed bed compression. Three common and commercially available bead materials were examined throughout the study: agarose, cellulose and ceramic that enabled comparison between different resins in terms of tomographic structure and subsequent characterisation.

6.1.1 Technique selection and optimisation

The use of tomography for investigations at the individual bead scale built on existing studies using CLSM and electron microscopy that had been applied to enable imaging of the bead internals and the detailed surface structure respectively, however the discussed limitations with each approach prevented the internal structure of beads to be imaged in sufficient detail to resolve the intricate, porous network and features crucial to bead mechanistic function.

Therefore, focused ion beam and X-ray CT were selected to image the internal bead structures given that various literature examples had used these approaches successfully and also performed quantitative characterisation on analogous porous geometry, although studies were often on harder materials than the chromatography sorbents. This required imaging optimisation and sample preparation that had been discussed by Angelo *et al*. [24] as having risk to alter the sample from the true form, although was necessary for imaging, where eventual optimised digital samples could be stored and used for the required purpose.

Sample preparation was found to be more extensive for focused ion beam compared to X-ray CT, which also made using a microtome to perform tomography infeasible due to the combined extensive and destructive preparation with the lack of success when using softer materials such as chromatography sorbents. These issues highlighted some of the major hurdles to overcome for imaging sub-micron samples at a representative quality.

X-ray CT did not require physical sectioning and thus did not destroy the sample, enabling multiple image acquisition for optimisation and comparison, although the shrinkage issues encountered for agarose and cellulose samples due to X-ray exposure presented complications; compromising overall image quality in comparison to ceramic counterparts due to decreased signal to noise ratios so that beam time exposure could be minimised.

Both techniques were able to visualise the internal structure of all three materials, achieving different pixel sizes that were a trade-off with the overall field of view. The impact of the voxel size between techniques was an important comparative issue as to whether a better pixel size was needed to resolve the smallest features within the structure, or this was unnecessary and needlessly sacrificing the overall field of view; which would be indicated by both visual differences in 2D slices and 3D renders in addition to quantitative measures.

6.1.2 Quantification of chromatographic structure

The pixel sizes achieved at individual bead scale for X-ray CT are currently the best available, where further improvements via new and improved technology would be beneficial to porosity and pore size measurements but unlikely to impact tortuosity. The conservation of the larger, major pore networks was found to be more prevalent for characteristics such as overall porosity and tortuosity, however high resolution X-ray CT and FIB determined a significantly higher surface area to volume ratio and smaller average pore diameters, demonstrating that absolute resolution is more important to some factors but not to others.

This indicated that selection of tomographic imaging technique employed should depend upon the desired end-goal of quantification; as higher resolution approaches would enable finer features to be identified and so ascertain a more accurate measurement of intricate pore sizes that are closer to values suggested using orthogonal techniques such as inverse size exclusion chromatography and BET. Albeit the porosity values obtained even with the higher resolution X-ray CT and FIB microscopy were still found to be ~10-15% lower than expected, where potential pixel size improvements were not available.

However, the additional processing stages required for focused ion beam etc. in order to achieve a high resolution may not be necessary if only the the overall structure is required for imaging and quantification, as demonstrated in the cases of porosity and tortuosity where the smallest parts of the geometry were not found to have any considerable impact. Other benefits of reduced pixel size X-ray CT included reduced preparation as well as being capable of imaging an entire reasonably sized chromatography bead, rather than sub-sections required for higher resolution counterparts that were also more time intensive.

Versatility of X-ray CT was further demonstrated when commercially available chromatography pre-packed columns of the three materials were imaged in detail sufficient to resolve each ~50µm bead after optimisation. This was performed in order to resolve the beads within the bed without interference, where other techniques were deemed unsuitable and previous literature attempts relied on tracers and markers using scaled-down versions.

By achieving high-quality imaging of a real column, determination of known phenomenon such as wall effects that are indicated by differences in packing density between the edge and centre of a packed bed were quantitatively verified via porosity readings from the 3D volumes imaged using X-ray CT. Producing representative packed bed geometry enabled other important factors that relate to column performance to be investigated, such as the presence of channels that impact axial dispersion of the mobile phase and mass transfer to the beads could be probed. However, no serious incidents of channelling or general bed voids were found, which was supported by the high packing density indicated by surface area to volume ratio values for all three materials investigated compared to literature, where if possible would be applied to large scale, industrial packed bed chromatography research.

6.1.3 Compression and fouling applications

The application of distance maps, flux-density grids and geometric overlays were useful for both producing visual comparisons between materials and imaging approaches, for example between X-ray CT images of beads at different pixel sizes. Overlays and comparisons were particularly insightful when investigating changes to packed bed structure relating to industrial challenges such as compression and life-time usage. For example, directly comparing 2D slices and 3D meshes before, during and after compression due to flow, based upon previously established optimised imaging conditions that had to be discerned using an approach that found different column materials behaviours under extreme fluxes.

The findings that the fast-flow agarose and ceramic pre-packed beds did not structurally change even when excessive flow was applied demonstrated both the strength of the individual beads as well as the high packing density, highlighting the quality of 1mL pre-packed beds which eliminate the need for manual packing and thus additional variation attributed to the skill of an operator. Cellulose packed beds were found to also resist compression within the conditions set by the vendor, however X-ray CT was able to visualise changes to the packed bed when excessive and unrepresentative flowrates, again enabling visual and quantitative measurements and comparisons to be made.

The main limitations associated with the compression study included the fact that dynamic imaging of packed beds was only possible at the macro scale due to the long scan-time requirements for performing high quality CT that could resolve individual beads. If this was possible, then a more direct frame-by-frame comparison of detailed packed bed analysis under compression could be performed. Scan quality, particularly during compression, was also found to be compromised likely due to the flow of liquid during imaging particularly at high flow rates, as well as the reduced scan time required to logistically perform the before, during and after X-ray CT runs. Whilst the number of captured frames remained the same, ring artefacts occurred as part of the compromise that negatively impacted the tomographic quality, particularly in the centre of imaged volumes.

Imaging of packed beds was also applied to relate the degradation of chromatography column performance due to usage to structural changes both at the packed bed and individual bead scales, with an *intra*-cycle study used as a proof of concept. It was found that the presence of protein resulted in a loss of contrast when loaded, before returning to original quality once eluted and the column cleaned. Protein causing this issue was of particular issue when attempting to image protein-A columns such as Purolite, MabSelect SuRe and Kaneka KanCapA variants, no bead definition could be achieved at either scale.

This prevented capture column evaluation of structural integrity using X-ray CT which would have been of great interest as a tool for furthering understanding of lifecycle fouling as this type of column would experience the dirtiest feed over a lifetime. If this could have been overcome the industrially applications investigated here and the variants that could have been investigated, however this analysis was found to be infeasible with available technology. Overall, tomographic approaches such as X-ray CT and FIB have been demonstrated as effective tools for chromatography structure visualisation and characterisation that enable observation of internal geometry of packed beds and beads. Column volumes were also intentionally restricted to 1mL as larger packed beds would result in pixel size loss and overall image quality which would detrimentally impact quantification.

Further research and development could enable the discussed issues to be overcome, allowing various opportunities for continuation of tomographic research for chromatography. Overall this research developed the use of 3D imaging techniques for visualisation of chromatography bead and packed bed structure that had previously been limited to approximate models, low resolution CLSM or surface restrictions for EM imaging. This enabled quantification of aspects such as porosity, tortuosity and pore sizes at both scales using three commercially relevant materials, in addition to further exploring industrially relevant topics such as compression and fouling, providing a platform for future research.

6.2. Research implementation and impact

The most suitable roles for X-ray CT, and to a lesser extend FIB, in the bioprocessing and chromatography sector is quality control checks, product development and failure analysis. These aspects fit more into industrial application as a supporting technique rather than commercialisation, as having an X-ray CT system or FIB for external contracts would require competition with established institutes such as the London Centre for Nanotechnology which already provides FIB services amongst others, or UCL's EIL X-ray CT suite or the manufacturer part time use provided as a service by Nikon charging per scan or hour.

If one was to approach commercialisation as a service for scanning and reconstructing various items, the capital outlay of purchasing one or multiple X-ray CT systems would dominate cost requirements compared to the running and servicing of the systems, requiring large investment up-front unless sufficient loans could be secured, although large monthly repayments would require regular use of the system to cover costs and would be in jeopardy if a system were unavailable due to failures, which as experienced here was not uncommon.

Whilst a service-based company could specialise in imaging chromatography materials or bioprocessing items using the approaches detailed in this thesis, considering items in this field only would restrict access to other areas of the market. For example battery development for novel technologies or quality control scans on high value and precision items, such as pieces of high specification equipment for an aircraft or racing car. However, imaging these materials would likely require different imaging conditions and so would require optimisation and expertise, albeit this could increase target market size and so the depth and breadth of projects that could be undertaken would need to be discussed with key party members in order to ensure sufficient market capture without overstretching.

6.2.1. Potential company considerations

For companies or institutions that require high-detail 3D imaging of their materials, for example chromatography columns and beads, then either purchasing systems or paying for scans are the two main options. By using an external contractor, then the business can benefit from the general expertise of the operators in terms of achieving high quality imaging relatively quickly, which could also include doctoral or postdoctoral students to be included in a project if a university institution was to be used or collaborated with, such as in this project.

However, disadvantages do exist when using this approach which is most relevant if a large number of scans or ongoing work is required. Firstly extensive use would require ongoing cost and so an economic value proposition should be carefully considered to determine whether external contracting versus purchasing of in-house equipment is most suitable.

Dependence upon a contractor could also result in long lead times if their schedule is busy or has been affected by equipment failure issues and servicing requirements that could delay other parts of a product development timeline, missing important release dates. Contracting scans out could also cause confidentiality issues to arise in case a competitor was also performing similar work, although would not be as much of a problem if an in-house scanner was acquired and the relevant employees did not join a rival company.

However it would also require extensive staff training or hiring of someone who was already proficient, albeit downtime and servicing would always be an inherent part of maintaining complicated equipment such as X-ray CT or FIB systems that could be covered by using an external company to cover any immediate deficits; depending on whether the company could justify heavy capital expenditure by achieving a continuous, high productivity usage.

Once the in-house versus contractor decision has been resolved for imaging bioprocessing based materials such as chromatography columns, then there are several areas identified as potentially beneficial to use tomographic representation for both visual and quantitative analysis where required in relation to chromatography and the bioprocessing discipline.

The first and simplest is for fault and failure analysis, where there has been a clear issue with a product, for example a filter unit not clearing the required size of debris, leaving a feed stream that would cause considerable fouling at the capture chromatography stage, leading to both step and lifetime performance loss that would be undesirable to manufacturers. This specific example would require foulants to be easier identified and imaged to a high standard, where in **Chapter 5** this was found to be inherently difficult.

6.3. Future work

The use of X-ray CT and FIB was suitable for characterising the structure of chromatography packed beds and individual beads, however there were limitations that would be of interest to further investigate. Firstly issues with microtomy combined with the success of the similar FIB technique resulted in any microtome attempts ceased to being pursued. This was in part due to sample preparation, so future efforts could be directed into using microtomy to perform tomography, particularly with serial block face methods. SBFSEM would be more desirable than conventional microtomy as the degree of automation would allow for comparable resolution whilst reducing the labour intensive processing.

This could be achieved by attaining a better pixel size, although as previously discussed there is a trade-off that would either compromise field of view or time spent milling and imaging that could have also been further improved for FIB. Alternative systems to the one used in the study may be more appropriate if this area was to be pursued, for example a Zeiss Orion NanoFab that enables finer cutting than the equipment used than the results presented here but does take considerably longer to process a volume of interest.

Advancements to imaging chromatography bead using either FIB or microtomy approaches would enable the smallest features within the internal structure to image at higher quality and thus more representative, particularly when combined with improvements to sample preparation and epoxy impregnation likely to be important. When working with soft materials such as agarose and cellulose, sample preparation and handling are of particular interest and require serious consideration for any future research endeavours. Whilst attaining a very high resolution is one of the key desirable traits to provide improvement to bead imaging once the technology is available, there are other important factors to consider that would also provide a clear benefit. For example, an issue throughout X-ray CT imaging was that signal to noise ratios were often poor for the agarose and cellulose samples relative to the ceramic, particularly when considering other industrially relevant issues such as shrinkage.

Other X-ray modes such as advanced Zernike were not found to be successful for improving image quality, however the potential benefits of using this approach include superior phase contrast between bead and void space and also lower count requirements that would reduce scan time and thus mitigate shrinkage effects. Therefore once advancements are made to the technology that make it feasible for high-quality imaging using alternative modes, then improvements in terms of quality and reducing the number of compromises required for soft bead scanning could be achieved without being constrained by the current limitations.

Imaging using other approaches could be investigated, for example using X-ray diffraction in order to study the ligand structure in relation to the current scales being investigated. At the packed bed scale, the beads could clearly be seen using the current capabilities and so resolution issues when imaging 1mL pre-packed beds was not a major requirement for future work, although any improvements would be beneficial particularly if bead-bead boundaries could be better clarified that cause image processing problems.

An interesting area for future work would be the capability for imaging larger beds closer to industrial scale, as the current trade-off between pixel size and field of view prevented any successful attempts on columns with a larger diameter, as well as signal loss in a larger object. This may be more achievable using an alternative system such as the Zeiss Xradia Versa 520 used in a comparative study as a better pixel size when imaging the same columns when examining 1mL pre-packed beds, so by extension could counteract the voxel size losses experienced here that limited.

However drawbacks experiencing soft-material beads such as agarose and cellulose may not be feasible and so a recommended start point would be ceramic or relevant materials using similar X-ray conditions to those determined in this project as a basis for larger scale imaging optimisation efforts. One of the most important goals to achieve in future work would be the successful visualisation of protein based resins which includes many commercially important affinity ligands such as protein A and also the capability to determine state of fouling for all relevant samples that are either protein based or saturated with feed.

Many attempts in this project included further X-ray CT condition optimisation in conjunction with radiocontrast agent use to achieve any imaging definition, but with no real progress made this presented a major hurdle for both imaging very important resin types as well as any actual lifetime studies. If this could be overcome then several avenues of application based tomography research on affinity based materials could be undertaken. However, future studies must consider the implications of directly interfering with the packed beds if required such as using radiocontrast agents. This could lead to unwanted changes that misrepresent the volume of interest, particularly in the case of where external influences for applications such as compression, fouling or other materials such as filters being measured.

Given that X-ray CT is an effective method of non-invasive tomographic imaging, then by requiring introduction of extra components into the sample then this defeats one of the main advantages of the technique. If this is required for successful future imaging, then a decision as to what degree of interference is acceptable in the pursuit of results would need to be considered or whether an alternative approach such as FIB or SBFSEM would be suitable.

Overall, there are several aspects of imaging chromatography systems using X-ray CT and electron microscopy approaches that could be improved in the future to produce more representative reconstructions of individual beads and packed beds. These are often obvious such as improved resolution, field of view or employing an orthogonal imaging technique, which will likely be overcome with improvements to the existing technology when improved pixel sizes are achievable, or a greater degree of versatility can be attained, particularly when considering the issues provided by the softer bead materials.

Areas of future research interest primarily involve expanding upon the applications of compression and fouling that have been investigated using X-ray CT at both scales. Whilst dynamic compression imaging is not currently feasible due to the long acquisition periods required, the use of before, during and after scans proved an effective approach to directly compare structure due to changes and should be implemented in further investigations. Detection of tracer flow throughout the column during compression would be an area of interest that was not achieved here due to masking and quality loss when scanning column whilst flow was occurring, but would enable several interesting areas for research.

Wall effects and the differences in packing density have been identified in this project and so building upon these findings in combination with the flow-based compression study could lead to mobile phase flow-path imaging and interactions. Whilst current scan-times would make this difficult, improved CT systems in combination with the right radioactive tracers through a packed bed could provide visual data to compare with theoretical models. Axial and radial dispersion throughout the column and any disparities due to known structural phenomena would also be of interest to investigate if scan times could capture this.

Relation of HETP, peak asymmetry and other metrics for measuring column packing efficiency to the tomographic structure of columns would also be useful to contextualise results, further highlighting a potential route for X-ray CT to be used in a QA/QC role. Whilst direct relation of these packed bed characteristics may be difficult, quantification of tomographic aspects such as packing density may lead to further development where a representative comparison could be made. The flow path based visualisation demonstrated in this project would also have a profound impact on packing understanding, however would require further development and likely collaboration with other methods to be effective.

For future flow-based studies at the individual bead scale, one of the main hurdles to performing any experiments is the logistics of inserting liquid into the bead whilst imaging at the same time; although the potential to visualise diffusion through the porous structure would allow a greater degree of understanding compared to current CLSM research which cannot image the detailed internal network, where MRI may be suitable for packed beds.

Wet beads were imaged during this project but were found to suffer from quality loss compared to dry beads, so this would need to be overcome in a similar manner to the issues already discussed at the packed bed scale. If imaging of diffusion within beads could be achieved; requiring considerable experimental development for both bead preparation and X-ray CT scanning conditions, then the next step would be to use the diffusional flow-path data as a basis for accurate transfer models between the mobile phase and ligand for greater understanding of the mechanistic actions relating to the internal bead structure. Further aforementioned improvement to pixel size would be desirable, however X-ray CT would not be capable of resolving the actual ligand and so other techniques and studies would have to be done to compliment this research, for example neutron scattering.

6.3.1. Continued chromatography applications

The major application for continued future research would be lifetime column usage if the previously discussed hurdles could be overcome. Assuming that this could be achieved without compromising sample integrity, then several areas of interest could be investigated relating structural characteristics visualised by X-ray CT to changes in performance to a column as it is repeatedly used. Evaluation of quantitative measures used in this project such as porosity and tortuosity due to flow path restriction could be used as indicators for change within the packed bed over time for various column types or conditions applied.

This would be of interest to both academia and industry for improving understanding of the fouling mechanisms *in-situ* and thus enabling development of process and product, based upon the results obtained from tomographic results. Optimisation of feed streams, cleaning regimes and sorbent usage would have been performed in the project if possible and so would be the most advisable metrics to use for improving packed bed quality of life for bioprocessing purposes. The designed approach in this study before abandonment due to issues would have allowed direct comparison between results at various stages, where column imaging would be staggered at set intervals of column cycles up to expiry.

For example, imaging a new column at the top and bottom before use and every 10 identical cycles until a set-point determined either by manufacturers recommendation or performance cut-off had been reached. By repeating this with different types of columns, feed or cleaning conditions applied then future research could provide further insight into structural changes to packed beds when used with conditions that greater resemble industrial manufacturing.

This study was also intended to increasingly include individual bead scans once previously discussed logistical obstacles could be overcome to observe the foulant within the detailed, internal porous structure to build upon existing CLSM and SEM studies. The capability for X-ray CT to visualise chromatography structure at both scales should be utilised in all future studies where relevant, as it would be expected that both bead and bed information for the research area of choice would be beneficial compared to being restricted to one scale.

Further examination of continuous chromatography and simulated moving bed technology using similar approaches already discussed and demonstrated to use X-ray CT as an effective tool for analysis and indication of performance. This will be of particular relevance as the bioprocessing industry beings to adopt and implement continuous chromatography alongside or to replace conventional batch chromatography in patented bioprocesses for industrial production, for example monoclonal antibodies.

The comparisons made in this project in terms of X-ray CT between batch and continuous chromatography beds in relation to life-cycle usage could be used as a template alongside conventional methods of evaluation for future investigations performed by industrial entities that want to determine the most suitable approach for using continuous systems in a bioprocess compared to an existing batch chromatography step.

Whilst X-ray CT has been considered the most suitable technique for the majority of the suggested cases, alternative imaging methods may be more suitable for certain applications. For example, if a very high resolution is required for imaging a filter section with integral pore features smaller than 32 nm then FIB would be recommended due to the sub-nanometre pixel size achievable whilst still imaging a 3D structure rather than just the surface.

However, X-ray CT has been demonstrated to be effective and versatile for representing chromatography packed bed and individual bead structure, considering several industrially relevant applications when using commercially available pre-packed beds. This would be the recommended technique of choice for future investigations due to the non-destructive and intrusive nature which is also capable of providing geometries that can be used to visualise and quantify key characteristics based upon the work presented in this project.

Therefore, the use of X-ray CT and other tomographic approaches provides a lot of potential for both academic and industrial future research by using the optimised imaging approach and findings to represent packed beds and individual beads at a high quality. The compression and fouling studies also provide a platform for further investigation into key chromatography applications, which could implement software based modelling to further aid understanding of structural behaviour of beads and beds in relation to existing literature.

References

Permission has been granted to use images under creative common or RightsLink® licences

[1] A. Kumar and A. Awasthi, *Bioseparations Engineering*, no. June. New Delhi: I. K. International Pvt Ltd, 2009. 9780444504418.

[2] M. Flickinger, “Encyclopedia of industrial biotechnology: bioprocess, bioseparation, and cell technology,” *Choice Rev. Online*, vol. 48, no. 03, pp. 48–1218–48–1218, Nov. 2010. 10.5860/CHOICE.48-1218.

[3] M. Flickinger and S. Drew, *Encyclopaedia of Bioprocess Technology*. John Wiley and Sons, 2014. ISBN: 0471138223.

[4] J. Critterden, R. Trussell, D. Hand, K. Howe, and G. Tchobanoglous, *Water Treatment (Chapter 17)*. 2012, pp. 1335–1414. ISBN: 978-0-470-40539-0.

[5] T. Scheper, J. Zhong, F. Bai, and W. Zhang, *Biotechnology in China*. 2009. ISBN: 0724-6145.

[6] E. Polykarpou, “Optimisation of Chromatography for Downstream Protein Processing,” University College London Thesis, 2011.

[7] R. D. Simoni, R. L. Hill, and M. Vaughan, “The Use of Chromatography in Biochemistry,” *Biol. Chem.*, 2002. PMID: 12354818.

[8] T. M. Przybycien, N. S. Pujar, and L. M. Steele, “Alternative bioseparation operations: life beyond packed-bed chromatography.,” *Curr. Opin. Biotechnol.*, vol. 15, no. 5, pp. 469–78, Oct. 2004. 10.1016/j.copbio.2004.08.008.

[9] P. M. Doran, *Bioprocess Engineering Principles*, no. May. Elsevier, 1995. ISBN: 978-0-12-220855-3.

[10] J. Bailey and D. Ollis, *Biochemical Engineering Fundamentals*. McGraw-Hill Science, 1986. ISBN: 0070032122.

[11] R. Ghosh, *Principles of Bioseparations Engineering*. World Scientific, 2006. ISBN: 981-256-892-1.

[12] J. Jin, S. Chhatre, N. J. Titchener-Hooker, and D. G. Bracewell, “Evaluation of the impact of lipid fouling during the chromatographic purification of virus-like particles from Saccharomyces cerevisiae,” *J. Chem. Technol. Biotechnol.*, no. June 2009, 2009. 10.1002/jctb.2290.

[13] D. E. Cherrak and G. Guiochon, “Phenomenological study of the bed–wall friction in axially compressed packed chromatographic columns,” *J. Chromatogr. A*, vol. 911, no. 2, pp. 147–166, Mar. 2001. 10.1016/S0021-9673(01)00518-0.

[14] S. C. Siu, H. Baldascini, D. C. Hearle, M. Hoare, and N. J. Titchener-Hooker, “Effect of fouling on the capacity and breakthrough characteristics of a packed bed ion exchange chromatography column.,” *Bioprocess Biosyst. Eng.*, vol. 28, no. 6, pp. 405–14, May 2006. 10.1007/s00449-006-0046-3.

[15] A. A. Shukla and J. Thömmes, “Recent advances in large-scale production of monoclonal antibodies and related proteins.,” *Trends Biotechnol.*, vol. 28, no. 5, pp. 253–61, May 2010. 10.1016/j.tibtech.2010.02.001.

[16] S. C. Siu, C. Chia, Y. Mok, and P. Pattnaik, “Packing of large-scale chromatography columns with irregularly shaped glass based resins using a stop-flow method.,” *Biotechnol. Prog.*, vol. 30, no. 6, pp. 1319–25, 2014. 10.1002/btpr.1962.

[17] S. S. Farid, “Process economics of industrial monoclonal antibody manufacture.,” *J. Chromatogr. B. Analyt. Technol. Biomed. Life Sci.*, vol. 848, no. 1, pp. 8–18, Mar. 2007. 10.1016/j.jchromb.2006.07.037.

[18] N. Ioannidis, “Manufacturing of Agarose-based Chromatographic media with controlled pore and particle size,” University of Birmingham Thesis, 2009.

[19] R. Hahn, P. Bauerhansl, K. Shimahara, C. Wizniewski, A. Tscheliessnig, and A. Jungbauer, “Comparison of protein A affinity sorbents II. Mass transfer properties.,” *J. Chromatogr. A*, vol. 1093, no. 1–2, pp. 98–110, Nov. 2005. 10.1016/j.chroma.2005.07.050.

[20] R. N. Keener, J. E. Maneval, K. C. E. Ostergren, and E. J. Fernandez, “Mechanical deformation of compressible chromatographic columns.,” *Biotechnol. Prog.*, vol. 18, no. 3, pp. 587–96, 2002. 10.1021/bp020051v.

[21] B. J. Stanley, M. Sarker, and G. Guiochon, “Consolidation of the packing material in chromatographic columns under dynamic axial compression IV. Mechanical properties of some packing materials,” *J. Chromatogr. A*, vol. 741, no. 2, pp. 175–184, Aug. 1996. 10.1016/0021-9673(96)00163-X.

[22] D. Skoob, *Principles of Instrumental Analysis*, vol. 152. 2006, p. 314. 10.1016/S0003-2670(00)84936-3.

[23] I. Tatárová, M. Gramblicka, M. Antosová, and M. Polakovic, “Characterization of pore structure of chromatographic adsorbents employed in separation of monoclonal antibodies using size-exclusion techniques.,” *J. Chromatogr. A*, vol. 1193, no. 1–2, pp. 129–35, Jun. 2008. 10.1016/j.chroma.2008.04.023.

[24] J. M. Angelo, A. Cvetkovic, R. Gantier, and A. M. Lenhoff, “Characterization of cross-linked cellulosic ion-exchange adsorbents: 1. Structural properties.,” *J. Chromatogr. A*, vol. 1319, pp. 46–56, Dec. 2013. 10.1016/j.chroma.2013.10.003.

[25] P. DePhillips and A. M. Lenhoff, “Pore size distributions of cation-exchange adsorbents determined by inverse size-exclusion chromatography,” *J. Chromatogr. A*, vol. 883, no. 1–2, pp. 39–54, Jun. 2000. 10.1016/S0021-9673(00)00420-9.

[26] A. M. Striegel, W. W. Yau, J. J. Kirkland, and D. D. Bly, *Modern size-exclusion liquid chromatography*. New Jersey: John Wiley and Sons, 2009. 10.1002/9780470442876.

[27] D. V Mccalley, “A study of column equilibration time in hydrophilic interaction chromatography,” *J. Chromatogr. A*, vol. 1554, pp. 61–70, 2018. 10.1016/j.chroma.2018.04.016.

[28] R. Tran, “Evaluation of Challenges to the Ubiquitous Nature of Chromatography,” University Colege London Thesis, 2011.

[29] S. Großhans, G. Wang, C. Fischer, and J. Hubbuch, “An integrated precipitation and ion-exchange chromatography process for antibody manufacturing : Process development strategy and continuous chromatography exploration,” *J. Chromatogr. A*, vol. 1533, pp. 66–76, 2018. 10.1016/j.chroma.2017.12.013.

[30] “Ceramic HyperD ® F Ion Exchange Chromatography Sorbents (Q , S , DEAE , and CM) Description,” *Pall Life Sciences*, 2014. [Online]. Available: http://www.pall.com/main/laboratory/product.page?id=35865. [Accessed: 27-Jan-2018].

[31] A. Lees, A. Topping, A. Razzaq, K. Reiter, and A. Acosta, “Purifying a Recalcitrant Therapeutic Recombinant Protein with a Mixed- Mode Chromatography Sorbent,” *Bioprocess Tech.*, pp. 1–5, 2009. https://www.researchgate.net/publication/237118773_Purifying_a_Recalcitrant_Therapeutic_Recombinant_Protein_with_a_Mixed_Mode_Chromatography_Sorbent

[32] C. Jiang, J. Liu, M. Rubacha, and A. A Shukla, “A mechanistic study of Protein A chromatography resin lifetime.,” *J. Chromatogr. A*, vol. 1216, no. 31, pp. 5849–55, Jul. 2009. 10.1016/j.chroma.2009.06.013.

[33] S. Farid, “Economic Drivers and Trade-Offs in Antibody Purification Processes,” *BioPharm Int.*, pp. 38–42, 2009. http://www.processdevelopmentforum.com/articles/economic-drivers-and-trade-offs-in-antibody-purification-processes/

[34] N. J. Titchener-Hooker, P. Dunnill, and M. Hoare, “Micro biochemical engineering to accelerate the design of industrial-scale downstream processes for biopharmaceutical proteins.,” *Biotechnol. Bioeng.*, vol. 100, no. 3, pp. 473–87, Jun. 2008. 10.1002/bit.21788.

[35] A. J. Weinberg, S. Zhang, and A. Kirkby, “Chemical modification of Protein A chromatography ligands with polyethylene glycol. II: Effects on resin robustness and process selectivity,” *J. Chromatogr. A*, 2018. 10.1016/j.chroma.2018.03.011.

[36] A. J. Weinberg, S. Zhang, G. Crews, G. Carta, and T. Przybycien, “Chemical modification of Protein A chromatography ligands with polyetyhlene glycol. 1: Effects on IgG adsorption equilibrium, kinetics and transport,” *J. Chromatogr. A*, 2018. 10.1016/j.chroma.2018.02.024

[37] S. Hober, K. Nord, and M. Linhult, “Protein A chromatography for antibody purification.,” *J. Chromatogr. B. Analyt. Technol. Biomed. Life Sci.*, vol. 848, no. 1, pp. 40–7, Mar. 2007. 10.1016/j.jchromb.2006.09.030.

[38] S. Sommerfeld and J. Strube, “Challenges in biotechnology production—generic processes and process optimization for monoclonal antibodies,” *Chem. Eng. Process. Process Intensif.*, vol. 44, no. 10, pp. 1123–1137, Oct. 2005. 10.1016/j.cep.2005.03.006.

[39] B. Sheth, “Characterisation of chromatography adsorbents for antibody bioprocessing,” University College London Thesis, 2009.

[40] L. Grilo, M. Mateus, M. R. Aires-barros, and A. M. Azevedo, “Monoclonal Antibodies Production Platforms : An Opportunity Study of a Non-Protein-A Chromatographic Platform Based on Process Economics Ant,” vol. 1700260, pp. 1–10, 2017. 10.1002/biot.201700260.

[41] S. Oshinbolu, L. J. Wilson, W. Lewis, R. Shah, and D. G. Bracewell, “Trends in Analytical Chemistry Measurement of impurities to support process development and manufacture of biopharmaceuticals,” *Trends Anal. Chem.*, vol. 101, pp. 120–128, 2018. 10.1016/j.trac.2017.10.026.

[42] S. R. Aggarwal, “What ’ s fueling the biotech engine — 2012 to 2013,” *Nat. Am.*, vol. 32, no. 1, 2014. 10.1038/nbt.2794.

[43] M. Herper, “The world ’ s most expensive drugs,” 2010. [Online]. Available: https://www.forbes.com/2010/02/19/expensive-drugs-cost-business-healthcare-rare-diseases.

[44] G. E. Healthcare, “Strategies for Protein Purification Handbook,” *GE Healthcare*, 2010. [Online]. Available: http://wolfson.huji.ac.il/purification/PDF/Others/GE_StratProtPurificHanbook.pdf. [Accessed: 04-Jan-2018].

[45] EMEA, “Synagis Scientific Discussion,” 2004. [Online]. Available: http://www.ema.europa.eu/docs/en_GB/document_library/EPAR_-_Scientific_Discussion/human/000257/WC500056731.pdf. [Accessed: 07-Jan-2018].

[46] F. W. Moler, R. W. Brown, R. G. Faix, and J. R. Gilsdorf, “Comments on Palivizumab (Synagis),” *Pediatrics*, vol. 103, no. 2, pp. 495–496, Feb. 1999. 10.1542/peds.103.2.495.

[47] Janssen, “New Zealand Data Sheet Remicade® Powder for Injection,” 2014. [Online]. Available: http://www.medsafe.govt.nz/profs/datasheet/r/Remicadeinj.pdf. [Accessed: 09-Jan-2018].

[48] B. A. S. Rathore, P. Latham, O. Kaltenbrunner, J. Curling, and H. Levine, “Costing Issues in the Production of Biopharmaceuticals,” *BioPharm Int.*, 2004. ttps://pdfs.semanticscholar.org/e987/e88397cb14b46adbe626838d2d1bfb5786c1.pdf

[49] S. Gerontas, M. Asplund, R. Hjorth, and D. G. Bracewell, “Integration of scale-down experimentation and general rate modelling to predict manufacturing scale chromatographic separations.,” *J. Chromatogr. A*, vol. 1217, no. 44, pp. 6917–26, Oct. 2010. 10.1016/j.chroma.2010.08.063.

[50] L. Konieczna, M. Belka, M. Oko, and M. Pyszka, “New 3D-printed sorbent for extraction of steroids from human plasma preceding LC – MS analysis,” *J. Chromatogr. A*, vol. 1545, pp. 1–11, 2018. 10.1016/j.chroma.2018.02.040.

[51] Y. Chen, W. Zhang, Y. Zhang, Z. Deng, W. Zhao, H. Du, X. Ma, D. Yin, F. Xie, Y. Chen, and S. Zhang, “In situ preparation of core – shell magnetic porous aromatic framework nanoparticles for mixed – mode solid – phase extraction of trace multitarget analytes,” *J. Chromatogr. A*, vol. 1556, pp. 1–9, 2018. 10.1016/j.chroma.2018.04.039.

[52] R. Hahn, R. Schlegel, and A. Jungbauer, “Comparison of protein A affinity sorbents,” *J. Chromatogr. B. Analyt. Technol. Biomed. Life Sci.*, vol. 790, pp. 35–51, 2003. 10.1016/j.chroma.2005.07.050.

[53] S. Schweiger and A. Jungbauer, “Scalability of pre-packed preparative chromatography columns with different diameters and lengths taking into account extra column effects,” *J. Chromatogr. A*, vol. 1537, pp. 66–74, 2018. 10.1016/j.chroma.2018.01.022.

[54] D. Szarafinski, “Flexible, Scalable and Configurable Single-Use Systems for Biopharmaceutical Research and Manufacture,” *Chemie Ing. Tech.*, vol. 85, no. 1–2, pp. 34–39, Feb. 2013. 10.1002/cite.201200138.

[55] T. P. Munro, S. M. Mahler, E. P. Huang, D. Y. Chin, and P. P. Gray, “Bridging the gap: facilities and technologies for development of early stage therapeutic mAb candidates.,” *MAbs*, vol. 3, no. 5, pp. 440–52, 2011. 10.4161/mabs.3.5.16968.

[56] P. J. Beckett, “Ultra Scale-Down of Elution Chromatography,” University College London Thesis, 2005.

[57] M. Juza, M. Mazzotti, and M. Morbidelli, “Simulated moving-bed chromatography and its application to chirotechnology,” *Trends Biotechnol.*, vol. 18, no. March, pp. 108–118, 2000. 10.1016/S0167-7799(99)01419-5.

[58] J. Winderl, T. Spies, and J. Hubbuch, “Packing characteristics of winged shaped polymer fiber supports for preparative chromatography,” *J. Chromatogr. A*, vol. 1553, pp. 67–80, 2018. 10.1016/j.chroma.2018.04.020.

[59] T. Scharl, C. Jungreuthmayer, A. Dürauer, S. Schweiger, T. Schröder, and A. Jungbauer, “Trend analysis of performance parameters of pre-packed columns for protein chromatography over a time span of ten years.,” *J. Chromatogr. A*, vol. 1465, pp. 63–70, Sep. 2016. 10.1016/j.chroma.2016.07.054.

[60] B. Tjaden, S. J. Cooper, D. J. Brett, D. Kramer, and P. R. Shearing, “On the origin and application of the Bruggeman correlation for analysing transport phenomena in electrochemical systems,” *Curr. Opin. Chem. Eng.*, vol. 12, pp. 44–51, May 2016. 10.1016/j.coche.2016.02.006.

[61] J. P. Vissers, M. A. Hoeben, J. Laven, H. A. Claessens, and C. A. Cramers, “Hydrodynamic aspects of slurry packing processes in microcolumn liquid chromatography,” *J. Chromatogr. A*, vol. 883, no. 1–2, pp. 11–25, Jun. 2000. 10.1016/S0021-9673(00)00276-4.

[62] E. J. Close, J. R. Salm, T. Iskra, E. Sørensen, and D. G. Bracewell, “Fouling of an anion exchange chromatography operation in a monoclonal antibody process: Visualization and kinetic studies.,” *Biotechnol. Bioeng.*, vol. 110, no. 9, pp. 2425–35, Sep. 2013. 10.1002/bit.24898.

[63] H. Zhang, I. Hussain, M. Brust, and a. I. Cooper, “Emulsion-Templated Gold Beads Using Gold Nanoparticles as Building Blocks,” *Adv. Mater.*, vol. 16, no. 1, pp. 27–30, Jan. 2004. 10.1002/adma.200306153.

[64] C. Lin, H. Zhan, M. Liu, S. Fu, and L. a Lucia, “Novel preparation and characterization of cellulose microparticles functionalized in ionic liquids.,” *Langmuir*, vol. 25, no. 17, pp. 10116–20, Sep. 2009. 10.1021/la9008703.

[65] M. C. Nweke, M. Turmaine, R. G. Mccartney, and D. G. Bracewell, “Drying techniques for the visualisation of agarose-based chromatography media by scanning electron microscopy” *Biotechnol. J.*, no. March, 2017. 10.1002/biot.201600583.

[66] M. C. Nweke, A. S. Rathore, and D. G. Bracewell, “Lifetime and Aging of Chromatography Resins during Biopharmaceutical Manufacture,” *Trends Biotechnol.*, pp. 1–4, 2018. 10.1016/j.tibtech.2018.01.001.

[67] M. Pathak, K. Lintern, and D. G. Bracewell, “Protein A Chromatography Resin Lifetime — Impact of Feed Composition,” *Biotechnol. Prog.*, pp. 1–8, 2018. 10.1002/btpr.2608.

[68] S. C. Siu, R. Boushaba, V. Topoyassakul, A. Graham, S. Choudhury, G. Moss, and N. J. Titchener-Hooker, “Visualising fouling of a chromatographic matrix using confocal scanning laser microscopy.,” *Biotechnol. Bioeng.*, vol. 95, no. 4, pp. 714–23, Nov. 2006. 10.1002/bit.21028.

[69] A. Susanto, T. Herrmann, and J. Hubbuch, “Short-cut method for the correction of light attenuation influences in the experimental data obtained from confocal laser scanning microscopy.,” *J. Chromatogr. A*, vol. 1136, no. 1, pp. 29–38, Dec. 2006. 10.1016/j.chroma.2006.09.053.

[70] M. Pathak and A. S. Rathore, “Mechanistic understanding of fouling of protein A chromatography resin.,” *J. Chromatogr. A*, vol. 1459, pp. 78–88, Aug. 2016. 10.1016/j.chroma.2016.06.084.

[71] T. Iskra, G. R. Bolton, J. L. Coffman, and R. Godavarti, “The effect of protein A cycle number on the performance and lifetime of an anion exchange polishing step.,” *Biotechnol. Bioeng.*, vol. 110, no. 4, pp. 1142–52, Apr. 2013. 10.1002/bit.24781.

[72] L. Yang, J. D. Harding, A. V Ivanov, N. Ramasubramanyan, and D. D. Dong, “Effect of cleaning agents and additives on Protein A ligand degradation and chromatography performance.,” *J. Chromatogr. A*, vol. 1385, pp. 63–8, Mar. 2015. 10.1016/j.chroma.2015.01.068.

[73] G. Hale, A. Drumm, P. Harrison, and J. Phillips, “Repeated cleaning of protein A affinity column with sodium hydroxide,” *J. Immunol. Methods*, vol. 171, no. 1, pp. 15–21, May 1994. 10.1016/0022-1759(94)90223-2.

[74] A. Grönberg, M. Eriksson, M. Ersoy, and H. J. Johansson, “A tool for increasing the lifetime of chromatography resins,” *MAbs*, vol. 3, no. 2, pp. 192–202, Oct. 2014. 10.4161/mabs.3.2.14874.

[75] M. Gilar, T. S. Mcdonald, F. Gritti, G. T. Roman, J. S. Johnson, B. Bunner, J. D. Michienzi, R. A. Collamati, J. P. Murphy, D. D. Satpute, M. P. Bannon, D. Dellarovere, R. A. Jencks, T. A. Dourdeville, K. E. Fadgen, and G. C. Gerhardt, "Chromatographic performance of microfluidic liquid chromatography devices : Experimental evaluation of straight versus serpentine packed channels," *J. Chromatogr. A*, vol. 1533, pp. 127–135, 2018. 10.1016/j.chroma.2017.12.031.

[76] P. Gzil, J. De Smet, N. Vervoort, H. Verelst, G. V. Baron, and G. Desmet, "Computational study of the band broadening in two-dimensional etched packed bed columns for on-chip high-performance liquid chromatography," *J. Chromatogr. A*, vol. 1030, no. 1–2, pp. 53–62, Mar. 2004. 10.1016/j.chroma.2003.12.038.

[77] S. Gerontas, M. S. Shapiro, and D. G. Bracewell, "Chromatography modelling to describe protein adsorption at bead level.," *J. Chromatogr. A*, vol. 1284, pp. 44–52, Apr. 2013. 10.1016/j.chroma.2013.01.102.

[78] F. Dolamore, C. Fee, and S. Dimartino, "Modelling ordered packed beds of spheres : The importance of bed orientation and the influence of tortuosity on dispersion," *J. Chromatogr. A*, vol. 1532, pp. 150–160, 2018. 10.1016/j.chroma.2017.12.004.

[79] J. Halvorson, A. M. Lenhoff, M. Dittmann, and D. R. Stoll, "Implications of turbulent flow in connecting capillaries used in high performance liquid chromatography," *J. Chromatogr. A*, vol. 1536, pp. 185–194, 2018. 10.1016/j.chroma.2016.12.084.

[80] J. N. Mait, "A History of Imaging : Revisiting the Past to Chart the Future," *Opt. Photonics*, pp. 22–27, 2006. 10.1364/OPN.17.2.000022.

[81] R. Weissleder and M. J. Pittet, "Imaging in the era of molecular oncology.," *Nature*, vol. 452, no. 7187, pp. 580–9, Apr. 2008. 10.1038/nature06917.

[82] E. H. Seeley, K. Schwamborn, and R. M. Caprioli, "Imaging of intact tissue sections: moving beyond the microscope.," *J. Biol. Chem.*, vol. 286, no. 29, Jul. 2011. 10.1074/jbc.R111.225854.

[83] G. William, "History of Medical Imaging," *Am. Physiol. Soc.*, vol. 152, no. 3, pp. 349–361, 2008. http://www.jstor.org/stable/40541591.

[84] M. D. Bentley, M. C. Ortiz, E. L. Ritman, J. C. Romero, and D. Michael, "The use of microcomputed tomography to study microvasculature in small rodents," *J. Histochem. Cytochem.*, vol. 48, no. 4, pp. 569–577, 2002. 10.1152/ajpregu.00560.2001.

[85] J. I. Goldstein, D. E. Newbury, P. Echlin, D. C. Joy, C. Fiori, and E. Lifshin, *Scanning Electron Microscopy and X-ray Microanalysis*. Springer, 2003. 10.1007/978-1-4939-6676-9.

[86] "The Nobel Prize in Physics 1986," 1986. [Online]. Available: http://www.nobelprize.org/nobel_prizes/physics/laureates/1986/. [Accessed: 08-Jan-2018].

[87] E. Ruska, "The development of the electron microscope and of electron microscopy," *Biosci. Rep.*, vol. 7, no. 8, pp. 607–629, Aug. 1987. 10.1007/BF01127674.

[88] G. E. Palade, “A Study of Fixation for Electron Microscopy,” *J. Exp. Med.*, vol. 95, no. 3, 1951. PMID: 14927794.

[89] A. Zankel, J. Wagner, and P. Poelt, “Serial sectioning methods for 3D investigations in materials science.,” *Micron*, vol. 62, pp. 66–78, Jul. 2014. 10.1016/j.micron.2014.03.002.

[90] H. Reingruber, a. Zankel, C. Mayrhofer, and P. Poelt, “A new in situ method for the characterization of membranes in a wet state in the environmental scanning electron microscope,” *J. Memb. Sci.*, vol. 399–400, pp. 86–94, May 2012. 10.1016/j.memsci.2012.01.031.

[91] G. D. Danilatos, “Optimum beam transfer in the environmental scanning electron,” *J. Microsc.*, vol. 234, pp. 26–37, 2009. 10.1111/j.1365-2818.2009.03148.x.

[92] J. M. Thomas and C. Ducati, “16. Transmission Electron Microscopy,” in *Characterization of Solid Materials and Heterogeneous Catalysts: From Structure to Surface Reactivity, Volume 1&2*, Wiley VCH, 2012, pp. 655–701.

[93] A. V. Crewe, “The current state of high resolution scanning electron microscopy,” *Q. Rev. Biophys.*, vol. 3, no. 01, p. 137, Mar. 2009. 10.1017/S0033583500004431.

[94] M. Pilhofer, M. S. Ladinsky, A. W. McDowall, and G. J. Jensen, “Bacterial TEM: new insights from cryo-microscopy.,” in *Methods in cell biology*, vol. 96, no. 10, Elsevier Inc., 2010, pp. 21–45. 10.1016/S0091-679X(10)96002-0.

[95] K. M. Harris, E. Perry, J. Bourne, M. Feinberg, L. Ostroff, and J. Hurlburt, “Uniform serial sectioning for transmission electron microscopy.,” *J. Neurosci.*, vol. 26, no. 47, pp. 12101–3, Nov. 2006. 10.1523/JNEUROSCI.3994-06.2006.

[96] B. D. Bowes, H. Koku, K. J. Czymmek, and A. M. Lenhoff, “Protein adsorption and transport in dextran-modified ion-exchange media. I: adsorption.,” *J. Chromatogr. A*, vol. 1216, no. 45, pp. 7774–84, Nov. 2009. 10.1016/j.chroma.2009.09.014.

[97] M. Schossig-Tiedemann and D. Paul, “Improved preparation of membrane surfaces for field-emission scanning electron microscopy,” *J. Memb. Sci.*, vol. 187, no. 1–2, pp. 85–91, Jun. 2001. 10.1016/S0376-7388(00)00668-2.

[98] W. Denk and H. Horstmann, “Serial block-face scanning electron microscopy to reconstruct three-dimensional tissue nanostructure.,” *PLoS Biol.*, vol. 2, no. 11, Nov. 2004. 10.1371/journal.pbio.0020329.

[99] H. Reingruber, a. Zankel, C. Mayrhofer, and P. Poelt, “Quantitative characterization of microfiltration membranes by 3D reconstruction,” *J. Memb. Sci.*, vol. 372, no. 1–2, pp. 66–74, Apr. 2011. 10.1016/j.memsci.2011.01.037.

[100] C. A. Volkert and A. M. Minor, “Focused Ion Beam Microscopy and Micromachining,” *MRS Bull.*, vol. 32, pp. 389–399, 2007. 10.1557/mrs2007.62.

[101] N. Yao, *Focused Ion Beam Systems Basics and Applications*. Cambridge, 2011. ISBN: 9780521831994.

[102] J. B. Robinson, L. D. Brown, R. Jervis, O. O. Taiwo, T. M. M. Heenan, J. Millichamp, T. J. Mason, T. P. Neville, R. Clague, D. S. Eastwood, C. Reinhard, P. D. Lee, D. J. L. Brett, and P. R. Shearing, "Investigating the effect of thermal gradients on stress in solid oxide fuel cell anodes using combined synchrotron radiation and thermal imaging," *J. Power Sources*, vol. 288, pp. 473–481, Aug. 2015. 10.1016/j.jpowsour.2015.04.104.

[103] P. R. Shearing, J. Golbert, R. J. Chater, and N. P. Brandon, "3D reconstruction of SOFC anodes using a focused ion beam lift-out technique," *Chem. Eng. Sci.*, vol. 64, no. 17, pp. 3928–3933, Sep. 2009. 10.1016/j.ces.2009.05.038.

[104] J. J. Bailey, T. M. M. Heenan, D. P. Finegan, X. Lu, S. R. Daemi, F. Iacoviello, N. Backeberg, O. O. Taiwo, D. J. L. Brett, A. Atkinson, and P. R. Shearing, "Laser-preparation of geometrically optimised samples for X-ray nano-CT," *J. Microsc.*, vol. 267, no. 3, pp. 384–396, 2017. 10.1111/jmi.12577.

[105] L. A. Giannuzzi and F. A. Stevie, "A review of focused ion beam milling techniques for TEM specimen preparation," *Micron*, vol. 30, no. 3, pp. 197–204, Jun. 1999. 10.1016/S0968-4328(99)00005-0.

[106] F. Peyrin and P. Douek, "X-Ray Tomography," in *Photon-Based Medical Imagery*, H. Fanet, Ed. Wiley, 2011. ISBN: 978-1-84821-241-1.

[107] "Nobel prize in 1979 for Physiology or Medicine," 1979. [Online]. Available: http://www.nobelprize.org/nobel_prizes/medicine/laureates/1979/. [Accessed: 13-Feb-2018].

[108] W. H. Oldendorft, "Pattern of a Complex Object," *Trans. Biomed. Electron.*, pp. 68–72, 1961.

[109] R. A. Ketcham and W. D. Carlson, "Acquisition, optimization and interpretation of X-ray computed tomographic imagery: applications to the geosciences," *Comput. Geosci.*, vol. 27, no. 4, pp. 381–400, May 2001. 10.1016/S0098-3004(00)00116-3.

[110] E. Maire and P. J. Withers, "Quantitative X-ray tomography," *Int. Mater. Rev.*, vol. 59, no. 1, pp. 1–43, Jan. 2014. 10.1179/1743280413Y.0000000023.

[111] T. L. Burnett, S. a McDonald, a Gholinia, R. Geurts, M. Janus, T. Slater, S. J. Haigh, C. Ornek, F. Almuaili, D. L. Engelberg, G. E. Thompson, and P. J. Withers, "Correlative tomography.," *Sci. Rep.*, vol. 4, p. 4711, Jan. 2014. 10.1038/srep04711.

[112] P. R. Shearing, J. Gelb, and N. P. Brandon, "X-ray nano computerised tomography of SOFC electrodes using a focused ion beam sample-preparation technique," *J. Eur. Ceram. Soc.*, vol. 30, no. 8, pp. 1809–1814, Jun. 2010. 10.1016/j.jeurceramsoc.2010.02.004.

[113] P. J. Withers, "X-ray nanotomography," *Mater. Today*, vol. 10, no. 12, pp. 26–34, Dec. 2007. 10.1016/S1369-7021(07)70305-X.

[114] E. L. Ritman, "Micro-computed tomography-current status and developments.," *Annu. Rev. Biomed. Eng.*, vol. 6, pp. 185–208, Jan. 2004. 10.1146/annurev.bioeng.6.040803.140130.

[115] "Zeiss XRadia 810 Ultra website." [Online]. Available: http://www.zeiss.com/microscopy/en_de/products/x-ray-microscopy/xradia-810-ultra.html#introduction. [Accessed: 24-Feb-2018].

[116] M. Doyle, T. F. Fuller, and J. Newman, "Modeling of Galvanostatic Charge and Discharge of the Lithium / Polymer / Insertion Cell," vol. 140, no. 6, pp. 1526–1533, 1993. 10.1149/1.2221597.

[117] J. R. Izzo, A. S. Joshi, K. N. Grew, W. K. S. Chiu, A. Tkachuk, S. H. Wang, and W. Yun, "Nondestructive Reconstruction and Analysis of SOFC Anodes Using X-ray Computed Tomography at Sub-50 nm Resolution," *J. Electrochem. Soc.*, vol. 155, no. 5, p. B504, 2008. 10.1149/1.2895067.

[118] P. R. Shearing, L. E. Howard, P. S. Jørgensen, N. P. Brandon, and S. J. Harris, "Characterization of the 3-dimensional microstructure of a graphite negative electrode from a Li-ion battery," *Electrochem. commun.*, vol. 12, no. 3, pp. 374–377, Mar. 2010. 10.1016/j.elecom.2009.12.038.

[119] S. C. Mayo, P. R. Miller, T. Gureyev, and S. W. Wilkins, "Attainment of < 60nm Resolution in Phase-Contrast X-ray Microscopy using an add-on to an SEM," pp. 343–345, 2005.

[120] D.-W. Chung, M. Ebner, D. R. Ely, V. Wood, and R. Edwin García, "Validity of the Bruggeman relation for porous electrodes," *Model. Simul. Mater. Sci. Eng.*, vol. 21, no. 7, p. 074009, Oct. 2013. 10.1088/0965-0393/21/7/074009.

[121] B. Tjaden, D. J. L. Brett, P. R. Shearing, B. Tjaden, D. J. L. Brett, P. R. Shearing, B. Tjaden, D. J. L. Brett, and P. R. Shearing, "Tortuosity in electrochemical devices : a review of calculation approaches," *Int. Mater. Rev.*, vol. 6608, 2018. 10.1080/09506608.2016.1249995.

[122] T. M. M. Heenan, D. P. Finegan, B. Tjaden, X. Lu, F. Iacoviello, J. Millichamp, and D. J. L. Brett, "4D Nano-Tomography of Electrochemical Energy Devices using Lab-based X-ray Computed Tomography," *Nano energy*, 2018. 10.1016/j.nanoen.2018.03.001.

[123] F. Tariq, V. Yufit, M. Kishimoto, P. R. Shearing, S. Menkin, D. Golodnitsky, J. Gelb, E. Peled, and N. P. Brandon, "Three-dimensional high resolution X-ray imaging and quantification of lithium ion battery mesocarbon microbead anodes," *J. Power Sources*, vol. 248, pp. 1014–1020, Feb. 2014. 10.1016/j.jpowsour.2013.08.147.

[124] A. Funk, M. Zeilinger, A. Miehe, D. Sopu, J. Eckert, and F. Dötz, "MnFePSi-based magnetocaloric packed bed regenerators : Structural details probed by X-ray tomography," *Chem. Eng. Sci.*, vol. 175, pp. 84–90, 2018. 10.1016/j.ces.2017.09.030.

[125] M. Davidson and M. Abramowitz, "Optical microscopy," *Encycl. Imaging Sci. Technol.*, p. 41, 2002.

[126] Nobel-Website, "Nobel Prize 2014 Press release," 2014. [Online]. Available: http://www.nobelprize.org/nobel_prizes/chemistry/laureates/2014/press.html. [Accessed: 09-Jan-2018].

[127] M. Ehrenberg, "Super-resolved Fluorescence microscopy review," 2014.

[128] S. Amelinckx, D. Van Dyck, J. Van Landuyt, and G. Van Tendeloo, *Handbook of Microscopy Methods*. 1997. ISBN: 3527292802.

[129] C. U. M. Smith, *Biology of Sensory Systems, Second Edition (Chapter 16 - The human eye)*. John Wiley and Sons, 2008. ISBN: 9780470518625.

[130] W. M. Farmer, “Measurement of particle size, number density, and velocity using a laser interferometer.,” *Appl. Opt.*, vol. 11, no. 11, pp. 2603–12, Nov. 1972. PMID: 20119379.

[131] G. Mie, “Contributions to the optics of turbid media, particularly of colloid metal solutions (TRANSLATED - 1976),” 1908.

[132] V. Bordo and H.-G. Rubahn, *Optical Microscopy*. Wiley VCH, 2005. ISBN: 3527405607.

[133] H. Dehghani, B. W. Pogue, J. Shudong, B. Brooksby, and K. D. Paulsen, “Three-Dimensional Optical Tomography: Resolution in Small-Object Imaging,” *Appl. Opt.*, vol. 42, no. 16, p. 3117, 2003. 10.1364/AO.42.003117.

[134] C. A. Teske, M. Schroeder, R. Simon, and J. Hubbuch, “Protein-labeling effects in confocal laser scanning microscopy.,” *J. Phys. Chem. B*, vol. 109, no. 28, pp. 13811–7, Jul. 2005. 10.1021/jp050713+.

[135] N. S. Claxton, T. J. Fellers, and M. W. Davidson, “Laser Scanning Confocal Microscopy,” *Encycl. Med. Devices Instrum.*, no. 21, 1979. 10.1002/0471732877.emd291.

[136] C. Gu, “Confocal Scanning Laser Microscopy : Fundamentals and Uses on Membrane Fouling Characterization and Opportunities for Online Monitoring,” in *Monitoring and Visualising Membrane-based processes*, 2009, pp. 55–75. ISBN: 9783527320066.

[137] B. J. Haupt, A. E. Pelling, and M. A. Horton, “Integrated confocal and scanning probe microscopy for biomedical research.,” *ScientificWorldJournal.*, vol. 6, pp. 1609–18, Jan. 2006. 10.1100/tsw.2006.269.

[138] M. S. Shapiro, S. J. Haswell, G. J. Lye, and D. G. Bracewell, “Design and Characterization of a Microfluidic Packed Bed System for Protein Breakthrough and Dynamic Binding Capacity Determination,” *Biotechnol. Prog.*, pp. 277–285, 2009. 10.1021/bp.99.

[139] I. Schmidt, M. Minceva, and W. Arlt, “Selection of stationary phase particle geometry using X-ray computed tomography and computational fluid dynamics simulations ಙ,” *J. Chromatogr. A*, vol. 1225, pp. 141–149, 2012. 10.1016/j.chroma.2011.12.072.

[140] L. E. Blue, E. G. Franklin, J. M. Godinho, J. P. Grinias, K. M. Grinias, D. B. Lunn, and S. M. Moore, “Recent advances in capillary ultrahigh pressure liquid chromatography,” *J. Chromatogr. A*, vol. 1523, pp. 17–39, 2017. 10.1016/j.chroma.2017.05.039.

[141] “Nobel Prize for Physics in 1952,” 1952. [Online]. Available: http://www.nobelprize.org/nobel_prizes/physics/laureates/1952/. [Accessed: 19-Jan-2018].

[142] “Nobel Prize in Chemistry in 1991,” 1991. [Online]. Available: http://www.nobelprize.org/nobel_prizes/chemistry/laureates/1991/. [Accessed: 19-Jan-2018].

[143] “2003 Nobel Prize in Physiology or Medicine,” 2003. [Online]. Available: http://www.nobelprize.org/nobel_prizes/medicine/laureates/2003/. [Accessed: 19-Jan-2018].

[144] L. F. Gladden, “Nuclear Magnetic Resonance Engineering: principles and Applications,” *Chem. Eng. Sci.*, vol. 49, no. 20, pp. 3339–3408, 1994. :3339-3408.

[145] L. Marciani, R. C. Spiller, P. A. Gowland, and P. D. Thurley, “Magnetic resonance imaging,” in *Textbook of Clinical Gastroenterology and Hepatology, Second Edition*, Wiley, 2012, pp. 1014–1020.

[146] L. F. Gladden and P. Alexander, “Applications of nuclear magnetic resonance imaging in process engineering,” *Meas. Sci. Technol.*, vol. 7, no. 3, pp. 423–435, Mar. 1996. 10.1088/0957-0233/7/3/026.

[147] A. Sederman, P. Alexander, and L. Gladden, “Structure of packed beds probed by Magnetic Resonance Imaging,” *Powder Technol.*, vol. 117, no. 3, pp. 255–269, Jun. 2001. 10.1016/S0032-5910(00)00374-0.

[148] M. H. Sankey, D. J. Holland, A. J. Sederman, and L. F. Gladden, “Magnetic resonance velocity imaging of liquid and gas two-phase flow in packed beds.,” *J. Magn. Reson.*, vol. 196, no. 2, pp. 142–8, Feb. 2009. 10.1016/j.jmr.2008.10.021.

[149] M. P. Hollewand and L. F. Gladden, “Heterogeneities in Structure and Diffusion within Porous Catalyst Support Pellets Observed by NMR Imaging,” *J. Catal.*, vol. 144, pp. 254–272, 1993. 10.1006/jcat.1993.1328.

[150] M. D. Abràmoff, I. Hospitals, P. J. Magalhães, and M. Abràmoff, “Image Processing with ImageJ,” *Biophotonics Int.*, vol. 11, no. 7, pp. 36 – 42, 2004.

[151] F. Gustafsson and N. Bergman, *MATLAB® for Engineers Explained*. London: Springer London, 2003. 10.1007/978-1-4471-0029-4.

[152] C. Jungreuthmayer, P. Steppert, G. Sekot, A. Zankel, H. Reingruber, J. Zanghellini, and A. Jungbauer, “The 3D pore structure and fluid dynamics simulation of macroporous monoliths: High permeability due to alternating channel width.,” *J. Chromatogr. A*, vol. 1425, pp. 141–149, Nov. 2015. 10.1016/j.chroma.2015.11.026.

[153] X. Lu, O. O. Taiwo, A. Bertei, T. Li, K. Li, D. J. L. Brett, and P. R. Shearing, “Multi-length scale tomography for the determination and optimization of the effective microstructural properties in novel hierarchical solid oxide fuel cell anodes,” *J. Power Sources*, vol. 367, pp. 177–186, 2017. 10.1016/j.jpowsour.2017.09.017.

[154] J. M. Angelo, A. Cvetkovic, R. Gantier, and A. M. Lenhoff, “Characterization of cross-linked cellulosic ion-exchange adsorbents : 2 . Protein sorption and transport,” *J. Chromatogr. A*, vol. 1438, pp. 100–112, 2016. 10.1016/j.chroma.2016.02.019.

[155] J. B. Robinson, D. P. Finegan, T. M. M. Heenan, K. Smith, E. Kendrick, and D. J. L. Brett, “Microstructural Analysis of the Effects of Thermal Runaway on Li-Ion and Na-Ion Battery Electrodes,” *J. Electrochem. Energy Conserv. Storage*, vol. 15, no. February, pp. 1–9, 2018. 10.1115/1.4038518.

[156] J. Hack, T. M. M. Heenan, F. Iacoviello, N. Mansor, Q. Meyer, P. Shearing, N. Brandon, and D. J. L. Brett, “A structure and durability comparison of membrane electrode assembly farbrication methods: self-assembled versus hot-pressed,” *J. Electrochem. Soc.*, vol. 165, no. 6, pp. 3045–3052, 2018. 10.1149/2.0051806jes.

[157] D. P. Finegan, E. Darcy, M. Keyser, B. Tjaden, T. M. M. Heenan, R. Jervis, J. J. Bailey, N. T. Vo, O. V Magdysyuk, M. Drakopoulos, M. Di Michiel, A. Rack, G. Hinds, D. J. L. Brett, and P. R. Shearing, “Identifying the Cause of Rupture of Li-Ion Batteries during Thermal Runaway,” *Adv. Sci.*, 2018. 10.1002/advs.201700369.

[158] D. Bray, “Critical Point Drying of Biological Specimens for Scanning Electron Microscopy,” *Supercrit. Fluid Methods Protoc. Methods Biotechnol.*, vol. 13, pp. 235–243, 2000. 10.1385/1-59259-030-6:235.

[159] A. M. Glauert, “Technical Data Sheet: 471 Poly / Bed 812 - BDMA Embedding Kit Infiltration,” *Polysciences*, pp. 1–2, 2012.

[160] T. F. Johnson, J. J. Bailey, F. Iacoviello, J. H. Welsh, P. R. Levison, P. R. Shearing, and D. G. Bracewell, “Three dimensional characterisation of chromatography bead internal structure using X-ray computed tomography and focused ion beam microscopy,” *J. Chromatogr. A*, vol. 1566, pp. 79-88, 2018. 10.1016/j.chroma.2018.06.054.

[161] G. Mantanis, R. Young, and R. Rowell, “Swelling of compressed cellulose fiber webs in organic liquids,” *Cellulose*, pp. 1–22, 1995. 10.1007/BF00812768.

[162] C. Lopez-Molina, B. De Baets, and H. Bustince, “Quantitative error measures for edge detection,” *Pattern Recognit.*, vol. 46, no. 4, pp. 1125–1139, Apr. 2013. 10.1016/j.patcog.2012.10.027.

[163] B. Nordestgaard and J. Rostgaard, “Critical-point drying versus freeze drying for scanning electron microscopy: a quantitative and qualitative study on isolated hepatocytes,” vol. 137, no. October 1984, pp. 189–207, 1985.

[164] W. Yun, Y. Wang, and D. R. Trapp, “Low pass X-ray scintilator system,” US Patent number 7,800,072, 2010.

[165] W. Yun, Y. Wang, and D. R. Trapp, “Lens bonded X-ray scintillator system and manufacturing method therefor,” US Patent number 7,297,959, 2007.

[166] W. Yun, F. W. Duewer, and Y. Wang, “X-ray microscope capillary condenser system,” US Patent number 7,170,969, 2007.

[167] W. Yun, Y. Wang, and D. R. Trapp, “Scintillator optical system and method of manufacture,” US Patent number 7,057,181, 2006.

[168] W. Yun, A. F. Lyon, and Y. Feng, “High aspect-ratio X-ray diffractive structure stabilization methods and systems,” US Patent number 7,864,426, 2011.

[169] T. F. Johnson, P. R. Levison, P. R. Shearing, and D. G. Bracewell, “X-ray computed tomography of packed bed chromatography columns for three dimensional imaging and analysis,” *J. Chromatogr. A*, vol. 1487, pp. 108–115, Jan. 2017. 10.1016/j.chroma.2017.01.013.

[170] A. Kumar, P. Mandal, Y. J. Zhang, and S. Litster, “Image Restoration of Phase Contrast Nano Scale X-ray CT Images,” pp. 280–285, 2014. 10.1007/978-3-319-09994-1_28.

[171] K.-F. Du, M. Yan, Q.-Y. Wang, and H. Song, “Preparation and characterization of novel macroporous cellulose beads regenerated from ionic liquid for fast chromatography.,” *J. Chromatogr. A*, vol. 1217, no. 8, pp. 1298–304, Feb. 2010. 10.1016/j.chroma.2009.12.037.

[172] J. Bearden, “X-ray Wavelengths and X-ray Atomic Energy Levels,” *Rev. Mod. Phys.*, vol. 31, no. 01, 1967.

[173] “Thermo Fisher Scientific Users-Guide Avizo Software.” https://www.fei.com/WorkArea/DownloadAsset.aspx?id=34359741225.

[174] S. J. Cooper, A. Bertei, P. R. Shearing, J. A. Kilner, and N. P. Brandon, “TauFactor : An open-source application for calculating tortuosity factors from tomographic data,” *SoftwareX*, vol. 5, pp. 203–210, 2016. 10.1016/j.softx.2016.09.002.

[175] M. Barrande, R. Bouchet, and R. Denoyel, “Tortuosity of Porous Particles,” *Anal. Chem.*, vol. 79, no. 23, pp. 9115–9121, 2007. 10.1021/ac071377r

[176] B. Stanislawski, E. Schmit, and J. Ohser, “Imaging of Fluorophores in Chromatographic Beads, Reconstruction of Radial Density Distributions and Characterisation of Protein Uptaking Processes,” *Image Anal. Stereol.*, vol. 29, no. 3, pp. 181–189, Nov. 2010. 10.5566/ias.v29.p181-189.

[177] D. E. Cherrak, M. Al-bokari, E. C. Drumm, and G. Guiochon, “Behavior of packing materials in axially compressed chromatographic columns,” *J. Chromatogr. A*, vol. 943, no. 2001, pp. 15–31, 2010. 10.1016/S0021-9673(01)01432-7.

[178] A. S. Kim and H. Chen, “Diffusive tortuosity factor of solid and soft cake layers: A random walk simulation approach,” *J. Memb. Sci.*, vol. 279, no. 1–2, pp. 129–139, Aug. 2006. 10.1016/j.memsci.2005.11.042.

[179] H. Kempe, P. Persson, A. Axelsson, B. Nilsson, and G. Zacchi, “Determination of Diffusion Coefficients of Proteins in Stationary Phases by Frontal Chromatography,” 2005. 10.1002/bit.20738.

[180] J. Vajda, W. Conze, and E. Müller, “Kinetic plots in aqueous size exclusion chromatography of monoclonal antibodies and virus particles,” *J. Chromatogr. A*, vol. 1426, pp. 118–125, 2015. 10.1016/j.chroma.2015.11.057.

[181] A. K. Gaígalas, J. B. Hubbard, M. Mccurley, and S. Woo, “Diffusion of Bovine Serum Albumin in Aqueous Solutions,” *J. Phys. Chem.*, no. 1, pp. 2355–2359, 1992. 10.1021/j100184a063.

Appendix

Chapter 2

Figure 26: Further images for each technique that were analysed, 3 examples per condition.

Permutation 1: No column preparation, no drying (environmental)

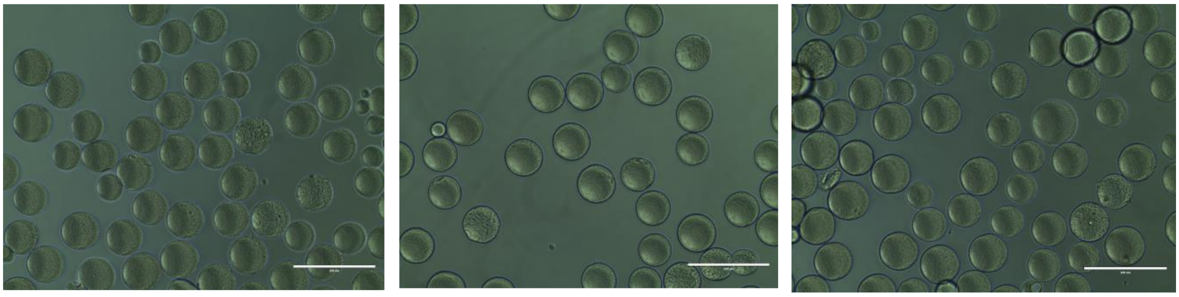

Permutation 2: Preparation up to 100% ethanol, no drying

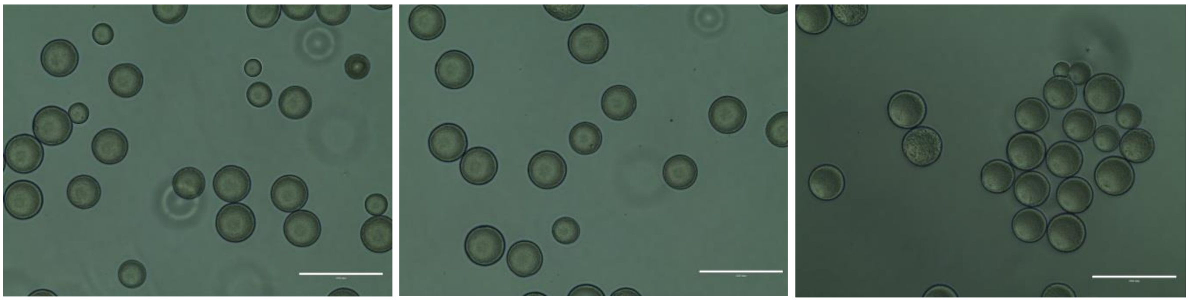

Permutation 3: Preparation down to 20% ethanol, no drying

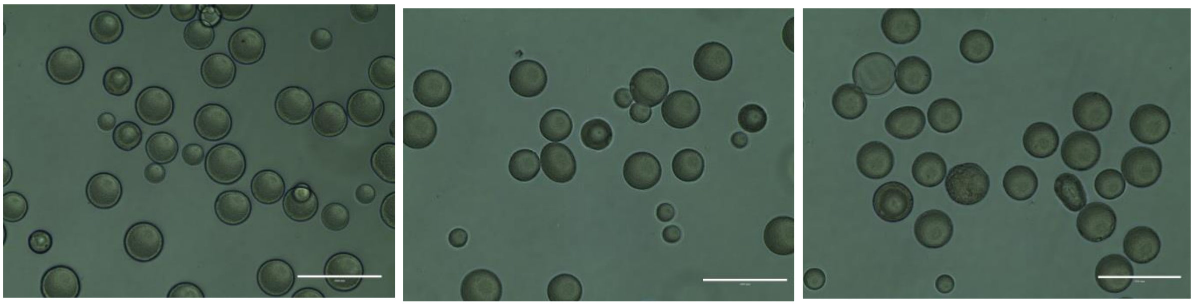

Permutation 4: No column preparation, air dried

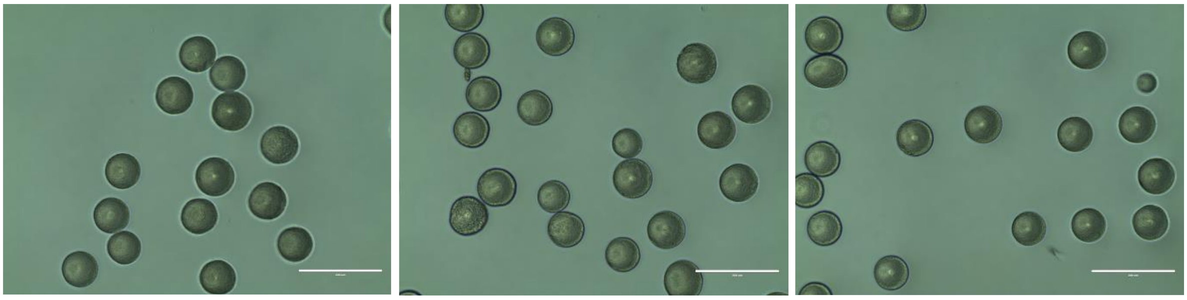

Permutation 5: Preparation up to 100% ethanol, air dried

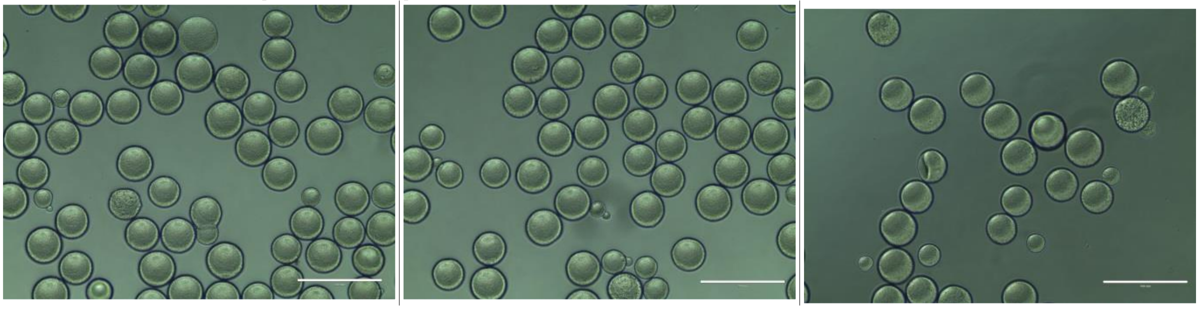

Permutation 6:Preparation down to 20% ethanol, air dried

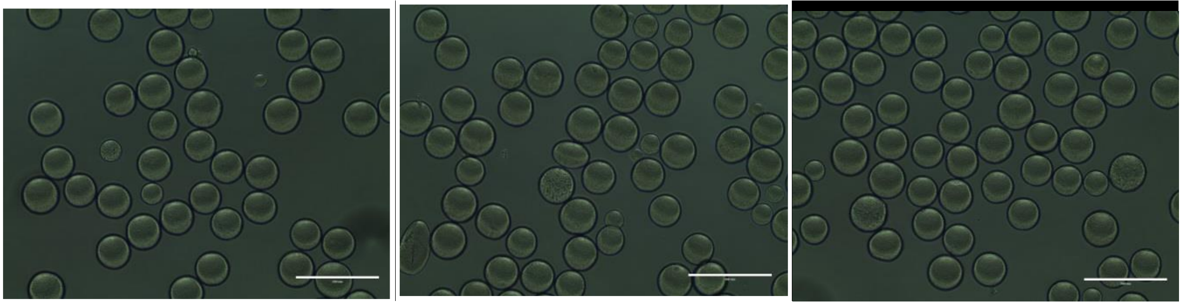

Permutation 7: No column preparation, Critical Point Dried

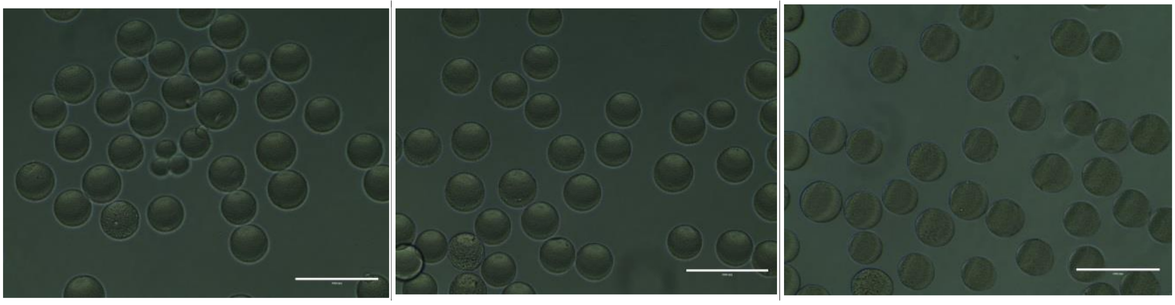

Permutation 8: Preparation up to 100% ethanol, Critical Point Dried

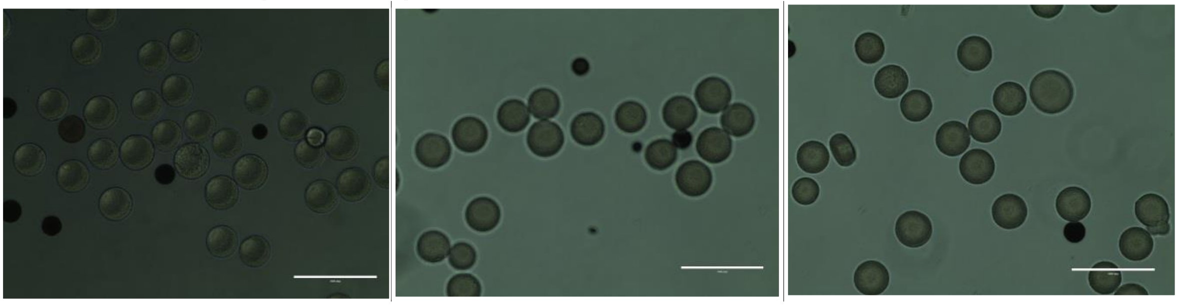

Permutation 9: Preparation down to 20% ethanol, Critical Point Dried

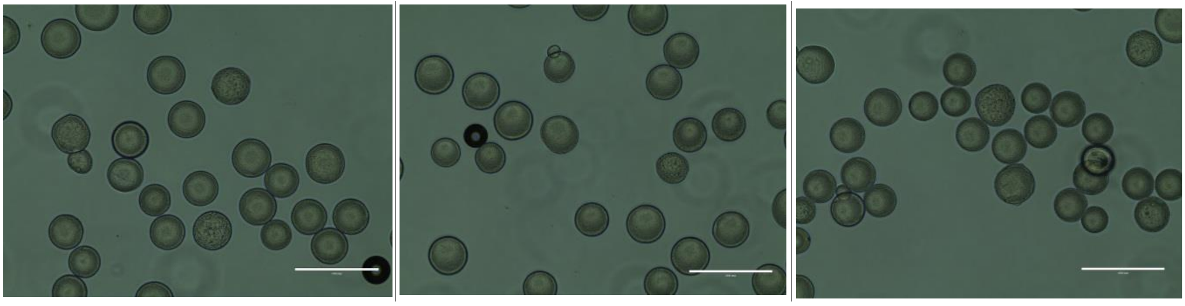

Figure 27: PSD graphs for each permutation (plus conventional overall for each drying set)

P1

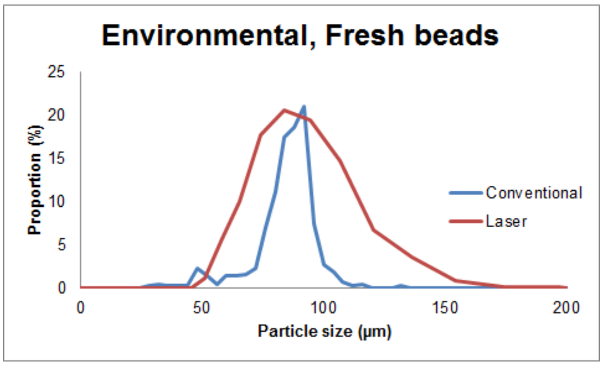

P2

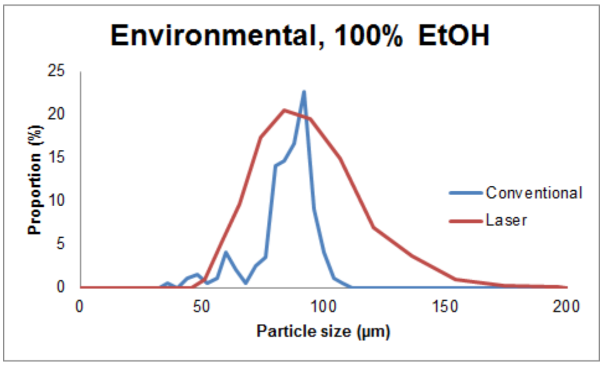

P3

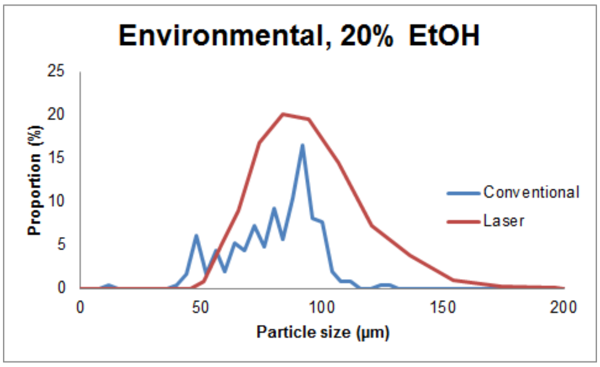

Conventional overlay

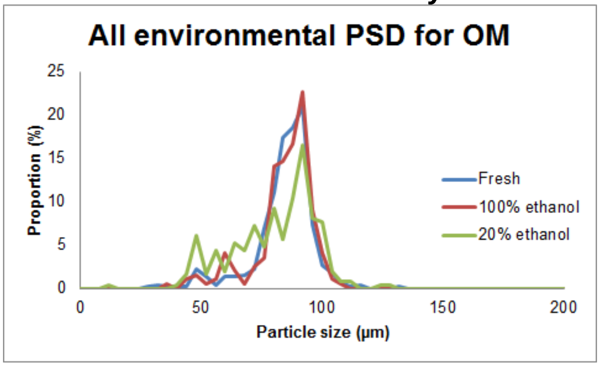

P4

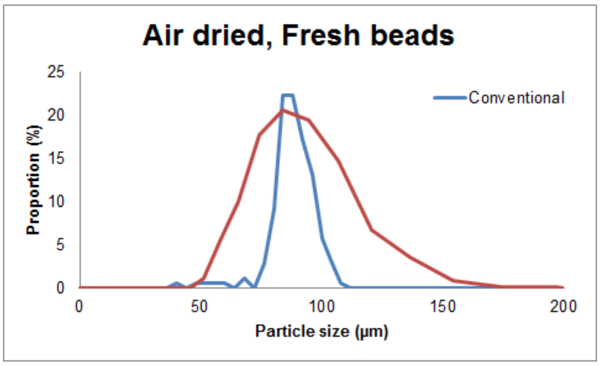

P5

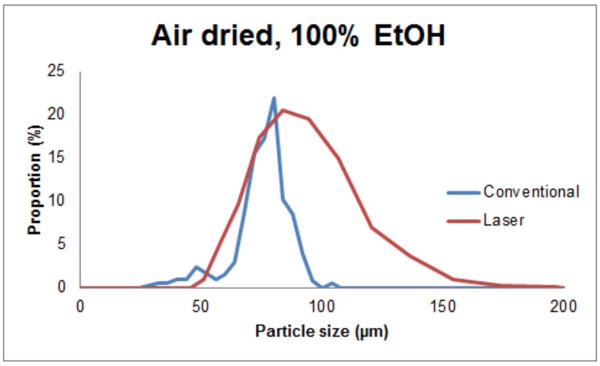

P6

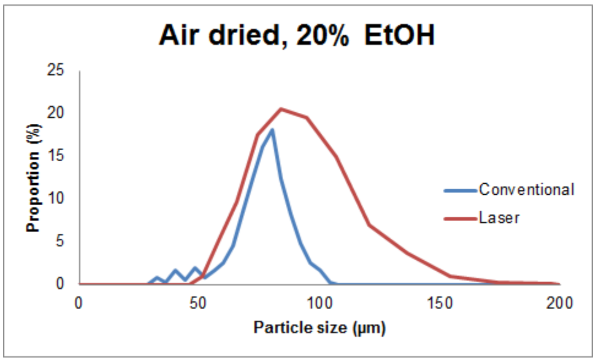

Conventional overlay

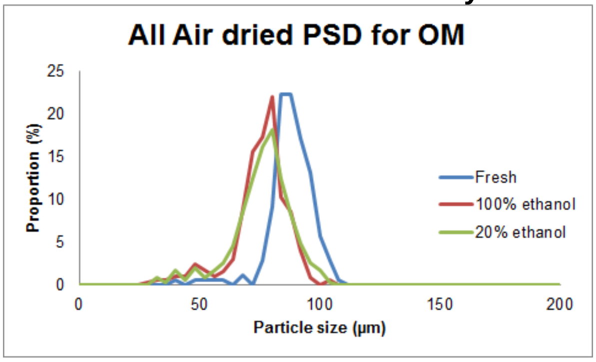

P7

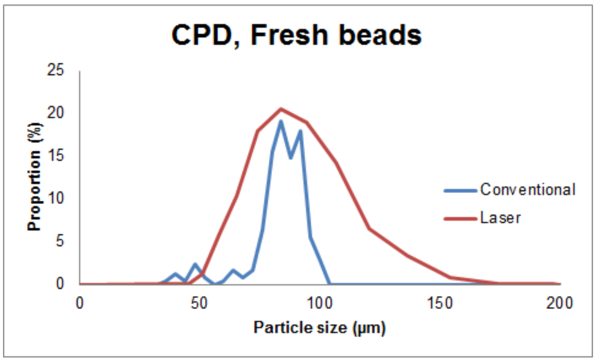

P8

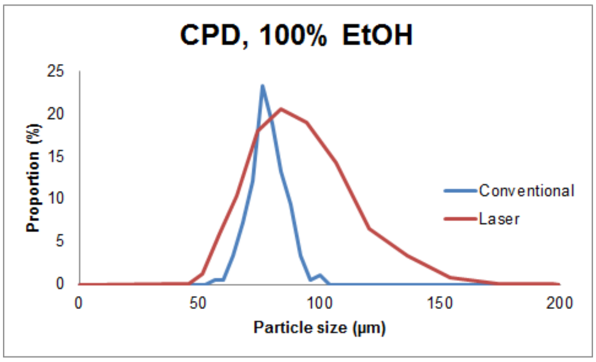

P9

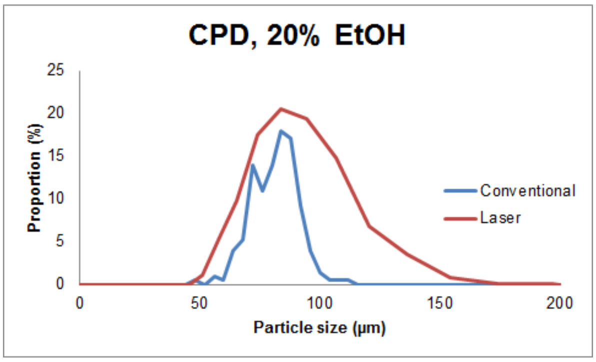

Conventional overlay

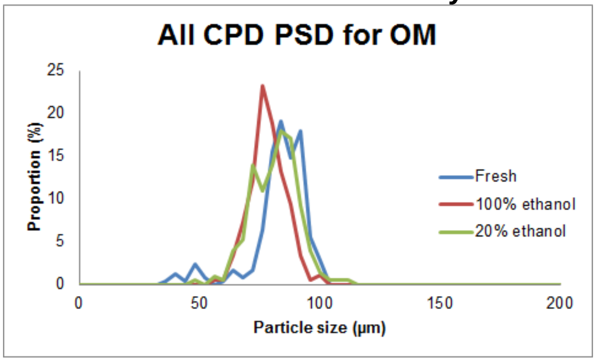

Visual evidence of sample damage due to Mastersizer damage at 1,000 RPM dispersion.

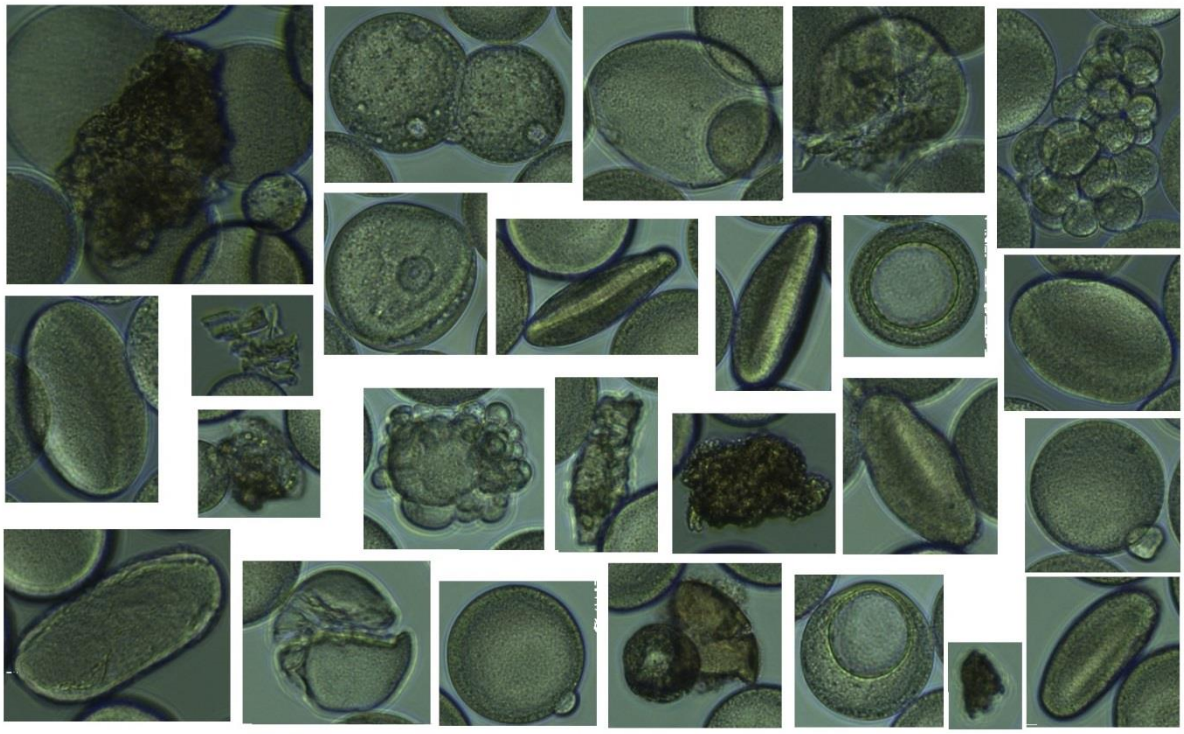

Figure 28: SEM imaging of prepared samples of surface details of MEP HyperCel resin

Permutation 1: No column preparation, no drying (environmental), uncoated

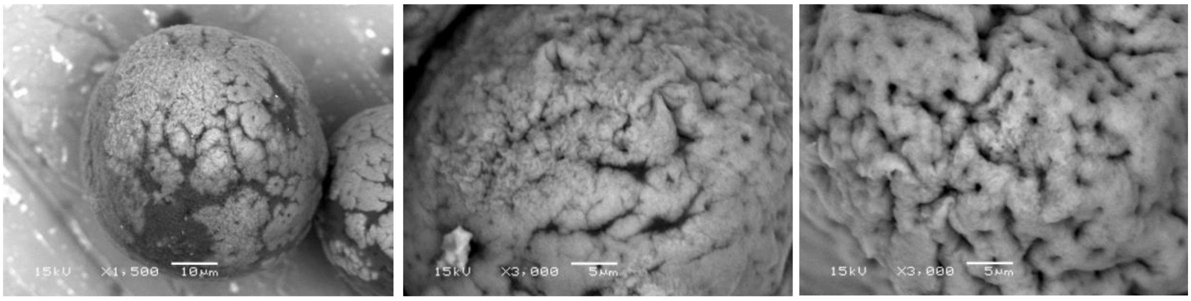

Permutation 1C: No column preparation, no drying (environmental), coated

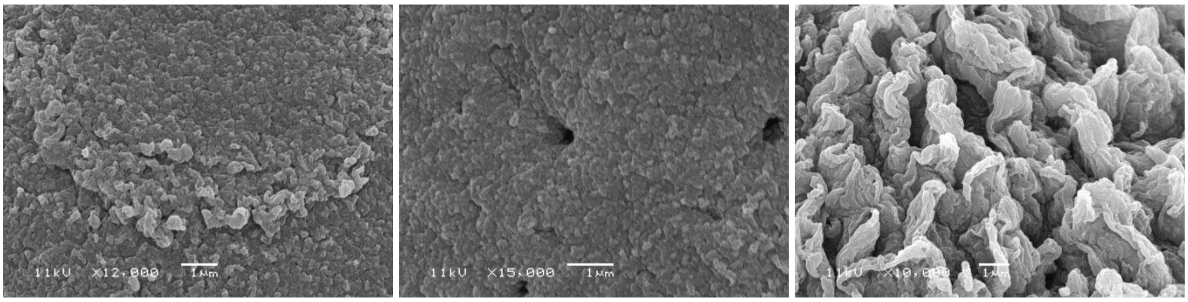

Permutation 2: Preparation up to 100% ethanol, no drying (environmental), uncoated

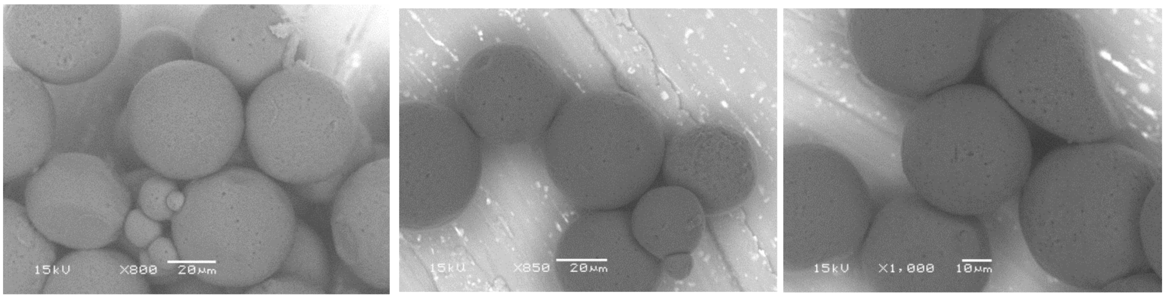

Permutation 2C: Preparation up to 100% ethanol, no drying (environmental), coated

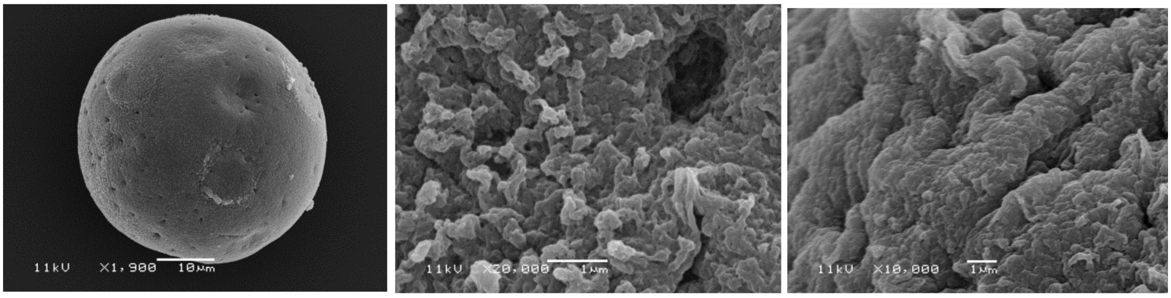

Permutation 3: Preparation down to 20% ethanol, no drying (environmental), uncoated

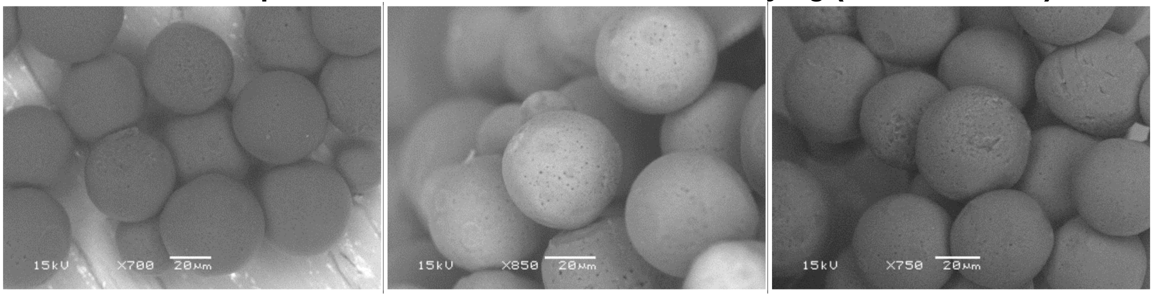

Permutation 3C: Preparation down to 20% ethanol, no drying (environmental), coated

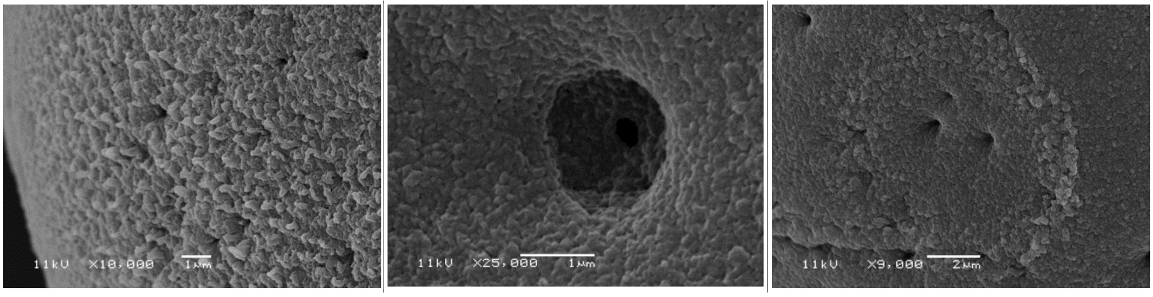

Permutation 4: No column preparation, air dried, uncoated

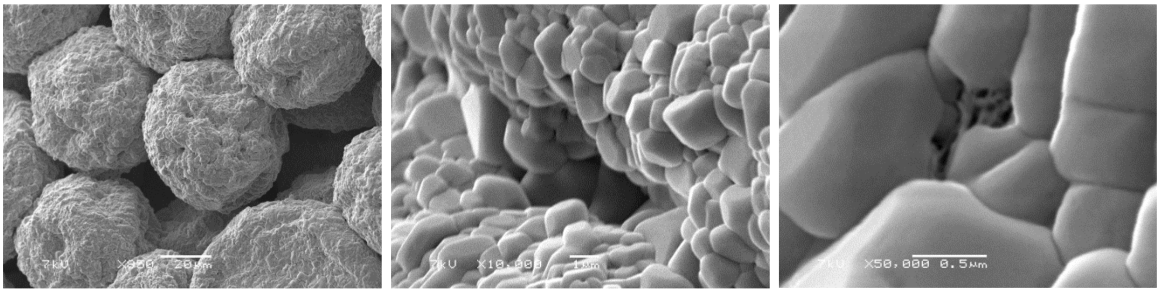

Permutation 4C: No column preparation, air dried, coated

Permutation 5: Column preparation up to 100% ethanol, air dried, uncoated

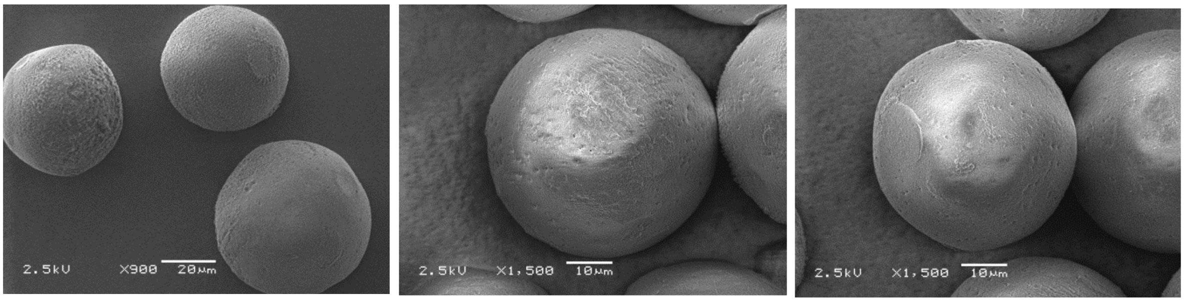

Permutation 5C: Column preparation up to 100% ethanol, air dried, coated

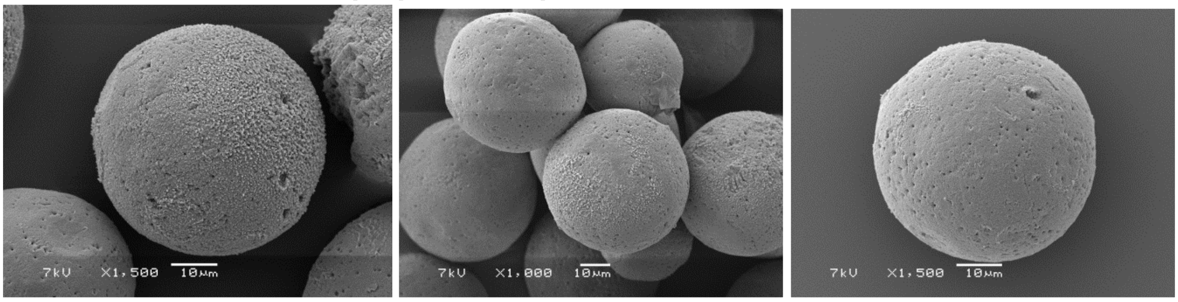

Permutation 6: Column preparation down to 20% ethanol, air dried, uncoated

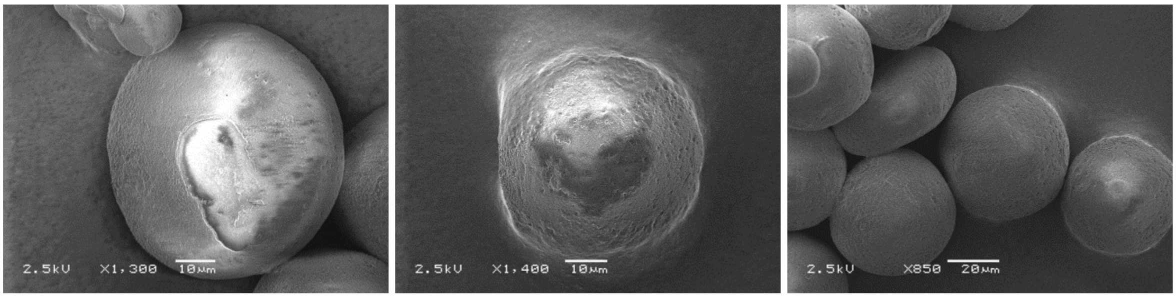

Permutation 6C: Column preparation down to 20% ethanol, air dried, coated

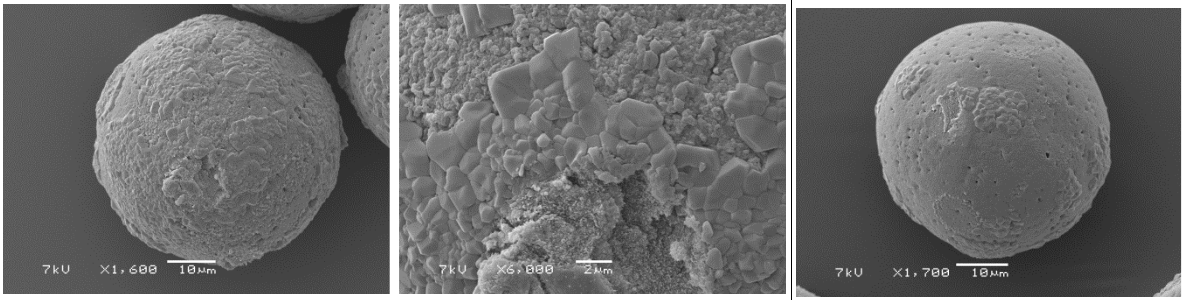

Permutation 7: No column preparation, CPD, uncoated

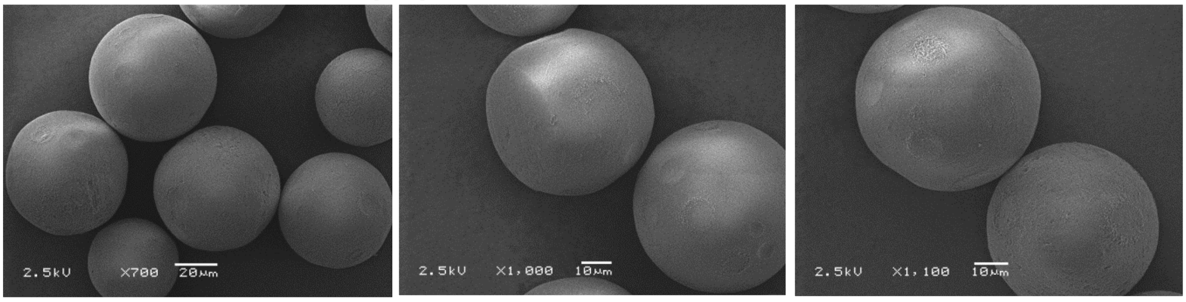

Permutation 7C: No column preparation, CPD, coated

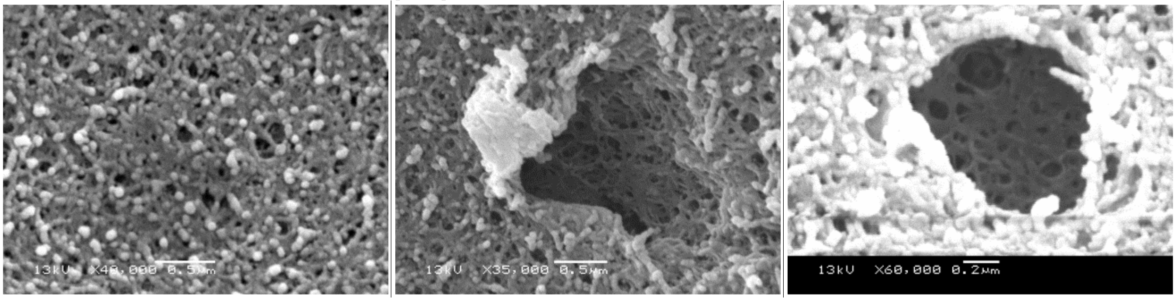

Permutation 8: Column preparation up to 100% ethanol, CPD, uncoated

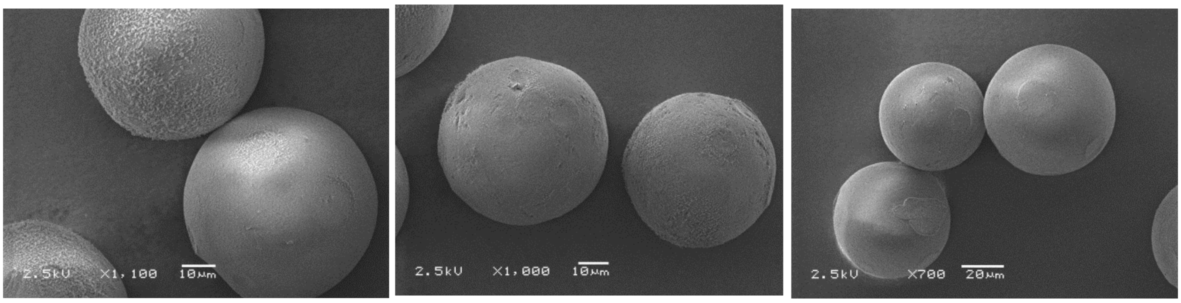

Permutation 8C: Column preparation up to 100% ethanol, CPD, coated

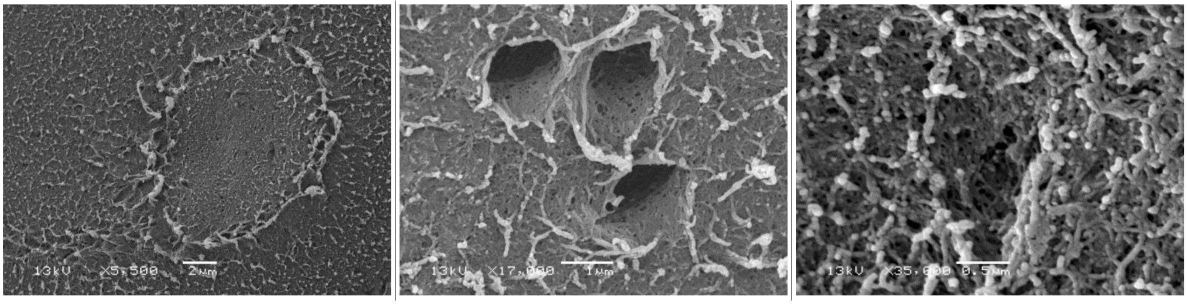

Permutation 9: Column preparation down to 20% ethanol, CPD, uncoated

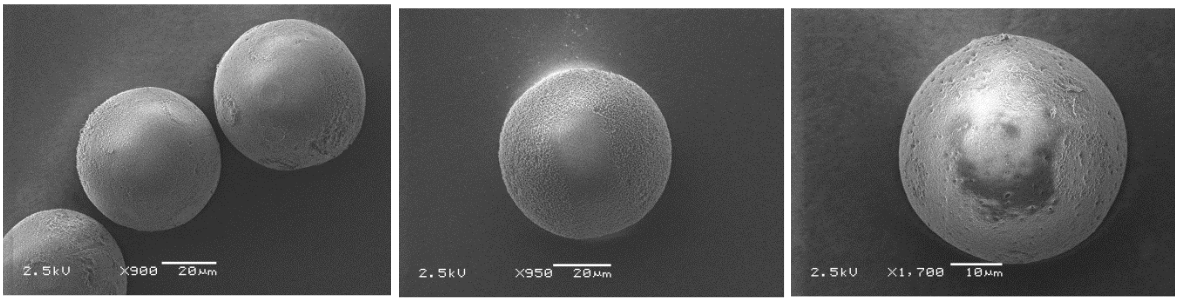

Permutation 9C: Column preparation down to 20% ethanol, CPD, coated

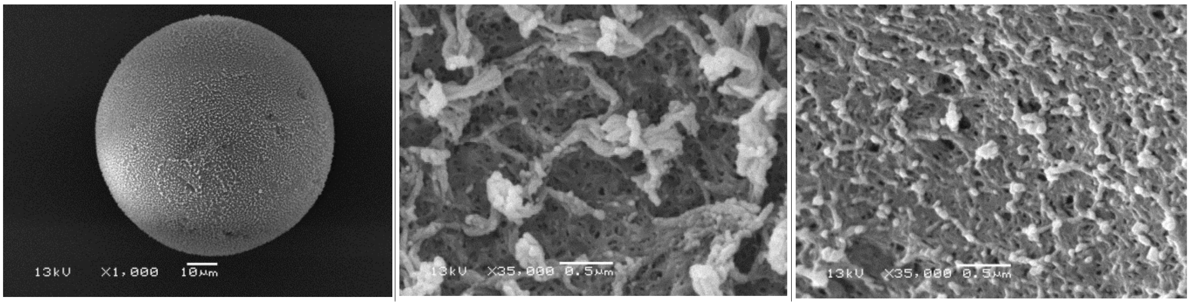

Figure 29: Further EDS data based upon preparation permutations using SEM (Note that other is often Aluminium, which is the sample stand material, Sulphur likely contaminant)

Permutation 1: No column preparation, no drying (environmental), uncoated

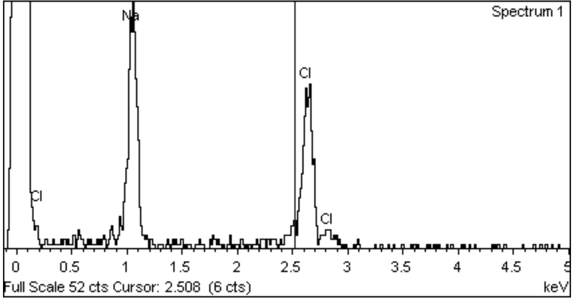

Element	Weight (%)	Atomic (%)
Sodium	35.25	40.56
Chlorine	52.49	39.16
Oxygen	12.26	20.28
Total	100	100

Permutation 1C: No column preparation, no drying (environmental), coated

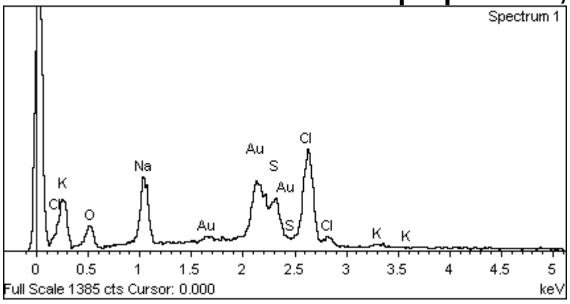

Element	Weight (%)	Atomic (%)
Potassium	1.63	0.97
Sodium	18.63	18.77
Sulphur	11.96	8.64
Chlorine	33.38	21.81
Oxygen	34.4	49.81
Total	100	100

Permutation 2: Column prep. to 100% Ethanol, no drying, uncoated

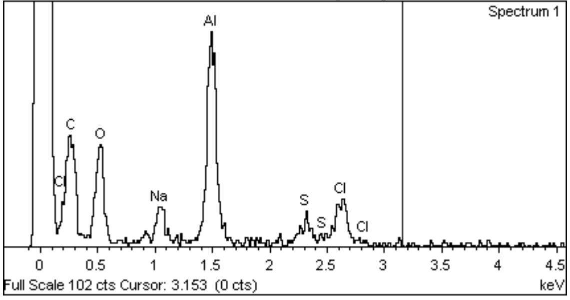

Element	Weight (%)	Atomic (%)
Carbon	8.77	13.62
Sodium	4.93	4
Sulphur	2.79	1.62
Chlorine	7.62	4.01
Oxygen	51.21	59.69
Aluminium	24.68	17.06
Total	100	100

Permutation 2C: Column prep. to 100% Ethanol, no drying, coated

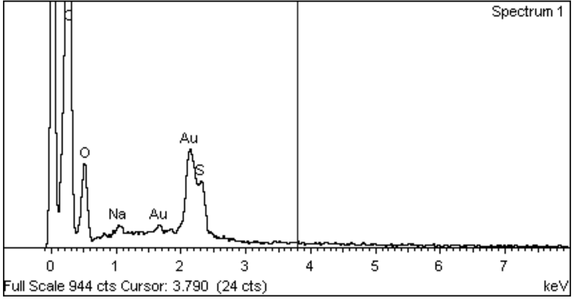

Element	Weight (%)	Atomic (%)
Carbon	70.4	76.94
Oxygen	26.4	21.67
Sodium	0.43	0.25
Sulphur	2.77	1.14
Total	100	100

Permutation 3: Column prep. to 20% ethanol, no drying, uncoated

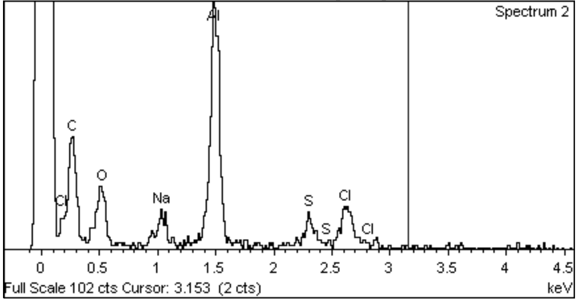

Element	Weight (%)	Atomic (%)
Sulphur	15.64	39.04
Sodium	11.86	15.98
Chlorine	29.29	15.6
Aluminium	43.21	29.38
Total	100	100

Permutation 3C: Column prep. to 20% ethanol, no drying, coated

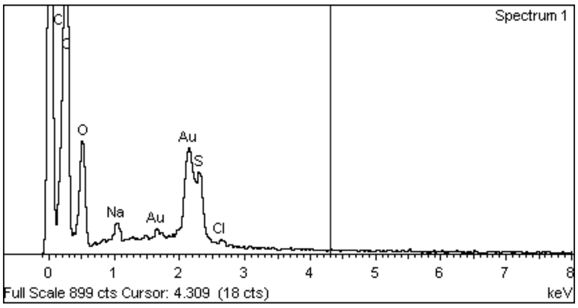

Element	Weight (%)	Atomic (%)
Carbon	62.56	70.3
Sodium	32.64	27.54
Sulphur	0.97	0.57
Chlorine	3.5	1.47
Oxygen	0.33	0.12
Total	100	100

Permutation 4: No column preparation, air dried, uncoated

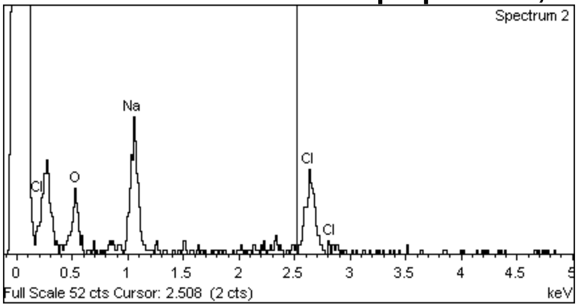

Element	Weight (%)	Atomic (%)
Sodium	35.48	40.67
Chlorine	52.18	38.91
Oxygen	12.34	20.42
Total	100	100

Permutation 4C: No column preparation, air dried, coated

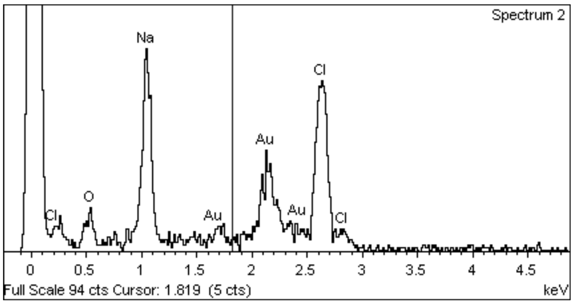

Element	Weight (%)	Atomic (%)
Sodium	36.47	41.6
Chlorine	50.84	37.6
Oxygen	12.69	20.8
Total	100	100

Permutation 5: Column prep. to 100% Ethanol, air dried, uncoated

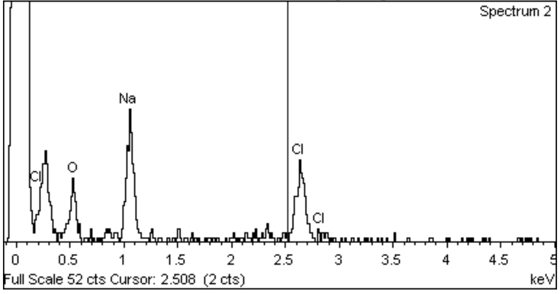

Element	Weight (%)	Atomic (%)
Oxygen	35.48	40.75
Sodium	52.18	38.87
Chlorine	12.34	20.38
Total	100	100

Permutation 5C: Column prep. to 100% Ethanol, air dried, coated

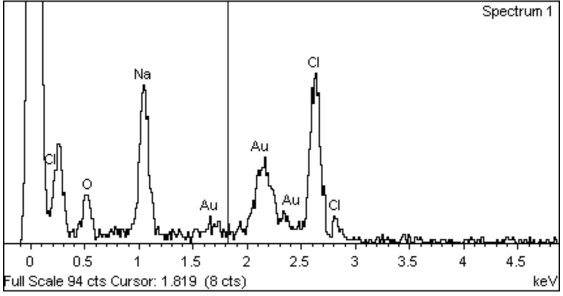

Element	Weight (%)	Atomic (%)
Sodium	33.47	39.01
Chlorine	54.89	41.49
Oxygen	11.64	19.5
Total	100	100

Permutation 6: Column prep. to 20% Ethanol, air dried, uncoated

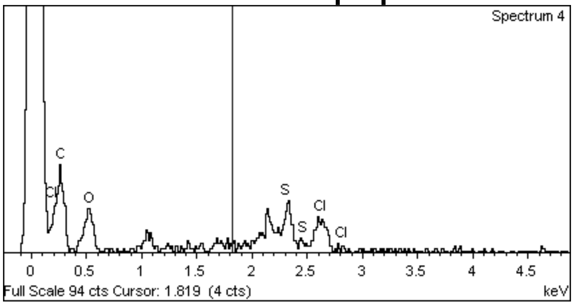

Element	Weight (%)	Atomic (%)
Sulphur	0.79	0.36
Chlorine	3.64	2.91
Oxygen	67.54	51.52
Carbon	28.03	45.21
Total	100	100

Permutation 6C: Column prep. to 20% Ethanol, air dried, coated

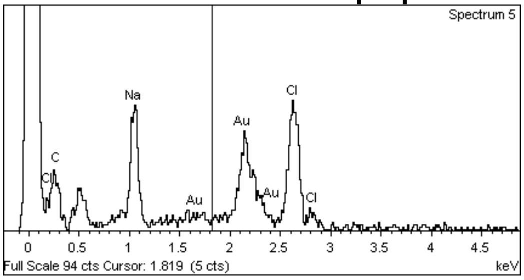

Element	Weight (%)	Atomic (%)
Sodium	1.61	1.01
Chlorine	2.33	0.95
Oxygen	67.54	63.89
Carbon	28.52	34.15
Total	100	100

Permutation 7: No column preparation, CPD, uncoated

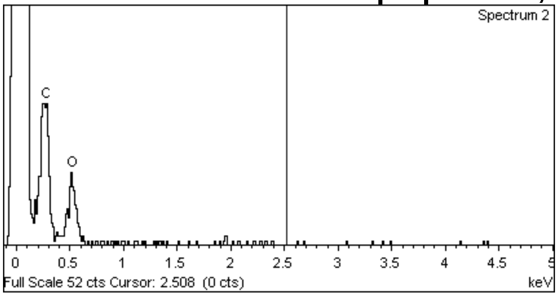

Element	Weight (%)	Atomic (%)
Carbon	27.29	33.33
Oxygen	72.71	66.67
Total	100	100

Permutation 7C: No column preparation, CPD, coated

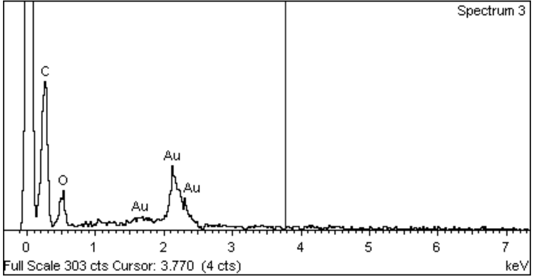

Element	Weight (%)	Atomic (%)
Carbon	60.94	67.51
Oxygen	39.06	32.09
Total	100	100

Permutation 8: Column prep. to 100% ethanol, CPD, uncoated

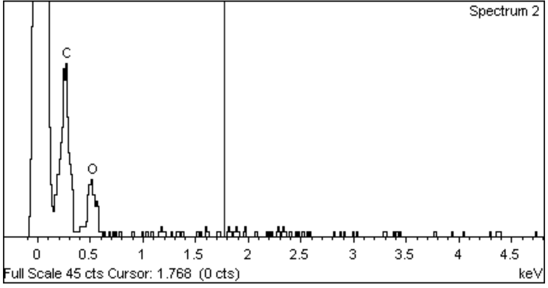

Element	Weight (%)	Atomic (%)
Carbon	27.29	33.33
Oxygen	72.71	66.67
Total	100	100

Permutation 8C: Column prep. to 100% ethanol, CPD, coated

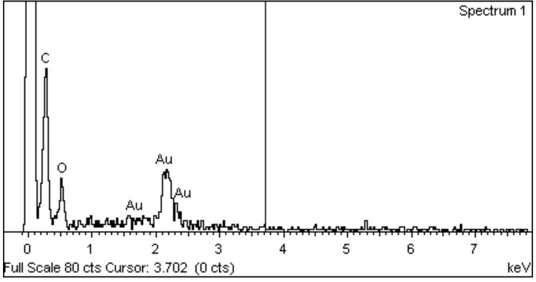

Element	Weight (%)	Atomic (%)
Carbon	57.54	64.35
Oxygen	42.46	35.65
Total	100	100

Permutation 9: Column prep. to 20% ethanol, CPD, uncoated

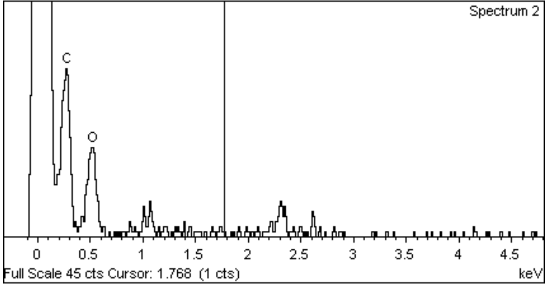

Element	Weight (%)	Atomic (%)
Carbon	27.29	33.33
Oxygen	72.71	66.67
Total	100	100

Permutation 9C: Column prep. to 20% ethanol, CPD, coated

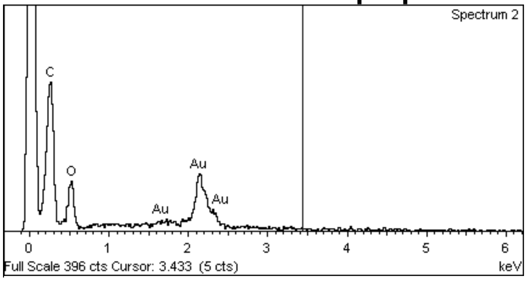

Element	Weight (%)	Atomic (%)
Carbon	65.21	71.4
Oxygen	34.79	28.6
Total	100	100

Figure 30: Enlarged selected images of an agarose (top) and ceramic (bottom) SEM images

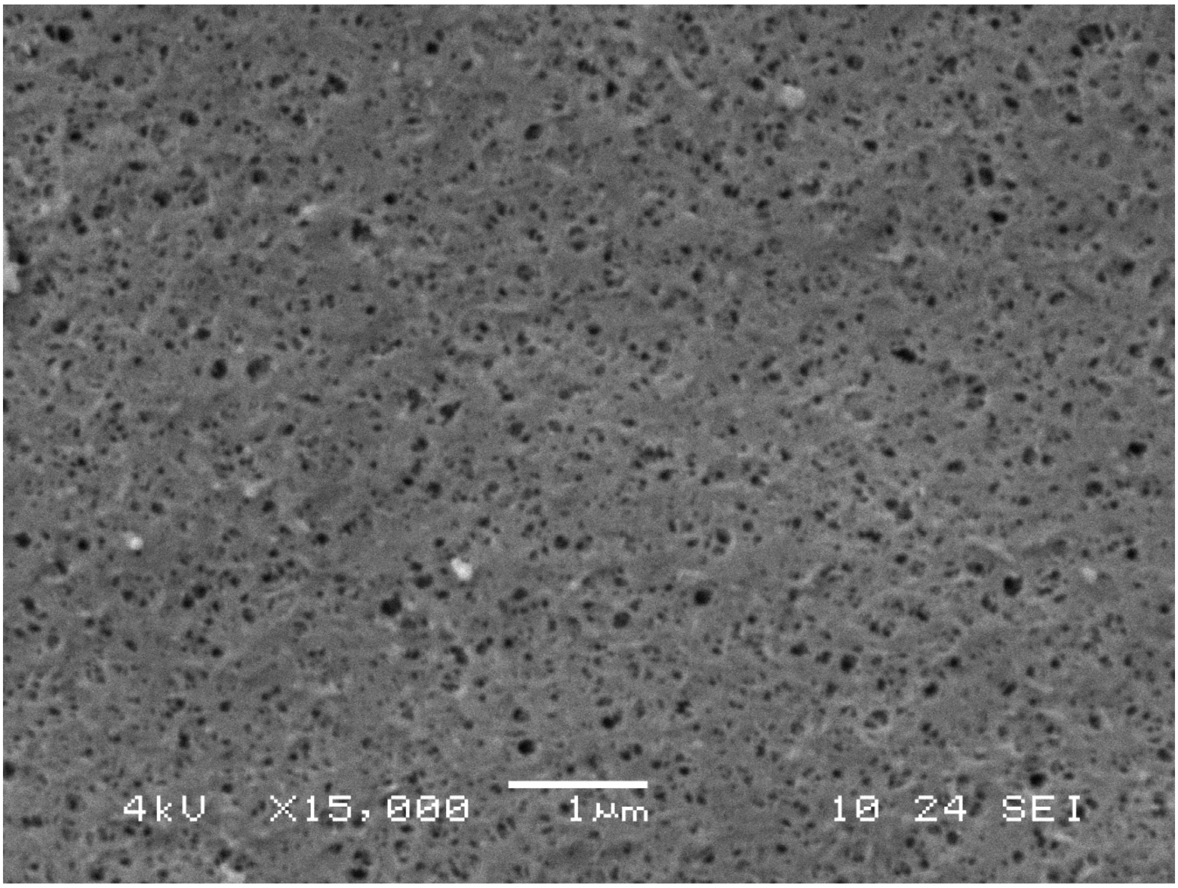

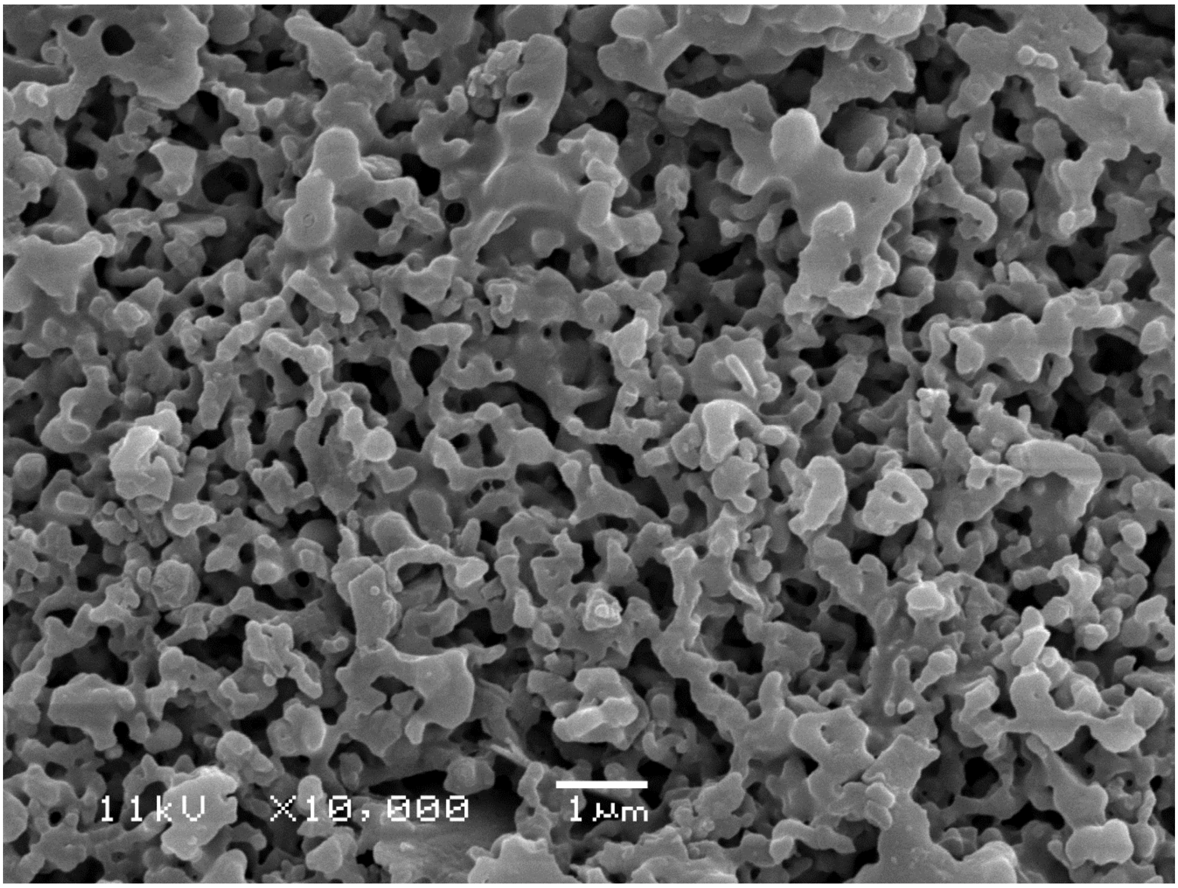

Figure 30: Further images of agarose and ceramic beads using thermionic SEM

Agarose

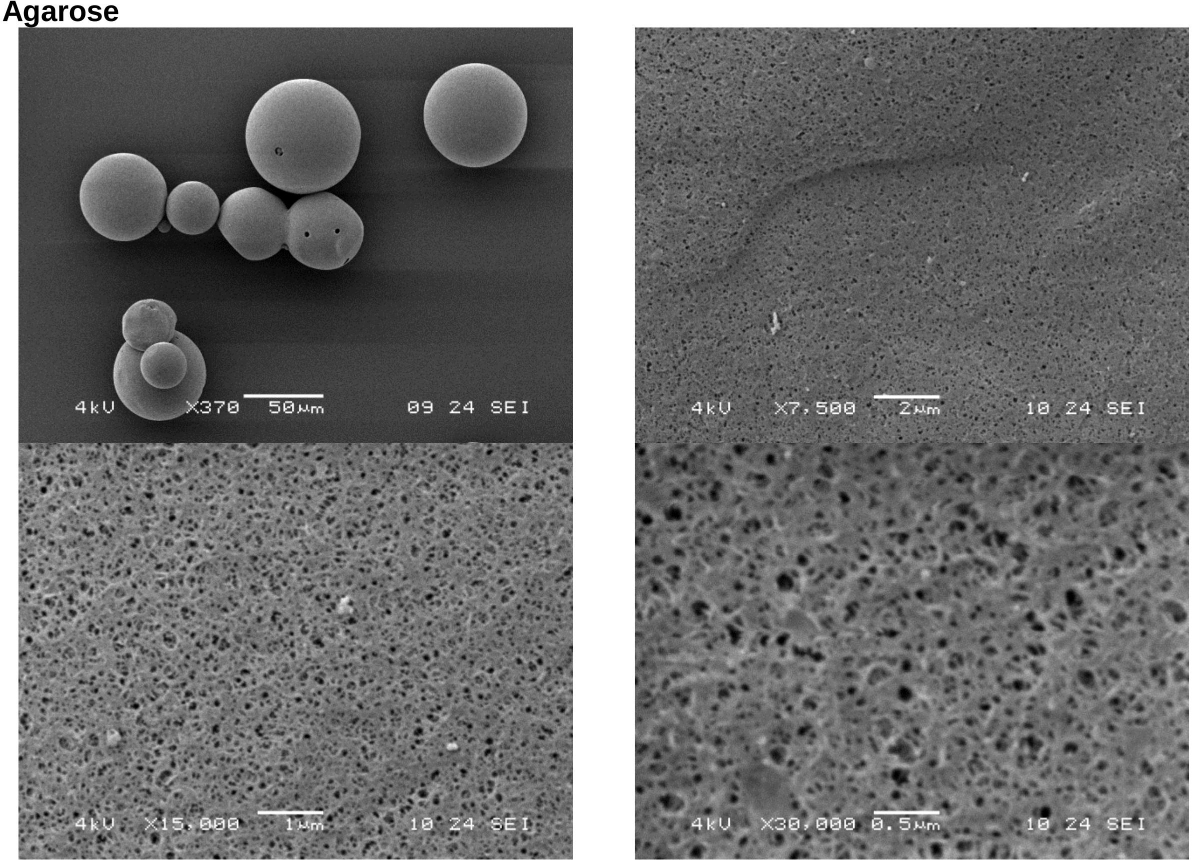

Ceramic

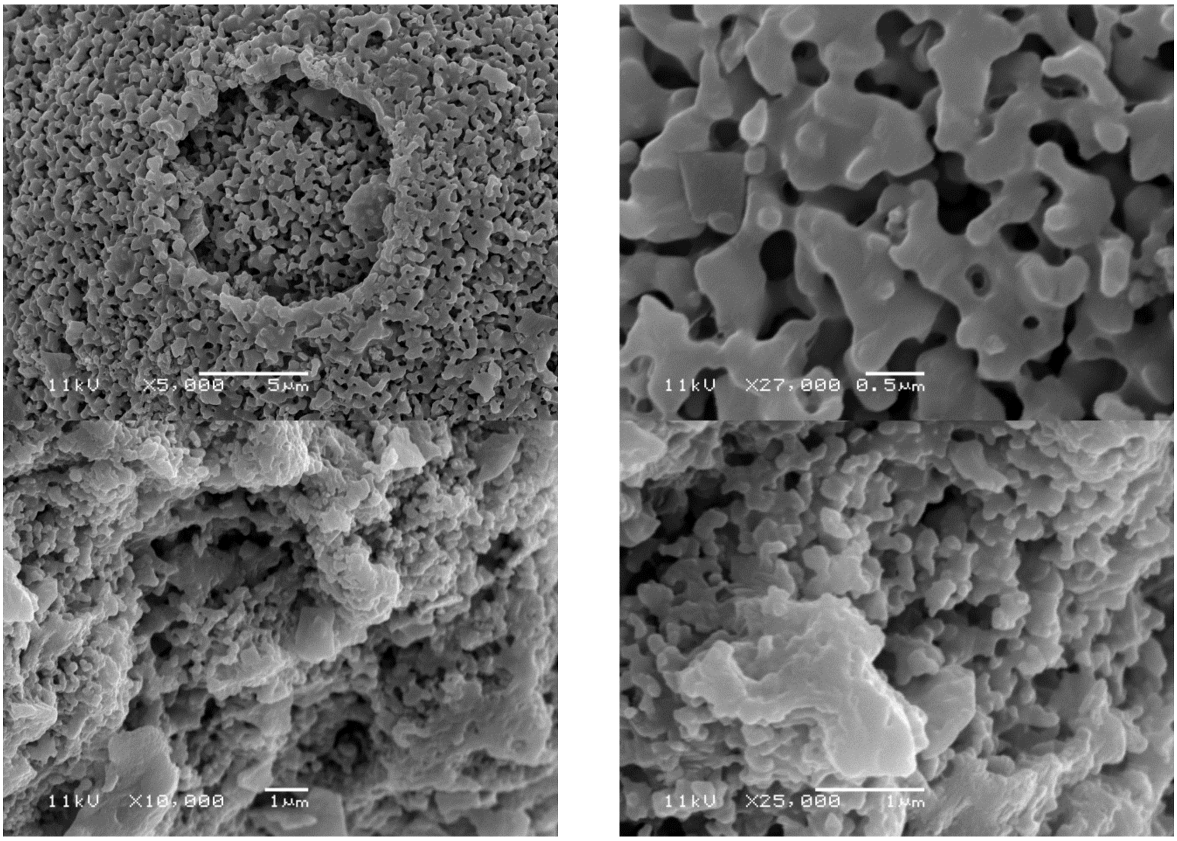

Figure 31: Selected enlarged images of cellulose beads using field emission SEM

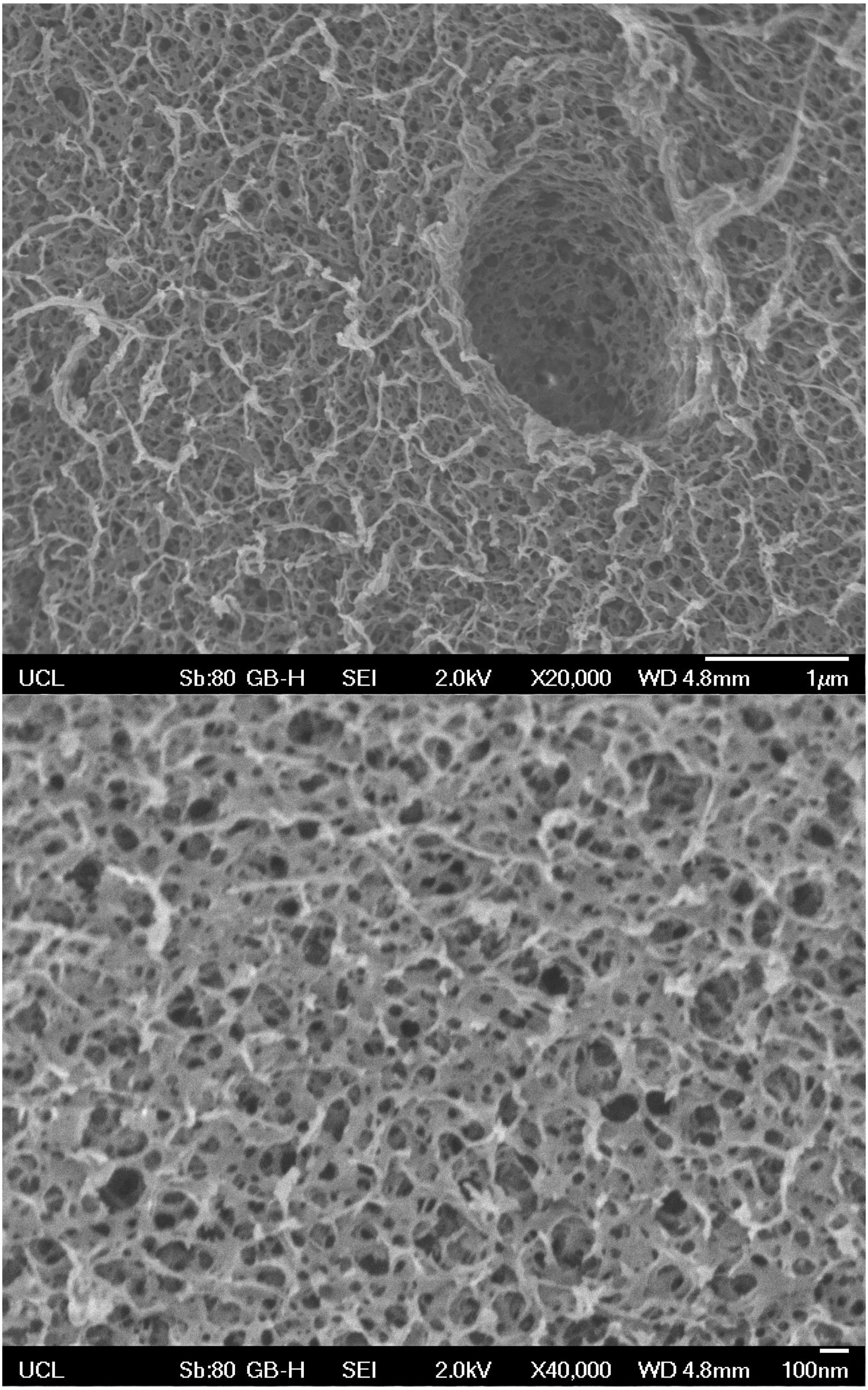

Figure 31: Further images of MEP HyperCel, with CPD and coating for preparation.

Field Emission Scanning Electron Microscopy used.

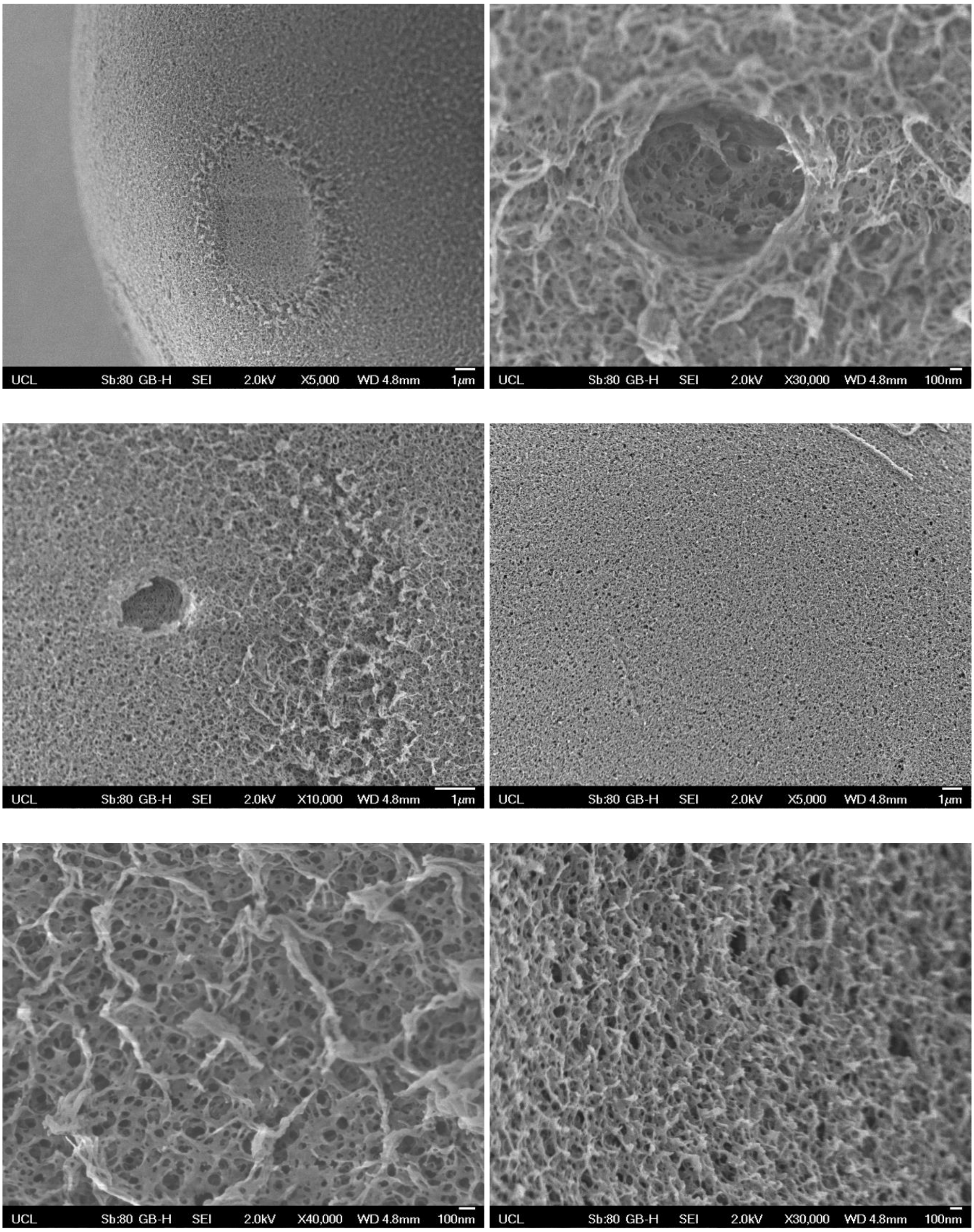

Figure 35: Further FIB slice and view images of agarose, cellulose and ceramic (2) beads

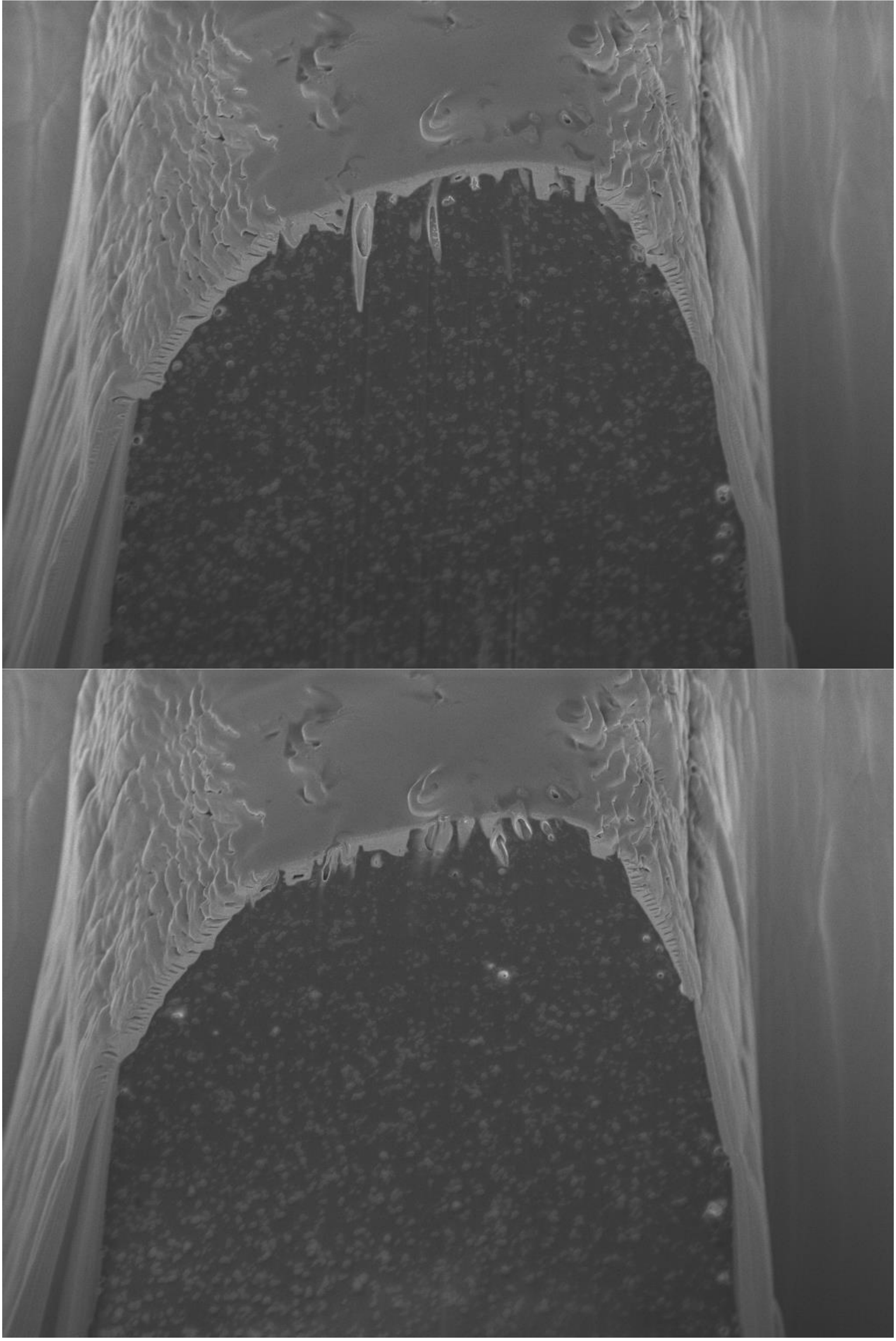

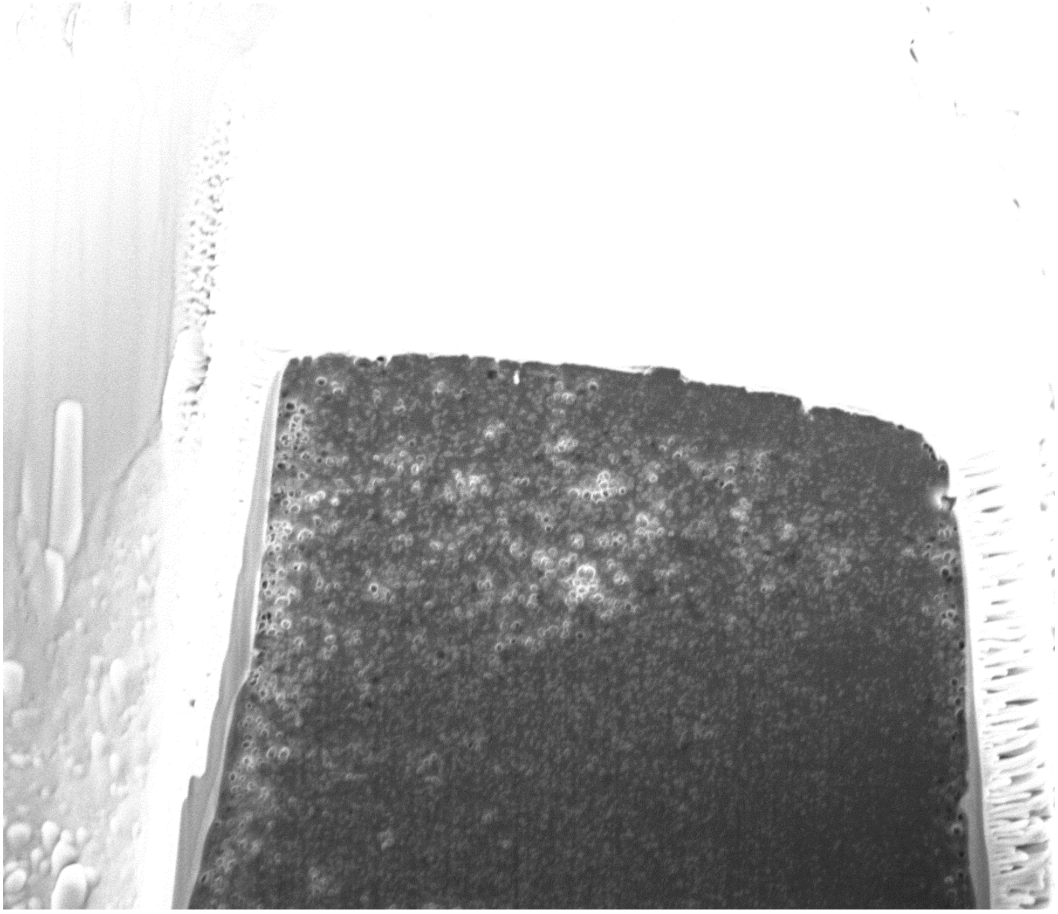

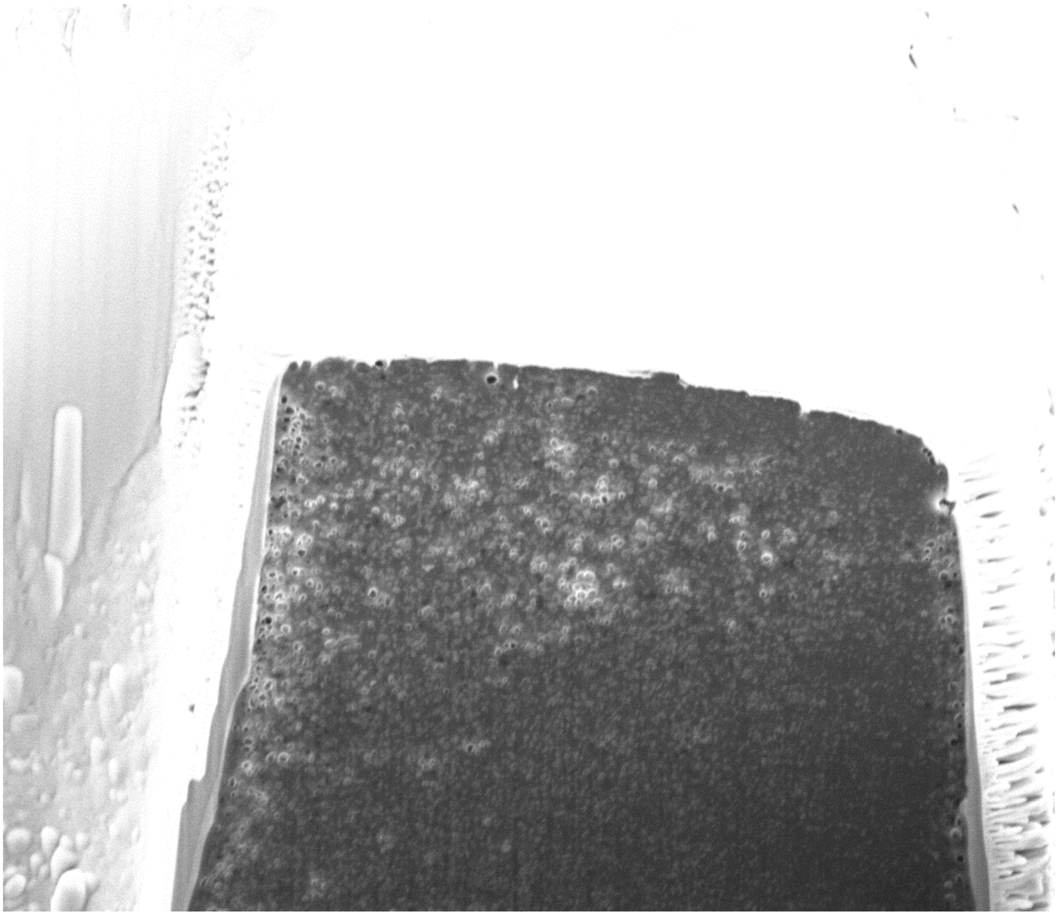

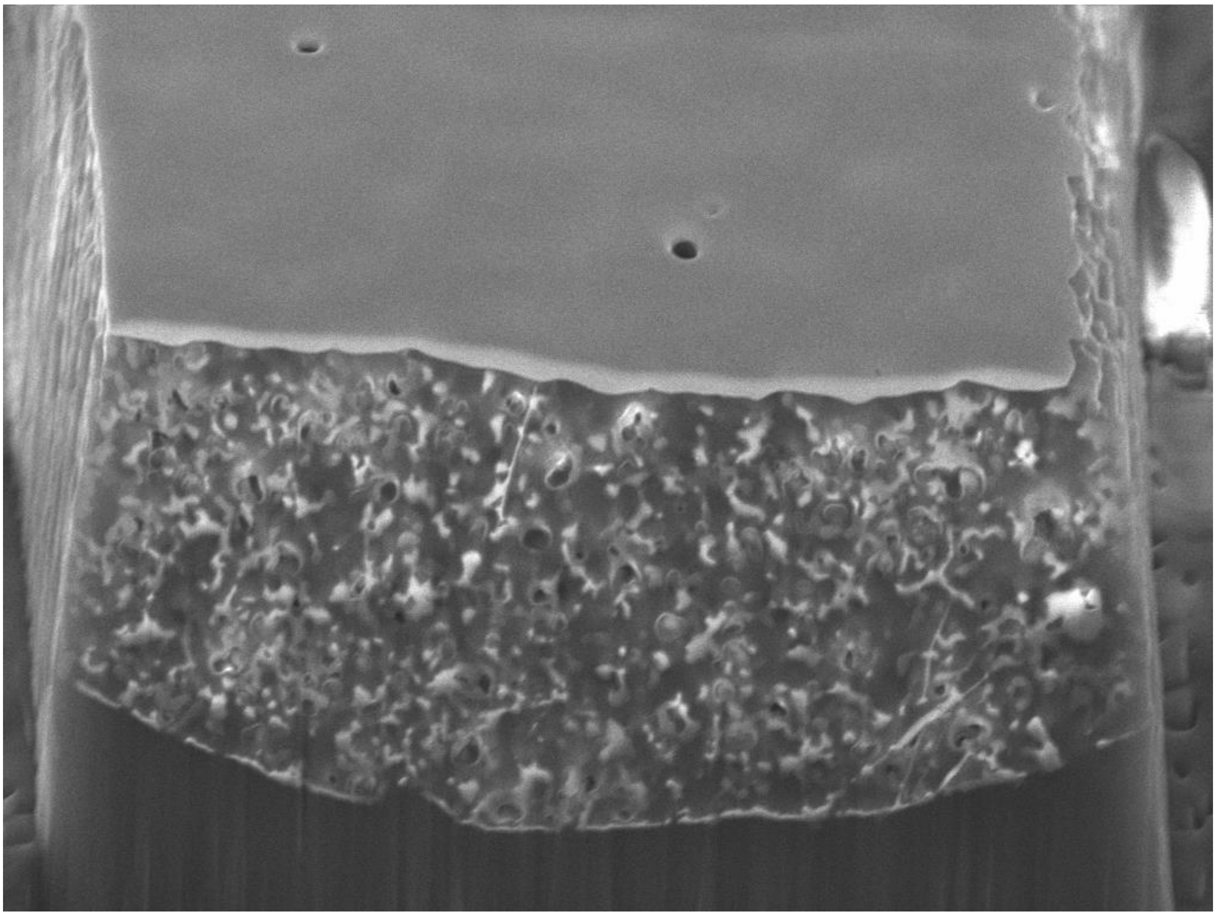

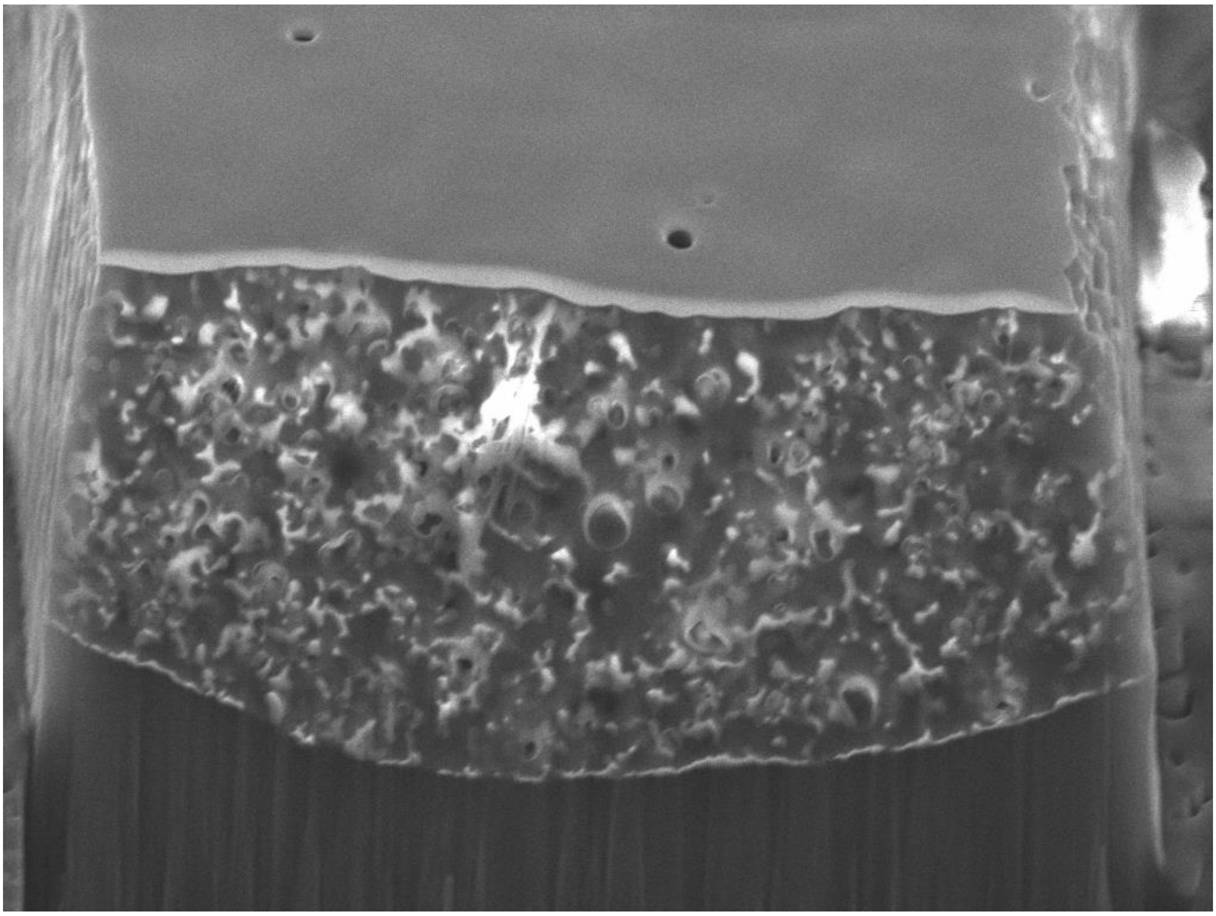

Chapter 3

Figure 44: Optimisation results for KeV values, green box – good quality, yellow box – beads visible but poorer than others, red – no definition, ↓ – carried forward to next stage.

Agarose and cellulose (Identical findings) – Final selection being Silver 100KeV at stage 3.

Stage 1 - Copper

KeV	80	90	100	110	120	130	140	150	160	170	180	190	200	210	220
	🟥	🟥	🟥	🟥	🟥	🟥	🟥	🟥	🟥	🟥	🟥	🟥	🟥	🟥	🟥

Stage 1 - Molybdenum

KeV	80	90	100	110	120	130	140	150	160	170	180	190	200	210	220
	🟥	🟨	🟩 ↓	🟨	🟨	🟥	🟥	🟥	🟥	🟥	🟥	🟥	🟥	🟥	🟥

Stage 1 - Silver

KeV	80	90	100	110	120	130	140	150	160	170	180	190	200	210	220
	🟥	🟨	🟩 ↓	🟩 ↓	🟨	🟨	🟥	🟥	🟥	🟥	🟥	🟥	🟥	🟥	🟥

Stage 1 - Tungsten

KeV	80	90	100	110	120	130	140	150	160	170	180	190	200	210	220
	🟥	🟥	🟥	🟥	🟥	🟥	🟥	🟥	🟥	🟥	🟥	🟥	🟥	🟥	🟥

Stage 2 - Molybdenum

KeV	95	100	105
	🟨	🟩 ↓	🟨

Stage 2 – Silver

KeV	95	100	105	110	115
	🟨	🟩 ↓	🟨	🟨	🟨

Ceramic – Final selection being Tungsten 140KeV at Stage 3.

Stage 1 - Copper

KeV	80	90	100	110	120	130	140	150	160	170	180	190	200	210	220
	🟥	🟥	🟥	🟥	🟥	🟥	🟥	🟥	🟥	🟥	🟥	🟥	🟥	🟥	🟥

Stage 1 - Molybdenum

KeV	80	90	100	110	120	130	140	150	160	170	180	190	200	210	220
	🟥	🟥	🟥	🟥	🟥	🟥	🟥	🟨	🟩 ↓	🟨	🟥	🟥	🟥	🟥	🟥

Stage 1 - Silver

KeV	80	90	100	110	120	130	140	150	160	170	180	190	200	210	220
	🟥	🟥	🟥	🟥	🟥	🟨	🟨	🟩 ↓	🟩 ↓	🟨	🟥	🟥	🟥	🟥	🟥

Stage 1 - Tungsten

KeV	80	90	100	110	120	130	140	150	160	170	180	190	200	210	220
	🟥	🟥	🟨	🟨	🟨	🟩 ↓	🟩 ↓	🟩 ↓	🟨	🟨	🟥	🟥	🟥	🟥	🟥

Stage 2 - Molybdenum

KeV	155	160	165
	🟨	🟩 ↓	🟨

Stage 2 – Silver

KeV	145	150	155	160	165
	🟨	🟩 ↓	🟨	🟨	🟨

Stage 2 - Tungsten

KeV	125	130	135	140	145	150	155
	🟨	🟨	🟩	🟩 ↓	🟩	🟨	🟨

Figure 46 – Enlarged versions of agarose, cellulose and ceramic packed bed slices.

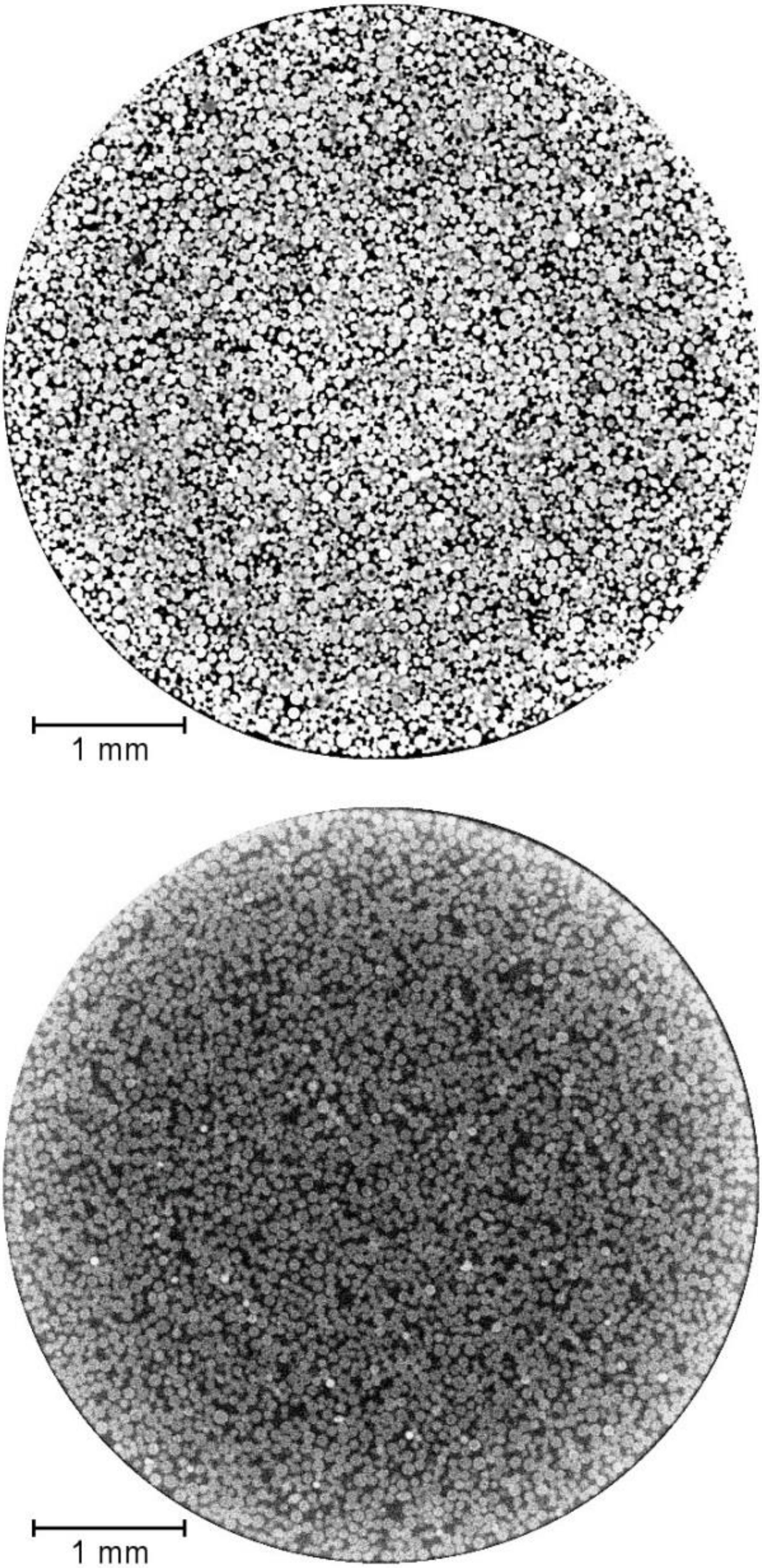

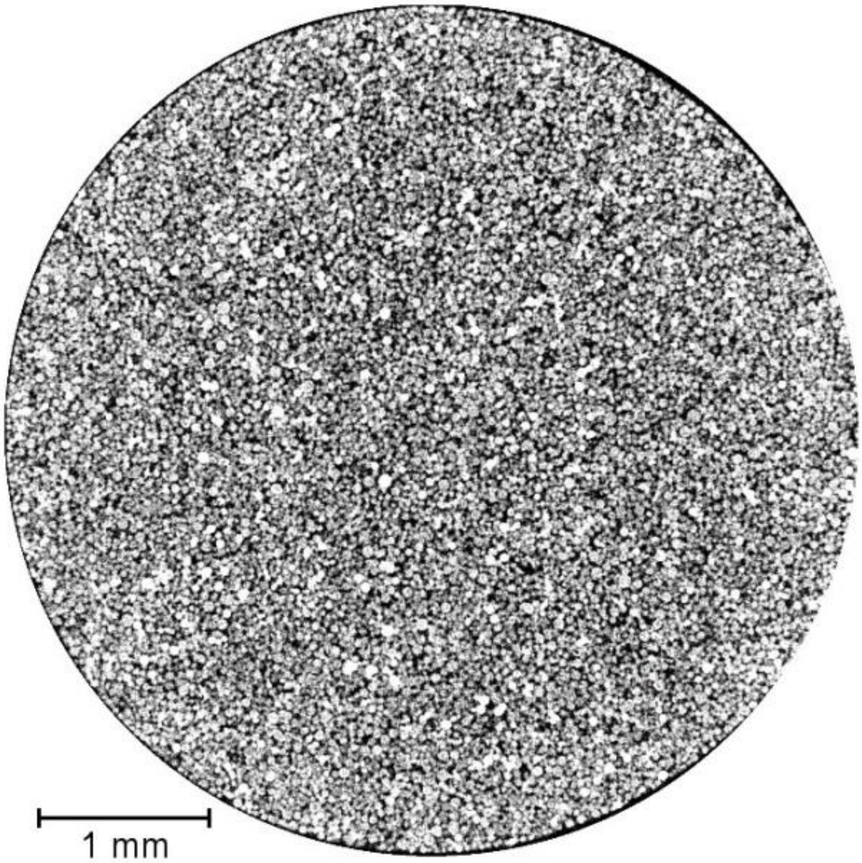

Figure 47 – Enlarged version of ceramic packed bed slice imaged using a Zeiss Versa 520

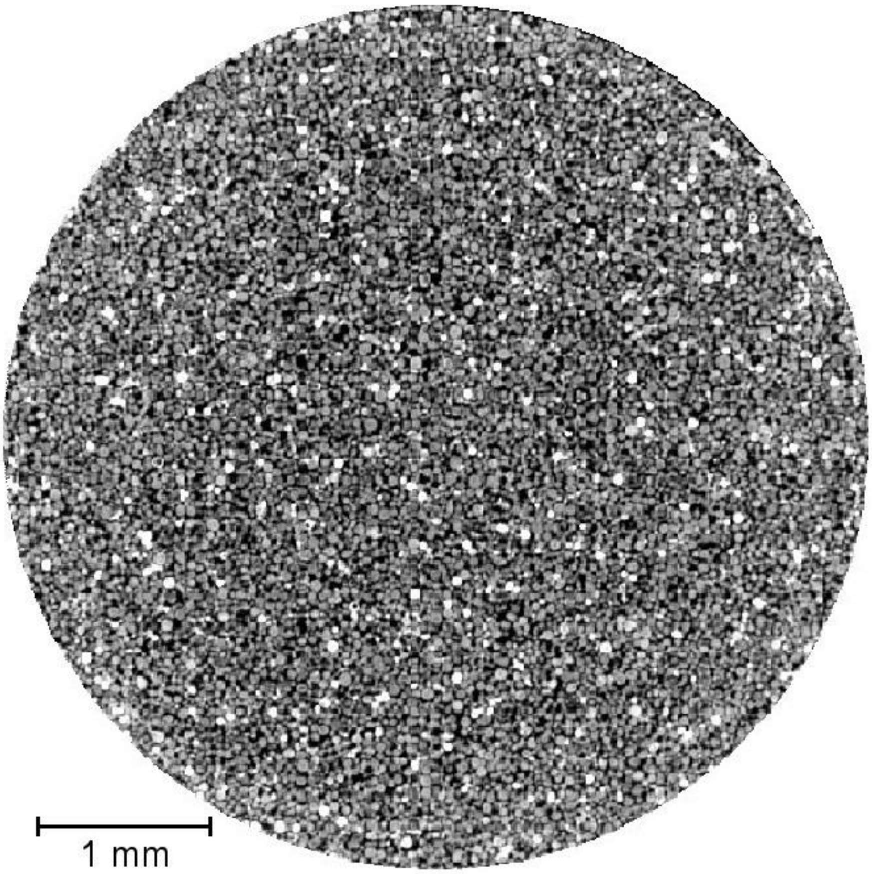

Chapter 4

Figure 56 and **57**: Enlarged distance map at the packed bed scale and TauFactor readout.

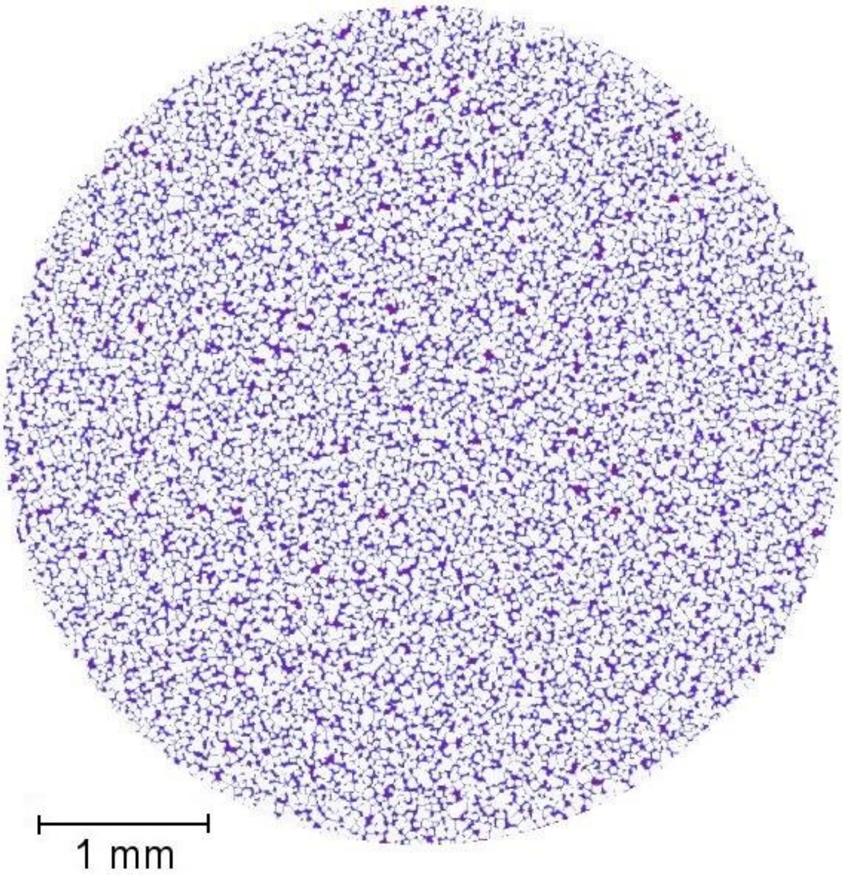

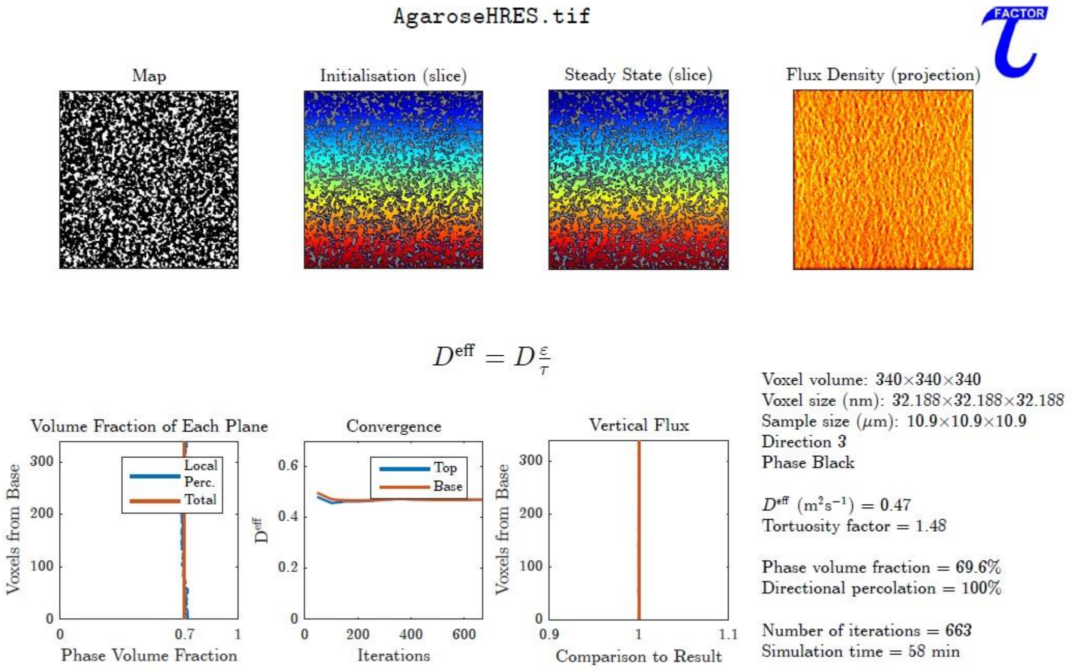

$$D^{\mathrm{eff}} = D\frac{\varepsilon}{\tau}$$

Voxel volume: 340×340×340
Voxel size (nm): 32.188×32.188×32.188
Sample size (μm): 10.9×10.9×10.9
Direction 3
Phase Black

D^{eff} ($\mathrm{m^2s^{-1}}$) = 0.47
Tortuosity factor = 1.48

Phase volume fraction = 69.6%
Directional percolation = 100%

Number of iterations = 663
Simulation time = 58 min

Table 7: Statistical determination examples of similarity or difference, with a 5% confidence interval selected. Tables below used analysis of variance via t and F tests: Values below 5% indicate a statistical likelihood that the means or variance are in different to each other, with findings above 5% suggesting that the difference in values is due to random variation. Results are presented to 2 decimal places.

1 - Means of ADJ and HRES (same volume) bead volume porosity are the same								
Agarose	32.76%	True	Cellulose	46.89%	True	Ceramic	34.64%	True
2 - Means of HRES geometric and transfer tortuosity are different								
Agarose	1.38%	True	Cellulose	2.76%	True	Ceramic	4.15%	True
3 - Different SA/V ratio of ADJ and HRES (same volume) bead volumes								
Agarose	0%	True	Cellulose	0%	True	Ceramic	0%	True
4 - Different average pore size of ADJ and HRES bead volumes								
Agarose	0%	True	Cellulose	0%	True	Ceramic	0%	True
5 - Mean geometric tortuosity is different between FIB and HRES X-ray CT								
Agarose	0%	True	Cellulose	0%	True	Ceramic	0%	True

Table 8: Statistical determination examples of similarity or difference at packed bed scale. Note that Zeiss imaging of agarose and cellulose samples was not possible.

1 - Means of packed bed porosity are different to the centre								
Agarose	1.33%	True	Cellulose	2.53%	True	Ceramic	0.04%	True
2 – Packed bed tortuosity is different to the centre compared to the edges								
Agarose	1.94%	True	Cellulose	2.81%	True	Ceramic	0.03%	True
3 - Variance of packed bed porosity is the same axially (averaged between 3 comparisons)								
Agarose	32.55%	True	Cellulose	44.8%	True	Ceramic	40.29%	True
4 - Different SA/V ratio between edge and centre sub-volumes								
Agarose	0.03%	True	Cellulose	0.48%	True	Ceramic	0%	True
5 – No difference in average pore diameter between edge and centre sub-volumes								
Agarose	25.64%	True	Cellulose	20.98%	True	Ceramic	25.64%	True
6 – No difference in porosity variance between Zeiss and Nikon images (averaged 3)								
Agarose not investigated			*Cellulose not investigated*			Ceramic	23.79%	True

Chapter 5

Figure 71: Agarose packed bed before use.

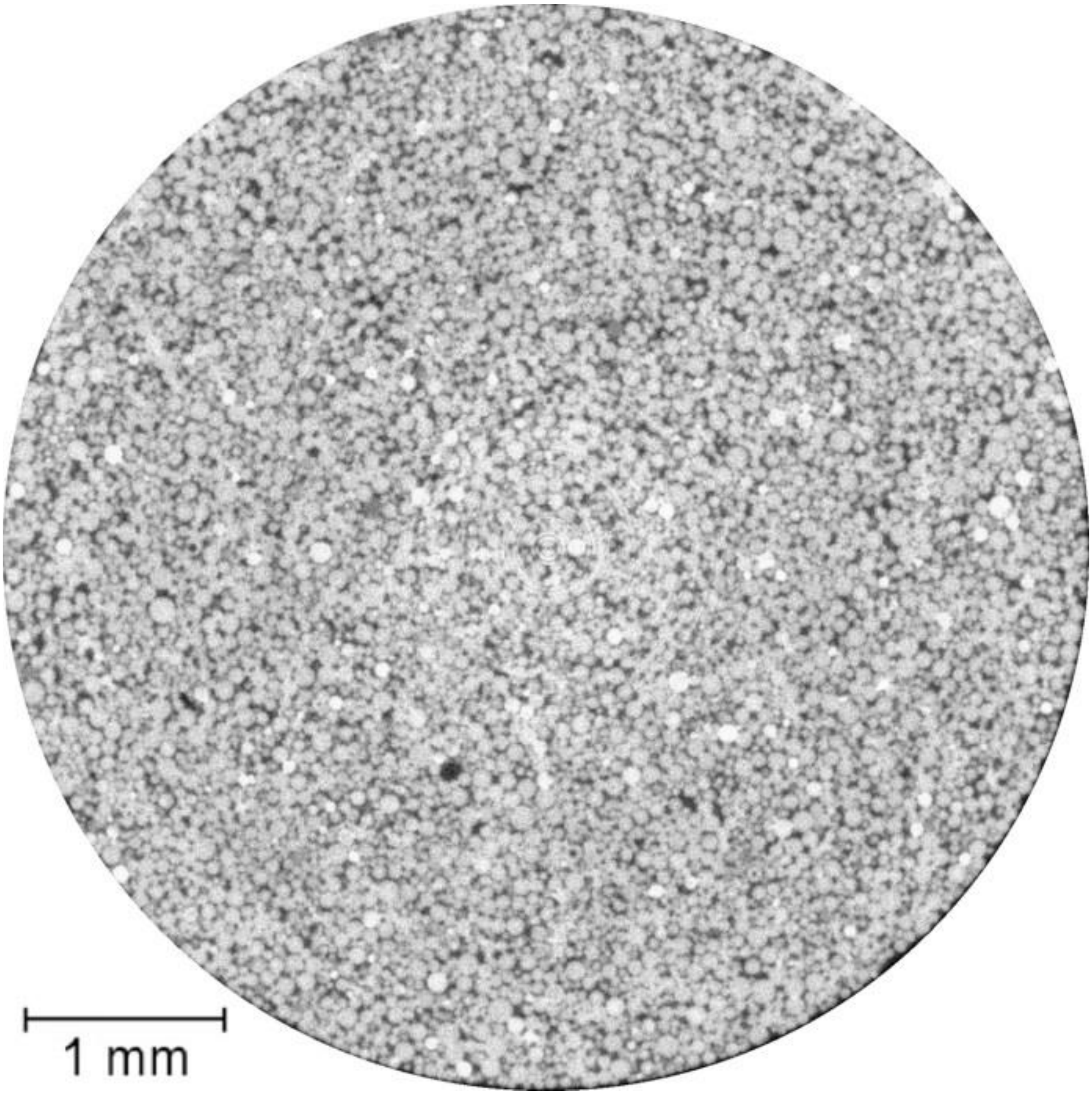

Figure 71: Agarose packed bed loaded using a 100g/L IgG feed.